MINERALOGY AND GEOCHEMISTRY OF IRON-OXIDES IN PRECAMBRIAN BANDED IRON FORMATIONS OF THE MIDDLEBACK RANGES, SOUTH AUSTRALIA

William Mark Keyser

This thesis is submitted for the degree of Doctor of Philosophy

in the

School of Chemical Engineering and Advanced Materials,

Faculty of Engineering, Computer and Mathematical Sciences

at

The University of Adelaide

THE UNIVERSITY of ADELAIDE

June 2019

TABLE OF CONTENTS

ABSTRACT

The Gawler Craton in South Australia is host to hundreds of Fe-rich deposits of varying types, most well-known are those of iron-oxide copper gold (IOCG) type within the ~1.6 Ga Olympic Cu-Au Province. However, only iron ore deposits of the Archean-aged Middleback Ranges (Eyre Peninsula) belt are unequivocally recognized as being banded iron formation (BIF)-derived. Although other deposits are alleged to be of BIF origin, their formation remains ill-constrained. Petrography and geochemistry of iron-oxides from the Middleback Ranges are studied at various scales of observation to constrain ore formation in BIFs from a terrane with a protracted geological history. The age, petrography and geochemistry of granites and mafic lithologies associated with the ores are used to constrain ore formation from deposition to ore enrichment. Several Fe-rich prospects from different parts of the Gawler Craton are studied in further detail to test the reliability of iron-oxides to track ore formation.

Petrography and trace elements signatures of iron-oxides from deposits along the Middleback Ranges indicate domain heterogeneity throughout the belt with respect to depositional environment and interaction with fluids of both granitic (U, W, Sn) and mafic affiliation (Cr, Ni, Zn). The discovery of U-bearing hematite in BIF ores is followed by LA-ICP-MS U–Pb dating in one prospect, Iron Count. The age (~1790 Ma) is concordant with monazite ages in the same sample and coincident with emplacement of the adjacent Wertigo Granite. This proves the reliability of hematite for dating the overprinting events that contributed to upgrading of BIF to ore.

Archean ages are documented from SHRIMP dating of zircon in granites (3.0-3.24 Ga) adjacent to ore along the belt and for amphibolites (~2.5 Ga) within the BIFs. The youngest age (~780 Ma) is obtained from dolerites crosscutting the ores, the first confirmation of Gairdner-affiliated dikes in the Eyre Peninsula. This supports an Archean environment of BIF

deposition post-dating the granite basement and contemporaneous with mafic magmatic activity. The youngest tectono-magmatic event is also recorded by U–Pb dating of Iron Knight hematite (~680 Ma). Alkali-calcic alteration of granites, typical of ~1.6 Ga Hiltaba granitoids, gives indication for undiscovered IOCG mineralization.

Iron-oxides from the Island Dam prospect within the Olympic Cu-Au Province show both BIF-like and IOCG (W-Sn-rich) signatures. The ore is associated with actinolite skarn formed on behalf of ~1.75 Ga Wallaroo volcano-sedimentary formation, with carbonate- and Fe-rich horizons affected by emplacement of Hiltaba-aged granitoids.

High-grade, Zr- and Ti-rich hematite from Peculiar Knob deposit (Mount Woods Inlier, northern Gawler Craton) was studied from micron- to nanoscale. Baddeleyite (nm-wide needles in hematite) accounts for high-Zr (up to 650 ppm) in hematite whereas interstitial zircon gives an age of ~1.74 Ga, concordant with the Kimban Orogeny. The ore, previously considered BIF, is re-interpreted as a metamorphosed Fe-rich sediment with detrital titanomagnetite sourced from mafic rocks, and also featuring a Hiltaba overprint (W-, Nb-, Sb-, Sn-rich rims in hematite).

Whereas BIF-hosted iron-oxides share generic characteristics, the transformation from BIF to ore must be understood in the context of the local geological setting underpinned by sound petrographic characterization at appropriate scales. The petrographic and geochemical approach used here, combined with hematite dating, can be used to understand ore genesis. Bridging micron- to nano- scales of observation gives insights into trace element incorporation into, and later release from, iron-oxides.

DECLARATION

I certify that this work contains no material which has been accepted for the award of any other degree or diploma in my name, in any university or other tertiary institution and, to the best of my knowledge and belief, contains no material previously published or written by another person, except where due reference has been made in the text. In addition, I certify that no part of this work will, in the future, be used in a submission in my name, for any other degree or diploma in any university or other tertiary institution without the prior approval of the University of Adelaide and where applicable, any partner institution responsible for the joint-award of this degree.

I acknowledge that copyright of published works contained within this thesis resides with the copyright holder(s) of those works.

I also give permission for the digital version of my thesis to be made available on the web, via the University's digital research repository, the Library Search and also through web search engines, unless permission has been granted by the University to restrict access for a period of time.

Signed ___ ___ Date 02/06/2019

ACKNOWLEDGEMENTS

I would like to express my deepest gratitude towards my academic supervisors, Dr. Cristiana Ciobanu and Prof. Nigel Cook, for their support, encouragement and guidance, without which none of this would have been possible. Cristi, thank you for your determination to make me better, for your help on late night analytical sessions and for always being ready and willing to help, no matter the time or day. Nigel, thank you for being patient and for always having positive words. Thank you both for the tremendous amount of time and effort you have dedicated to me over the past few years and for helping me reach the end.

I would also like to thank my external supervisor, Dr. Kathy Ehrig, for being incredibly supportive and giving direction throughout the course of my studies, and without whom the FOX project would not have been possible. I would also like to thank Dr. Geoff Johnson, Miss Holly Feltus, Mr. Steve Johnson and Mrs. Phung Nguyen for their geology expertise, interest in my project and willingness to sacrifice time to assist.

I would also like to thank the analytical staff at Adelaide Microscopy, Mr. Ken Neubauer, Mr. Animesh Basak, Dr. Ashley Slattery, and especially Dr. Benjamin Wade and Dr. Sarah Gilbert. I greatly appreciate your professionalism, patience and willingness to help, and for having positive attitudes while doing so.

A big thanks to my fellow PhD colleagues, Maria, Liam, Danielle, Urs, Mark, Nick, Jing, Wenyuan Gao, and especially Max V.-I., for being there with me throughout good and bad times and for all your help and advice over the years. Thanks also to those PhDs that were here before me, Alkis, Luke and Sasha.

Lastly, I am forever grateful for my amazing family and all my friends, and the tremendous amount of support they have provided me with throughout my studies. I would especially like to thank my parents, Bonnie and Mark, for their love, support and encouragement, and for raising me to be who I am today. Thank you, my brothers, Daniel and Matthew, my grandmother, Cora, and my stepparents Karen and Pearson, for your love and support, and for being here for me throughout this whole journey. Thanks to my close friends Trevor, Crystal and Natasha Padgett and Ben Mercer, for advice, great conversations and help through tough times. Thanks to the Liew Family, Calvin, Sheldon and Cherrie, for the support and good times over the years and for treating me like family. Lastly, thank you Prof. Chin-Ho Tsai for getting me into geology in the first place and for the continued support over the years.

PREFACE

This thesis comprises of a portfolio of manuscripts which have been submitted or published in international peer-reviewed journals. The journals in which these papers have been submitted or published are *'Ore Geology Reviews'* (Chapter 2, published), *'Lithos'* (Chapter 3, published), *'Precambrian Research'* (Chapter 4, published; Chapter 5, submitted), *'Proceedings of the 14th SGA Biennial Meeting'* (Chapter 6; extended conference abstract) and *'Minerals'* (Chapter 7, published). All five manuscripts and the extended abstract are closely related and summarize key findings and interpretations of iron-oxides and their trace element geochemistry within banded iron formation and related deposits, that were made as part of this project. Recommendations have been made at the end of this thesis as a direct result of the key findings of this research, and it is hoped that these are explored at a later date.

The six papers which form the basis of this thesis are:

1. Keyser, W., Ciobanu, C.L., Cook, N.J., Johnson, G., Feltus, H., Johnson, S., Dmitrijeva, M., Ehrig, K., Nguyen, P.T., 2018. Petrography and trace element signatures of iron-oxides in deposits from the Middleback Ranges, South Australia: From banded iron formation to ore. Ore Geology Reviews 93, 337-360.

2. Keyser, W., Ciobanu, C.L., Cook, N.J., Dmitrijeva, M., Courtney-Davies, L., Feltus, H., Gilbert, S., Johnson, G., Ehrig, K., 2019. Iron-oxides constrain BIF evolution in terranes with protracted geological histories: The Iron Count prospect, Middleback Ranges, South Australia. Lithos 324-325, 20-38.

3. Keyser, W., Ciobanu, C.L., Cook, N.J., Courtney-Davies, L., Kennedy, A., Wade, B.P., Ehrig, K., Dmitrijeva, M., Kontonikas-Charos, A., Feltus, H., Johnson, G., 2019.

Petrographic and geochronological constraints on the granitic basement to the Middleback Ranges, South Australia. Precambrian Research 324, 170-193.

4. Keyser, W., Ciobanu, C.L., Cook, N.J., Wade, B.P., Kennedy, A., Kontonikas-Charos, A., Ehrig, K., Feltus, H., Johnson, G. (in review). Episodic mafic magmatism in the Eyre Peninsula: defining syn- and post-depositional BIF environments for iron deposits in the Middleback Ranges, South Australia. Precambrian Research.
5. Keyser, W., Ciobanu, C.L., Cook, N.J., Courtney-Davies, L., Ehrig, K., Gilbert, S., McPhie, J., 2017. Links between sedimentary protoliths and IOCG-skarn alteration, Island Dam, South Australia. Proceedings of the 14th SGA Biennial Meeting, Québec, Canada, August 20-23rd, 2017. ISBN: 978-2-9816898-0-1, Volume 3, 935-938.
6. Keyser, W., Ciobanu, C.L., Cook, N.J., Feltus, H., Johnson, G., Slattery, A., Wade, B.P., Ehrig, K., 2019. Mineralogy of zirconium in iron-oxides: A micron- to nanoscale study of hematite ore from Peculiar Knob, South Australia. Minerals 9, 224.

Key findings and implications of this work, as well as future avenues of research, are summarized in Chapter 8.

Chapter 9 contains all supplementary material for the main papers outlined above, as well as additional co-authored publications and conference abstracts that have been generated during the PhD candidature. The additional material is as follows:

A. Supplementary material for Chapter 2 (Paper 1).

B. Supplementary material for Chapter 3 (Paper 2).

C. Supplementary material for Chapter 4 (Paper 3).

D. Supplementary material for Chapter 5 (Paper 4).

E. Supplementary material for Chapter 6 (Paper 5).

F. Supplementary material for Chapter 7 (Paper 6).

G. Dmitrijeva, M., Metcalfe, A.V., Ciobanu, C.L., Cook, N.J., Frenzel, M., Keyser, W.M., Johnson, G., Ehrig, K., 2018. Discrimination and variance structure of trace element signatures in hematite: a case study of BIF-mineralization from the Middleback Ranges, South Australia. Mathematical Geosciences 50, 381-414.

H. Courtney-Davies, L., Ciobanu, C.L., Verdugo-Ihl, M.R., Slattery, A., Cook, N.J., Dmitrijeva, M., Keyser, W.M., Wade, B.P., Domnick, U.I., Ehrig, K., Xu, J., Kontonikas-Charos, A., (in review). Zircon down to the nanoscale: A record of metasomatic processes leading to large magmatic-hydrothermal ore systems. Minerals.

I. Keyser, W.M., Ciobanu, C.L., Cook, N.J., Feltus, H., Johnson, S., Johnson, G., Ehrig, K., Courtney-Davies, L., Kamenetsky, V.S., 2016. BIF-style iron deposits of the Middleback Ranges, South Australia: Trace element signatures of Fe-oxides and implications for ore formation. Australian Earth Science Convention 2016, 'Uncover Earth's Past to Discover Our Future', Adelaide, Australia, June 26th–30th.

J. Ciobanu, C.L., Cook, N.J., Ehrig, K., Keyser, W.M., Courtney-Davies, L., Wade, B.P., Kamenetsky, V.S., Maunders, C., 2016. Towards a suitable natural standard for routine U-Pb dating of iron oxides. Australian Earth Science Convention 2016, 'Uncover Earth's Past to Discover Our Future', Adelaide, Australia, June 26th–30th.

K. Keyser, W.M., Ciobanu, C.L., Cook, N.J., Feltus, H., Johnson, S., Johnson, G., Ehrig, K., Courtney-Davies, L., Kamenetsky, V.S., 2016. Trace element signatures of iron-oxides in BIF-style iron deposits of the Middleback Ranges, South Australia. 35th

International Geological Congress, Cape Town, South Africa, August 25th–September 4th.

L. Ciobanu, C.L., Cook, N.J., Ehrig, K., Keyser, W.M., Courtney-Davies, L., Wade, B.P., Kamenetsky, V.S., Maunders, C., 2016. Iron-oxides: a versatile tool for geochemical fingerprinting and geochronology. 35th International Geological Congress, Cape Town, South Africa, August 25th–September 4th.

M. Dmitrijeva, M., Ciobanu, C.L., Metcalfe, A.V., Cook, N.J., Verdugo-Ihl, M.R., Keyser, W.M., Ehrig, K., 2017. Multivariate statistical analyses of LA-ICP-MS trace element data for iron-oxides: examples from genetically distinct ore deposits from South Australia. 18th Annual IAMG Conference, Perth, Australia, September 2nd-9th.

N. Dmitrijeva, M., Ciobanu, C.L., Metcalfe, A.V., Cook, N.J., Verdugo-Ihl, M.R., Keyser, W.M., Ehrig, K., 2017. Copula functions as a tool for statistical modelling of trace element signatures in iron-oxides: examples from South Australian ore deposits. 18th Annual IAMG Conference, Perth, Australia, September 2nd-9th.

O. Keyser, W.M., Ciobanu, C.L., Cook, N.J., Feltus, H., Slattery, A., Ehrig, K., 2018. Nanoscale mineralogy of zirconium in iron-oxides. Goldschmidt 2018 Conference, Boston, USA, August 12th–17th.

P. Keyser, W.M., Ciobanu, C.L., Cook, N.J., Courtney-Davies, L., Feltus, H., Johnson, G., Kennedy, A., Ehrig, K., 2018. Geological setting of BIF ores, Middleback Ranges, South Australia. 15th Quadrennial IAGOD Symposium, Salta, Argentina, August 28th–31st.

The final chapter of this thesis consists of a complete reference list of all publications cited within any of the manuscripts, chapters, supplementary and additional material submitted as a component this thesis.

CHAPTER 1

INTRODUCTION

CHAPTER 1: INTRODUCTION

Banded iron formations (BIFs) are a chemically precipitated rock type that result from complex mantle, tectonic and biospheric processes with a peak volume at ~2.4 Ga (Bekker et al., 2014 and references therein), and as such, play a crucial role in deciphering the geological history of Earth. They have a worldwide distribution and represent the most economically significant iron ore resources on the global scale. The scientific and economic importance of BIFs has catalyzed extensive studies that target their origins and formation mechanisms.

Early studies of BIFs focused on their global distribution, age constraints and stratigraphy, whereas sedimentary facies and basin analysis were a central focus of many later studies (James, 1954; MacLeod et al., 1963; Trendall, 1968). Current BIF research has addressed depositional environments and mechanisms (e.g., Gourcerol et al., 2016a; Rasmussen et al., 2019), digenesis and mineral crystallization (e.g., Alibert, 2016), oxidation and ore-forming processes (Hagemann et al., 2016 and references therein) and the orchestration of each of these topics in a temporal setting. Many of these topics are investigated through geochemical studies, since trace elements (including the rare earth elements, REE) in ore and specific component minerals have been shown to be valuable proxies for ancient seawater compositions from which BIFs precipitated and to infer depositional settings (Craddock et al., 2010; Planavsky et al., 2010). A large part of contemporary work centers on detailing the mineralogy and stratigraphic sequence of formations and constraining stages of deposition and enrichment.

While the conditions leading to the formation of BIFs are generally agreed upon (Holland, 2005), opinions remain equivocal regarding the depositional mechanisms, timing and environmental setting of BIFs. Other key research has focused on the later processes of transformation of BIF to high-grade iron ore, which has resulted in deposit-specific genetic

models for iron ore formation and has been comprehensively discussed by Hagemann et al. (2016). As such, a significant gap in BIF studies results from an inability to readily link field observations and petrographic and geochemical datasets with sequential stages of evolution of iron formations, from original BIF protore to high-grade iron ore. This includes how one of the main constituent minerals of BIF, iron-oxides, evolve, physically and chemically.

The iron-oxide group of minerals comprises more than 5 wt.% of Earth's crust and they are found in all types of rocks and ore deposits. Although composed only of essential iron and oxygen, the iron-oxides, mainly magnetite (Fe_3O_4) and hematite (Fe_2O_3), form a mineral series with numerous other species and thus can show broad compositional variation (e.g., Bowles et al., 2011). Magnetite and hematite are also known for their versality to replace one another by pseudomorphic replacement under redox conditions, an observation that can be used for petrological interpretations (Mücke and Cabral, 2005).

Classification diagrams, using large empirical electron microprobe datasets of minor element concentrations in the two iron-oxides, and showing specific fields for different deposit types, have become popular in recent years (e.g., Dupuis and Beaudoin, 2011). Many studies in the past 20 years have addressed the presence of trace elements in minerals following the development of laser-ablation inductively-coupled plasma mass spectrometry (LA-ICP-MS) analytical techniques that can accurately measure concentrations of elements down to ppm level (Cook et al. 2016 and references therein). The amount of trace element data for sulfides is still far greater than for iron-oxides due to uncertainty over the use of non-matrix-matched standards (Cook et al. 2016). However, following establishment of natural basalt material as a suitable standard for LA-ICP-MS trace element analysis of iron-oxides (Nadoll and Koenig, 2011), geochemical studies of iron-oxides from different deposits have greatly accelerated. Many of such studies have shown that the classification diagrams of Dupuis and Beaudoin

(2011) are highly simplistic and do not adequately reflect variation at the scale of a single deposit (e.g., Gourcerol et al., 2016b; Broughm et al., 2017; Wen et al., 2017; Yin et al., 2017).

The discovery of U-bearing (up to several wt.% UO_2), oscillatory-zoned hematite from Olympic Dam allowed U–Pb dating of this mineral using LA-ICP-MS with zircon as a standard (Ciobanu et al., 2013). Considering the meaningful ages obtained, the approach has been followed by testing the applicability of the method using solution standards (Courtney-Davies et al., 2016), and the reliability of hematite as mineral geochronometer has been assessed by high-precision, U–Pb ID–TIMS methods (Courtney-Davies et al., 2019a). Importantly, although bulk methods such as (U–Th)/^{21}Ne-(U–Th)/He have been applied to date hematite with ultra-low U concentration from BIFs (Farley and McKeon, 2015), the use of microbeam techniques such as LA-ICP-MS is important for hematite wherever grain-scale heterogeneity is observed. U–Pb dating using LA-ICP-MS has been successfully applied for the first time to low-U (up to 14 ppm) hematite from BIF ores (Keyser et al., 2019a, in review). Development of a matrix-matched standard for hematite using homogeneous material prepared synthetically (Courtney-Davies et al., 2019b) is currently ongoing.

Iron-oxide compositions can be quite variable regionally, or even locally, between individual BIFs as a result of the local tectonic setting of each formation, allowing for the use of their compositions to fingerprint domain heterogeneity throughout the same metallogenetic belt or evolving trends within a given deposit (e.g., Dmitrijeva et al., 2018; Keyser at al., 2018). Geochemical studies have also allowed improved discrimination of magmatic and hydrothermal generations of iron-oxides in deposits kin to IOCG type (e.g., Dare et al., 2015; Knipping et al., 2015).

1.1 Banded iron formations

1.1.1 Definition

Banded iron formations are Fe-rich Precambrian sedimentary chemical precipitates that display thin bedding comprised of iron-, silica- and carbonate-rich minerals (James, 1954; Gross, 1980; Trendall, 1983). The bedding occurs as bands ranging from macrobands (m-scale) to laminated mesobands (cm-scale) in thickness, giving them the characteristic striped appearance after which they have been named: banded iron formations (Holland, 2005; Klein, 2005). However, coarser grain-sized formations with crossbedding and lacking fine lamination have been referred to as granular iron formations (GIFs; Bekker et al., 2010, 2014). Despite hosting more than 90 % of the world's economic iron ores, prompting extensive studies on their origin, depositional environment, and spatial and temporal distribution, a lack of present-day analogues has left open many questions surrounding their origin and the processes by which they are enriched into iron ore.

James (1954, 1966) distinguished four major iron formation facies based on predominant iron minerals constituting iron layers: 1) *oxide*, hematite, magnetite, or both; 2) *carbonate*, siderite and ankerite; 3) *silicate*, iron silicate minerals; 4) *sulfide*, pyrite with lesser pyrrhotite and carbonates. James (1954) suggested that the progressive formation of minerals corresponding to these facies from oxide through sulfide reflected precipitation in successively more reduced environments. Although aspects of these classifications have since become outdated (e.g., sulfide-facies), these classifications served well for understanding the large variability present in different BIF settings. BIFs were further classified as (*Lake) Superior-type* or *Algoma-type* based on depositional environments and associated rock types by Gross (1980), and later the addition of the rare *Rapitan-type* was added (Young, 1976; James, 1983; Klein and Beukes, 1993).

The *Superior-type* iron formations were deposited in marine environments near passive margin continental shelves and are typically thick and can cover large areas up to 10^5 km^2, making them the largest of the iron formation types. These interbedded units consist of alternating layers of carbonates, quartzite and black shales with minor volcanic rocks. Classic examples of Superior-type iron formations include the Animikie Basin of North America, Hamersley Group (Western Australia), the Kaapvaal Craton (South Africa), Krivoy Rog-Kursk (Ukraine), the Singhbhum region (India), and the type locality Lake Superior region in the U.S.A (Fig. 1.1).

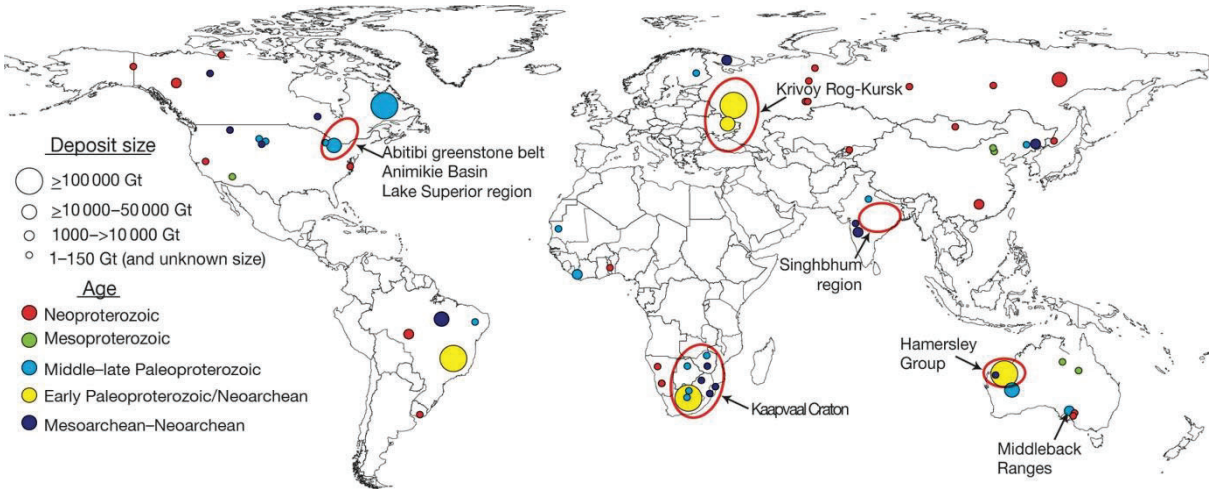

Figure 1.1: Major iron formations of the world with examples mentioned in the text circled in red. Modified after Bekker et al. (2014).

Algoma-type iron formations are smaller and are associated with volcanic arc regions or rift zones and result from exhalative-hydrothermal processes. These units form less extensive regions and rarely exceed 50 meters in thickness. Algoma-type iron formations are hosted within volcanic rocks and greywackes and can be found in greenstone belts of Eoarchean to Phanerozoic age such as the Abitibi greenstone belt in Ontario, Canada (Taner and Chemam, 2015). The *Rapitan-type* iron formations are rather limited in occurrence and are associated

with glaciogenic sediments of the Neoproterozoic ice age events during the so-called 'Snowball Earth' (Hoffman et al., 2008).

Distinguishing between the various types of BIF, however, can sometimes be complex, and classifications may better serve as pure end-members, as sediments from some iron formations may span shallow continental shelves to deeper environments (Bekker et al., 2014). Additionally, Superior- and Algoma-type formations were contemporaneously deposited during a time of submarine volcanism and hydrothermal activity, leading to some overlap in lithology association. However, the 'pure end-members' of each can be further distinguished in regard to their geochemistry. The composition of Superior-type formations strongly reflects the seawater composition at the time of deposition whereas that of the Algoma-type reflects conditions of local volcanism and hydrothermal activity (Huston and Logan, 2004).

1.1.2 Origin and timing

Deposition of iron formations is observed to have occurred throughout three main periods of Earth's history: 3.5-3.0 Ga, 2.5-2.0 Ga and 1000-500 Ma (Robb, 2005). However, BIF are found to have been deposited as late as 527 Ma (Li et al., 2018). Nonetheless, the majority of BIFs are Archean to Paleoproterozoic age. GIFs began to appear after ~2.4 Ga and may owe their textural distinctiveness to events of this time (Fig. 1.2). The restriction of BIFs to the Precambrian was used in early studies to argue for formation under conditions vastly different from those of the present, with a more anoxic atmosphere and ocean system (Cloud, 1973; Holland, 1984). As Fe^{3+} is effectively insoluble at circumneutral pH values (James, 1954; Lepp and Golditch, 1964), large accumulations of iron required that it be transported as Fe^{2+}. BIF-style mineralization requires initial precipitation from seawater containing sufficient levels of dissolved ferrous iron. Such iron reservoirs in deep marine settings was possible due to either a reducing atmosphere or one with low oxidizing potential, or hydrothermal iron fluxes.

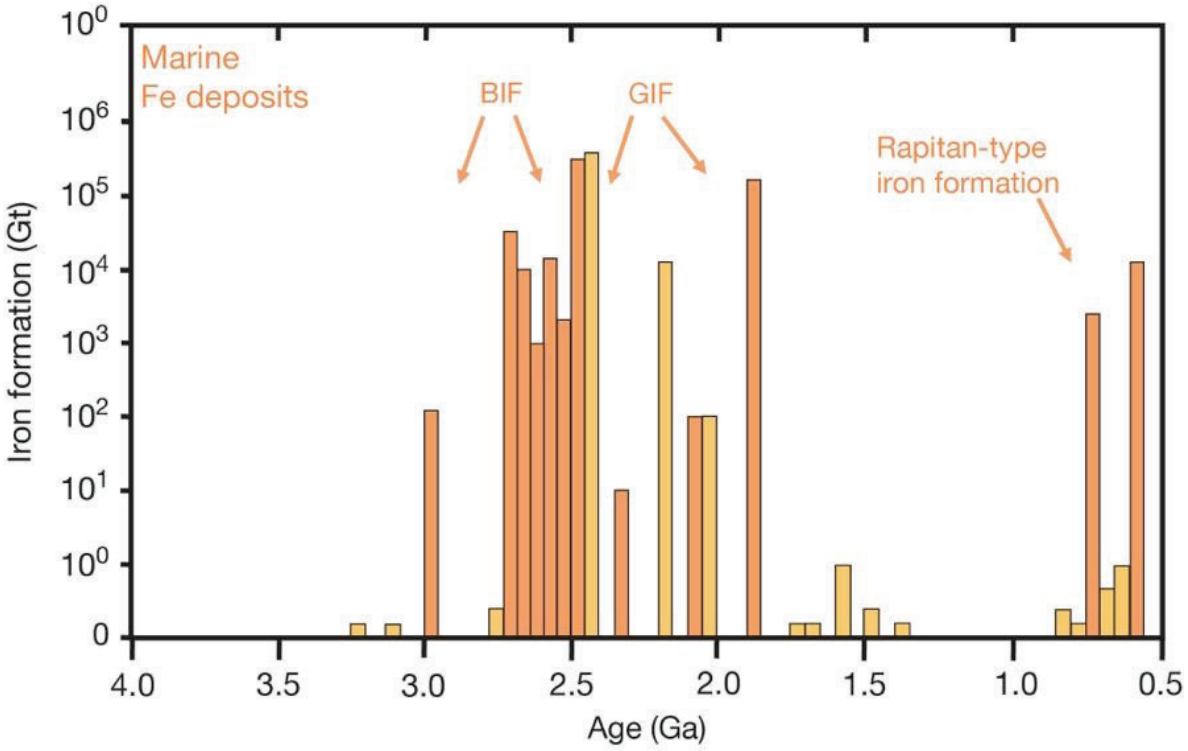

Figure 1.2: Secular distribution of banded iron formations (BIF), granular iron formations (GIF) and Rapitan-type iron formations, from Bekker et al. (2014).

The initial deposition of BIFs resulted from the mixing of deep Fe-rich waters with oxygenated surface waters. The first great rise in oxygen levels is referred to as the Great Oxidation Event (GOE), which is thought to have occurred between ~2.4 and 2.2 Ga (Bekker et al., 2004; Bekker and Kaufman, 2007). A second rise in atmospheric oxygen appears to have occurred in distinct stages between ~800-500 Ma. These dates coincide with the deposition of various styles of iron formation, their disappearance ~1.8 Ga, and reappearance during the Neoproterozoic, collectively suggesting fluxes in oxygen level. However, contrary to this belief is the idea that atmospheric oxygen levels of 1.5% of present-day levels existed during the time 3.0-2.2 Ga (Ohmoto, 1996), similar to atmospheric levels post-1.9 Ga. Frei et al. (2009) used chromium isotopes to similarly suggest that elevated oxygen levels existed ~3.0 Ga, prior to the GOE. Hoashi et al. (2009) reported primary hematite in the Pilbara Craton, Australia, suggesting not only deposition during oxygenated conditions at ~3.46 Ga, but raised the

possibility of oxygenic photosynthesis 700 million years earlier than previously recognized. Supporting evidence was discovered in pseudomicrofossils found in 3.5-billion-year-old chert from the Pilbara Craton in Australia (Marshall et al., 2011), suggesting microbial life and the possibility of elevated oxygen levels before the GOE.

While the basic conditions of deposition of iron formations is generally agreed to result from sediments precipitated from seawater containing micromolar levels of ferrous iron (Holland, 1973, 1984, 2005), deposition mechanisms remain poorly constrained. The most widely accepted model of iron deposition suggests that iron formation occurred where upwelling iron-rich reduced waters mixed with oxidized shallow waters (Cloud, 1965). Alternative arguments suggest biological influence on iron formation, whereby photosynthesizers or metabolic ferrous oxidation altered the chemical composition within water columns (Harder, 1919; Cloud, 1965, 1973), or microbially catalyzed Fe^{3+} (hydr)oxide precipitation was provoked by temperature fluctuations in the ocean (Posth et al., 2008). Later studies found deep water hydrothermal plumes to be a significant contributor to iron formations (Isley, 1995). Wang et al. (2009) used thermodynamic calculations to suggest that alternating Fe- and Si-rich layers can be generated from fluids derived from the leaching of low-Al oceanic crustal rocks.

Bekker et al. (2010) noted the geochronological significance of the episodic deposition of Superior-type iron formations. Their occurrence appears to be coeval with, and genetically linked to, time periods where large igneous provinces (LIPs) were prominent, suggesting a correlation between deposition of iron formations and heat flux at the core-mantle boundary during continent building. From ~2.6-2.4 Ga, widespread mafic magmatism may have contributed significantly to the deposition of Superior-type BIFs in Australia, South Africa, Russia, Ukraine and Brazil. These BIFs likely formed in anoxic conditions, whereas those of

the Paleoproterozoic and on were deposited in a redoxcline where biological and nonbiological oxidation occurred.

1.1.3 BIF Mineralogy

The mineralogy of BIFs is apparently simple, consisting predominantly of silica and Fe-rich minerals. However, there is much debate as to which minerals, iron-oxides or iron-silicates, constituted the primary iron phase during BIF deposition (e.g., Rasmussen et al., 2013; Sun and Li, 2017). Silica layers are made up of chert or, in metamorphosed BIFs, crystalline quartz. Chert typically forms layers, alternating with mm-thick iron-rich silicate or carbonate laminae. As mentioned above, BIFs are often characterized by facies according to the main mineral comprising Fe-rich layers. The main constituent Fe-minerals of BIF have been described by Bekker et al. (2014) and are summarized below.

The main mineral constituting Fe-rich layering in *oxide-facies* BIF are magnetite and/or hematite. The latter is the most common iron-oxide in BIFs and results from the oxidation of magnetite, although some hematite is reported to be primary (e.g. Hoashi et al., 2009). In *carbonate-facies* BIF, siderite ($FeCO_3$) is the main carbonate mineral, whereas ankerite [$Ca(Fe,Mg,Mn)(CO_3)_2$] and dolomite ($CaMgCO_3$) are among the last minerals to form, as indicated by the frequent inclusions of chert, magnetite, hematite and Fe-silicates. The variety of silicate minerals in *silicate-facies* BIFs becomes more complex depending on the extent of metamorphism. Common silicate minerals comprising this facies type at low-grade metamorphism include stilpnomelane [$K(Fe^{2+},Mg,Fe^{3+})_8(Si,Al)_{12}(O,OH)_{27}\cdot n(H_2O)$], minnesotaite [$(Fe^{2+},Mg)_3Si_4O_{10}(OH)_2$], riebeckite [$Na_2(Fe^{2+}{}_3Fe^{3+}{}_2)Si_8O_{22}(OH)_2$], chlorite and greenalite [$(Fe^{2+},Fe^{3+})_{2\text{-}3}Si_2O_5OH_4$]. Stilpnomelane is an indication of lower greenschist facies metamorphism whereas minnesotaite forms during metamorphism or late hydrothermal alteration. Riebeckite is a sodic amphibole that gives BIFs a bluish hue and is common to those

of the Hamersley region, Western Australia (Klein and Gole, 1981). Greenalite is less abundant and occurs as a late-stage mineral in BIFs. Grunerite [$Fe_7Si_8O_{22}(OH)_2$], cummingtonite [$(Mg,Fe^{2+})_2(Mg,Fe^{2+})_5Si_8O_{22}(OH)_2$], pyroxene [$(Ca,Na,Fe^{2+},Mg)(Al,Fe^{3+},Mg)(Si,Al)_2O_6$], garnet [$(Ca,Mg,Fe,Mn)^{2+}{}_3(Al,Fe,Cr)^{3+}{}_2(SiO_4)_3$] and fayalite ($Fe_2SiO_4$) can occur at higher-grades of metamorphism, as found in the present study.

1.2 Iron-oxides

The iron-oxides are relatively simple minerals yet differ significantly from one another with respect to crystal structure and degree of complexity in terms of extensive solid solution series with other minerals. If hydrogen is added, the iron-oxide and -hydroxide group expands to a total of sixteen minerals (Cornell and Schwertmann, 2003). Generically, the crystal structures of iron-oxides are composed of close-packed arrays of Fe cations (with either 2+ or 3+ charge) and O^{2-} anions. Anion arrangements in iron-oxides form sheets and are most commonly of the hexagonal close packing type, forming stacks in an alternating 'ABAB' formation, and in the cubic close packing, where sheets are arranged as ABCABC stacking and are held together by cation bonds.

Magnetite ($Fe^{2+}Fe^{3+}{}_2O_4$), is one of the '2-3 oxide spinels', $A^{2+}B^{3+}{}_2O_4$ (Biagioni and Pasero 2014 and references therein). The oxide spinel structure has a cubic close packing of anions (O), with the cations hosted either in tetrahedral (T) or octahedral (M) sites (e.g., Hill et al., 1979). Cation disorder over T and M sites expressed as parameter i can vary from i = 0 in normal spinels, ${}^{T}A^{M}B_2O_4$, to i = 1 in inverse spinels, ${}^{T}B^{M}(AB)O_4$, such as magnetite. Electron hopping (exchange of Fe^{2+} and Fe^{3+} in the M sites; Verwey and de Boer, 1936), or the semi-conductor character (defect structure of natural magnetite at room temperature; Fleet, 1981) of magnetite introduces further complexity in evaluating the ordering, full/partial occupancy of the T and M sites in magnetite. Oxide spinels form numerous and extended solid solutions with

one another (Table 1.1.; Fig. 1.3; Biagioni and Pasero, 2014; Bosi et al., 2019) and thus magnetite can incorporate a broad range of minor/trace elements, e.g., Mg, Mn, Ni, Co, Zn, Al, Cr, V, Ti, Si, etc. For example, tetravalent cations such as Ti^{4+} can be incorporated in the B site, provided that charge balance is maintained via a coupled substitution (e.g., $Fe^{3+} \leftrightarrow Ti^{4+} + Fe^{2+}$).

For example, hydrothermal magnetite has been shown to contain concentrations of Mg, Al, Ti, Mn, Cr, Co, Ni, Zn and Ga that measure consistently above detection limit using the LA-ICP-MS approach and these are considered as 'incorporated' into the magnetite structure (e.g., Nadoll et al., 2014 and references therein). Whereas many of these elements can be easily incorporated into magnetite due to the crystal structural similarity among oxide spinel group (Biagioni and Pasero, 2014), others, such as Ga, may be due to inclusions of silicates.

Magnetite with SiO_2 content (up to several wt.%), termed 'silician magnetite', has been reported from a variety of deposit types, e.g., BIF, skarns, IOCG from microprobe analysis (e.g., Huberty et al., 2012). Nonetheless, nanoscale studies using Z-contrast techniques for imaging have shown that presence of Si-Fe-nanoprecipitates along preferential directions in magnetite rather than in solid solution (Xu et al., 2014; Ciobanu et al., 2019). Silician magnetite is prevalent throughout the outer shell at Olympic Dam and this has been shown to be rich in U, W, Sn, Mo and rare earth elements and yttrium (hereafter REY) (Verdugo-Ihl et al., 2019).

Table 1.1: Selected spinel group minerals.

Spinel Group (cubic)	
Spinel $MgAl_2O_4$	Ulvöspinel $TiFe^{2+}{}_2O_4$
Hercynite $Fe^{2+}Al_2O_4$	Franklinite $(Zn,Mn^{2+},Fe^{2+})(Fe^{3+},Mn^{3+})_2O_4$
Gahnite $ZnAl_2O_4$	Jacobsite $(Mn^{2+},Fe^{2+},Mg)(Fe^{3+},Mn^{3+})_2O_4$
Galaxite $(Mn,Mg)(Al,Fe^{3+})_2O_3$	Trevorite $Ni^{2+}Fe^{3+}{}_2O_4$
Magnesioferrite $MgFe^{3+}{}_2O_4$	Magnesiochromite $Mg^{2+}Cr^{3+}{}_2O_4$
Magnetite $Fe^{2+}Fe^{3+}{}_2O_4$	Chromite $Fe^{2+}Cr^{3+}{}_2O_4$
Cuprospinel $(Cu,Mg)Fe^{3+}{}_2O_4$	

An example of a solid solution involving coupled substitutions (Ti^{4+} for Fe^{3+} in the octahedral sites and Fe^{2+} for Fe^{3+} in the tetrahedral sites; White et al., 1994) is titanomagnetite solid-solution with a disordered spinel structure above 600 ºC and exsolution products as magnetite + ulvöspinel (Fe_2TiO_4) followed by ilmenite due to redox re-equilibration (Buddington and Lindsley; 1964). The exsolution products are used for geothermometry (Ghiorso and Sack, 1991) with wide applicability to a variety of rock and ore types.

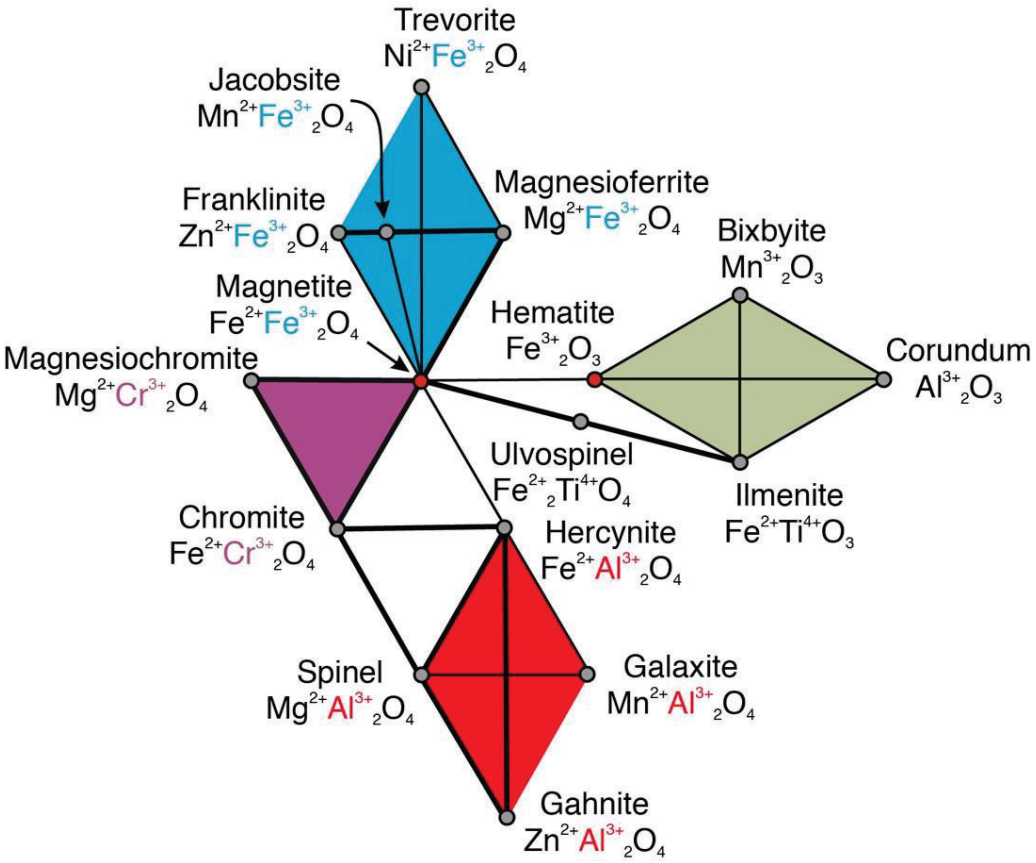

Figure 1.3: Classification of iron-oxides across solid-solution series (modified after Deer et al., 1997).

Hematite (α-Fe_2O_3; rhombohedral; e.g., Maslen et al., 1994) is one of the five polymorphs known at present (Lee et al., 2008) and displays great morphological variability, ranging from tabular to platy to spherical but may also crystallize in octahedral crystals when forming as a pseudomorph after magnetite ('martite') (Davis et al., 1968). Although not inherently

magnetic, hematite may also show some degree of magnetism depending on the remaining magnetite after pseudomorphic replacement. It can similarly be pseudomorphically replaced by magnetite in which case it is termed "mushketovite." Due to the similarity in crystal structure, hematite forms a solid solution with ilmenite and corundum at temperatures above 950 °C.

Recent studies have shown a wide-range of trace elements in hematite from BIF and IOCG deposits, including high field strength elements, REY and also U-W-Sn-Mo, a group of elements called 'granitophile' elements. For example, Hensler et al. (2015) report measurable concentrations of Mg, Al, Mn, Ti, Cr, V, Co, Ni, W, As in hematite from itabirite and iron ores of the Quadrilátero Ferrífero in Brazil. Following the reconnaissance studies of Ciobanu et al. (2013; 2015), U-W-Sn-Mo-oscillatory-zoned hematite was found throughout the entire strike and depth of the IOCG deposit at Olympic Dam (Verdugo-Ihl et al., 2017). This type of hematite also forms early in the outer shell of the deposit and is characterized by HFSE-enrichment (Verdugo-Ihl et al., 2019). High concentrations of W (up to several thousand ppm) and measurable Sn was also reported in hematite from Island Dam, an IOCG prospect in the same district (Keyser et al., 2017). The U-W-Sn-Mo-signature is considered to fingerprint affiliation with ~1.6 Ga granitic plutons throughout deposits in South Australia, and particularly from those in the Olympic Cu-Au Province. For example, enrichment in W (and Sb) was shown in high-grade hematite ores from the northern part of the province, at Peculiar Knob (Keyser et al., 2019b).

Keyser et al. (2018) measured wt.% Si in oscillatory zoned microplaty hematite from ores of the Middleback Ranges. However, while LA-ICP-MS resolved depth profiles may suggest elemental incorporation into the hematite crystal lattice, nanoscale studies are needed for validate LA-ICP-MS data and determine whether these elements are in solid solution or are

present as included nanoscale particles of discrete minerals. For example, Zr concentrations of up to 680 ppm were measured in granoblastic hematite from the Peculiar Knob iron deposit in South Australia (Keyser et al., 2019b). While depth profiles showed clean, steady signals without any indication of inclusions, TEM analysis found the Zr to be attributable to nano-inclusions of baddeleyite within hematite.

1.3 Formation of ore from BIF

The vast majority of high-grade iron ores mined today are hosted within Precambrian BIFs. Although BIFs are iron-rich in nature (~30 wt.% Fe), their true economic value follows enrichment processes, when BIFs are transformed into high-grade iron ores (≥65% Fe). This transformation takes place as a result of fluid-rock interactions leading to mineral (inter)conversions, the onset of which begins with rock permeability and introduction of fluids, which themselves evolve over time (e.g., Hensler at al., 2015). Although variability exists between deposits with respect to processes leading to ore formation as a result of different geological environments for BIF deposition (e.g., Algoma-type settings vs. Lake Superior-type settings), two general geochemical mechanisms are attributed to formation of BIF-hosted iron ore deposits: 1) dissolution of both silica and carbonates leading to compaction and; (2) hematite replacement of magnetite (martitization) and Fe-rich silicates ± crystallization of microplaty hematite. Although these processes occur throughout various hypogene and supergene enrichment processes, three major hypogene and one supergene enrichment stages are commonly recognized in most major deposits (Hagemann et al., 2016).

The dissolution and removal of silica and carbonate from BIFs is primarily attributed to hot, silica and carbonate under-saturated hydrothermal fluids, which ascend and descend through deposit-scale structures such as faults or grabens. Such fluids can be produced by basin brines, local intrusions, and/or descending meteoric waters (Hagemann et al., 2006). Hematite

replacing chert-bands may be an indication that iron was added to the system via this fluid mobility. However, recent nanoscale studies have identified chert to contain micro-inclusions of hematite colloids that accumulate during quartz dissolution to form microplaty hematite and that additional iron from an external source is required for its formation (Egglseder et al., 2019). Alteration of magnetite to hematite is generally attributed to the oxidation by hydrothermal fluids. However, this transformation can also occur through non-redox acid-based reactions (Ohmoto, 2003; Otake et al., 2007, 2010), which results in leaching of Fe^{2+} from magnetite. This is expressed by the reaction:

$$Fe_3O_{4(Mt)} + 2H^+ = Fe_2O_{3(Hm)} + Fe^{2+} + H_2O.$$

While this may be an alternative explanation for BIFs and/or ore formation, for the most part hematite enrichment can be accounted for by dissolution of silica and carbonates, compaction and increasing porosity (Taylor et al., 2001).

1.4 Geological background of the Eyre Peninsula, the Middleback Ranges and other case studies within this thesis

The Eyre Peninsula occupies the southern extent of the Gawler Craton: a major crustal province in South Australia (Fig. 1.4) with a record of continental evolution spanning the Archean to Mesoproterozoic. The roughly oval-shaped craton covers an area of 800 x 600 km and is flanked to the east by the Torrens Hinge Zone, and to the northeast, northwest and west by faulted margins of sedimentary basins, and diminishes to the south along the continental shelf (Thompson, 1969; Daly et al., 1998). Formation of the Gawler Craton is attributed to two major phases of tectonism separated by a 500 Ma gap where the craton was essentially stable (Hand et al., 2007).

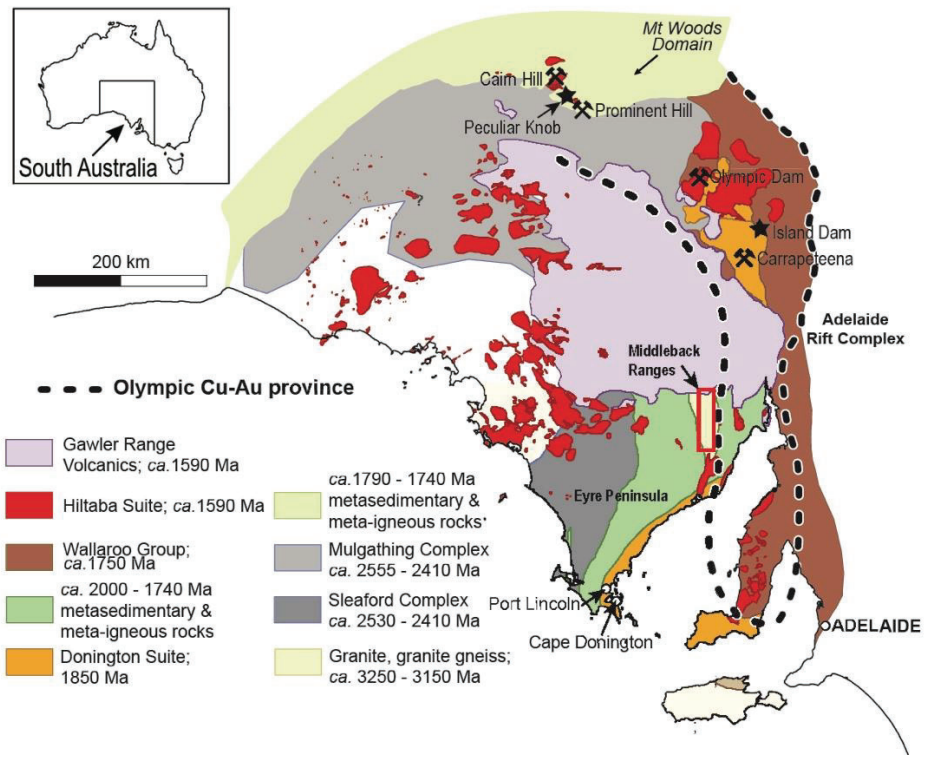

Figure 1.4: Simplified geological map showing location of the Middleback Ranges within the Eyre Peninsula, and the Island Dam and Peculiar Knob prospects in the Olympic Cu-Au province. Modified after Reid and Fabris (2015).

The eastern Eyre Peninsula in South Australia contains the oldest basement rocks yet discovered in the Gawler Craton, the ~3.15 Ga Cooyerdoo Granite (Parker and Lemon, 1982; Daly et al., 1988; Fraser et al., 2010; Keyser et al., 2019c), however, it is composed mainly of three main terrains: the Archean Sleaford Complex, the overlying chemical and clastic Hutchison Group metasedimentary rocks and the Donington Suite Granitoids. Extensional tectonism and coeval sedimentation with minor intrusives in the Eyre Peninsula between 2.55-2.50 Ga lead to the formation of the Sleaford Complex, which includes the ~2.6 Ga Carnot Gneisses (Fanning, 1988) and the ~2520-2460 Ma felsic to intermediate intrusive Dutton Suite, all metamorphosed to granulite-facies during the early Paleoproterozoic Sleaford Orogeny (~2450 Ma) (Fanning, 1997; Dutch et al., 2010). Contemporaneous to the volcanism and sedimentation processes forming the Sleaford Complex was the deposition of the banded-iron-

formation-hosting Middleback Subgroup ~2560 Ma in the eastern Eyre Peninsula (Szpunar at al., 2011). After a roughly 500 Ma period of cratonic stability was the emplacement of the magmatic protolith that would become the Miltalie Gneiss ~2000 Ma (Daly et al., 1998). This was followed by deposition of the Darke Peak Subgroup between 2000-1865 Ma and finally by the Cleve Subgroup from ~1790 Ma (Szpunar et al., 2011). Together, the Middleback, Dark Peake and Cleve subgroups comprise the Hutchison Group metasediments.

Tectonism between 1900-1450 Ma began with magmatism related to the onset of compressional tectonics during the Cornian Orogeny at ~1850 Ma (Reid et al., 2008). Emplacement of the Donington Suite and the related Jussieu, Williams and Tournefort mafic dikes (Schaefer, 1998) occurred prior to and synchronously with contractional deformation and granulite-facies metamorphism during this orogenic period, interrupting rifting in the eastern Gawler Craton. However, rifting reactivated along the eastern margin of the craton following the Cornian Orogeny as evidenced by the eruption of the Myola Volcanics and deposition of the Broadview Schist and the Cleve Subgroup metasediments. The Kimban Orogeny of 1.73-1.69 Ga is responsible for the formation of a crustal-scale Kalinjala Shear Zone (Vassallo and Wilson, 2002), and large craton-scale magmatism manifested in the south as syn-and post-Kimban Camp Granite and Moody Suite, respectively, which intruded the Sleaford Complex and Hutchison Group around 1730-1710 Ma. Although not extensively expressed in the Eyre Peninsula, a major tectonothermal event at 1595-1575 Ma impacting much of the Gawler Craton led to eruption of the Gawler Range Volcanics and emplacement of Hiltaba Suite intrusives. This has been interpreted as a silicic large igneous province (SLIP) (Allen et al., 2008) and was associated with formation of major IOCG deposits (Skirrow et al., 2002). The Charleston Granite, northern Eyre Peninsula, is of similar age and considered to be an equivalent of the Hiltaba Suite (Creaser and Fanning, 1993).

1.4.1 The Middleback Ranges

The Middleback Ranges (MR), located in the northeastern Eyre Peninsula (Fig. 1.5), is the major iron ore-producing region in South Australia. Current hematite and magnetite reserves are 32.2 Mt and 56 Mt, respectively, at ~50-55% Fe (Arrium Mining, 2016). Hutchison Group metasediments, extending discontinuously roughly 600 km from the southern Eyre Peninsula to the Olympic Dam region host the MR deposits. This succession consists of a 5,000 m-thick mixed sequence of chemical and clastic sediments and extrusive basic and felsic volcanics. Parker and Lemon (1982) considered the deposition age of the Hutchison Group to be between ~2000 and ~1865 Ma, however more recent isotopic and geochemical data suggests the group consists of three distinct subgroups deposited between ~2.55 and ~1.73 Ga (Szpunar et al., 2011). The subgroups are: the Cleve and the Darke Peak subgroups, exposed in the western Lincoln-Cleve uplands extending from Port Lincoln to the Cleve region as a semi-continuous elevated terrain and; the Middleback Subgroup, spanning a ~60 km-long N-S striking set of dipping hills 53 km southwest of Whyalla in the north-eastern region of the Eyre Peninsula. These two regions are separated by the regional-scale 3 km-wide Kalinjala Mylonite Zone (Parker, 1980; Vassallo and Wilson, 2002), believed to be formed during the ~1.73-1.70 Ga Kimban Orogeny (Parker, 1980; Vassallo and Wilson, 2002).

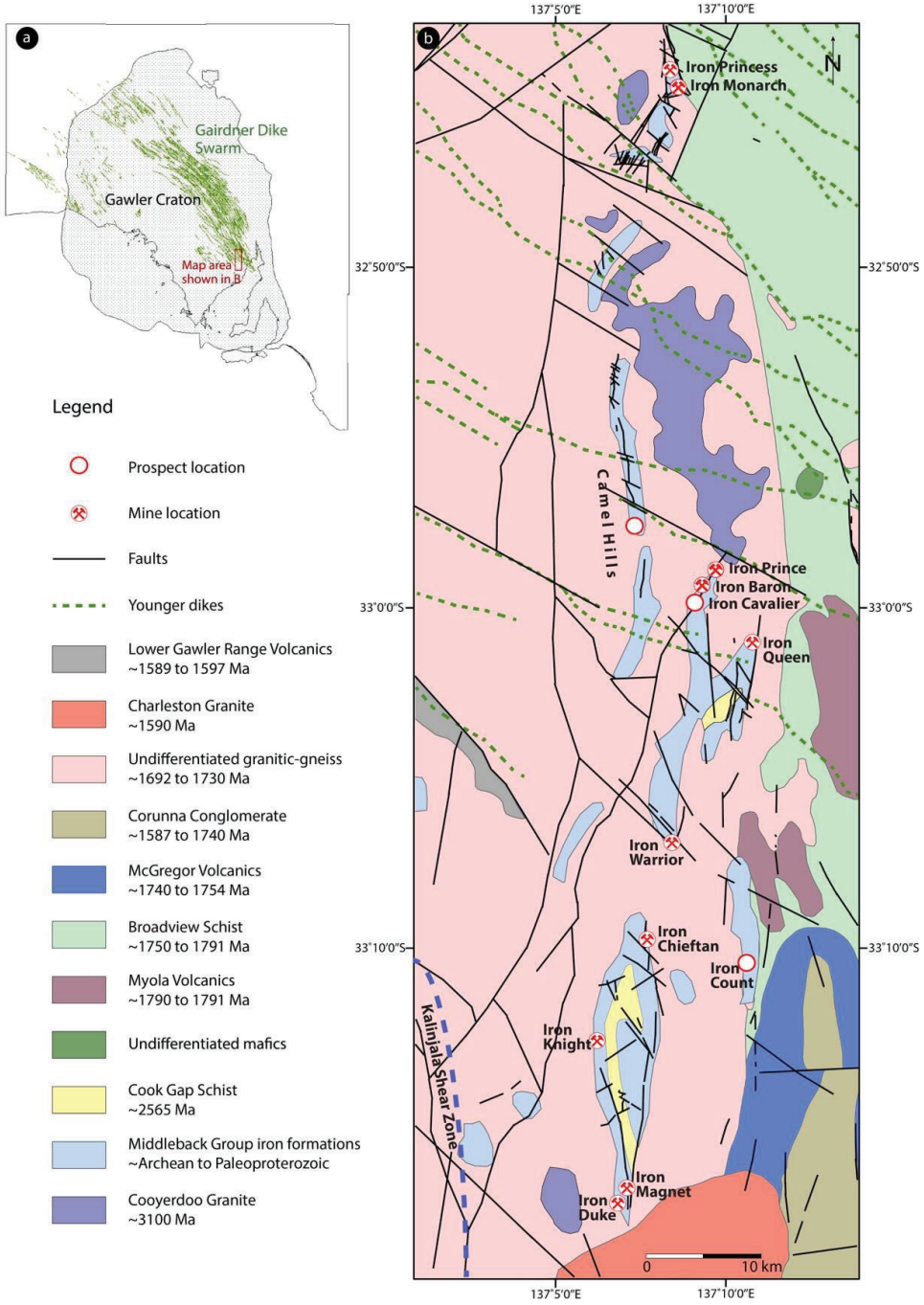

Figure 1.5: (a) Location of the MR within the Gawler Craton and extent of the Gairdner Dike Swarm. (b) Simplified geological map of the MR and locations of iron ore deposits, from Keyser et al. (2018).

The MR represent the Middleback Subgroup succession of the Hutchison Group metasediments. The MR lies unconformably on the ~3.15 Ga basement Cooyerdoo Granite

(Parker and Lemon, 1982; Daley et al., 1998; Fraser et al., 2010; Keyser et al., 2019c). These granites form scattered outcrops on the eastern side of the MR and have been found associated with the orebodies throughout the MR belt (Keyser et al., 2019c). To the south of the MR are the Hiltaba equivalent Charleston granites (1585 ± 5 Ma) (Creaser and Fanning, 1993). The basal unit of the Middleback Subgroup is a quartz-sericite schist, followed by the Katunga Dolomite, Lower Middleback Jaspilite (LMJ), a quartz-biotite-sillimanite-garnet-muscovite schist known as the Cook Gap Schist, and finally the Upper Middleback Jaspilite (UMJ; Parker and Lemon, 1982). Mafic dikes and sills show concordant and discordant relationships with BIF and occur extensively throughout the Middleback Ranges. It has been suggested that the similarity in lithology and mineralization of the LMJ and UMJ results from the structural repetition of the LMJ due to folding and thrusting (Yeates, 1990; Vassallo and Wilson, 2001).

BIF-like structures are restricted to the LMJ, which consists of a 'mixed' basal sequence, a lower iron carbonate unit, a middle iron talc unit and an upper iron silica unit, all grading up sequence and laterally with weathering to goethite-limonite rocks occurring near the surface (Leevers et al., 2005). Major iron ore mineralization occurs at lower levels (Iron Magnet), predominantly within the carbonate unit and are localized, thickened and upgraded in north-south plunging synclinal keels (Davies, 2000). Ore horizons are considered to be a replacement product of jaspilite sequences (Cook, 1971). Magnetite mineralization is hydrothermal and occurs as layer replacement (from laminae to beds), matrix to breccias and clasts within breccias, and within veins and fractures. At higher levels, hematite textures are varied, but pseudomorphic replacement of magnetite (martitization) is a common feature throughout all deposits. In massive ores, hematite occurs as lamellar or anhedral, fine-grained aggregates with abundant vugs, often with dusty inclusions of gangue minerals. In more oxidized samples, iron hydroxides replace hematite.

1.4.2 Island Dam

The Island Dam Cu prospect, located ~90 km southeast of the granite-hosted hematite-breccia Olympic Dam deposit (Fig. 1.4), lies within the Olympic Cu-Au Province and is an example of mineralization associated with skarn alteration prompted by the regional-scale ~1.6 Ga Hiltaba event and expressed within metasediments containing BIF-like protoliths. Mineralization is hosted within the ~1.75 Ga Wallaroo Group, which is a metasedimentary unit consisting mainly of siltstone, mafic and felsic metavolcanic rocks, and minor limestone and dolostone horizons associated with Fe-rich, BIF-like lithologies. This package was deposited atop gneissic-granites of the 1.85 Ga Donington Suite, and extends from the northern Mount Woods Inlier in the northern Gawler Craton to the upper Yorke Peninsula. Correlation of the Wallaroo Group in this region is obscured by a regional alkali-calcic + Fe-metasomatism, which has resulted in similar calcic skarn formation at the proximal Groundhog Zn-Cu prospect in the Punt Hill area (Reid et al., 2011) and at the Hillside Cu-Au prospect in the York Peninsula (Conor et al., 2010; Ismail et al., 2014). Sequences displaying similar BIF-like horizons and interbedded garnet skarn and banded calc-silicate-feldspar rocks have also been reported between the Gawler Range Volcanics and Donington Granite in drillholes west of Punt Hill. Mineralization within prospects hosted by Wallaroo Group are dated at ~1.6 Ga (Skirrow et al., 2007; Reid et al., 2011).

1.4.3 Peculiar Knob

The Peculiar Knob deposit, located in the Mount Woods Inlier of the northern Gawler Craton (Fig. 1.4), contains iron mineralization hosted within a poly-metamorphosed and poly-deformed Paleoproterozoic basement complex containing metasedimentary sequences assigned to BIF (Flint and Benbow, 1977; Chalmers, 2007). The region is characterized by an extensive alteration history linked to granites associated with major IOCG-mineralization in

the region (e.g., Belperio et al., 2007), which is expressed in neighboring Cu-Au deposits such as Prominent Hill, Cairn Hill and the Manxman prospect. The basement complex consists of the Skylark Metasediments, mafic and felsic intrusive rocks including the 1691 ± 25 Ma Enginina Adamellite and the 1584 ± 18 Ma Hiltaba-affiliated Balta Granite (Creaser and Fanning, 1993), and interbedded conglomerate and quartz sandstones of the unconformably overlying Coodnambanna Metaconglomerate, which contains clasts of high-grade assemblages interpreted to be derived from the underlying Skylark Metasediments. Sequences comprising the Skylark Metasediments include garnet-cordierite-sillimanite gneisses, metapelitic-, psammitic- and quartz-feldspar-biotite-schists, clinopyroxene- and hornblende-bearing gneissic-calcsilicates, and quartz-magnetite-feldspar-clinopyroxene-orthopyroxene-apatite units considered as BIF (Flint and Benbow, 1977; Chalmers, 2007). Iron mineralization at Peculiar Knob was previously interpreted to result from hydrothermal replacement of host BIF to form supergene ores followed by later metamorphism and recrystallization (Morris and Hough, 1997). More recent micron- to nanoscale studies of hematitic ores have reevaluated the prospect to have formed from metamorphism of supergene ores derived from an Fe-rich detrital horizon containing mafic input followed by hydrothermal recrystallization during the ~1.6 Ga Hiltaba event (Keyser et al., 2019b).

1.5 Research objectives and thesis structure

This thesis is a contribution to the research project, ‘Trace elements in iron-oxides: deportment, distribution and application in ore genesis, geochronology, exploration and mineral processing’. An important part of the project addressed Fe-ores from two major types of deposits present in South Australia (BIFs and IOCGs) with the following aims:

(1) to understand the formation and transformation of iron ores through mineral characterization at various scales and through evolutionary stages; and

(2) show how trace element endowment in iron-oxides from IOCG and BIF ores have potential for improvement of exploration and ore genesis models.

The datasets and interpretation generated during the course of this study dealing with BIF-derived ores not only expand on the current knowledge on the mineralogy and geochemistry of iron-oxides, but also contributes to a better understanding of regional geology in the Gawler Craton, ore evolution in the Middleback Ranges, and relationships to other BIF-hosted ore deposits worldwide.

The samples studied for this project include hand specimens from outcrops and open pits and portions of drillcore, which were subsequently prepared as polished blocks and polished thin sections. Sample characterization included preliminary identification of constituent minerals and rock fabrics using reflected and transmitted light optical microscopy, followed by scanning electron microscopy (SEM) to allow micron-scale characterization and assessment of grain-scale compositional homogeneity. Quantitative mineral compositions were determined using electron probe microanalysis (EPMA) and trace element concentrations were measured using laser-ablation inductively-coupled mass spectrometry (LA-ICP-MS). This main body of this thesis comprises six chapters (Chapters 2-7), each of which is a stand-alone manuscript. These chapters, including one peer-reviewed extended abstract (Chapter 6) have been published during the course of the candidature; Chapter 5 is, however, under review at the time of writing. Each chapter represents a publication to be read independently, in which the individual samples and analytical methodologies are explained in detail.

Chapter 2 is a study of textural and chemical variations in iron-oxides from BIFs and ores of the Middleback Ranges. Samples ranging from magnetite-BIF to friable hematite ore contain iron-oxides that exhibit a wide range of textures and geochemical signatures indicative of varying depositional environments along the belt. Petrographic and geochemical study also

indicate multiple stages of iron-oxide formation and replacement (e.g., hematite pseudomorphically replacing magnetite – martite). A genetic model for ore formation is proposed based on textural and geochemical evidence. Following initial deposition, BIFs interacted with fluids from various sources (e.g., granite-derived fluids) that contribute to upgrading of protore to high-grade iron ore. The results highlight the impact of local deposit setting on the ore forming process.

The genetic model from Chapter 2 is tested in **Chapter 3**, a case study of the Iron Count prospect, located on the eastern margin of the Middleback Ranges. Two N-S striking ridges (West and East ridge) display different magnetic and U-radiometric signatures. Hematite mineralization is characterized by geochemical signatures and U–Pb hematite ages indicating interaction between BIFs and granite-derived fluids generated during emplacement of the adjacent Wertigo Granite during a 1.79 Ga intracontinental rifting event. The work reported in this chapter is the first integrated petrographic, geochemical and geochronological study of iron-oxides aimed at constraining hematite mineralization in BIF environments, and also the first to provide geochronological constraints on ore formation in the Middleback Ranges.

Granitoids of hitherto unknown ages are spatially associated with orebodies throughout deposits of the Middleback Ranges. These are characterized with respect to petrography and geochronology in **Chapter 4**. Sensitive high-resolution ion microprobe (SHRIMP) dating of zircon from the granites show them to be Archean in age (3.0-3.2 Ga), while alteration features indicate post-emplacement interactions with metasomatic fluids. The results of this study provide evidence for a more extensive distribution of Mesoarchean crust than previously recognized beneath the entire Middleback Ranges BIF sequence. Furthermore, it can be inferred from overprint features that fluid-rock interactions and granite leaching took place

during BIF upgrading and iron-oxide formation, consistent with trace element signatures recorded in iron-oxides from BIF and ores studied in Chapter 2.

Chapter 5 is a petrographic and geochronological study on mafic lithologies that display contrasting relationships to orebodies throughout the Middleback Ranges. Amphibolites at the southern Iron Magnet deposit are interbedded with BIF and contain complex mineral assemblages reflecting extensive overprinting, including metamorphic Mg-Fe- and Ca-amphiboles and relict titaniferous magnetite, which distinguish them from NW-striking dolerite dikes that contain igneous magnesiohornblende and plagioclase. SHRIMP ages of zircon from amphibolites and dolerites yield two age groups at ~2.5 Ga and ~780 Ma, while hematite from ores adjacent to an altered dolerite dike yield U–Pb ages of ~680 Ma. The results of this study indicate mafic magmatism contemporaneous with BIF deposition and provide the first evidence for the presence of a ~800 Ma craton-scale Gairdner large igneous province in the Middleback Ranges. The young hematite ages from ores are younger than those described in Chapter 3, and provide further evidence for multiple events leading to BIF upgrading and iron-oxide formation, which is again consistent with trace element signatures recorded in iron-oxides from BIF and ores studied in Chapter 2.

Skarn alteration (actinolite + magnetite/hematite) of BIF-like mineralization at the Island Dam prospect in the eastern Gawler Craton is discussed in **Chapter 6**. Iron-oxide textures and geochemical signatures define the two contrasting mineralization styles at the prospect, where BIF iron-oxides are represented as martite with relative enrichment in Ni, Co, Mn, As, Sb U, Y and REE. Coarse-grained (cm-scale) hematite in skarn lithologies shows enrichment in W and Sn (thousands of ppm, and compositionally zoned with respect to these elements). Skarn overprinting of BIF mineralization at Island Dam is attributed to a ~1.6 Ga magmatic-hydrothermal event that led to IOCG-skarn-style mineralization in other parts of the Olympic

Cu-Au Province. This chapter highlights the capacity of iron-oxides to distinguish protolith from alteration products in BIF-IOCG-associated terranes.

A case study on high-grade, Zr- and Ti-rich hematite ores from the Peculiar Knob deposit, Mount Woods Inlier, SA, is the focus of **Chapter 7**. High zirconium concentrations (up to 650 ppm) are measured in granoblastic hematite and result from fine-grained (nm-wide) baddeleyite inclusions. Zircon within the same sample occurs interstitial to hematite and was dated by SHRIMP, giving an age of ~1.74 Ga, coincident with the Kimban Orogeny. The orebody at Peculiar Knob, previously considered of BIF origin, is reinterpreted as a metamorphosed Fe-rich sediment containing detrital titanomagnetite sourced from mafic rocks. An overprint associated with the ~1.6 Ga Hiltaba event is recognized by W-, Nb-, Sb-, Sn-rich rims on hematite and zircon overgrowths.

A summary of the key findings and implications of this research are provided in **Chapter 8**. This chapter also identifies open questions and areas of potential future investigation. Additional material, including chapter appendices, co-authored publications, and conference contributions, are compiled as **Chapter 9.** A full reference list is provided in **Chapter 10**.

References

Alibert, C., 2016. Rare earth elements in Hamersley BIF minerals. Geochimica et Cosmochimica Acta 184, 311-328.

Allen, S., McPhie, J., Ferris, G., Simpson, C., 2008. Evolution and architecture of a large felsic igneous province in western Laurentia: the 1.6 Ga Gawler Range Volcanics, South Australia. Journal of Volcanology and Geothermal Research 172, 132-147.

Arrium Mining, 2016. Ore Reserves and Resources Statement, 30th June 2016. Arrium Mining Ltd.

Bekker, A., Holland, H.D., Wang, P.-L, Rumble III, D., Stein, H.J., Hannah, J.L., Coetzee, L.L., Beukes, N.J., 2004. Dating the rise of atmospheric oxygen. Nature 427, 114-120.

Bekker, A., Kaufman, A.J., 2007. Oxidative forcing of global climate change: A biogeochemicxal record across the oldest Paleoproterozoic ice age in North America. Earth and Planetary Science Letters 258, 486-499.

Bekker, A., Slack, J., Planavsky, N., Krapež, B., Hofmann, A., Konhauser, K.O., Rouxel, O.J., 2010. Iron formation: The sedimentary product of complex interplay among mantle, tectonic, oceanic, and biospheric processes. Economic Geology 105, 467-508.

Bekker, A., Planavsky, N.J., Krapež, B., Rasmussen, B., Hofmann, A., Slack, J.F., Rouxel, O.J., Konhauser, K.O., 2014. Iron formations: Their origins and implications for ancient seawater chemistry. In Holland, H. and Turekein, K. (ed), Treatise on Geochemistry, Volume 9, pp.561-628. Netherlands: Elsevier.

Biagioni, C., Pasero, M., The systematics of the spinel-type minerals: An overview. American Mineralogist 99, 1254-1264.

Bosi, F., Biagioni, C., Pasero, M., 2019. Nomenclature and classification of the spinel supergroup. European Journal of Mineralogy 31, 183-192.

Bowles, J.F.W., Howie, R.A., Vaughan, D.J., Zussman, J., 2011. Rock-forming Minerals: non-silicates: oxides, hydroxides and sulphides. Volume 5A. The Geological Society, London, UK.

Broughm, S.G., Hanchar, J.M., Tornos, F., Westhues, A., Attersley, S., 2017. Mineral chemistry of magnetite from magnetite-apatite mineralization and their host rocks: examples from Kiruna, Sweden, and El Laco, Chile. Mineralium Deposita 52, 1223-1244.

Buddington, A.F., Lindsley, D.H., 1964. Iron-titanium oxide minerals and synthetic equivalents. Journal of Petrology 5, 310-357.

Chalmers, N., 2007. The Mount Woods Domain: a geological review and discussion on mineralisation potential. South Australia. Department of Primary Industries and Resources Report Book 2007/7, 62 pp.

Ciobanu, C.L., Cook, N.J., Ehrig, K., Wade, B.P., Kamenetsky, V.S., 2015. Trace element signatures in iron oxides from the Olympic Dam IOCG deposit, South Australia. 13th SGA Biennial Meeting 2015. Mineral Resources in a Sustainable World 3, 1071-1074.

Ciobanu, C.L., Wade, B.P., Cook, N.J., Mumm, A.S. Giles, D., 2013. Uranium-bearing hematite from the Olympic Dam Cu–U–Au deposit, South Australia: A geochemical tracer and reconnaissance Pb–Pb geochronometer. Precambrian Research 238, 129-147.

Ciobanu, C.L., Verdugo-Ihl, M.R., Slattery, A., Cook, N.J., Ehrig, K., Courtney-Davies, L., Wade, B.P., 2019. Silician magnetite: Si-Fe-nanoprecipitates and other mineral inclusions in magnetite from the Olympic Dam deposit, South Australia. Minerals 9, 311. https://doi.org/10.3390/min9050311.

Cloud, P., 1965. Significance of Gunflint (Precambrian) microflora–photosynthetic oxygen may have important local effects before becoming a major atmospheric gas. Science 148, 27-35.

Cloud, P., 1973. Paleogeological significance of banded iron-formation. Economic Geology 68, 1135-1143.

Conor, C., Raymond, O., Baker, T., Teale, G., Say, P., Lowe, G., 2010. Alteration and Mineralisation in the Moonta-Wallaroo Cu-Au Mining Field Region, Olympic Domain, South Australia. In: Porter, T.M. (ed), Hydrothermal Iron Oxide Copper-Gold and Related Deposits: A Global Perspective 3, PGC Publishing, Adelaide, 1-24.

Cook, J.N., 1971. Grade control procedures at the Iron Prince quarry Whyalla, South Australia. Australasian Institute of Mining and Metallurgy, Adelaide Regional Conference, Adelaide, South Australia, August 1971, Paper No. 4.

Cook, N.J., Ciobanu, C.L., George, L., Zhu, Z.-Y., Wade, B., Ehrig, K., 2016. Trace element analysis of minerals in magmatic-hydrothermal ores by laser ablation inductively-coupled plasma mass spectrometry: approaches and opportunities. Minerals 6, 11. https://dx.doi.org/10.3390/min6040111.

Cornell, R.M., Schwertmann, U., 2003. The Iron Oxides: Structure, Properties, Reactions, Occurrences and Uses. Wiley-VCH. pp. 573, ISBN 3-527-30274-3.

Courtney-Davies, L., Zhu, Z., Ciobanu, C.L., Wade, B.P., Cook, N.J., Ehrig, K., Cabral, A.R., Kennedy, A., 2016. Matrix-matched iron-oxide laser ablation ICP-MS U-PB Geochronology using mixed solution standards. Minerals 6, 85; doi:10.3390/min6030085.

Courtney-Davies, L., Tapster, S.R., Ciobanu, C.L., Cook, N.J., Verdugo-Ihl, M.R., Ehrig, K.J., Kennedy, A.K., Gilbert, S.E., Condon, D.J., Wade, B.P., 2019a. A multi-technique evaluation of hydrothermal hematite U–Pb isotope systematics: Implications for ore deposit geochronology. Chemical Geology 513, 54-72.

Courtney-Davies, L., Ciobanu, C.L., Richardson, M.W., Prosser, N., Verdugo-Ihl, M., Wade, B.P., Gilbert, S.E., Ehrig, K.J., Cook, N.J., 2019b. Synthesis of U-Pb doped hematite using a hydrated ferric oxide approach. Journal of Crystal Growth 513, 48-57.

Courtney-Davies, L., Zhu, Z., Ciobanu, C.L., Wade, B.P., Cook, N.J., Ehrig, K., Cabral, A.R., Kennedy, A., 2016. Matrix-matched iron-oxide laser ablation ICP-MS U–Pb geochronology using mixed solution standards. Minerals 6, 85. https://doi.org/10.3390/min603008.

Craddock, P.R., Bach, W., Seewald, J.S., Rouxel, O.J., Reeves, E., Tivey, M.K., 2010. Rare earth element abundances in hydrothermal fluids from the Manus Basin, Papua New Guinea: Indicators of sub-seafloor hydrothermal processes in back-arc basins. Geochemica et Cosmochimica Acta 74, 5494-5513.

Creaser, R.A., Fanning, C.M., 1993. A U-Pb zircon study of the Mesoproterozoic Charleston Granite, Gawler Craton, South Australia. Australian Journal of Earth Sciences 40, 519-526.

Daly, S.J., Fanning, C.M., Fairclough, M.C., 1998. Tectonic evolution and exploration potential of the Gawler Craton, South Australia. AGSO Journal of Australian Geology and Geophysics 17, 145-168.

Dare, S.A.S., Barnes, S.-J., Beaudoin, G., 2015. Did the massive magnetite “lava flows” of El Laco (Chile) form by magmatic or hydrothermal processes? New constraints from magnetite composition by LA-ICP-MS. Mineralium Deposita 50, 607-617.

Davies, M., 2000. Iron ore in South Australia. Primary Industries and Resources SA. Commodity Review No. 8, 35.

Davis, B.L., Rapp, G. Jr., Walawender, M.J., 1968. Fabric and structural characteristics of the martitization process. American Journal of Science 266, 482-496.

Deer, W.A., Bowles, J.F.W., Howie, R.A., Vaughan, D.J., 1997. Rock-forming Minerals: Non-silicates: oxides, hydroxides and sulphides. Volume 5A. The Geological Society, London, UK.

Dmitrijeva, M., Metcalfe, A.V., Ciobanu, C.L., Cook, N.J., Frenzel, M., Keyser, W.M., Johnson, G., Ehrig, K., 2018. Discrimination and variance structure of trace element signatures in hematite: a case study of BIF-mineralization from the Middleback Ranges, South Australia. Mathematical Geosciences 50, 381-415.

Dupuis, C., Beaudoin, G., 2011. Discrimination diagrams for iron oxide trace element fingerprinting of mineral deposit types. Mineralium Deposita 46, 319-335.

Dutch, R.A., Hand, M., Kelsey, D.E., 2010. Unravelling the tectonothermal evolution of reworked Archean granulite facieses metapelites using in situ geochronology: an example from the Gawler Craton, Australia. Journal of Metamorphic Geology 28, 293-316.

Egglseder, M.S., Cruden, A.R., Tomkins, A.G., Wilson, S.A., Dalstra, H.J., Rielli, A., Li, C., Baumgartner, J., Faivre, D., 2019. Tiny particles building huge ore deposits – Particle-based crystallisation in banded iron formation-hosted iron ore deposits (Hamersley Province, Australia). Ore Geology Reviews 104, 160-174.

Fanning, C.M., 1997. Geochronological synthesis of Southern Australia. Part II. The Gawler Craton. South Australia Department of Mines and Energy, Open File Envelope 8918 (unpublished).

Fanning, C.M., Flint, R.B., Parker, A.J., Ludwig, K.R., Blissett, A.H., 1988. Refined Proterozoic evolution of the Gawler Craton, South Australia, through U-Pb Zircon geochronology. Precambrian Research 40/41, 363-386.

Farley, K.A., McKeon, R., 2015. Radiometric dating and temperature history of banded iron formation-associated hematite, Gogebic iron range, Michigan, USA. Geology 43, 1083-1086.

Fleet, M., 1981. The structure of magnetite: Acta Crystallographica 37, 917- 920.

Flint, R.B., Benbow, M.C., 1977. Geology of the Mount Woods Inlier. Department of Mines, South Australia Report Book 77/134, 50 pp.

Fraser, G., McAvaney, S., Neumann, N., Szpunar, M., Reid, A., 2010. Discovery of early Mesoarchean crust in the eastern Gawler Craton, South Australia. Precambrian Research 179, 1-21.

Frei, R., Gaucher, C., Poulton, S.W., Canfield, D.E., 2009. Fluctuations in Precambrian atmospheric oxygenation record by chromium isotopes. Nature 461, 250-253.

Ghiorso, M.S., Sack, O., 1991. Fe-Ti oxide geothermometry: thermodynamic formulation and the estimation of intensive variables in silicic magmas. Contributions to Mineralogy and Petrology 108, 485-510.

Gourcerol, B., Thurston, P.C., Kontak, D.J., Côté-Mantha, O., Biczok, J., 2016a. Depositional setting of Algoma-type banded iron formation. Precambrian Research 281, 47-79.

Gourcerol, B., Kontak, D.J., Thurston, P.C., 2016b. Do magnetite layers in Algoma-type banded iron formations preserve their primary geochemical signature? A case study of samples from three Archean BIF-hosted gold deposits. The Canadian Mineralogist 54, 605-624.

Hagemann, S.G., Angerer, T., Duuring, P., Rosière, C.A., Figueiredo e Silva, R.C., Lobato, L., Hensler, A.S., Walde, D.H.G., 2016. BIF-hosted iron mineral system: A review. Ore Geology Reviews 76, 317-359.

Hagemann, S.G., Rosière, C.A., Lobato, L., Baars, F., Zucchetti, M., Figueiredo e Silva, R.C., 2006. Controversy in genetic models for Proterozoic high-grade, banded iron formation (BIF)-related iron deposits – unifying or discrete model(s)? Applied Earth Science 115, 147-151.

Hand, M., Reid, A., Jagodzinski, L., 2007. Tectonic framework and evolution of the Gawler Craton, southern Australia. Economic Geology 102, 1377-1395.

Harder, E.C., 1919. Iron-depositing bacteria and their geological relations: U.S. Geological Survey Professional Paper 113, 89 p.

Hensler, A.-S., Hagemann, S.G., Rosière, C.A., Angerer, T., Gilbert, S., 2015. Hydrothermal and metamorphic fluid-rock interaction associated with hypogene "hard" iron ore mineralisation in the Quadrilátero Ferrífero, Brazil: Implications from in-situ laser ablation ICP-MS iron oxide chemistry. Ore Geology Reviews 69, 325-351.

Hill, R.J., Craig, J.R., Gibbs, G.V., 1979. Systematics of the spinel structure type. Physics and Chemistry of Minerals 4, 317-339.

Hoashi, M., Bevacqua, D.C., Otake, T., Watanabe, Y., Hickman, A.H., Utsunomiya, S., Ohmoto, H., 2009. Primary haemetite formation in an oxygenated sea 3.46 billion years ago. Nature Geoscience 2, 301-306.

Hoffman, P.F., Kaufman, A.J., Halverson, G.P., Schrag, D.P., 1998. A Neoproterozoic snowball Earth. Science 281, 1342-1346.

Holland, H.D., 1973. The oceans: A possible source of iron in iron-formations. Economic Geology 68, 1169-1172.

Holland, H.D., 1984. The Chemical Evolution of the Atmosphere and Oceans. Princeton, NJ: Princeton University Press.

Holland, H. D. 2005. 100th Anniversary special paper: sedimentary mineral deposits and the evolution of Earth's near-surface environments. Economic Geology 100, 1489-1509.

Huberty, J.M., Konishi, H., Heck, P.R., Fournelle, J.H., Valley, J.W., Xu, H., 2012. Silician magnetite from the Dales Gorge Member of the Brockman Iron Formation, Hamersley Group, Western Australia. American Mineralogist 97, 26-37.

Huston, D.L., Logan, B.W., 2004. Barite, BIFs and bugs: Evidence for the evolution of the Earth's early hydrosphere. Earth and Planetary Science Letters 220, 41-55.

Isley, A.E., 1995. Hydrothermal plumes and the delivery of iron to banded iron formation. Journal of Geology 103, 169-185.

Ismail, R., Ciobanu, C.L., Cook, N.J., Teale, G.S., Giles, D., Mumm, A.S., Wade, B., 2014. Rare earths and other trace elements in minerals from skarn assemblages, Hillside iron oxide-copper-gold deposit, Yorke Peninsula, South Australia. Lithos 184-187, 456-477.

James, H.L., 1954. Sedimentary facies of iron-formation. Economic Geology 49, 235-293.

James, H.L., 1966. Data of geochemistry, 6th Edition, Chemistry of the iron-rich sedimentary rocks. U.S. Geological Survey Professional Paper 440-W, 61p. Washington DC, USA.

James, H.L., 1983. Distribution of banded iron-formations in space and time. In: Trendall, A.F. and Morris, R.C. (ed.), Iron-formation: Facts and problems: Amsterdam, Elsevier, Developments in Precambrian Geology 6, 471-490.

Keyser, W.M., Ciobanu, C.L., Cook, N.J., Courtney-Davies, L., Ehrig, K., Gilbert, S., McPhie, J., 2017. Links between sedimentary protoliths and IOCG-skarn alteration, Island Dam, South Australia, Extended abstract, 14th Biennial SGA Conference, Québec, Canada, vol. 3, pp. 935-938.

Keyser, W., Ciobanu, C.L., Cook, N.J., Johnson, G., Dmitrijeva, M., Courtney-Davies, L., Feltus, H., Gilbert, S., Johnson, G., Ehrig, K., 2019a. Iron-oxides constrain BIF evolution in terranes with protracted geological histories: the Iron Count prospect, Middleback Ranges, South Australia. Lithos 324-325, 20-38.

Keyser, W., Ciobanu, C.L., Cook, N.J., Feltus, H., Johnson, G., Slattery, A., Wade, B.P., Ehrig, K., 2019b. Mineralogy of zirconium in iron-oxides: A micron- to nanoscale study of hematite ore from Peculiar Knob. Minerals 9, 244. https://doi.org/10.3390/min9040244.

Keyser, W., Ciobanu, C.L., Cook, N.J., Courtney-Davies, L., Kennedy, A., Wade, B.P., Ehrig, K., Dmitrijeva, M., Kontonikas-Charos, A., Feltus, H., Johnson, G., 2019c. Petrographic and geochronological constraints on the granitic basement to the Middleback Ranges, South Australia. Precambrian Research 324, 170-193.

Keyser, W.M., Ciobanu, C.L., Cook, N.J., Johnson, G., Feltus, F., Johnson, S., Dmitrijeva, M., Ehrig, K., Nguyen, P., 2018. Petrography and trace element signatures of iron-oxides in deposits from the Middleback Ranges, South Australia: from banded iron formation to ore. Ore Geology Reviews 93, 337-360.

Keyser, W., Ciobanu, C.L., Cook, N.J., Wade, B.P., Kennedy, A., Kontonikas-Charos, A., Ehrig, K., Feltus, H., Johnson, G., (in review). Episodic mafic magmatism in the Eyre Peninsula: defining syn- and post-depositional BIF environments for iron deposits in the Middleback Ranges, South Australia. Precambrian Research.

Klein, C. 2005. Some Precambrian banded iron-formations (BIFs) from around the world: Their age, geological setting, mineralogy, metamorphism, geochemistry, and origin. American Mineralogist 90, 1473-1499.

Klein, C., Beukes, N.J., 1993. Sedimentology and geochemistry of the glaciogenic late Proterozoic Rapitan iron-formation in Canada. Economic Geology 88, 542-565.

Klein, C., Gole, M.J., 1981. Mineralogy and petrology of parts of the Marra Mamba Iron Formation, Hamersley Basin, Western Australia. American Mineralogist 66, 507-525.

Knipping, J., Bilenker, J., Simon, A., Reich, M., Barra, F., Deditius, A., Wälle, M., Heinrich, C. Holtz, F., Munizaga, R., 2015. Trace elements in magnetite from massive iron oxide-apatite deposits indicate a combined formation by igneous and magmatic-hydrothermal processes. Geochimica et Cosmochimica Acta, 171, 15-38.

Lee, C.,-W., Jung, S.,-S., Lee, J.,-S., 2008. Phase transformations of β-Fe_2O_3 hollow nanoparticles. Materials Letters 62, 561-563.

Leevers, P., Gaughan, C., Bubner, G., 2005. The Iron Magnet deposit. Australasian Institute of Mining and Metallurgy Publication Series, Iron Ore Conference, Fremantle, WA, 19-21 September 2005.

Lepp, H., Golditch, S.S., 1964. Origin of Precambrian iron-formations. Economic Geology 59, 1025-1060.

Li, Zhi-., Q., Zhang, L-., C., Xue, C-., J., Zheng, M-., T., Zhu, M-., T., Robbins, L.J., Slack, J.F., Planavsky, N.J., Konhauser, K.O., 2018. Earth's youngest banded iron formation implies ferruginous conditions in the Early Cambrian ocean. Scientific Reports 8, 1-10.

MacLeod, W.N., de la Hunty, L.E., Jones, W.R., Halligan, R., 1963. Preliminary report on the Hamersley Iron Province, North West Division. West. Aust. Geological Survey, Annual Report, 1962: 44-54.

Marshall, C.P., Emry, J.R., Marshall, A.O., 2011. Haematite pseudomicrofossils present in the 3.5-billion-year-old Apex Chert. Nature Geoscience 4, 240-243.

Maslen, E.N., Streltsov, V.A., Streltsov, N.R., Ishizawa, N., 1994. Synchrotron X-ray study of electron density in α-Fe_2O_3. Acta Crystallographica Section B 50, 435-441.

Morris, B.J., Hough, J.K., 1997. South Australia Steel and Energy Project, Peculiar Knob Prospect, South Australia. Department of Mines and Energy Resources. Report Book 97/9.

Mücke, A., Cabral, A.R., 2005. Redox and nonredox reactions of magnetite and hematite in rocks. Chemie der Erde 65, 271-278.

Nadoll, P., Angerer, T., Mauk, J.L., French, D., Walshe, J., 2014. The chemistry of hydrothermal magnetite: A review. Ore Geology Reviews 61, 1-32.

Nadoll, P., Koenig, A.E., 2011. LA-ICP-MS of magnetite: Methods and standards. Journal of Analytical Atomic Spectrometry 26, 1872-1877.

Ohmoto, H., 1996. Evidence in pre-2.2 Ga paleosols for the early evolution of atmospheric oxygen and terrestrial biota. Geology 12, 1135-1138.

Ohmoto, H., 2003. Nonredox transformations of magnetite-hematite in hydrothermal systems. Economic Geology 98, 157-161.

Otake, T., Wesolowski, D.J., Anovitz, L.M., Allard, L.F., Ohmoto, H., 2007. Experimental evidence for non-redox transformations between magnetite and hematite under H_2-rich hydrothermal conditions. Earth and Planetary Science Letters 257, 60-70.

Otake, T., Wesolowski, D.J., Anovitz, L.M., Allard, L.F., Ohmoto, H., 2010. Mechanisms of iron oxide transformations in hydrothermal systems. Geochimica et Cosmochimica Acta 74, 6141-6156.

Parker, A.J., 1980. The Kalinjala Mylonite Zone, eastern Eyre Peninsula. Quarterly Geological Notes 76, 6-11 (Geological Survey of South Australia).

Parker, A.J., Lemon, N.M., 1982. Reconstruction of the early Proterozoic stratigraphy of the Gawler Craton, South Australia. Journal of the Geological Society of Australia 29, 221-238.

Planavsky, N., Bekker, A., Rouxel, O.J., Kamber, B., Hofmann, A., Knudsen, A., Lyons, T.W., 2010. Rare earth elements and yttrium compositions of Archean and Paleoproterozoic Fe formations revisited: New perspectives on the significance and mechanisms of depositions. Geochimica et Cosmochimica Acta, 74, 6387-6405.

Posth, N.R., Hegler, F., Konhauser, K.O., Kappler, A., 2008. Alternating Si and Fe deposition caused by temperature fluctuations in Precambrian oceans. Nature Geoscience 1, 703-708.

Rasmussen, B., Meier, D.B., Krapež, B., Muhling, J.R., 2013. Iron silicate microgranules as precursor sediments to 2.5-billion-year-old banded iron formations. Geology 41, 435-438.

Rasmussen, B., Muhling, J.R., Fischer, W.W., 2019. Evidence from laminated chert in banded iron formations for deposition by gravitational settling of iron-silicate muds. Geology 47, 167-170.

Reid, A.J., Fabris, A., 2015. Influence of pre-existing low metamorphic grade sedimentary successions on the distribution of iron oxide copper-gold mineralization in the Olympic Cu-Au province, Gawler Craton. Economic Geology 110, 2147-2157.

Reid, A., Hand, M., Jagodzinski, E., Kelsey, D., Pearson, N., 2008. Paleoproterozoic orogenesis in the southeastern Gawler Craton, South Australia. Australian Journal of Earth Sciences 55, 449-471.

Reid, A.J., Swain, G., Mason, D., Maas, R., 2011. Nature and timing of Cu-Au-Zn-Pb mineralisation at Punt Hill, eastern Gawler Craton. MESA Journal 60, 7-17.

Robb, L., 2005. Introduction to ore-forming processes. Blackwell Science. pp. 373. ISBN 978-0-632-06378-9.

Schaefer, B., 1998. Insights into Proterozoic tectonics from the southern Eyre Peninsula, South Australia. Ph.D. Thesis, The University of Adelaide.

Schwertmann, U., 2008. Iron Oxides. In: Chesworth, W. (ed), Encyclopedia of Soil Science. Springer, Dordrecht, 363-369.

Skirrow, R., Bastrakov, E., Davidson, G., Raymond, O., Heithersay, P., 2002. The geological framework, distribution and controls of Fe-oxide Cu-Au mineralisation in the Gawler Craton, South Australia. Part II-alteration and mineralisation. In Porter, T.M. (Ed.), Hydrothermal Iron Oxide Copper-Gold and Related Deposits: A Global Perspective 2, PGC Publishing, Adelaide, 33-47.

Skirrow, R.G., Bastrakov, E.N., Barovich, K., Fraser, G.L., Creaser, R.A., Fanning, C.M., Raymond, O.L., Davidson, G.J., 2007. Timing of iron oxide Cu-Au-(U) hydrothermal activity and Nd isotope constraints on metal sources in the Gawler Craton, South Australia. Economic Geology 102, 1441-1470.

Sun, S., Li, Y.L., 2017. Geneses and evolutions of iron-bearing minerals in banded iron formations of >3760 to ca. 2200 million-year-old: Constraints from electron microscopic, X-ray diffraction and Mössbauer spectroscopic investigations. Precambrian Research 289, 1-17.

Szpunar, M., Hand, M., Barovich, K., Schwarz, M., Jagodzinski, E., Belousova, E., 2011. Isotopic and geochemical constraints on the Paleoproterozoic Hutchison Group, southern Australia: Implications for Paleoproterozoic continental reconstructions. Precambrian Research 187, 99-126.

Taner, M.F., Chemam, M., 2015. Algoma-type banded iron formation (BIF), Abitibi Greenstone Belt, Quebec, Canada. Ore Geology Reviews 70, 31-46.

Taylor, D., Dalstra, H.J., Harding, A.E., Broadbent, G.C., Barley, M.E., 2001. Genesis of high-grade hematite orebodies of the Hamersley Province, Western Australia. Economic Geology 96, 837-873.

Thompson, B.P., 1969. Precambrian basement cover – the Adelaide System. In: Parker, L.W. (ed), Handbook of South Australian geology. Adelaide, South Australia Geological Survey, 49-83.

Trendall, A.F., 1968. Three great basins of Precambrian banded iron deposits. Geological Society of America Bulletin 79, 1527-1544.

Trendall, A.F., 1983. Introduction. In: Trendall, A.F. and Morris R.C. (ed), Iron-Formation: Facts and Problems, 1-11. Elsevier, Amsterdam.

Vassallo, J.J., Wilson, C.J.L., 2001. Structural repetition of the Hutchison Group metasediments, Eyre Peninsula, South Australia. Australian Journal of Earth Sciences 48, 331-345.

Vassallo, J.J., Wilson, C.J.L., 2002. Palaeoproterozoic regional-scale non-coaxial deformation: an example from eastern Eyre Peninsula, South Australia. Journal of Structural Geology 24, 1-24.

Verdugo-Ihl, M.R., Ciobanu, C.L., Cook, N.J., Ehrig, K., Courtney-Davies, L., 2019. Defining early stages of IOCG systems: Evidence from iron-oxides in the outer shell of the Olympic Dam deposit, South Australia. Mineralium Deposita. Doi:10.1007/s00126-019-00896-2.

Verdugo-Ihl, M.R., Ciobanu, C.L., Cook, N.J., Ehrig, K.J., Courtney-Davies, L., Gilbert, S., 2017. Textures and U-W-Sn-Mo signatures in hematite from the Olympic Dam Cu-U-Au-Ag deposit, South Australia: Defining the archetype for IOCG deposits. Ore Geology Reviews 91, 173-195.

Verwey, E.J.W., de Boer, J.H., 1936. Cation arrangement in a few oxides with crystal structures of the spinel type. Recueil des Travaux Chimiques des Pays Bas, 55, 531-540.

Wang, Y., Xu, H., Merino, E., Konishi, H., 2009. Generation of banded iron formations by internal dynamics and leaching of oceanic crust. Nature Geoscience 2, 781-784.

Wen, G., Li, J.-W., Hofstra, A. H., Koenig, A. E., Lowers, H. A., Adams, D., 2017. Hydrothermal reequilibration of igneous magnetite in altered granitic plutons and its implications for magnetite classification schemes: Insights from the Handan-Xingtai iron district, North China Craton. Geochimica et Cosmochimica Acta 213, 255-270.

White, A.F., Peterson, M.L., Hochella, M.F., 1994. Electrochemistry and dissolution kinetics of magnetite and ilmenite. Geochemica et Cosmochimica Acta 58, 1859-1875.

Williams, P.J., Barton, M.D., Johnson, D.A., Fontboté, L., De Haller, A., Mark, G., Oliver, N.H.S., Marschik, R., 2005. Iron oxide copper-gold deposits: Geology, space-time distribution, and possible modes of origin. Economic Geology 100th Anniversary Volume, 371-405.

Xu, H., Shen, Z., Konishi, H., 2014. Si-magnetite nano-precipitates in silician magnetite from banded iron formation: Z-contrast imaging and ab initio study. American Mineralogist 99, 2196-2202.

Yeates, G., 1990. Middleback Range iron ore deposits. In: Hughes, F.E. (ed), Geology of the Mineral Deposits of Australia and Papua New Guinea. Australasian Institute of Mining and Metallurgy, Monograph Series 14, 1045-1048.

Yin, S., Ma, C., Robinson, P. T., 2017. Textures and high field strength elements in hydrothermal magnetite from a skarn system: Implications for coupled dissolution-reprecipitation reactions. The American Mineralogist 102, 1045-1056.

Young, G.M., 1976. Iron-formation and glaciogenic rocks of the Rapitan Group, Northwest Territories Canada. Precambrian Research 3 137-158.

CHAPTER 2

PETROGRAPHY AND TRACE ELEMENT SIGNATURES OF IRON-OXIDES IN DEPOSITS FROM THE MIDDLEBACK RANGES, SOUTH AUSTRALIA: FROM BANDED IRON FORMATION TO ORE

William Keyser[1], Cristiana L. Ciobanu[1], Nigel J. Cook[1], Geoff Johnson[2], Holly Feltus[2], Steve Johnson[2], Marija Dmitrijeva[1], Kathy Ehrig[3], Phung T. Nguyen[2]

[1]*School of Chemical Engineering, The University of Adelaide, Adelaide, SA 5005, Australia*

[2]*SIMEC Mining, Level 2 169 Fullarton Road, Dulwich, SA 5005, Australia*

[3]*BHP Olympic Dam, Adelaide, SA 5000, Australia*

Article published in Ore Geology Reviews 93 (2018), 337-360

Statement of Authorship

Title of Paper	Petrography and trace element signatures of iron-oxides in deposits from the Middleback Ranges, South Australia: From banded iron formation to ore
Publication Status	☑ Published ☐ Accepted for Publication ☐ Submitted for Publication ☐ Unpublished and Unsubmitted w ork w ritten in manuscript style
Publication Details	Keyser, W., Ciobanu, C.L., Cook, N.J., Johnson, G., Feltus, H., Johnson, S., Dmitrijeva, M., Ehrig, K., Nguyen, P.T., 2018. Petrography and trace element signatures of iron-oxides in deposits from the Middleback Ranges, South Australia: From banded iron formation to ore. Ore Geology Reviews 93, 337-360.

Principal Author

Name of Principal Author (Candidate)	William Keyser		
Contribution to the Paper	Performed analytical work, carried out data processing and interpretation, oversaw development of work and wrote manuscript.		
Overall percentage (%)	65		
Certification:	This paper reports on original research I conducted during the period of my Higher Degree by Research candidature and is not subject to any obligations or contractual agreements with a third party that would constrain its inclusion in this thesis. I am the primary author of this paper.		
Signature		Date	4/6/2019

Co-Author Contributions

By signing the Statement of Authorship, each author certifies that:

i. the candidate's stated contribution to the publication is accurate (as detailed above);

ii. permission is granted for the candidate in include the publication in the thesis; and

iii. the sum of all co-author contributions is equal to 100% less the candidate's stated contribution.

Name of Co-Author	Cristiana L. Ciobanu		
Contribution to the Paper	Helped define direction of research, supervised development of work, assisted with data collection and interpretation and contributed to manuscript preparation.		
Overall percentage (%)	10		
Signature		Date	6 June 2019

Name of Co-Author	Nigel J. Cook		
Contribution to the Paper	Helped define direction of research, supervised development of work, assisted with data interpretation and contributed to manuscript preparation.		
Overall percentage (%)	7		
Signature		Date	4/6/19

Name of Co-Author	Geoff Johnson		
Contribution to the Paper	Assisted with sample collection and evaluation of manuscript.		
Overall percentage (%)	4		
Signature		Date	30/5/2019

Name of Co-Author	Holly Feltus		
Contribution to the Paper	Assisted with sample collection and evaluation of manuscript.		
Overall percentage (%)	4		
Signature		Date	30/4/2019

Name of Co-Author	Steve Johnson		
Contribution to the Paper	Assisted with sample collection and evaluation of manuscript.		
Overall percentage (%)	3		
Signature		Date	30/4/2019

Name of Co-Author	Marija Dmitrijeva		
Contribution to the Paper	Assisted with construction of map and with evaluation of manuscript.		
Overall percentage (%)	3		
Signature		Date	30/4/2019

Name of Co-Author	Kathy Ehrig		
Contribution to the Paper	Helped define research direction and assisted with evaluation of manuscript.		
Overall percentage (%)	2		
Signature		Date	3/6/2019

Name of Co-Author	Phung T. Nguyen		
Contribution to the Paper	Assisted with sample collection and evaluation of manuscript.		
Overall percentage (%)	2		
Signature		Date	1/5/2019

Ore Geology Reviews 93 (2018) 337–360

Contents lists available at ScienceDirect

Ore Geology Reviews

journal homepage: www.elsevier.com/locate/oregeorev

Petrography and trace element signatures of iron-oxides in deposits from the Middleback Ranges, South Australia: From banded iron formation to ore

William Keyser[a,*], Cristiana L. Ciobanu[a], Nigel J. Cook[a], Geoff Johnson[b], Holly Feltus[b], Steve Johnson[b], Marija Dmitrijeva[a], Kathy Ehrig[c], Phung T. Nguyen[b]

[a] School of Chemical Engineering, The University of Adelaide, Adelaide, SA 5005, Australia
[b] SIMEC Mining, Level 2 169 Fullarton Road, Dulwich, SA 5065, Australia
[c] BHP Olympic Dam, Adelaide, SA 5000, Australia

ARTICLE INFO

Keywords:
Middleback Ranges
Banded iron formation
Fe-oxides
Trace element geochemistry
Hydrothermal overprinting

ABSTRACT

The Middleback Ranges is a major iron ore belt in the southeastern region of the Gawler Craton, South Australia, interpreted to be of BIF origin. Iron ore deposits are hosted within ~2550 Ma metasedimentary rocks of the Middleback Group and occur as a series of N-S trending hills, forming a ~60 km-long magnetic anomaly. A petrographic-geochemical study of iron-oxides from BIFs and iron ores was undertaken on samples from thirteen locations spanning the strike of the belt. Iron-oxides are texturally diverse due to multiple processes accompanying and postdating ore formation. Primary magnetite features preserved in the southern segment of the belt display distinct overprinting features (e.g., increased porosity, reworked grain boundaries) and multiple generations of growth associated with deposition of trace minerals, including native gold. Northwards along strike, this overprint is expressed by the pseudomorphic replacement of magnetite by hematite (martite) and is locally associated with brecciation, the presence of rare earth element (REE)-minerals, and replacement by iron-hydroxides. Whereas evidence of microplaty hematite accompanying martitization and predating iron-hydroxides is observed throughout the belt, distinct iron-oxide generations postdating the iron-hydroxides are inferred based on compositional zoning with respect to Si and intimate relationships between iron-oxides and -hydroxides. Chondrite-normalized fractionation trends obtained from the various iron-oxides and from different BIF types generally display LREE-enrichment and distinct positive Eu- and Y-anomalies. An increasing ΣREY- and LREE-trend accompanies martitization. The presence of specific element groups, e.g., granitophile elements (U, W, Sn, Mo), or transition metals (Cr, Mn, Co, Ni, Ti, V, Nb) within the lattice of iron-oxides suggests their formation in evolving environments associated with the emplacement of felsic and mafic lithologies, respectively. The impact of local setting on iron-oxide formation is highlighted by complex trace element signatures of iron-oxides; the northern segment of the belt is relatively enriched in As and Sb, while the southern segment is enriched in granitophile elements and REY. Further complexity is shown in the local variation of Mn and Zn in iron-oxides in the southern segment of the belt, where the Iron Magnet deposit shows the strongest correlation between the two elements. Various depositional settings for BIFs are inferred based upon Post-Archean Australian Shale-normalized REY fractionation trends of iron-oxides and various water types. These settings include environments where iron-minerals precipitate from mixtures of 1) anoxic seawater and high-temperature hydrothermal fluids, 2) anoxic seawater and low-temperature hydrothermal fluids, and 3) oxygen-richer seawater and low-temperature hydrothermal fluids. A genetic model for ore formation is proposed based upon textural and compositional variations observed in iron-oxides throughout the belt and includes formation resulting from supergene fluids rich in elements leached from local granites penetrating BIF, interaction with granite-derived hydrothermal fluids, and heat generated during emplacement of younger dikes. Recognition of petrographic features linked to changes in composition demonstrates the utility of iron-oxides to trace iron ore formation in a temporal and spatial context, with implications for ore genesis and models of mineral exploration.

* Corresponding author.
E-mail address: william.keyser@adelaide.edu.au (W. Keyser).

https://doi.org/10.1016/j.oregeorev.2018.01.006
Received 9 August 2017; Received in revised form 10 December 2017; Accepted 10 January 2018
Available online 10 January 2018

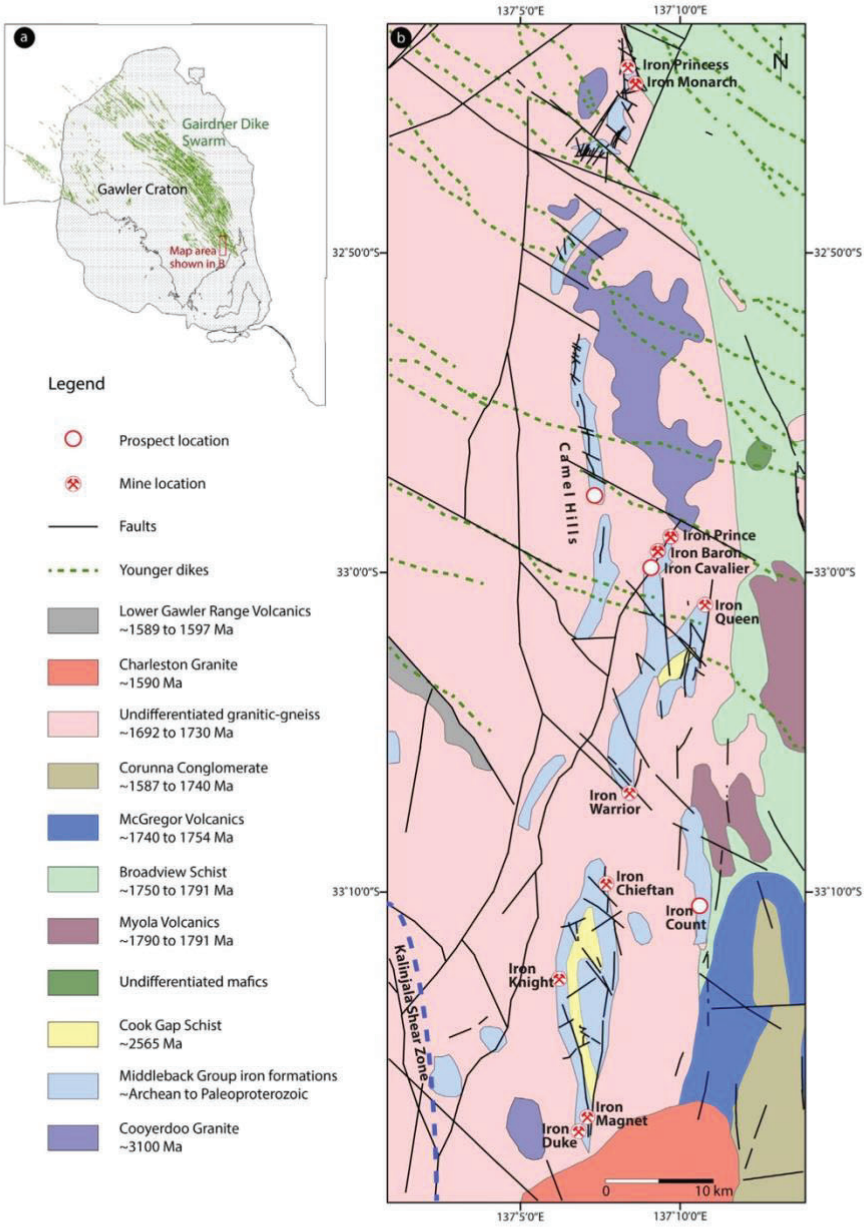

Fig. 1. (a) Location of the MR within the Gawler Craton and extent of the Gairdner Dike Swarms. (b) Simplified geological map of the MR and locations of iron ore deposits. State-wide and regional maps showing inferred Gairdner Dikes sourced from http://map.sarig.sa.gov.au/. Cooyerdoo Granite outcrop after McAvaney (2012).

1. Introduction

Trace element signatures in minerals can be used to trace the evolution of different types of mineral deposits if these are well-characterized and understood in their petrogenetic context (Cook et al., 2016, and references therein). The minerals in question may represent the ore commodity, be a common co-existing phase (e.g., pyrite in Au-deposits), or a gangue/accessory mineral (e.g., garnet-hosted Mo in

skarn-hosted Cu-deposits; Xu et al., 2016) formed at the same time within a given deposit type. The concentrations of different trace elements and their variations with respect to host rock, degree of alteration, or spatially with proximity to mineralization can provide valuable information about the evolution of the ore-forming environment, and potentially assist development of genetic or exploration models.

Iron- and Si-rich minerals are the primary constituents of banded iron formations (BIFs), chemically precipitated rock types deposited throughout the Precambrian in settings ranging from shallow, passive-continental shelves to deeper waters near volcanic centers (Gross, 1980). BIFs and their reworked and upgraded equivalents host the largest iron ore resources on Earth. Trace element studies of BIFs are generally focused on two topics: 1) changes in atmospheric and depositional conditions in a spatial and temporal context (e.g., Bekker et al., 2010); and 2) the transformation processes leading to the formation of iron ore from protore BIF (e.g., Hagemann et al., 2016, and references therein). Understanding rare earth element (REE) behavior in BIFs is of particular value for constraining atmospheric and depositional conditions in that they resemble those in seawater at the time of precipitation (Bau and Dulski, 1996; Slack et al., 2007; Planavsky et al., 2010). Many interpretations from BIF studies are derived from whole-rock geochemistry. However, whole-rock compositions have shown to be highly variable due to post-depositional processes and detrital contamination (Aoki et al., 2017). More holistic approaches toward understanding BIFs focus on detailed trace element analysis of minerals within BIFs (e.g., carbonates, phosphates and Fe-oxides; Alibert, 2016; Gourcerol et al., 2016a,b).

The Middleback Ranges (MR) is a major iron ore belt in South Australia, with hematite and magnetite reserves of 32.2 Mt and 56 Mt, respectively, @ ~50–55% Fe (Arrium Mining, 2016). Mineral resources within the MR were first identified in the mid-19th Century (Yeates, 1990). The iron ore deposits are interpreted to be of BIF origin and drew early comparisons to those hosted within well-known BIFs in the Lake Superior region or Krivoi Rog (Ward, 1949). Despite extensive mining, the age and geological evolution of the belt continues to be debated. Deposition of the MR has been interpreted as a Paleoproterozoic event (Parker and Lemon, 1982; Yeates, 1990) whereas other studies, including the most recent (Szpunar et al., 2011), argue for a late Archean depositional setting with possible links to giant BIF deposits of the Hamersley Basin, Pilbara Craton, Western Australia.

Trace element signatures in the two, common Fe-oxides that make up BIFs, magnetite and hematite, have been studied (e.g., Angerer et al., 2012; Huberty et al., 2012; Hensler et al., 2015; Gourcerol et al., 2016a,b), with the purpose of defining depositional environments and geochemical tracers for deposit evolution. This is the first petrographic-geochemical study of Fe-oxides from BIFs and iron ores from the MR belt. The primary objective is to demonstrate the utility of Fe-oxides to provide a temporal and spatial context for iron ore formation in the Middleback Ranges. Such an application could, potentially, provide a valuable tool for mineral exploration in the region or elsewhere. Additionally, fractionation trends for rare earth elements (La, Ce, Pr, Nd, Sm, Eu, Gd, Tb, Dy, Ho, Er, Tm, Yb, Lu) and yttrium (Y) are assessed with the purpose of deciphering depositional environments.

2. Geological background

2.1. Regional geology

The Middleback Ranges BIFs form part of the metasedimentary Hutchinson Group in the northeastern Eyre Peninsula (Fig. 1). Recent isotopic and geochemical data suggests this sedimentary succession consists of three distinct subgroups deposited between ~2550 and ~1730 Ma (Szpunar et al., 2011). The > 20 discrete iron ore deposits of the MR form a ~60 km-long belt and are hosted within metamorphosed chemical and clastic sediments and extrusive basic and acid volcanic rocks of the Middleback Group. There is debate as to whether the Middleback Group stratigraphy features two iron-bearing units (the Lower and Upper Middleback Iron Formations) separated by an index lithology (the ~2565 Ma Cook Gap Schist; Szpunar et al., 2011), or, alternatively, there is structural repetition of the Lower Middleback Iron Formation via thrusting and folding (e.g., Yeates, 1990). Southwards extension of the MR has been proposed (e.g., Bungalow prospect), based on recent geochronology results (Jagodzinski et al., 2011).

The majority of the deposits are hosted within the Lower Middleback Iron Formation, which belongs to a terrane also comprising undifferentiated gneissic-granitic rocks with a minimum age of ~1730–1750 Ma, and several intrusive suites, of which the oldest is the ~3100 Ma Cooyerdoo Granite (Fraser et al., 2010), and the youngest is the ~1600 Ma Hiltaba Intrusive Suite (hereafter referred to generically as 'Hiltaba Granites') (e.g., Charleston Granite; Creaser and Fanning, 1993) and contemporaneous Gawler Range Volcanics. Three orogenic events are recognized in the region. The ~2470–2410 Ma Sleafordian and ~1850 Ma Cornian Orogenies account for the granulite to amphibolite facies metamorphic overprint on the basement. The Cornian Orogeny is associated with a significant magmatic event leading to emplacement of the Donington Magmatic Suite (Reid and Hand, 2012). The ~1730–1690 Ma Kimban Orogeny accounts for amphibolite facies metamorphism and (re)-activation of major crustal structures in the region, notably the Kalinjala Shear Zone (Vassallo and Wilson, 2002), west of the MR (Fig. 1), which could conceivably have acted as a conduit for fluid focusing and ore transformation in the MR. The latest tectono-magmatic event recognized in the region is the emplacement of dolerite dikes associated with the ~800 Ma Gairdner large igneous province (Pirajno and Hoatson, 2012).

Extensive mining in the MR has led to a better understanding of iron deposit stratigraphy (Yeates, 1990; Leevers et al., 2005). However, many questions remain open, particularly with respect to the mechanisms of ore formation and the timing of major enrichment events. The recognition of Hiltaba-associated iron-oxide-copper-gold (IOCG)-style mineralization along the eastern flank of the MR (Moola prospect; Feltus et al., in prep.) emphasizes the need for further constraints on the geological evolution of the region.

2.2. Deposit geology

Orebodies of the MR are of irregular lenticular shape and variable size, up to 3 km in length and several hundred meters in width, and are predominantly hosted within the Lower Middleback Iron Formation, which grades upwards from a 'mixed' basal sequence to a lower iron-carbonate unit, a middle iron-talc unit and an upper iron-silica unit, all grading up sequence and laterally with weathering to goethite-limonite rocks occurring near the surface (Leevers et al., 2005). The orebodies are stratabound, concentrated and thickened in N–S synclinal keels (Davies, 2000), and are typically located on western-dipping limbs, with the exceptions of orebodies at Iron Knob and Iron Baron, which dipped east prior to being mined.

Dolerite dikes and sills often disrupt synclinal structures and are spatially associated with ore formation, e.g., mineralization is restricted between two apophyses of a V-shaped dike at Iron Duchess. In Iron Monarch, the orebody hosts at least two generations of dikes, one of which forms a boundary between BIF and ore, and is faulted against quartz-sericite gneiss lithologies to the northwest (Davies, 2000 and references therein). Roughly N–S-striking dikes in the Iron Magnet deposit vary in thickness from < 1 m up to 15 m. These can extend to 2 km in strike length, and such dikes mark the boundary between high-grade hematite mineralization (Iron Duke) from magnetite mineralization in the adjacent down-dip Iron Magnet orebody (Leevers et al., 2005). Major N–S shear zones bound the west and east sides of the Iron Magnet deposit, and crosscutting WNW-, NW-, NE- and ENE-trending faults displace mineralization. Similar striking faults can be seen throughout the belt. Local brecciation occurs in the Iron Princess

Table 1a
Index of samples studied from the southern segment of the Middleback Ranges.

Deposit	Sample	Location	Depth (m)	Rock Type	Texture	Iron Oxides			Fe-Hy	Sulfides and related	REE-min,	Index
						Mt	Mrt	Hm	(Goe, Lp)		Other minor	Minerals
Iron Duke	MB20	DX290	28.3	Hm-Goe ore	Banded, vuggy	x	X	x	x			
Iron Magnet	MB33	DD03IM001 MTS	83.5–100.5	Qz-Tal facies Mt-BIF	Fine banded, brown-green and black	X	x				Ap	Tal
	MB34a	DD03IM001 MTT	107.55–113.1	Qz-Tal facies Mt-BIF	Pale-green, white and black rhythms	X	x			Cp	Ap	Tal
	MB34b	DD03IM001 MTT	107.55–113.1	Qz-Tal facies Mt-BIF	Stockwork (crosscutting veins)	X	xx	x	x	Cp, Po	Ap	Tal
	MB35a	DD03IM001 MTO	308.6–316	Tal facies Mt-BIF	Fine banded, green–brown and black	X	x			Py	Ap	Tal
	MB35b	DD03IM001 MTO	308.6–316	Tal facies Mt-BIF	Banded, green–brown, black and white	X				Znc	Ap	Tal
	MB36a	DD03IM001 MTC	308.6–316	Tal-Cb facies Mt-BIF	Massive, dark green–brown	X				Py, Znc, Au	Ap	Tal, Cb
	MB36b	DD03IM001 MTC	308.6–316	Cb facies Mt-BIF	Breccia, angular fragm.in Cb matrix	X	x			Py, Znc	Ap	Cb
	MB80a	Open pit		Cb facies Mt-BIF	Banded, pale green, white and black	X				Cp		Cb, Tal
	MB80b	Open pit		Tal-Qz facies Mt-BIF	Banded, pale green, white and black	X	x	x			Ap, Mnz	Cb, Tal
	MB92a	Open pit		Cb facies Mt-BIF	Banded, coarse carbonates and Mt	X	x		x	Py, Cp	Ap, Mnz	Cb, Tal
	MB93	Open pit		Tal-Cb facies Mt-BIF	Pale-green, white and black rhythms	X						Psm, Cb, Tal
Iron Knight	MB22	KP232	247	Mrt-Goe ore	Rusty, vuggy, massive ore	xx	X	x	x	Py		
	MB97	Outcrop		Siliceous BIF	Banded		x	X	x		Mnz	
	MB98a	Outcrop		Hm-Goe ore	Massive, vuggy			X	x			
	MB98b	Outcrop		Jaspilite	Banded	x	x	X	x			
	MB98c	Outcrop		Limonite	Massive		x	X	x			Tal, Cb
	MB98d	Outcrop		Goe ore	Brecciated			X	x	Znc		
Iron Count	MB23	Outcrop		Mrt-Goe ore	Massive, vuggy	x	X	x	x	Znc		
	MB24	Outcrop		Goe ore	Massive, vuggy	x		X	x	Cob	Ap, Brt	
	MB40a	Outcrop		Siliceous BIF	Fine banded	x	X			Znc	Mnz, Xtm, Zrc	
	MB40b	Outcrop		Siliceous BIF	Banded	x	X		x	Cpy	Mnz, Xtm	
	MB40c	Outcrop		Siliceous BIF	Banded, veined	x	X	x	x		Mnz, Xtm, Zrc	
	MB41a	Outcrop		Siliceous BIF	Brecciated, relict banding	x	X					
	MB41b	Outcrop		Siliceous BIF	Brecciated, relict banding	x	X			Cp	Brt	
	MB41c	Outcrop		Siliceous BIF	Brecciated, relict banding	x	X	x				
	MB41d	Outcrop		Siliceous BIF	Brecciated, relict banding	x	X	x				
	MB41e	Outcrop		Siliceous BIF	Brecciated, relict banding	x	X					
	MB41f	Outcrop		Siliceous BIF	Brecciated, relict banding	x	X	x				
Iron Chieftain	MB4	CC-DD-0901	25.25	Hm-Goe ore	Vuggy, massive		X	x	x			
	MB5	CC-DD-0904	78.6	Siliceous BIF	Banded, white, black and brown	xx	xx		x			
	MB21	CHDDH0901	26.7	Hm-Goe ore	Massive		x	x	x			

Mineral abbreviations: Ap – apatite; Au – native gold; Brt – barite; Cb – carbonate; Cob – cobaltite; Cp – chalcopyrite; Goe – goethite; Hm – hematite (microplaty and/or microcrystalline); Lp – lepidocrocite; Mnz – monazite; Mrt – martite; Mt – magnetite; Po – pyrrhotite; Psm – pyrosmalite; Py – pyrite; Qz – quartz; Tal – talc; Xtm – xenotime; Znc – zincite; Zrc – zircon. X = main Fe-oxide phase; xx = major Fe-oxide component; x = relict or minor Fe-oxide component.

orebody, which is hosted within a sequence of breccias, conglomerates, sandstones, siltstones and shales known collectively as the 'Princess Beds.' In the eastern ridge at Iron Count, intense brecciation may be associated with emplacement of the Charleston Granite.

Magnetite mineralization in the Lower Middleback Iron Formation is thought to be diagenetic in nature (Yeates, 1990), and has been impacted by hydrothermal alteration (e.g., Iron Magnet; Leevers et al., 2005), predominantly within the carbonate-rich unit, where BIF-structures are well preserved. Economic magnetite mineralization begins above a sulfide unit at the boundary of an underlying dolomite unit (Katunga Dolomite) and the Lower Middleback Iron Formation (Leevers et al., 2005). Ore horizons are interpreted as hydrothermal replacement products of jaspilite sequences (Cook, 1971). At higher levels within the Lower Middleback Iron Formation (e.g., Iron Duke), hematite-rich ores are believed to be products of supergene enrichment of magnetite-rich BIF by descending and circulating meteoric waters (Yeates, 1990; Davies, 2000).

3. Sampling and methodology

The sample suite (Table 1) consists of seventy-eight hand-specimens of BIF and iron ore collected from drillcore, outcrop and open pits and represents 13 deposits and prospects spanning the strike of the belt (Fig. 1b). BIFs and iron ore types representative of the two deposit settings along MR are included: (A) deposits with known evidence of hypogene iron enrichment; and (B) supergene deposits without known evidence for hypogene iron enrichment.

Whole-rock assays were performed by Intertek Genalysis (Adelaide). Methodologies and minimum detection limits (mdl) are provided in Table A.1. Thin-sections and polished-blocks from each sample were examined in both transmitted- and reflected-light to assess mineral and textural relationships. An FEI Quanta 450 scanning electron microscope (SEM) equipped with a back-scatter electron (BSE) detector (Adelaide Microscopy, The University of Adelaide), and operated at 20 kV acceleration voltage and 10 nA beam current, was used for micron-scale

Table 1b
Index of samples studied from the central segment of the Middleback Ranges.

Deposit	Sample	Location	Depth (m)	Rock Type	Texture	Iron Oxides			Fe-Hy	Sulfides and related	REE-min,	Index
						Mt	Mrt	Hm	(Goe, Lp)		Other minor	Minerals
Iron Warrior	MB8	IWI06DD	66.5	Mrt ore	Vuggy, friable	xx	x	x		Py		
	MB9	IWI06DD	49.5–50	Mrt ore	Massive, brecciated	xx	x	x				
	MB10	IWI06DD	38	Mrt ore	Massive, brecciated	xx	x	x				
	MB11	IWI06DD	33.05	Mrt ore	Vuggy, brecciated, massive	xx	x	x				
	MB12	IWI06DD	2.4	Mrt ore	Massive, brecciated	xx	x	x				
Iron Queen	MB27	Open pit		Mrt ore	Massive, friable	xx	X	x				
	MB28	Open pit		Mrt ore	Massive, vuggy	x	X	x				
	MB29	Open pit		Hm-Goe ore	Massive, vuggy		x	x	x			
Iron Cavalier	MB25	ICAV001		Mrt-Goe ore	Banded, brown and grey	x	X		x			
	MB26	ICAV002		Siliceous BIF	Banded, brown and yellow	xx	xx		x			
Iron Baron	MB43	Open pit		Mrt ore	Earthy, massive	x	X	x	x			
	MB44a	Open pit		Mrt ore	Rusty, massive	x	X	x	x			
	MB44b	Open pit		Mrt ore	Rusty, massive	x	X	x	x			
	MB51	Open pit		Mrt ore	Rusty, massive	x	X	x				
	MB52	Open pit		Specularite ore	Brecciated, veins			X				
	MB99a	Open pit		Hm-Goe ore	Rusty, relict banding	x	x	X	x			Tal
	MB99b	Open pit		Mrt-pHm ore	Rusty, massive	x	x	X	x			
Iron Prince	MB45	Open pit		Mrt ore	Rusty, massive	x	X	x				
	MB54	Open pit		Mrt ore	Rusty, massive		X	x				
	MB57a	Open pit		Siliceous BIF	Banded, brown and yellow			X	x			
	MB57b	Open pit		Mrt-Goe Ore	Rusty, massive		X	x	x	Gn		
	MB59a	Open pit		Siliceous BIF	Banded, white and pink	x	X	x	x			
	MB59b	Open pit		Siliceous BIF	Banded, white and pink	x	x	X	x			
	MB60	Open pit		Specularite ore	Vuggy, friable			X				
Camel Hills	MB13	CA076DD	6.6	Limonite	BIF fragm. in calcrete	x	X		x			
	MB14	CA076DD	52	Limonite	earthy	x	X		x			
	MB15	CA076DD	97.6	Limonite	Earthy		X		x			
	MB16	CA076DD	111.8	Siliceous BIF	Earthy, banded		X		x			
	MB18	CA076DD	127.2	Qz-Tal facies Mt-BIF	Banded, white and black	X	x					Tal

Mineral abbreviations: Gn – galena; Goe – goethite; Hm – hematite (microplaty and/or microcrystalline); Lp – lepidocrocite; Mrt – martite; Mt – magnetite; pHm – microplaty hematite; Py – pyrite; Qz – quartz; Tal – talc.
X = main Fe-oxide phase; xx = major Fe-oxide component; x = relict or minor Fe-oxide component.

Table 1c
Index of samples studied from the northern segment of the Middleback Ranges.

Deposit	Sample	Location	Depth (m)	Rock Type	Texture	Iron Oxides			Fe-Hy	Sulfides and related	REE-min,	Index
						Mt	Mrt	Hm	(Goe, Lp)		Other minor	Minerals
Iron Monarch	MB66	Open pit		Mrt ore	Rusty, massive	x	X			Py		
	MB70	Open pit		Siliceous BIF	Brecciated		X	x				
	MB71a	Open pit		Siliceous BIF	Massive, banded	x	X	x	x			
	MB72a	Open pit		Siliceous BIF	Brecciated, relict banding	x	X	x	x			
	MB73	Open pit		Siliceous BIF	Massive, banded	x	X	xx				
	MB74	Open pit		Siliceous BIF	Brecciated, relict banding	x	X	x				
	MB75	Open pit		Leached BIF	Bleached, weathered			X				
	MB76	Open pit		Leached BIF	Bleached, weathered, veined			X			Ap	Cb
	MB77a	Open pit		Siliceous BIF	Brecciated, relict banding		X	xx				
	MB78	Open pit		Siliceous BIF	Brecciated	x	X	x	x			
Iron Princess	MB1	PS099RD	239.6	Mt-Hm-Goe ore	Massive	xx	X	x	x			
	MB2	NP001DD	889	Siliceous BIF	Fine banded	x	X	x	x	Py		Chl, Cb
	MB3	NP001DD	691.4	Siliceous BIF	Fine banded, veined	xx	xx			Py, Apy, Po, Sp		Chl, Cb
	MB65	Open pit		Mrt-Goe ore	Rusty, massive		X	x	x			
	MB66	Open pit		Mrt ore	Rusty, massive	x	X					
	MB67	Open pit		Siliceous BIF	Banded, black and white	x	X		x			
	MB68	Open pit		Mrt-Goe ore	Massive		X		x			

Mineral abbreviations: Ap – apatite; Apy – arsenopyrite; Cb – carbonate; Chl – chlorite; Goe – goethite; Hm – hematite (microplaty and/or microcrystalline); Lp – lepidocrocite; Mrt – martite; Mt – magnetite; Po – pyrrhotite; Py – pyrite; Sp – sphalerite.
X = main Fe-oxide phase; xx = major Fe-oxide component; x = relict or minor Fe-oxide component.

characterization, including assessment of grain-scale compositional homogeneity.

A Cameca SXFive Electron Microprobe (Adelaide Microscopy) running 'PeakSite' software and equipped with five wavelength-dispersive X-ray detectors was used for quantitative analysis of magnetite and hematite, as well as associated talc and pyrosmalite. Beam conditions were: accelerating voltage 20 kV; beam current 20 nA; and defocused 2 µm beam. Calibration and data reduction was carried out using 'Probe for EPMA' software. Elements analyzed, average mdl, peak/background positions, count times, and standards are listed in Table A.2.

Trace element concentrations of magnetite, hematite, Fe-hydroxides, carbonates and apatite, and element maps for hematite were obtained by laser-ablation inductively-coupled mass spectrometry (LA-ICP-MS) using a RESOlution excimer laser (Australian Scientific

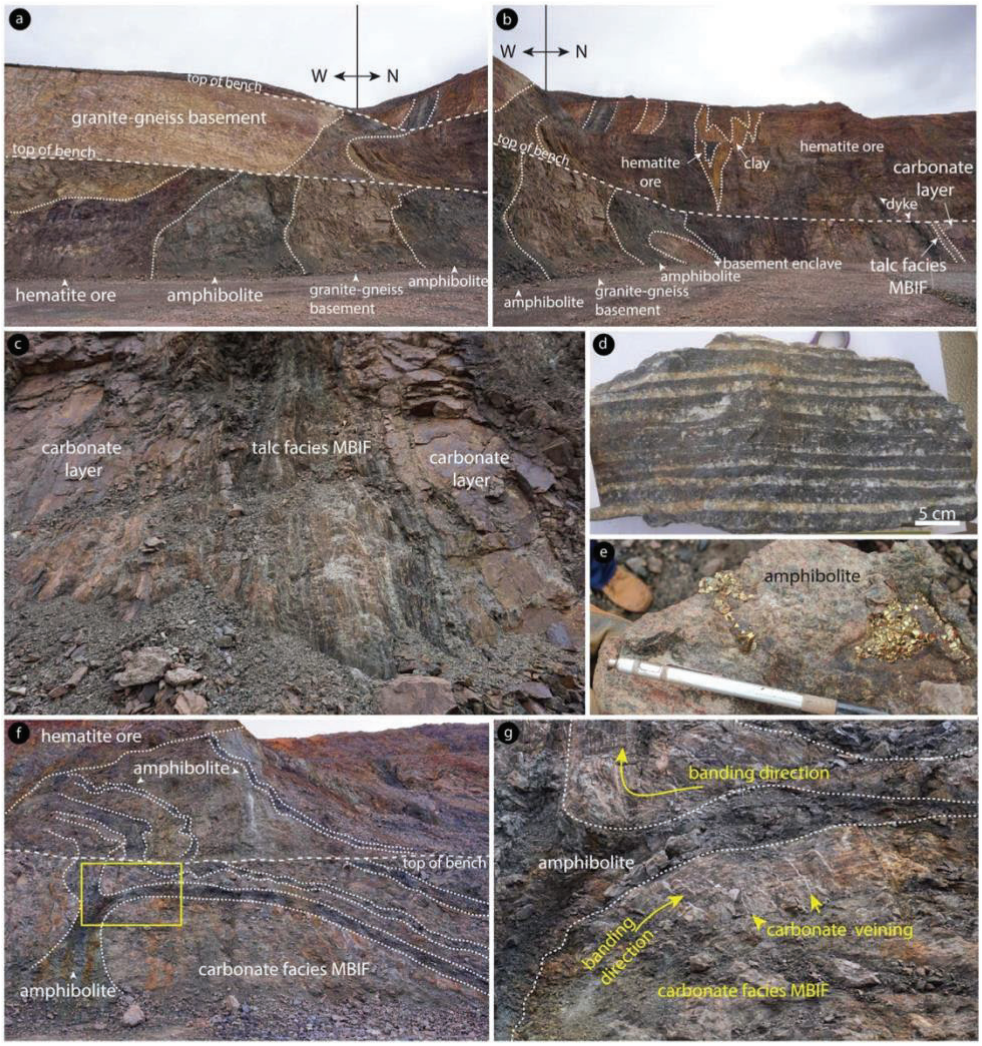

Fig. 2. Photographs showing lithologies on the northern wall at the junction with the western wall in the Iron Magnet open pit. (a) Western wall exposure showing granite-gneiss basement thrust above sub-vertical amphibolites. (b) Part of the northern wall showing occurrence of hematite facies at contact between basement rocks and the main MBIF ore. (c) Talc-facies MBIF between carbonate layers in a vertically-oriented sequence. (d) Typical carbonate-facies MBIF ore in Iron Magnet, featuring cm-scale rhythmic banding of magnetite and carbonate. (e) Altered amphibolite with coarse-grained pyrite. (f) Folded MBIF-amphibolite sequence with hematite ore above. Inset (g) shows detail of folding and carbonate veining perpendicular to MBIF banding.

Instruments) coupled to an Agilent 7900x Quadrupole ICP-MS (Adelaide Microscopy), following established laboratory practices (e.g., Ismail et al., 2014). ^{57}Fe was the internal standard for Fe-oxides and -hydroxides, whereas ^{24}Mg and ^{31}P were internal standards for Fe-Mg-carbonates and apatite, with EPMA data used for internal calibration in both cases. External reference materials were BHVO-2G and NIST-610. Data reduction was performed using 'GLITTER' (Van Achterbergh et al., 2001). Element maps were created using 'Iolite' software (Woodhead et al., 2007). Full details are provided in Appendix A.

In the following 'Results' section, normalization to chondrite is used for plotting REY fractionation patterns for ease of comparison with other important Fe-oxide bearing systems, including iron-oxide-copper-gold systems in South Australia and elsewhere. Comparison between chondrite- and PAAS-normalization follows in the 'Discussion' section.

4. Lithologies and whole-rock geochemistry data

Various mafic and granitic lithologies display close spatial associations with the orebodies (Figs. 2 and 3). Their characterization may be key to constraining those factors that have influenced or controlled ore-

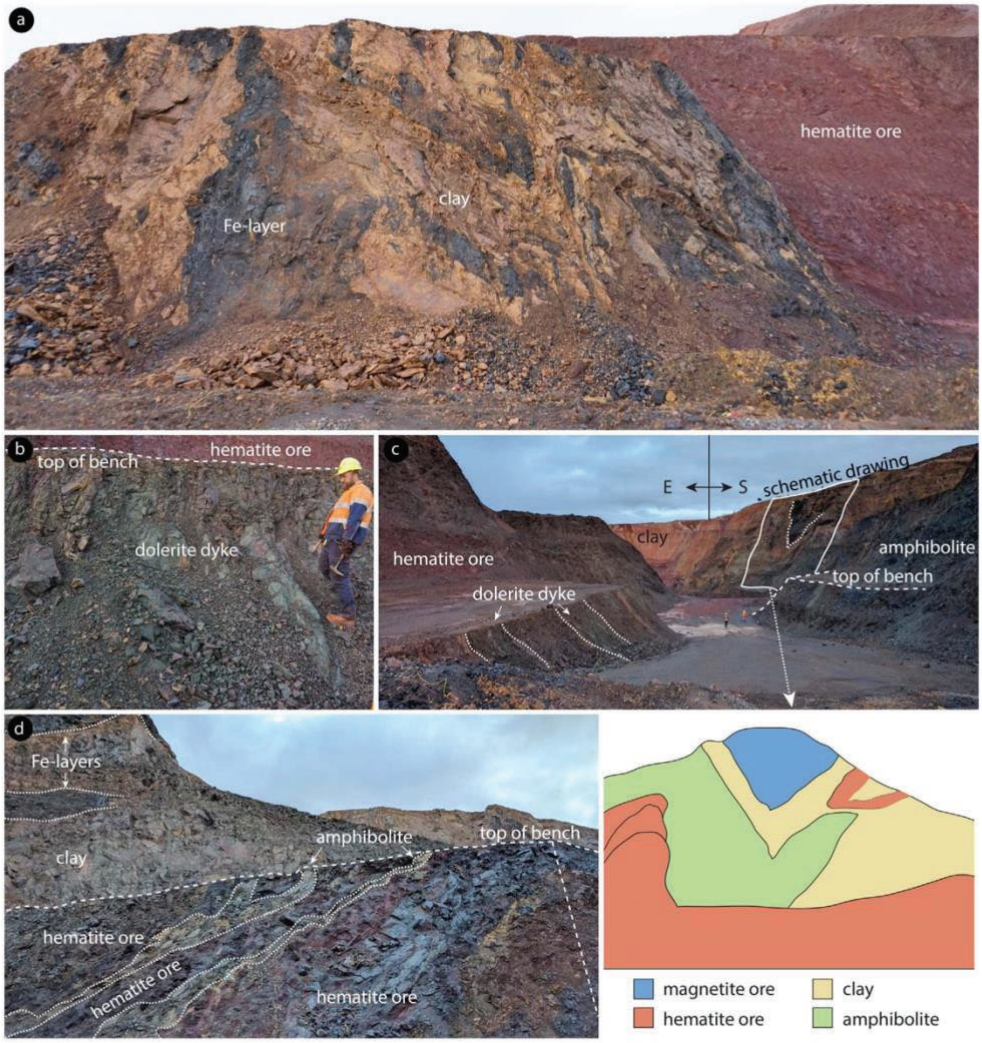

Fig. 3. Photographs showing lithologies from Iron Queen open pit. (a) Supergene-altered BIF showing alternating hematite- and clay-rich bands (interpreted as altered amphibolite) adjacent to hematite ore. (b) Crosscutting dolerite dike beneath the hematite ore. (c) View of Iron Queen deposit showing the crosscutting dolerite dikes in relation to iron ores and amphibolites. Schematic drawing shows magnetite-rich ores in the keel of a syncline with hematite-rich ore separated by clay and amphibolite. (d) Alternating layers of amphibolite and hematite ore.

forming processes, as well as possibly identifying BIF protoliths. The ores and BIFs are associated with one another within any given deposit, although their relative positions can vary, e.g., BIFs enclose the ores, or BIFs lie above the ores (Iron Monarch). Underlining the complexity of local settings is the presence of 'bleached BIF' packages comprising layered, vuggy, quartz-rich rocks enveloping the ores at Iron Chieftain. Although such aspects are not discussed here, the lithological context for iron ores exposed in open pits is briefly introduced below.

4.1. Associated lithologies

The exposed sequence outcrop across ~250 m on the north wall of the Iron Magnet open pit is illustrative of atypical magnetite-dominant ores within the MR belt (Fig. 2). The magnetite ores are always banded and occur within a sequence of other rhythmically banded, sub-vertical rocks. The mesobands within the rock sequence consist of variable mm- to cm-wide intervals of green and white rock, where the latter are either silica- or carbonate-rich. The green intervals consist of variably altered chlorite-, talc- and clay-bearing rocks with a marked schistosity, and close to faults, also graphite-bearing varieties. Intense pyrite alteration

occurs along faults (Fig. 2e). Larger, dm-sized pockets and lenses of pyrite are embedded within areas of intense argillic alteration nesting also coarse (up to cm-size), euhedral pyrite with cubic, or dodecahedral habit. The north wall outcrop also displays discrete strike-slip zones as sets of parallel fractures marked by pinch-and-swell gashes that are joined laterally by perpendicular fractures with quartz/carbonates. Thin, dm-sized, dark green mafic dikes with a dolerite-like appearance occur parallel to such zones. Along the margin of this rock sequence, granite-gneiss rocks are thrust onto the magnetite-rich amphibolites, which display sub-horizontal folding (Fig. 2a). The granites contain abundant feldspar porphyroblasts and are marked by lineation and schistosity, as well as by the presence of dm-scale intercalations of mica schist close to the contact with the magnetite-rich amphibolite sequences.

Amphibole-bearing rocks and analogous mafic dikes are observable in other open pits (Fig. 3) and in prospects sampled from drillcore, e.g., Prince South, Iron Monarch, Iron Warrior and Iron Princess, albeit at lesser abundance than in the Iron Magnet open pit. The freshest dolerite dikes occur at Iron Monarch. Strong pyrite alteration is also present in ores associated with amphibole-bearing rocks in some prospects, including Iron Warrior, or Camel Hills. Magnetite is also common in such ores (e.g., Iron Warrior). At the northern end of the belt (Iron Princess), magnetite ores hosted within chloritized amphibolites were intersected in drillholes at depths of ~ 240 m.

4.2. BIFs and iron ores

The Fe content in all analyzed BIF and ore samples, with few exceptions, ranges from ~20 to 99 wt% Fe_2O_{3total} (Appendix B). In the MR, there is a continuum of variation in the Fe content in magnetite-rich BIFs and magnetite ores (35–80 wt% Fe_2O_{3total}), however both are banded and are collectively referred to as magnetite BIF (MBIF). Siliceous rocks with rhythmic silica- and Fe-rich layers (mostly hematite and Fe-hydroxide-bearing), although relatively lower in Fe (20–40 wt% Fe_2O_{3total}), can also reach Fe_2O_{3total} values up to ~60 wt% (e.g., MB99a, Little Baron; Table B.2). Such rocks are hereafter defined as siliceous BIFs (SBIF); this name is, however, descriptive and carries no genetic implications.

The MBIFs display wide variation in the banding rhythms, coloring and textures over meter-intervals within a given location (Fig. 4a–d). Banding occurs on a mm- to cm-scale, with layers alternating between silica- and/or carbonate-rich layers and Fe-oxide layers (Fig. 4b, c), with less-common talc layers (Fig. 4d). The rhythm of the bands can fluctuate from regular to gradational. The color variations mostly relate to varying abundances of talc or carbonates. Crosscutting veinlets are also observed, locally leading to a 'stockwork'-like appearance. Carbonate-facies MBIFs are known only from Iron Magnet where they are often associated with intervals of talc-rich MBIFs. The SBIFs display a similar rhythmic banding between silica-/clay-rich layers and Fe-oxides and vary in color (Fig. 4e–h). Included with SBIFs are jaspilites and brecciated sub-types. Multiple brecciation stages leading to complex relationships between Fe-oxides and hydroxides were studied from outcrops in the eastern ridge from Iron Count (Fig. 4g, h).

High SiO_2, Fe_2O_{3total} and MgO characterize MBIFs (Fig. 5a; Table B.1), with all other elements generally < 1 wt%. Carbonate-rich MBIF has high CaO and CO_2 (6.09 and 19.71 wt%, respectively). Chondrite-normalized REE and Y (hereafter REY) trends of these rocks are light rare earth element- (La, Ce, Pr, Nd, Sm, Eu, Gd – LREE) enriched and heavy rare earth element- (Tb, Dy, Ho, Er, Tm, Yb, Lu – HREE) depleted, with pronounced positive Eu- and Y-anomalies (Fig. 5b). The ΣREY concentration in MBIFs averages < 20 ppm, with exception of one sample with stockwork veining (ΣREY = 103 ppm). Other trace elements generally measure < 5 ppm.

SBIFs consist predominantly of SiO_2 and Fe_2O_{3total} (Fig. 5a; Table B.2). All other elements are generally < 1 wt%, except for four samples for which loss-on-ignition (LOI) exceeds 2 wt%. The ΣREY concentration for SBIFs averages 22 ppm. Chondrite-normalized REY trends of the SBIFs are LREE-enriched and HREE-depleted, with no distinct anomalies (Fig. 5b). Other trace elements in SBIFs are generally higher than in MBIFs, with notable enrichment (> 10 ppm) of Ba, Ni, Cu, Zn, V, Zr, As, Sb and U in various samples throughout the belt.

The cut-off for what we here refer to as iron ores is samples with > 65 wt% Fe_2O_{3total}. The dominant ore type is massive, but with continuous variation towards vuggy, brecciated, rusty and limonitic varieties (Fig. 4i–k). Specular hematite is often present within vugs, particularly in the orebody from Iron Prince. Martite is the main component of the ores, although relict magnetite can also be present in abundance and rarely co-exists with hematite (e.g., sample MB1, Iron Princess). Fe-hydroxides make up a percentage of some ores, particularly in limonitic types, as seen from the LOI wt.% (Table B.3, B.4). The other ubiquitous component is SiO_2, (0.2–10 wt%) whereas other oxides with values > 1 wt%, noted in scarce abundance are Al_2O_3, MgO, MnO and CaO.

All ore types are generally characterized by chondrite-normalized REY trends featuring LREE-enrichment and HREE-depletion (Fig. 5b). Although a few exceptions occur, Eu- and Y-anomalies are typically slightly positive. The range of ΣREY concentrations is broad, but averages 34 ppm. Trace elements, including Ba, Cr, V, Ni, Co, Cu, Zn, As and Pb, are measurable at concentrations ranging from tens to hundred (s) of ppm. Uranium is measured at up to 77 ppm in ores from various deposits throughout the belt (e.g., Iron Prince). Limonite-dominant ore types have chondrite-normalized REY fractionation patterns characterized by LREE-enrichment and HREE-depletion, with pronounced negative Ce-, and weak positive Eu-anomalies (Fig. 5b).

5. BIF and iron ore petrography

Representative petrographic aspects of BIF types and ores are shown in Figs. 6–10, C.1 and C.2. Full compositional datasets for Fe-oxides and gangue minerals are given in Tables D.1–D.5.

5.1. Magnetite BIFs

Samples most representative of the MBIFs are from Iron Magnet. These generally display a marked banded texture seen in hand specimen and as fine-banding down to mm- and μm-scale (Fig. C.1) with alternating layers of magnetite and gangue minerals. The latter comprises carbonate, quartz and talc in variable proportions and associations. Modal abundances of these gangue minerals differentiate MBIF sub-types. Pyrosmalite $[Fe^{2+},Mn)_8Si_6O_{15}(OH,Cl)_{10}]$ has been identified as a locally abundant mineral in pyrite-altered, fault-associated MBIF from Iron Magnet (Fig. 6i and Fig. 7a, Table D.5).

Although MBIFs are the least altered at Iron Magnet, magnetite displays variation in grain size, changes in morphology, complex relationships with gangue minerals, and partial martitization. Millimeter-wide, massive bands of magnetite show fine-grained rims and are crosscut by fractures filled with gangue (Fig. 6a). Rounded clasts of carbonate are surrounded and crosscut by fine-grained magnetite (Fig. 6b). Scalloped boundaries between coarse and fine-grained magnetite, as well as the presence of interstitial quartz (or other gangue minerals) in the latter (Fig. 6c), are indicative of distinct magnetite generations. Coarser magnetite grains are tens to hundreds of μm in size and show changes in morphology from euhedral to sub-euhedral, often associated with pits and replacement by gangue minerals (Fig. 6d, e). Replacement of magnetite by gangue minerals can also lead to dense fields of inclusions and pores (Fig. 6f). Carbonates display grain-scale zoning with composition ranging between siderite and magnesite (Fig. 6 g). An overprint of Ca-Mn-richer carbonates is seen, often as late, crosscutting veinlets or interstitial to the Fe-Mg-dominant species. Pseudomorphic replacement of magnetite by hematite (martitization) is locally observed (Fig. 6h) particularly in samples with intense fracturing and where quartz veins are observed to crosscut BIF banding.

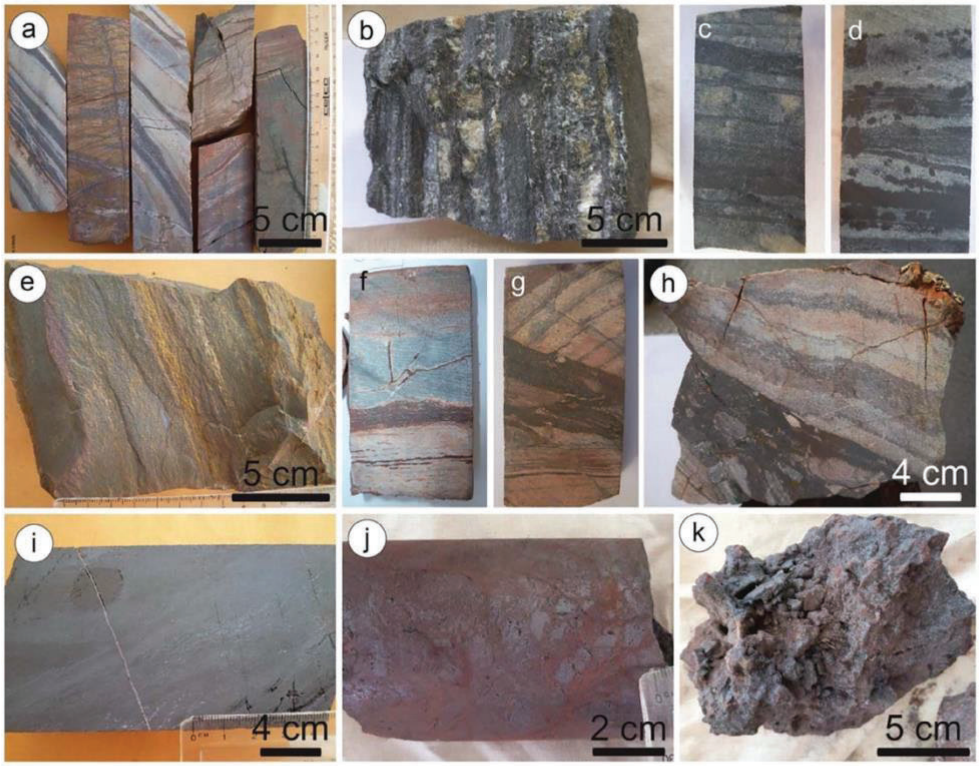

Fig. 4. Hand-specimen photographs of BIFs (a–h) and iron ores (i–k). (a) Variation in color and banding rhythms across few meters in MBIFs from drillhole in Iron Magnet. (b, c) Carbonate- and (d) talc-facies MBIFs showing comparable irregularities in band widths and rhythms in samples from the Iron Magnet pit. (e–h) Typical aspects of SBIFs. (e, f) Earthy-colored, limonite SBIFs showing rhythmic banding of clay-rich (orange), quartz-rich (grey) and hematite-/Fe-hydroxide-rich (red) bands (Iron Cavalier and Iron Prince). (g, h) SBIFs with banding rhythms of different orientations separated by a breccia-vein (containing quartz fragments) from Iron Count outcrop. Note micro-folding in layering on (h). (i) Massive iron ore comprising hematite, goethite and also subordinate magnetite (Iron Princess). (j) Rusty, brecciated martite ore with Fe-oxide clasts (bluish) in a quartz + fine-grained hematite cement (red; Iron Warrior). (k) Vuggy, friable specularite ore (Prince South). (For interpretation of the references to color in this figure legend, the reader is referred to the web version of this article.)

This is also associated with occurrence of fibrous hematite and Fe-hydroxides intergrown with talc. Pyrosmalite is present as short, stubby grains across bands of talc + carbonate in MBIFs (Fig. 6i) crosscut by cm-wide pyrite veins. Replacement of magnetite and pyrosmalite is indicated by scalloped boundaries (Fig. 7a).

Apatite is a ubiquitous mineral throughout the MBIFs, occurring either as aggregates along the banding or as single grains intergrown with magnetite (Fig. 7b). Apatite replacing magnetite, and occasionally magnetite replacing apatite, is often observed (Fig. 7c). Tiny inclusions of magnetite within apatite are present throughout most associations and are preserved, even in martite (Fig. 7d). Fields of μm- to sub-μm gangue inclusions in magnetite are relatively rare but include two-component quartz-apatite (Fig. 7e), or talc-zincite (Fig. 7f) inclusions. Zincite, rather than sphalerite is the most abundant base metal mineral found throughout the MBIFs, hosted in voids either within magnetite or gangue minerals (carbonates). Apart from pyrite, sulfides include rare chalcopyrite (Fig. 7g) and rounded, μm-size inclusions of pyrrhotite in pyrite (in the same sample with pyrosmalite). Native gold is observed as inclusions, up to 5 μm in size, within magnetite (Fig. 7h); this appears to be particularly associated with development of triangular pits in host magnetite (Fig. 6d). Small grains of monazite (Fig. 7i) are common either in magnetite or gangue minerals and are most abundant in overprinted assemblages.

5.2. Siliceous BIFs

There is a wide range of SBIFs with variable textures (Fig. C.2) that can be attributed to increasing Fe_2O_{3total}/SiO_2 and grain coarsening of Fe-oxides (Table B.2). Hematite is ubiquitous and Fe-hydroxides also occur in varying amounts. These include species recognizable in reflected light: goethite [FeO(OH)]; lepidocrocite [(γ-FeO(OH)]; and also Fe-oxide-hydroxides [(FeO(OH)·nH_2O)], with low optical reflectance which we refer to generically as 'limonite'. Relict magnetite is preserved throughout most SBIFs as inclusions in martite (Fig. 8a). Quartz is the dominant silicate in SBIFs, and in rare cases is present as recrystallized chert within jaspilite. Other phases that occur in SBIFs include kaolinite, which is prevalent where Fe-hydroxides are abundant, and to a lesser extent, siderite, calcite and chlorite.

Rhythmic banding between hematite (± Fe-hydroxides)- and quartz-rich layers is observed in most SBIF samples, although this may be weak in more silica-rich BIFs (Fig. C.2). In such cases, hematite within Fe-bands occurs as fine-grained disseminations (Fig. 8b). In SBIF samples that are richer in Fe (~40 wt% Fe_2O_3, e.g., Iron Monarch; Table B.2) banding is more massive. In most cases, the hematite consists

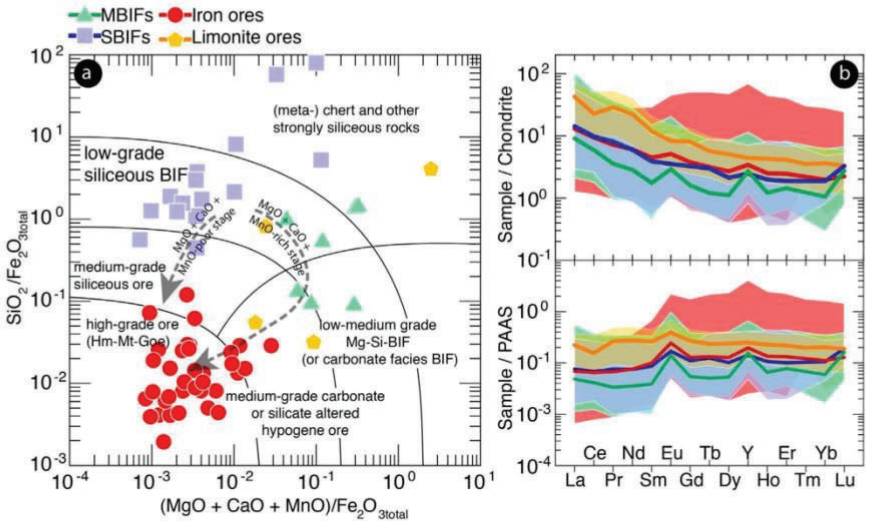

Fig. 5. (a) Whole-rock geochemistry discrimination diagram (after Angerer et al., 2012) depicting major element ratios (SiO_2/Fe_2O_{3total}) *vs.* $(MgO + CaO + MnO)/Fe_2O_{3total}$ and fields for various BIF and ore types. MBIFs, SBIFs and iron ores form three distinct groupings, with MBIFs from Iron Magnet following an MgO + CaO + MnO-rich trend. (b) Chondrite- and PAAS-normalized fractionation diagrams showing means (thick lines) and ranges (shaded areas) of REY abundances in MBIF, SBIF, iron ores and limonite ores.

of two varieties: martite and microcrystalline hematite (erratic anhedral hematite) (Fig. 8c). Martite is mostly associated with the Fe-bands or layers whereas microcrystalline hematite is present in Si-layers and shows various degrees of grain coarsening. Microplaty hematite is also present, but is mostly associated with fractures and veins (Fig. 8d). When present, goethite and other [$(FeO(OH)\cdot nH_2O$] species replace martite along the banding.

Brecciation is observed in more than half the SBIF samples, and is particularly strong at Iron Count (Fig. C.2). Breccias comprise fragments of BIF in a quartz-rich matrix, or vice versa, coarse-grained quartz supported by a groundmass of martite and microplaty hematite. At the grain-scale, such brecciation is accompanied by development of sub-μm-scale pores (Fig. 8e) and intra-grain microfracturing in martite (Fig. 8f), all of which likely serve as conduits facilitating alteration towards a more limonitic composition. The rare, relict clasts of jaspilite that are preserved display a reddish (Fig. 8g), amorphous texture and contain fine-grained inclusions of Fe-oxide phases, which display a layered appearance (Fig. 8g, inset). Towards the margins of such clasts, jaspilite is recrystallized into quartz grains containing abundant, fine-grained inclusions of hematite, as well as fibrous Fe-hydroxides (Fig. 8h).

5.3. Iron ores

The classification of iron ores is descriptive and based upon the main Fe-(hydr)oxide minerals present. The ores consist predominantly of hematite ± Fe-(hydr)oxides, although abundant magnetite is sometimes preserved in martite. In some cases, coarser magnetite coexists with hematite (Fig. 9a). Such ore types are typically massive and compact with less abundant gangue minerals (quartz and kaolinite). A layering may, however, still be preserved, in which case pre-existing Si-layers within BIF are replaced by Fe-(hydr)oxides.

Ores containing > 80% martite are referred to as martite ores and display varying degrees of porosity. In many cases, martite becomes more porous and filled with inclusions of quartz, kaolinite or secondary Fe-hydroxides (Fig. 9b). Relict magnetite is often preserved in the cores of such porous grains but can be so fine that it appears dust-like. The formation of pores can be accompanied by the adjacent growth of interlocking granoblastic hematite (Fig. 9b), which lacks inclusions and can contain up to 0.15 wt% TiO_2 (Table D.3).

Increase in goethite (± lepidocrocite) component leads to martite-goethite ores consisting of a martite framework with interstitial Fe-hydroxides (Fig. 9c), where martite typically has a skeletal appearance due to replacement by Fe-hydroxides (Fig. 9d). Microplaty hematite can also form within Fe-hydroxides (e.g., Iron Count, Fig. 9e). Fe-hydroxides in these ores have variable textures, including rhythmic, concentric textures consisting of sub-μm size mixtures of various species growing around cores of gangue minerals (Fig. 9f). Concentric, colloform textures between various Fe-hydroxides species are also present (Fig. 9g). At Iron Knight, where microplaty hematite postdates Fe-hydroxides, such fine-grained, concentric aggregates are replaced by zoned hematite (Fig. 9h).

As in the MBIFs, sulfides also occur throughout the SBIFs and iron ores and include pyrite, arsenopyrite, chalcopyrite, galena, sphalerite and rare cobaltite. Zincite is however more common than sphalerite. Barite is also present in a few samples. Apatite and monazite are relatively common whereas xenotime is far rarer.

5.4. Grain-scale hematite and Fe-hydroxide zoning

Grain-scale compositional zonation is one of the peculiar aspects of hematite found in SBIFs and ores where the relationships between microplaty hematite and Fe-hydroxides are more complex, including evidence for microplaty hematite postdating Fe-hydroxides. In such cases, the core-to rim zonation patterns visible in BSE images, are expressed as variable SiO_2 in both Fe-hydroxides and platy hematite (Fig. 10a–d). While patchy zonation, expressed by heterogeneous SiO_2 content, is more common in hematite developing pores and transforming to goethite, microplaty hematite crystallizing from a Si-rich, Fe-hydroxide precursor (Fig. 10a) can develop zonation expressed as acicular aggregates of Si-rich/Si-poor laths (Fig. 10b), or sectorial zonation (Fig. 10c). An exceptional example of core-to-rim oscillatory zonation is observed in Iron Knight (up to 1.8 wt% SiO_2; Fig. 10d, e; Table D.4).

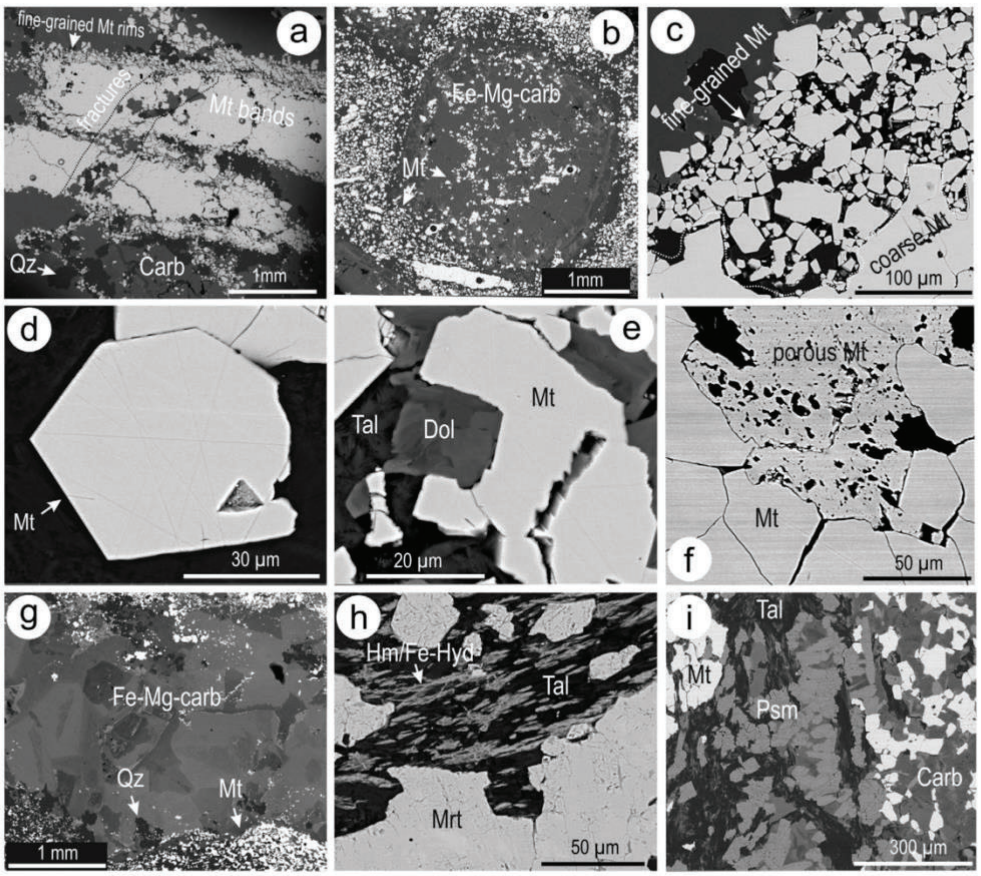

Fig. 6. Back-scatter electron (BSE) images showing magnetite (Mt) and gangue minerals in MBIFs. (a) Massive bands of Mt showing overprinting features. (b) Fine-grained Mt surrounding and crosscutting a rounded carbonate (Carb) clast. (c) Fine-grained Mt within scalloped embayment along coarser Mt band. (d) Euhedral Mt with typical triangular pit. (e) Dolomite (Dol) replacing Mt. (f) Porous/inclusion-rich Mt interstitial to coarse Mt aggregates. (g) Typical compositional zoning in terms of Fe-, Mg-, (major) and Ca-, Mn-minor elements in siderite-magnesite Carb. (h) Martite (Mrt) and intergrowths of fibrous hematite (Hm) + Fe-hydroxides (Fe-Hyd) and talc (Tal). (i) Pyrosmalite (Psm) crosscutting Tal + Carb bands.

5.5. Compositional data for Fe-oxides and associated minerals

Magnetite from different samples shows very close to ideal stoichiometry with only few minor elements detectable by EPMA. Exceptions are Si and Mg and in some samples, also Al and Mn (Tables D.1 and D.2). There is no statistical difference in minor element concentrations between magnetite from different lithologies. *Martite* is similarly close to stoichiometric and contains measurable Si, Ti, Al, Mg, and V, although not in all samples (Tables D.3 and D.4). Concentrations of these elements vary within textural categories and between samples. Porous martite generally has higher minor element concentrations. Cores of zoned microplaty hematite from Iron Knight have the highest SiO_2 content (mean 1.51 wt%). One sample of porous martite from Iron Princess stands out by higher Al_2O_3 (0.52 wt%). The highest measured TiO_2 content in hematite is 0.15 wt% (granoblastic hematite in SBIF from Iron Count). Concentrations of CaO and Cr_2O_3 are at or below minimum detection limits in all analyzed samples. Plots of Si, Al and Mg *vs.* Fe^{3+} (apfu) (Fig. 11) demonstrate the extent of this variation but also the tendency of data from any given sample to cluster on the plots.

Talc in a sample from Iron Magnet (Table D.5) is found to be an intermediate member of the talc-minnesotaite series with Fe/(Fe + Mg) ratio of ~0.25. *Pyrosmalite-(Fe)* in a different sample from Iron Magnet (Table D.5) is compositionally zoned. Brighter domains on BSE images have Fe/(Fe + Mg + Mn) = 0.95 with Mn > Mg, whereas darker domains are richer in Mg with Fe/(Fe + Mg + Mn) = 0.92.

6. Trace element geochemistry

Trace element concentrations were measured in Fe-oxides and -hydroxides from BIFs and iron ores. Within MBIFs, carbonates were also analyzed with the purpose of comparing their trace element signatures with magnetite in the alternating layers. Trace element data are listed in Tables E.1–E.6 and shown as plots and element maps (Figs. 12–16). Rare earth elements are normalized to chondrite (CN) following McDonough and Sun (1995). The LREE/HREE ratio is defined as $Ce_{(CN)}/Lu_{(CN)}$, where (CN) = chondrite normalized. Anomalies are defined here as:

$$Ce/Ce* = (Ce_{(CN)}/(La_{(CN)} + Pr_{(CN)})/2); \quad (1)$$

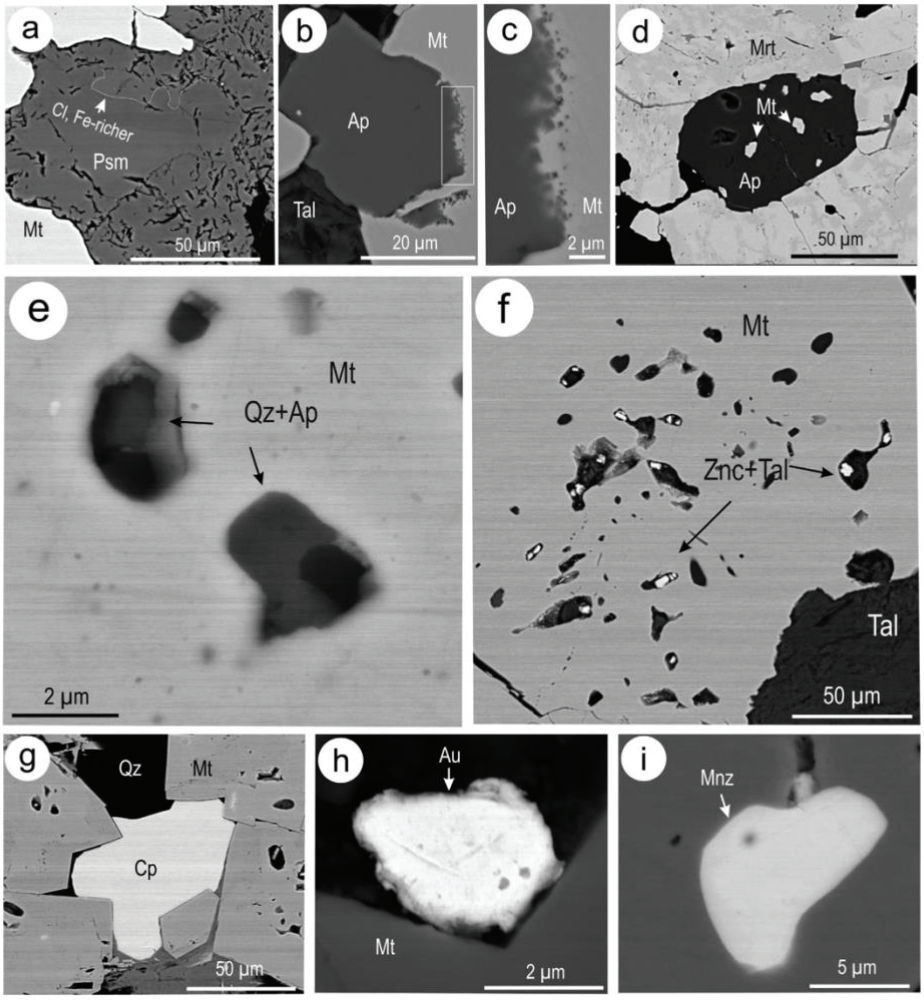

Fig. 7. BSE images showing details of magnetite (Mt) and associated minerals in MBIFs. (a) Pyrosmalite (Psm) with Cl- and Fe-zonation replacing Mt. (b, c) Fine-scale boundary replacement of apatite (Ap) by Mt. (d) Mt inclusions in Ap enclosed within martite (Mrt). (e) Two-component, µm-scale inclusions of Ap and quartz (Qz) in Mt. (f) Pore-attached zincite (Znc) and talc (Tal) inclusions in Mt. (g) Chalcopyrite (Cp) interstitial to coarse Mt. (h) Native gold (Au) hosted in Mt pit. (i) Monazite (Mnz) inclusion in Mrt.

$$Eu/Eu* = (Eu_{(CN)}/(Sm_{(CN)} + Gd_{(CN)})/2); \text{and} \quad (2)$$

$$Y/Y* = (Y_{(CN)}/(Dy_{(CN)} + Ho_{(CN)})/2. \quad (3)$$

6.1. Magnetite

With exception of Si, Mg, Ca, Al and P, magnetite has the lowest trace element concentrations within the dataset. Magnetite from all lithologies (MBIF, SBIF, hematite-rich ores) consistently contains high concentrations of Si (mean 800 ppm), Mg (100 ppm), Ca (110 ppm), Al (90 ppm) and P (20 ppm). Magnetite is similarly rich in Mn (mean 348 ppm), more so in MBIF from Iron Magnet than in other lithologies. Zinc concentrations exceed 10 ppm in more than half the sample suite. Higher concentrations of Al, V, Ni, Co and Cr (means 226, 30, 10, 3, and 2 ppm, respectively) occur in magnetite from hematite-rich iron ores than in MBIFs and SBIFs. Titanium is highest in magnetite from MBIFs (mean 14 ppm). A broad range of other trace elements are present, including As, Sb, Ga, W and U, although generally not exceeding 10 ppm.

Absolute concentrations of REY vary little amongst magnetite from the different lithologies and are generally either < mdl, or low concentrations (< 2 ppm). ΣREY ranges from 0.001 to 10 ppm (mean < 3 ppm). No discrimination between lithologies can be made on the basis of ΣREY concentrations alone. Such low concentrations result in poorly constrained chondrite-normalized REY fractionation trends due to the greater scatter at concentrations close to the minimum limits of detection. However, the average magnetite from individual MBIF and SBIF samples display similar trends that are slightly LREE-enriched and

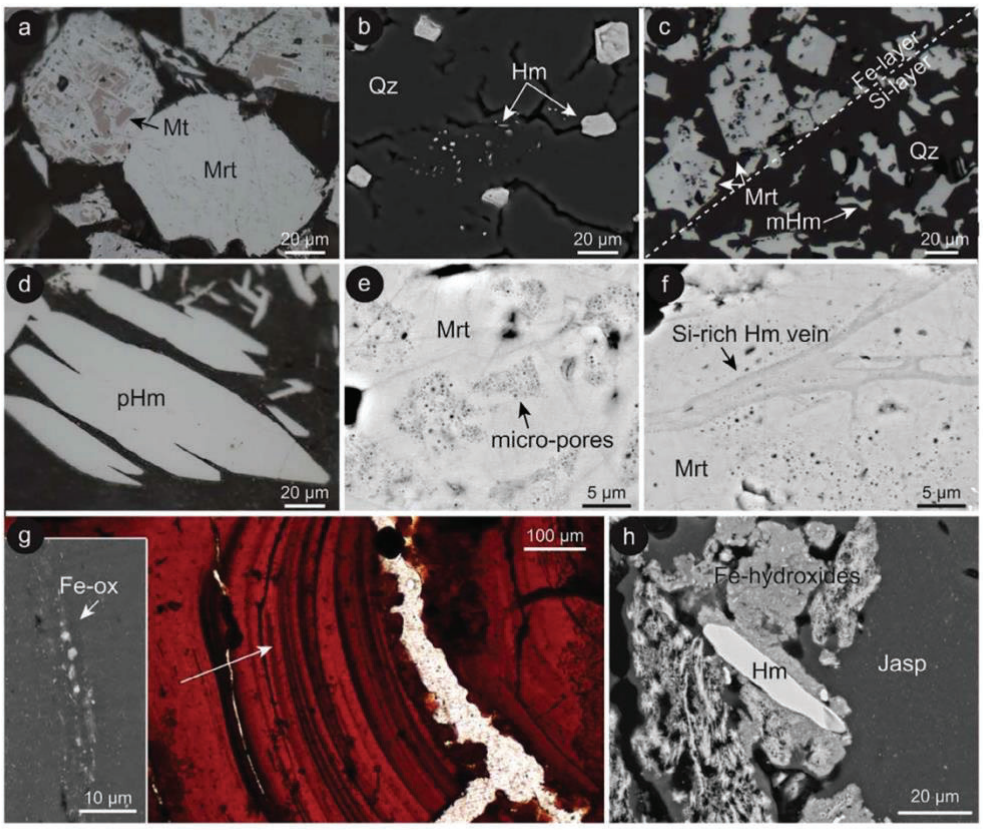

Fig. 8. Reflected light photomicrographs (a, c and d) and BSE images (b, e, f and g inset) showing petrologic aspects of SBIFs. (a) Martitization showing complete (Mrt) and partial replacement of magnetite (Mt) by hematite (Hm). (b) Hematite within recrystallized quartz (Qz) showing coarsening from dusty to µm-scale grains. (c) Martite and microcrystalline hematite (mHm) in Fe-rich and Si-rich layers, respectively. (d) Typical morphology of microplaty hematite (pHm) growth on various scales in quartz. (e, f) Incipient transformation between Mrt types (clean to porous) shown as development of micro-pores and Si-rich veinlets (g) Red, layered jaspilite (Jasp) with fine-grained Fe-oxides (Fe-ox) along the layers (inset) (h) Hematite forming from Fe-hydroxides along margins of Jasp layers. (For interpretation of the references to color in this figure legend, the reader is referred to the web version of this article.)

display Eu- and Y-anomalies (Fig. 12a). Cerium-anomalies vary in sign. In hematite-rich ores, these trends have a wider variation and lack consistent patterns.

6.2. Hematite

Trace element concentrations in each of the three hematite textures illustrated and defined above as (i) martite, (ii) porous martite, and (iii) microplaty hematite, are analyzed throughout the sample suite. Although rarely exceeding concentrations of hundreds of ppm (with the exception of Si and Al), trace element concentrations in these hematite categories are generally higher than in precursor magnetite.

6.2.1. Rare earth elements and yttrium

The average ΣREY throughout these hematite textures ranges from < 1 to 25 ppm. The transformation from magnetite → martite → porous martite within individual samples is generally accompanied by an increase in ΣREY, typically over one to two orders of magnitude. Chondrite-normalized REY fractionation trends become more consistent throughout such textural transformations (Fig. 12b). This is not always the case when microplaty hematite is observed to co-exist with another hematite texture (e.g., porous martite), in which cases the ΣREY in microplaty hematite can be lower (Fig. 12c). However, REY fractionation patterns vary within each textural type and among different lithologies. Based on such variation, three categories of REY fractionation trend can be defined throughout all textural types of hematite (Fig. 12d): (i) trends displaying pronounced positive Eu- and Y-anomalies and enrichment in LREE relative to HREE; (ii) trends with a flat overall pattern, lacking Ce- and Y-anomalies; and (iii) flatter trends with a pronounced negative Ce-anomaly.

6.2.2. Other trace elements

Hematite from across the dataset can be enriched in a variety of elements, notably Ti (mean 146 ppm), V (53 ppm), Cr (10 ppm), Zn (26 ppm), As (18 ppm) and Pb (15 ppm). Magnesium (mean 280 ppm), Al (615 ppm), Si (2,800 ppm), P (120 ppm), Ca (210 ppm) and Mn (400 ppm) are also measured but may be influenced by fine-grained inclusions of Fe-hydroxides, carbonates, quartz, or clays. However, in some cases, hematite shows grain-scale compositional zonation (particularly microplaty hematite; see above), and is indeed enriched in such

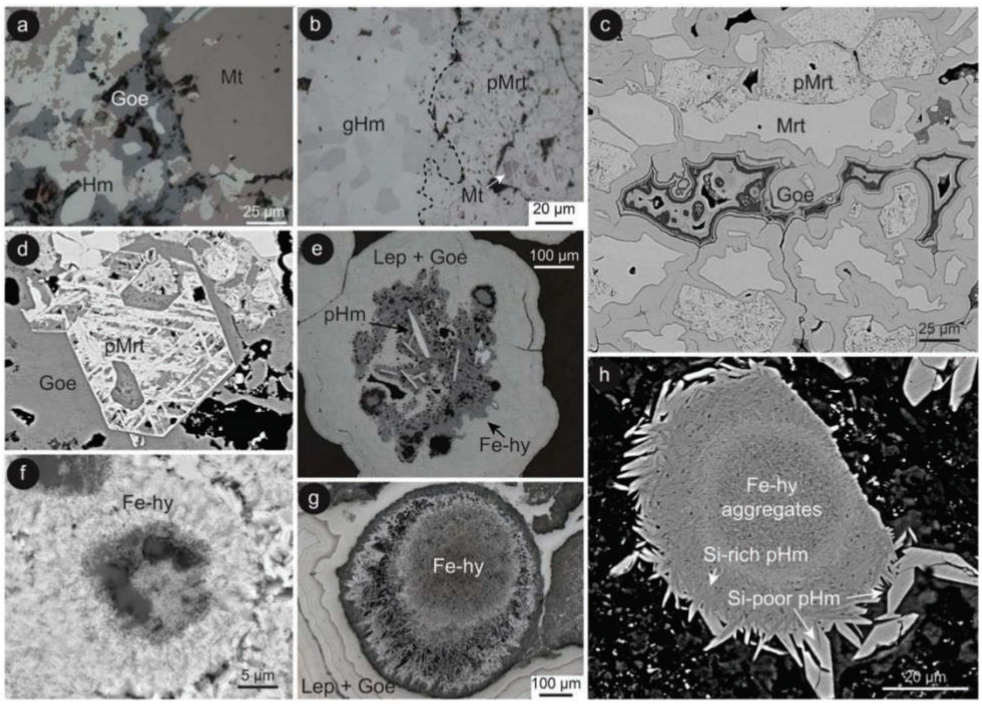

Fig. 9. Reflected light photomicrographs (a, b, e and g) and BSE images (c, d, f and h) showing petrologic aspects of iron ores. (a) Co-existing magnetite (Mt), hematite (Hm) and goethite (Goe). (b) Boundary between porous martite (pMrt) with relict Mt and granoblastic hematite (gHm). (c) Aggregates of Mrt-pMrt with interstitial Fe-hydroxides (Goe-rich) displaying colloform textures. (d) Skeletal pMrt preserving euhedral habit of Mt replaced by Fe-hydroxides (Goe). (e) Microplaty hematite (pHm) growing within aggregates of fine-grained Fe-hydroxides in the center of botryoidal lepidocrocite (Lep) + Goe. (f) Fine-grained aggregates of Fe-hydroxides growing around the core of a gangue mineral. (g) Concentric aggregates of Fe-hydroxides (Fe-hy) (core) and Lep + Goe (margin). (h) Concentric aggregates of Fe-hydroxides (Fe-hy) replaced by Si-rich microplaty hematite (pHm) with Si-poor microplaty rims. See more detail in Fig. 10e.

elements (e.g., Si; Iron Knight). In general, time-resolved LA-ICP-MS depth-profiles suggest the aforementioned elements are not associated with mineral inclusions (Fig. C.3a).

Unlike martite, porous hematite is more likely to contain discrete mineral inclusions, due to the presence of vugs and secondary Fe-hydroxides present within such vugs. Nonetheless, there are exceptions where trace elements (e.g., V, Pb, U) can be considered as incorporated within porous martite (Fig. C.3b).

Other elements present at measurable concentrations include U, W, Sb, Zr, Ni, and Co, and although their average values are < 10 ppm, they may reach concentrations ranging from tens to hundred(s) of ppm within individual samples.

6.2.3. Trace element distributions and patterns among hematite categories

Trace element trends for hematite show subtle or marked differences in the distribution of elements and strengths of correlation between elements when considering the three main categories (Figs. 14 and 15). Such differences are highlighted on trace element maps for porous martite and granoblastic hematite showing preferential concentration of Co and Ni into the porous type whereas granoblastic hematite is richer in other transition metals and HFSE (Ti, V and Nb), as well as in granitophile elements (maps for U, Pb and W are shown on Fig. 13, but this is also valid for Sn and Th).

In general, however, porous martite displays the greatest compositional variation (Fig. 14). Positive correlations are noted between several element pairs in hematite of all categories, including Sb *vs.* As, Zn *vs.* Mn, Ta *vs.* Nb, and Ga *vs.* Al (Fig. 14a–d). Martite shows the strongest correlation on the Sb *vs.* As plot (r' = 0.77), whereas both porous and microplaty hematite have weaker correlations (r' = 0.65). Data from Iron Princess and Iron Chieftain form small clusters on the Sb *vs.* As plot (Fig. 14a). On the Zn *vs.* Mn plot, all categories display a positive correlation (r' = 0.61; Fig. 14b). Trends of variable strengths are also observed for Ta *vs.* Nb: microplaty hematite shows a very weak positive correlation (r' = 0.38) whereas the martite categories show stronger positive correlations (r' = 0.73 and 0.70; Fig. 14c). Porous martite occurring as fragments within near-surface pedogenic calcrete form separate clusters on both the Zn *vs.* Mn and Ta *vs.* Nb plots (Fig. 14b, c). The Ga *vs.* Al trends show strongest correlation for microplaty hematite (r' = 0.74), and weakest for porous martite (r' = 0.65). Nickel *vs.* Co also displays a positive correlation amongst all three textures (r' = 0.68), with the exception of Si-zoned microplaty hematite from Iron Knight (negative correlation r' = −0.59; Fig. 14e).

Combining trace elements into groups that have significance for the presence of granitoids (granitophile elements, U + W + Sn + Mo), mafic rocks (transitional elements, V + Cr + Co + Ni), and mineralization (chalcophile elements, Cu + Zn + Ga + As + Sb + Pb), displays some positive correlations. These include ΣREY *vs.* granitophile elements, ΣREY *vs.* chalcophile elements, and ΣREY *vs.* transitional elements (Fig. 14f–h). On such plots, microplaty hematite consistently gives the strongest correlations on plots of ΣREY *vs.* granitophile or chalcophile elements (r' = 0.74 and 0.65, respectively), whereas the other hematite types show markedly weaker correlations (e.g., 0.55 for

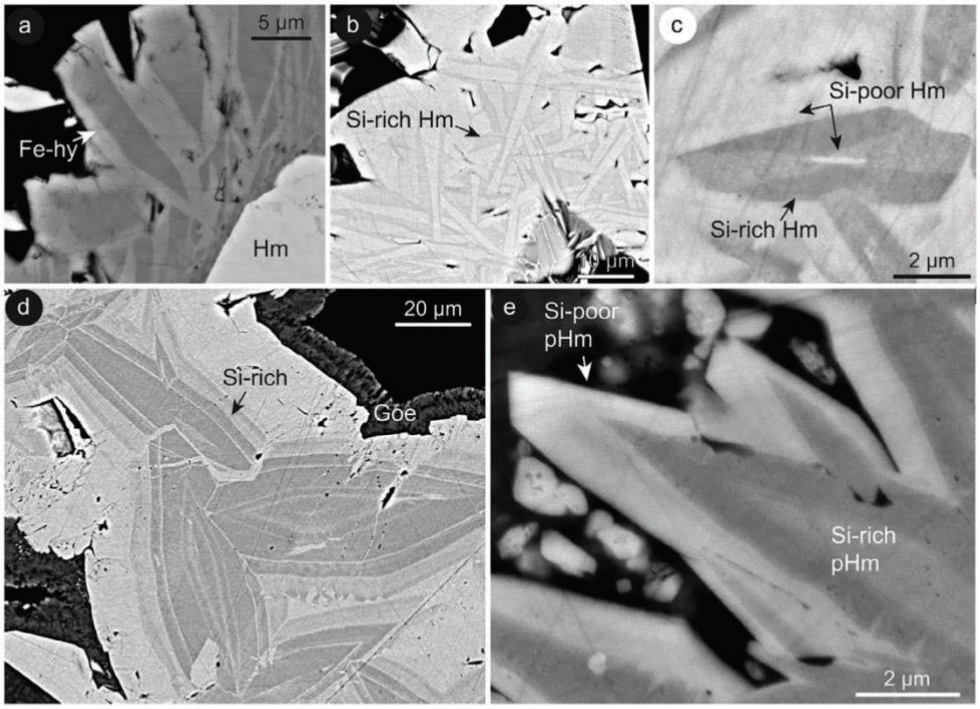

Fig. 10. (a–d) BSE images showing aspects of silica-rich hematite (Hm) and Fe-hydroxides (Fe-hy). (a) Fe-hy with 'tooth-texture' growing radially on a grain of microplaty Hm. Darker domains are Si-rich. (b) Acicular aggregates of Si-poor Hm in a Si-rich (darker) matrix. (c) Sectorial zoning (Si-rich as darker domains) in Hm. (d) Oscillatory zonation in microplaty Hm from Iron Knight. (e) Detail of the Si-rich/poor core to rim zoning in microplaty hematite (pHm) from Fig. 9h.

martite in Fig. 14f; and 0.63 and 0.4 for martite and porous martite, respectively, in Fig. 14g). Positive correlations for martite and microplaty hematite are shown on the ΣREY *vs.* transitional elements plot (Fig. 14h). Porous martite in general shows weak positive correlation.

6.2.4. Trace element trends of hematite types across the strike of the Middleback Ranges

Hematite from deposits in the northern, central and southern segments of the MR (see Table 1 for segment divisions) displays trace element trends with distinct strengths of correlation (Fig. 15).

Hematite compositions from all three segments of the MR show positive correlations between Sb and As, Zn and Mn, and ΣREY and granitophile elements (Fig. 15a–d). The Sb *vs.* As plot shows the strongest correlation for the northern segment of the MR (r' = 0.81), with slightly weaker correlations for the central and southern segments (r' = 0.71 and 0.74, respectively; Fig. 15a). Similarly, the northern segment shows a strong Zn *vs.* Mn correlation (r' = 0.76) relative to the central segment (r' = 0.49) (Fig. 15b). Two distinct trends are observed on the Zn *vs.* Mn plot for the southern segment of the ranges (Fig. 15c): (i) martite from the Iron Magnet deposit; and (ii) hematite from all other deposits from the southern segment of the ranges. Hematite from Iron Magnet shows a strong correlation between Zn and Mn (r' = 0.84) while all other hematite from this domain displays a weak correlation (r' = 0.49). The plot of ΣREY *vs.* granitophile elements shows strong correlations for the northern (r' = 0.70) and southern (r' = 0.78) segments of the ranges whereas the central segment has only a very weak correlation (r' = 0.26) (Fig. 15d).

Often, no recognizable trends are present among different textures from the same segment of the MR. However, particularly in the south, distinct trace element trends can be observed relative to textures, as shown in the Zn *vs.* Mn, Ni *vs.* Cr, Th *vs.* U, and ΣREY *vs.* granitophile element plots (Fig. 15e, f). The Zn *vs.* Mn plot shows increasing correlation strength from martite to porous martite before decreasing in microplaty hematite (Fig. 15e). The Ni *vs.* Cr shows varying correlation strengths between the different hematite textures, albeit generally weak (Fig. 15f). However, martite from Iron Magnet displays a significantly weaker correlation (r' = 0.12) than martite from other deposits from the southern segment (r' = 0.71). All hematite types from the southern segment display a positive Th-U correlation; however, martite from Iron Chieftain forms a tight cluster, with the highest Th values, which is distinct from the general trend (Fig. 15g). The plot of ΣREY *vs.* granitophile elements shows a strong (r' = 0.78) correlation in the progression of abundances from martite → porous martite → microplaty hematite (Fig. 15h).

6.3. Fe-hydroxides

In all cases where Fe-hydroxides are observed to postdate Fe-oxides, their ΣREY (mean 27 ppm) exceeds that of the precursor Fe-oxide, often by as much as one to two orders of magnitude (Fig. 16a). Concentrations of Si, Al and P are high in all analyzed samples, with average concentrations of each element in the range of thousands of ppm, as well as hundreds of ppm Mg and Ca. Other elements, such as Mn, Cu, Zn, or As, can also be present at concentrations ranging up to thousands of ppm, especially in samples from Iron Prince (e.g., sample MB57b). In various samples throughout the belt, Ti, V, Mn, Cr, Cu, Zn, As, Pb, Zr

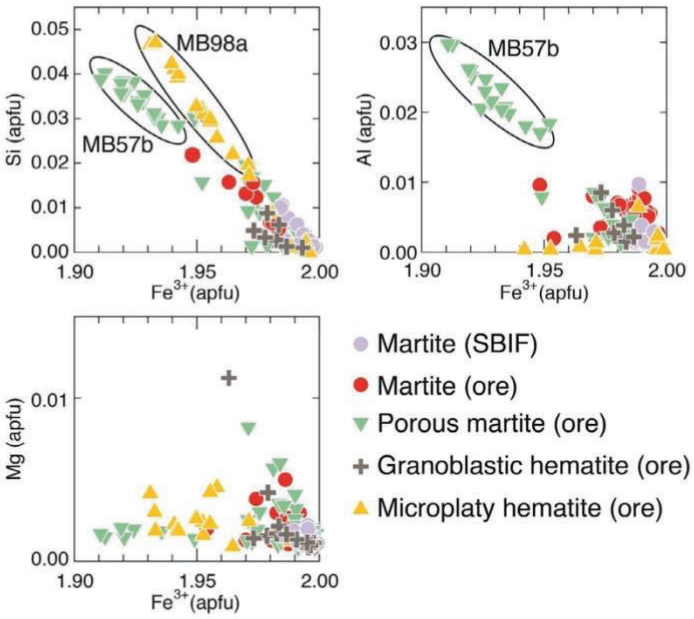

Fig. 11. Hematite compositions plotted on Si, Al and Mg *vs.* Fe^{3+} (apfu) binary diagrams.

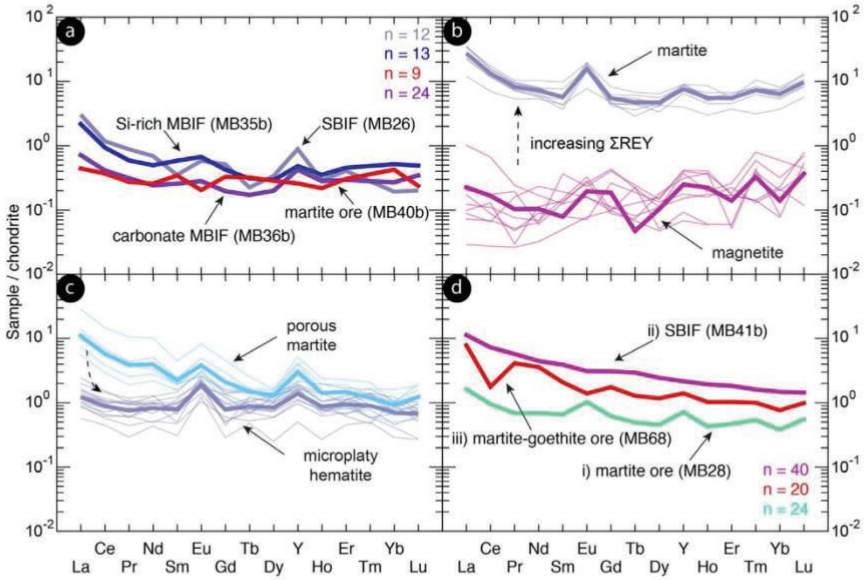

Fig. 12. Chondrite-normalized REY fractionation diagrams for Fe-oxides. (a) Trends for magnetite from carbonate-facies MBIF, Si-rich MBIF, SBIF and iron ore. (b) Increasing ΣREY and more consistent trends in transformation from magnetite to martite. (c) Trends showing decreasing LREE and ΣREY in transformation from porous martite to microplaty hematite. (d) The three trend categories observed in hematite throughout the MR belt.

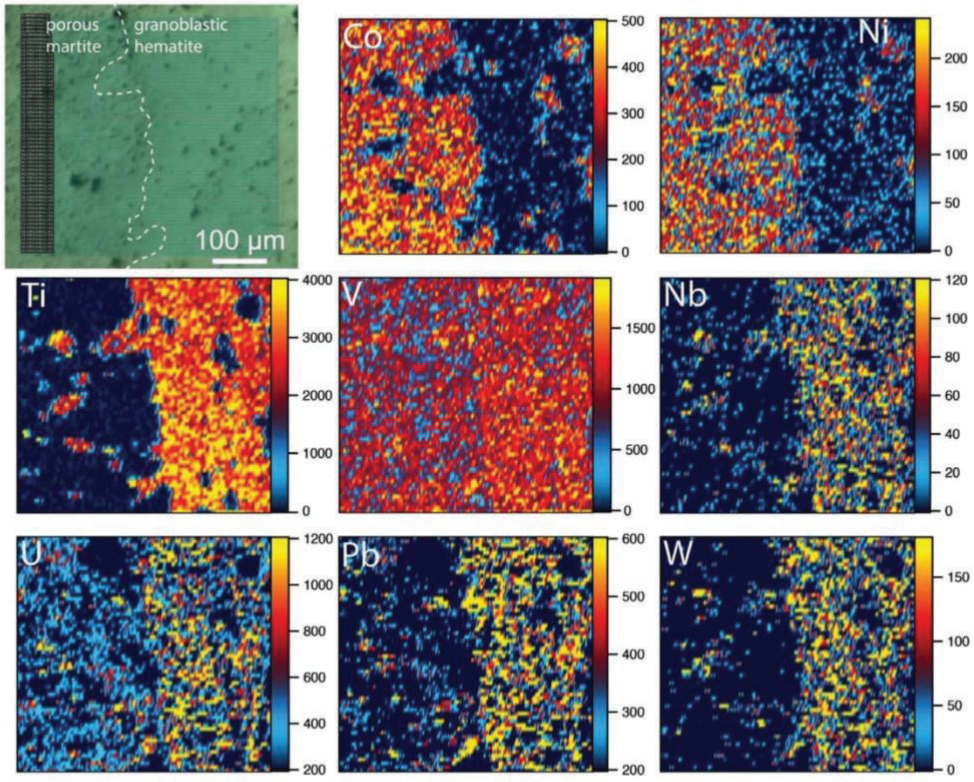

Fig. 13. LA-ICP-MS element maps of porous martite and granoblastic hematite in SBIF (MB40b) showing Co and Ni enrichment in porous martite and Ti-, V-, Nb-, U-, Pb- and W-enrichment in granoblastic hematite. Mapped area shown on the reflected light microphotograph at the top left. Scales in counts-per second.

and Ba are measured in Fe-hydroxides at concentrations in the hundreds of ppm range; whereas Sc, Co, Ni, Ga and Sr are typically each a few tens of ppm. In general, Mo, Sn, W and U concentrations in Fe-hydroxides are low. However, in samples containing U-rich hematite (mean 14 ppm), Fe-hydroxides are found to have even higher U concentration (e.g., Iron Knight; mean 32 ppm). This is one case in which, based on textures, a second generation of Si-zoned microplaty hematite replaces Fe-hydroxides (see above).

Unlike the chondrite-normalized REY fractionation trends for Fe-oxides, those for Fe-hydroxides vary greatly (Fig. 16b). To some extent, some of the trends resemble those found in magnetite and hematite (e.g., positive Eu- and Y-anomalies). Other characteristics include large variations in slope (LREE/HREE = 0.03 to 1.65), where LREE can be significantly depleted relative to HREE. Cerium- and Y-anomalies can have either positive or negative sign (Fig. 16b), and can be extremely pronounced in either case ($Ce/Ce* = 0.01$ to 3.7; $Y/Y* = 0.15$ to 1.6). The Eu-anomaly can similarly be prominent ($Eu/Eu*$ up to 0.6).

6.4. Carbonates

Carbonates alternating with magnetite layers in MBIFs have low concentrations of most trace elements (< 2 ppm), except for P. In a sample where carbonate displays strong overprinting features (e.g., patchy compositional zonation and cross-cutting magnetite veins), P is lower than samples lacking such features (mean 13 ppm and 55 ppm, respectively), but contains ~7 ppm Ni and ~2 ppm Co. Strontium in all carbonates is markedly low (mean < 1 ppm). Although carbonates are Fe- and Mg-rich, they contain Mn (mean 28,471 ppm), Ca (1,551 ppm) and Si (58 ppm).

Carbonates are relatively enriched in ΣREY (mean 5 ppm) compared to Fe-oxides in the same sample. Chondrite-normalized REY fractionation trends for carbonates show LREE enrichment ($Ce/Lu_{(CN)} = 2.1$) and strong positive Eu- and Y-anomalies ($Eu/Eu* = 0.5$; $Y/Y* = 1.32$, respectively; Fig. 16c). However, in carbonate that features alteration textures, LREE enrichment is less pronounced ($Ce/Lu_{(CN)} = 0.9$) and Eu- and Y-anomalies are absent (Fig. 16c).

6.5. Apatite

In general, the small grain-size of apatite in MBIF made it unsuitable for trace element analysis by LA-ICP-MS across the dataset. However, several grains of apatite from a MBIF and apatite stringers associated with stockwork veining in a MBIF were of adequate size for analysis and are included in the dataset. Although some analyses of apatite show the presence of inclusions (e.g., high Si), REY concentrations and chondrite-normalized fractionation trends are not significantly affected, and are comparable to inclusion-free analyses. Trace element data for apatite is listed in Table E.7 and shown in Fig. 16d.

Apatite from the MBIF shows notable concentrations of Mn (mean 788 ppm), Sr (176 ppm), Zn (21 ppm), As (24 ppm), Ti (10 ppm), Th (8

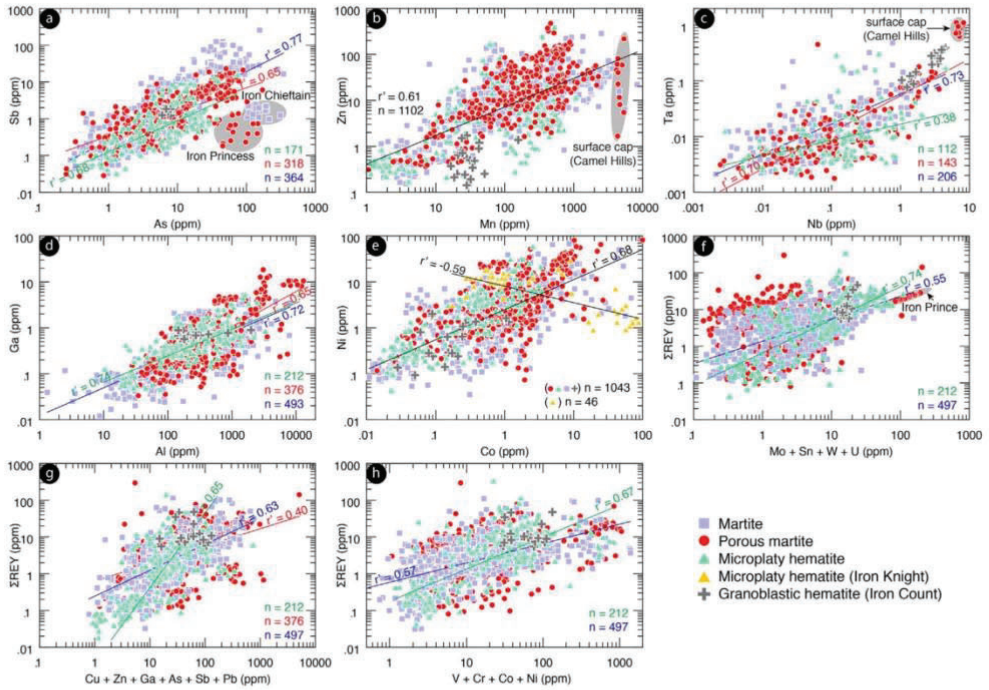

Fig. 14. LA-ICP-MS binary plots for trace element concentrations in hematite illustrating trends and correlations for different textural categories. (a) Sb *vs.* As. (b) Zn *vs.* Mn. (c) Ta *vs.* Nb. (d) Ga *vs.* Al. (e) Ni *vs.* Co. (f) ΣREY *vs.* Mo + Sn + W + U. (g) ΣREY *vs.* Cu + Zn + Ga + As + Sb + Pb. (h) ΣREY *vs.* V + Cr + Co + Ni. Granitophile, chalcophile and transition elements are tied to ΣREY concentrations. Note negative correlation of microplaty hematite from Iron Knight on (e).

ppm), and W (1 ppm). In MBIF showing stockwork veining, trace element concentrations in apatite are generally < 2 ppm. However, Mn (mean 65 ppm) and As (3 ppm) are measured, although lower than apatite from the MBIF. Strontium (mean 442 ppm) and W (6 ppm) are, however, higher.

REY are significantly enriched in apatite, albeit more so in the apatite from MBIF (mean ΣREY = 1,208 ppm) than from the MBIF with stockwork veining (mean ΣREY = 497 ppm). The chondrite-normalized REY fractionation trend for apatite in MBIF displays enrichment in LREE ($Ce/Lu_{(CN)}$ = 3.57), whereas apatite associated with stockwork veining is LREE-depleted ($Ce/Lu_{(CN)}$ = 0.76) and MREE-enriched. Pronounced Eu- and Y-anomalies are observed in both types of apatite, yet slight differences can be seen in the scale of the anomaly (Fig. 16d).

7. Discussion

The processes and timing of enrichment in BIF-associated iron ores is much debated (Hagemann et al., 2008), with the factors involved also impacted by local environment and geological history. The MR represents a unique BIF belt, which possesses its own specific makeup (existence of local structures, intense deformation etc.) but nevertheless also features a generic set of characteristics that are relevant for BIF systems elsewhere, e.g., a protracted geological history typical of Proterozoic granite-greenstone terranes (Angerer and Hagemann, 2010). In the following sections, we discuss how the correlation between petrography and trace element data for Fe-oxides leads to recognition of primary depositional environment, as well as overprinting events recorded by formation and transformation of Fe-oxides and -hydroxides. A model of ore formation is suggested by linking Fe-oxides to post-depositional events involving episodes of burial and uplift, interaction with surficial waters, thermal gradients and/or hydrothermal fluids associated with younger granitoids, and tectono-magmatic events with regional expression (e.g., younger dikes), and not least, proximity to faults.

7.1. Textures and mineral associations: Primary versus overprinting

The textural characteristics observed in Fe-oxides and associated minerals illustrate the significance of overprinting, on both regional and local scales, during transformation of Fe-oxides to form ores. Primary magnetite textures that infer hypogene enrichment during diagenesis are recognized at Iron Magnet (Figs. 6 and 7). Textural evidence for this interpretation includes equilibrium boundaries within the primary magnetite aggregates (not overprinted), inclusions of gangue minerals that are associated with the primary BIF depositional environment, and particularly, the co-crystallization relationships and reworking of mutual boundaries with apatite. Overprinting of primary magnetite and associated gangue mineral assemblages is also recognized as fractures crosscutting mineral banding, porosity, reworking of grain boundaries or primary zonation patterns (in carbonates), as well as the presence of 'exotic' trace mineral associations including sulfides, native gold and monazite. In addition, formation of martite is also closely associated with late veins crosscutting the MBIFs. At least two distinct generations of magnetite (primary and 'new') can be inferred based upon observed variation in size, grain morphology, and replacement relationships with gangue minerals. The late generation, consisting of smaller grains and often crosscutting gangue minerals, is associated with fluid percolation leading to the dissolution of primary

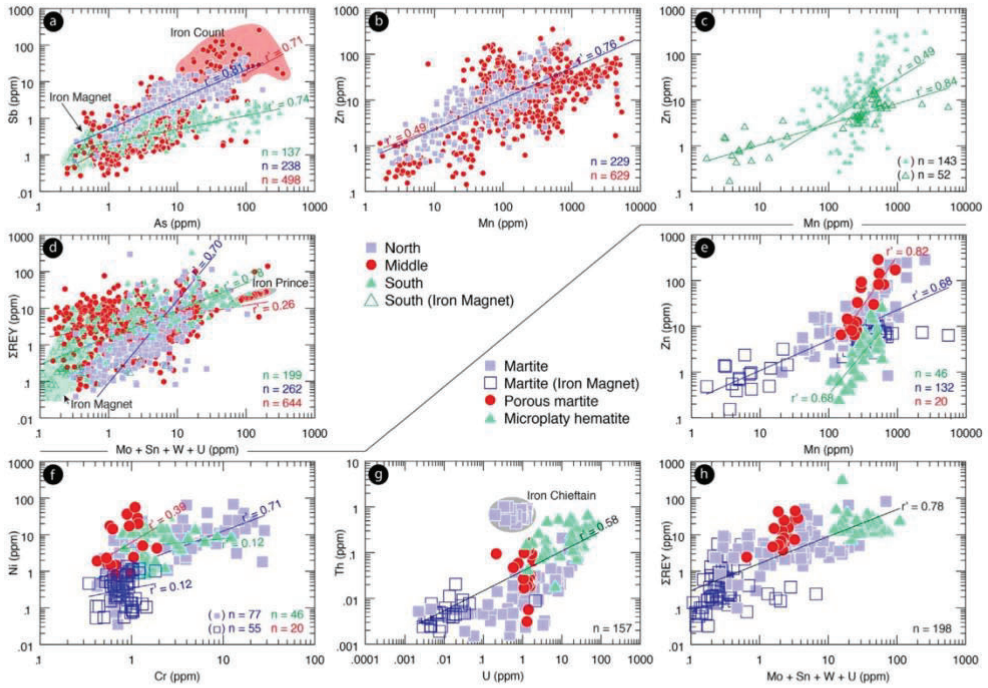

Fig. 15. LA-ICP-MS binary plots for trace element concentrations in hematite illustrating trends and correlations relative to location (a–d) and texture within a specific location (e-h). (a) Sb *vs.* As. (b) Zn *vs.* Mn in northern and central segments of the MR belt. (c) Zn *vs.* Mn in the southern segment of the MR belt. (d) ΣREY *vs.* (Mo + Sn + W + U). (e) Zn *vs.* Mn in the southern segment of the MR belt. (f) Ni *vs.* Cr in the southern segment of the MR belt. (g) Th *vs.* U in the southern segment of the MR belt. (h) ΣREY *vs.* (Mo + Sn + W + U) in the southern segment of the MR belt.

magnetite and the precipitation of 'new' magnetite along the margins of primary magnetite bands, and inclusion nucleation within pores. Such fluids are slightly reducing, and S-, and Cl-bearing, as shown by the presence of sulfides, which are clearly within the stability field of pyrite-pyrrhotite, magnetite, and Cl-bearing gangue minerals such as pyrosmalite. The latter assemblage is seen in the proximity of concordant metamorphosed mafic dikes (amphibolites) and intense pyrite alteration along the contacts to MBIFs (Fig. 2).

Unlike Iron Magnet, the other deposits of the MR sit shallower and display more extensive supergene alteration (e.g., Iron Duke; Davies, 2000). Martitization is abundant in these other deposits and is the most widespread expression of transformation among Fe-oxides (Figs. 8 and 9). To some extent, this alteration likely results from changes in fO_2 during supergene enrichment. However, martitization can also occur during pH adjustment as suggested elsewhere (Otake et al., 2010), with more acidic fluids creating increased porosity, and leading to veining and fracturing in Fe-oxides. All such features are extremely abundant at Iron Count, for example, and are also associated with brecciation, the presence of REE-minerals, and the juxtaposition of hematite displaying contrasting textures and composition.

Microplaty hematite, occurring throughout most deposits along the MR, clearly postdates BIF deposition, as seen from its complex association with Fe-hydroxides. Microplaty hematite can, however, be the result of precipitation at distinct stages, e.g., precipitation during martitization in massive ores (e.g., Iron Prince, Baron, or Monarch), co-precipitation or precipitation predating Fe-hydroxides (e.g., Iron Count), and postdating an earlier generation of Fe-hydroxides (e.g., Iron Knight, or Iron Monarch). The latter scenario is inferred based upon zonation patterns involving Si and an intimate relationship with Fe-hydroxides, which are characterized by similar Si-rich patterns (e.g., Iron Knight; Fig. 9h and Fig. 10d, e). This type of microplaty hematite is more restricted in occurrence and can be related to specific local settings whereby a second cycle of burial following diagenesis and uplift (indicated by Fe-hydroxides formed in a supergene environment) could have triggered growth of microplaty hematite from Fe-hydroxides. Such trends, prograde relative to formation of supergene Fe-hydroxides, could be also associated with thermal gradients during metamorphism, or to emplacement of younger intrusions or mafic dikes with regional expression. Dehydration of Fe-hydroxide to microplaty hematite has been proposed to account for formation of martite-microplaty hematite ores at low-temperatures (~80–100 °C) during regional metamorphism in the Hamersley Province, Western Australia (Morris and Kneeshaw, 2012).

7.2. Trace element signatures – Record of an evolving environment

Chondrite-normalized REY fractionation trends (Fig. 12) obtained for Fe-oxides of various types and from different BIF types are characterized by relatively flat trends, albeit with mild LREE enrichment for martite, when compared with Fe-oxides from other Fe-oxide-bearing deposits in South Australia, including iron-oxide-copper-gold (IOCG) deposits affiliated with Hiltaba Granites (e.g., Olympic Dam; Ciobanu et al., 2013, 2015; Verdugo-Ihl et al., 2017a,b). They do however resemble trends seen in martite from prospects near Olympic Dam (Island Dam; Keyser et al., 2017). The MR martite and microplaty hematite nevertheless show distinctive positive anomalies, which are not

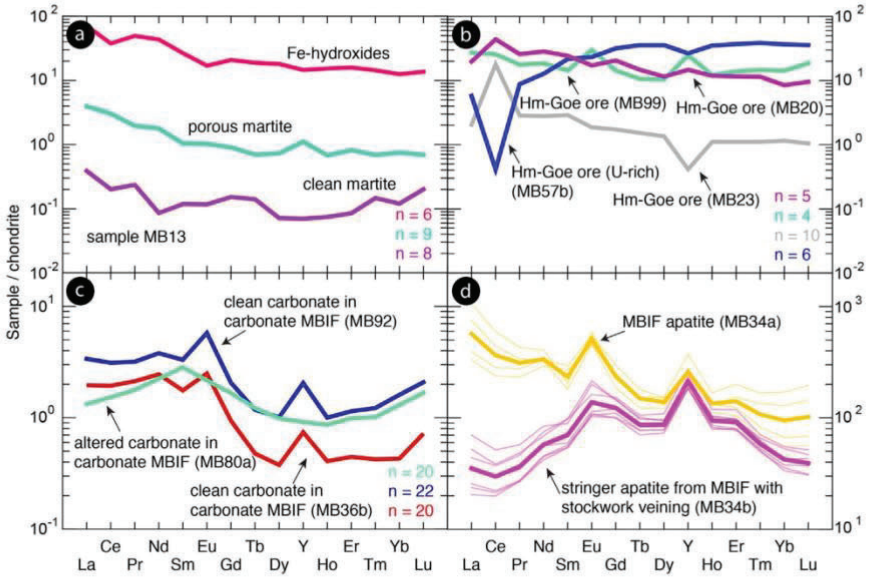

Fig. 16. Chondrite-normalized REY-fractionation patterns showing (a) Increasing ΣREY concentration associated with transformation from clean to porous martite in sample MB13; note highest ΣREY content is recorded in Fe-hydroxides. (b) Variation in REY-fractionation trends recorded in Fe-hydroxide from various lithologies showing geochemical differences in the supergene environment. (c, d) Variation in REY-fractionation trends for carbonates (c) and apatite (d) from MBIFs relating to degree of alteration (hydrothermal overprint). Note MREE-enriched trend, with strong positive Eu-anomaly for altered apatite.

recorded in the Island Dam martite. In the MR, there is a general enrichment in ΣREY and LREE from magnetite to martite (Fig. 12b). Although richer in ΣREY compared to martite, microplaty hematite does not always display LREE-enrichment. Carbonate and apatite associated with magnetite from MBIFs also show strong positive Eu- and Y-anomalies (Fig. 15c, d). The MREE-enriched trends in apatite stringers associated with stockwork veining in MBIF are noteworthy since similar trends, featuring MREE-enrichment and strong positive Eu-anomalies, are observed in apatite from quartz-magnetite BIF of the Isua Supracrustal Belt, Western Greenland, and have been attributed to percolating metasomatic fluids with a carbonate-rich composition or fluids associated with mafic dikes (Lepland et al., 2002).

Trace element signatures recorded by Fe-oxides (Figs. 13–15) show further evidence for formation in an evolving environment whereby emplacement of felsic and mafic lithologies is recognized in the presence of granitophile elements (Sn, U, W, Mo, Th), and transition metals (Ti, Cr, Ni, Co, Zn), respectively, throughout Fe-oxides along the entire belt. Enrichment in ΣREY, or in chalcophile elements (As and Sb), is attributable to mineralizing hydrothermal fluids presumably associated with metal-rich granitoid suites, e.g., Hiltaba Granites. Subtle changes in the correlation coefficients recorded by different hematite types for element pairs with similar geochemical behaviors, such as Sb-As, Zn-Mn, Nb-Ta, Ga-Al, or Co-Ni, indicates that martitization was followed by pore development (and granoblastic hematite growth). Martitization and formation of microplaty hematite are ore-enrichment stages distinct from one another in terms of geochemical environment.

More complex histories relative to the universal belt-wide trends are represented by outliers on various trace element diagrams, e.g., As-Sb for Iron Count and Iron Chieftain, or Zn-Mn and Ta-Nb for Camel Hills. Most striking is the inverse correlation between Ni and Co for Iron Knight, relative to the positive correlation between these elements in the same hematite category for all other deposits. This could be attributed to presence of mafic dikes of potentially, different generations and ages (see above). Decoupling between Co-Ni and Ti observed across porous *vs.* granoblastic hematite from Iron Count (element maps in Fig. 13) further indicates that martitization can be locally affected by fluids with signatures inherited from different sources. For example, Hiltaba-aged granites known to the east of Iron Count could have provided Ti(+U-W)-richer fluids, and moreover, would have represented a heat source inducing the recrystallization of porous martite into granoblastic hematite.

The influence of local setting is also highlighted by changes in the correlation slope for such elements or set of elements with distinct affiliation when grouped by location along the belt, e.g., granitophile elements *vs.* ΣREY, shows the strongest correlation for deposits in the south, and weakest for the middle segment. The latter domain is most likely more impacted by fluid movement along locally reactivated WNE-ESE-striking faults.

Other examples highlighting the impact of local setting relative to complex signatures are shown by trace elements in martite. In the northern segment of the MR, martite is relatively enriched in As and Sb compared to the central and southern segments. Such enrichment could be associated with fluids derived from granites responsible for mineralization north of the MR (e.g., Hiltaba-affiliated granites). Granite emplacement could also account for the observed enrichment in granitophile elements in the same domain. The southern segment is yet more enriched in granitophile elements, as well as in REY, and lies just north of the Hiltaba-related Charleston Granites. In the southern segment, however, local variation is observed with respect to Mn and Zn. Primary MBIFs are preserved at Iron Magnet, which is the deepest deposit in the MR and where the strongest correlation between these two elements is seen (Fig. 15c). Interbedded amphibolites and heavy pyrite alteration are largely restricted to this deposit and associated with MBIFs, and likely contribute to the local Fe-oxide compositional variation.

Statistical analysis of the same trace element dataset as that

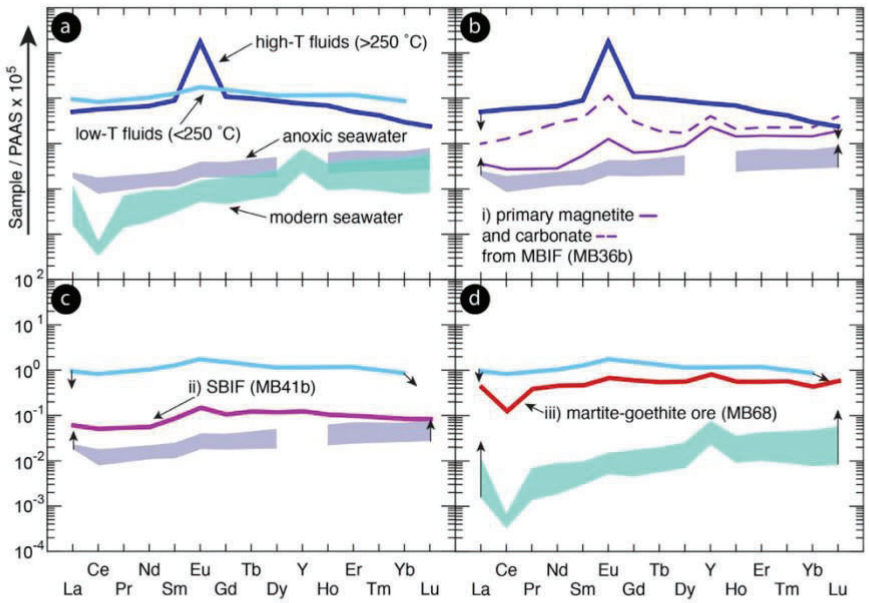

Fig. 17. PAAS-normalized REY fractionation diagrams comparing compositions of various water types and Fe-oxides. (a) Representative compositions of modern seawater (North Pacific Deep Water and South Pacific), anoxic seawater (Black Sea and Saanich Inlet), high-temperature hydrothermal fluids (Broken Spur site, Mid-Atlantic Ridge) and low-temperature hydrothermal fluids (submarine vents). (b) Comparison of REY trend (i) observed in magnetite and carbonate with mixture of anoxic seawater and high-temperature hydrothermal fluids. (c) Comparison of REY trend (ii) observed in hematite with mixture of anoxic water and low-temperature hydrothermal fluids. (d) Comparison of REY trend (iii) observed in hematite with mixture of modern seawater and low-temperature hydrothermal fluids. Note that yttrium was not measured in anoxic seawaters. Data sourced from German and Elderfield (1989), German et al. (1991), Zhang and Nozaki (1996) and Alibo and Nozaki (1999).

discussed here shows a comparable complexity in the geochemical signatures of different types of hematite, as well as the strong influence of local environment in pinpointing definitive trace element signatures (Dmitrijeva et al., in review).

7.3. Models of BIF formation using REY trends – Recognition of paleoenvironment

It is generally agreed that BIF deposition is initiated when anoxic, Fe^{2+}-rich waters mix with oxygenated seawaters during upwelling (e.g., Morris, 1993). Iron-oxyhydroxides and silica (chert) are considered to precipitate directly from seawater, settle on the seafloor, and undergo diagenesis. As such, BIFs have been used as proxies for ancient (Archean) seawater composition to make inferences about depositional environments and their physicochemical conditions. When normalized to Post-Archean Australian Shale (PAAS), the behavior of REY in such Archean proxies show discernable differences relative to dissolved REY in other types of fluid [e.g., anoxic seawater (Black Sea and Saanich Inlet) *vs.* modern seawater (North Pacific Deep Water and South Pacific); German and Elderfield, 1989; German et al., 1991; Zhang and Nozaki, 1996; Alibo and Nozaki, 1999; Fig. 17a]. Positive Y-anomalies and relative LREE depletion are attributes inherited from precipitation in a marine environment (Bau and Dulski, 1999), whereas Ce can be used as an indicator of redox conditions at the time of precipitation. Seawaters prior to the Great Oxidation Event (~2.45 Ga; Bekker et al., 2004) were largely anoxic and display REY fractionation trends with only slight Ce-anomalies if present at all. However, due to the scavenging behavior of tetravalent-Ce in oxygenated environments, negative Ce-anomalies are present in post-Archean oxygen-rich seawaters (Debaar et al., 1983) (Fig. 17a).

Hydrothermal fluids interacting with seawater have also been shown to display disparate REY fractionation behavior depending on fluid temperature. REY trends of high-temperature fluids (> 250 °C) associated with seafloor vents have slight LREE-enrichment and smooth overall patterns, except for characteristically pronounced positive Eu-anomalies (Bau and Dulski, 1999; Fig. 17a). Anomalies are absent in REY trends for low-temperature fluids (< 250 °C), which display similar smooth patterns with slight LREE-enrichment (Michard et al., 1993). Since the behavior of REY in various fluid types is reasonably well constrained, it should be possible to compare the REY trends of various fluids to those observed in minerals from the MR and hence deduce possible depositional environments/conditions.

Iron-oxides have been shown to retain seawater signatures through various diagenetic, metamorphic and hydrothermal processes (Gourcerol et al., 2016a,b). As such, various depositional settings can be inferred from the three categories of PAAS-normalized REY fractionation trends observed in Fe-oxides and related minerals from the MR (Fig. 17). Trend (i), observed in magnetite and carbonate from MBIF (Fig. 17b), displays LREE-depletion, a slight Ce-anomaly and pronounced Eu- and Y-anomalies, and may represent minerals precipitated from a mixture of anoxic seawater and high-temperature hydrothermal fluids. Such a trend is found in primary magnetite from Iron Magnet, where MBIF are associated with amphibolites. Carbonate from the layers alternating with the magnetite banding displays no Ce-anomaly and pronounced Eu- and Y-anomalies. These are, however, slightly more enriched in LREE, indicating that carbonates are better hosts for LREE. A less oxygenated environment and low-temperature fluid input, such as an inlet or a closed-off body of water, could explain the flatter pattern represented by trend (ii) (Fig. 17c). This pattern was observed mainly in samples from Iron Count, which is slightly offset from the

main strike of the MR belt. The smoother pattern and pronounced negative Ce-anomaly of trend (iii) (Fig. 17d) might result from mixing of more oxygenated seawater and low-temperature hydrothermal fluids. However, the influence of post-depositional, secondary Fe-hydroxide on such a trend cannot be ruled out. Iron-oxide REY fractionation trends that do not reflect primary signatures (e.g., magnetite in Fig. 12b) may result from overprinting on the primary Fe-oxide. In such cases, whole-rock REY trends may be better indication of primary signatures (Fig. 5b).

7.4. Genetic model for ore formation in the Middleback Ranges

Based on the evidence of textural and compositional variation among Fe-oxides presented above, it is likely that ore formation in the MR was governed by localized tectonothermal settings. The ores likely represent different stratigraphic levels within a sedimentary succession with varying uplift/burial histories and asynchronous interaction with fluids as the driving mechanism of ore formation. This would imply the penetration of fluids from multiple sources along fracture faults, probably on multiple occasions, and probably with substantial reactivation. Fracture faults are a common feature of major deposits in the MR and are observed to display a particular association with orebodies (Davies, 2000). Such tectonism and fluid interaction could relate to any of the numerous events impacting upon the MR throughout its evolution.

Our proposed model involves interaction between intrusion-related fluids and meteoric water with uplifted BIF as the driving mechanism behind ore formation in the MR (Fig. 18). The variable textures and geochemical signatures of Fe-oxides imply successive generations of overprinting post-BIF deposition. Ore formation may thus have been episodic, multi-stage and, in all likelihood, highly localized.

The first ore-forming scenario following BIF deposition (Fig. 18a) involves the leaching of exposed granites via surficial waters and incorporation of new elements within minerals crystallizing within adjacent BIF during superimposed tectonothermal events (Fig. 18b). Considering the proximity to igneous suites, geochemical signatures could have been inherited from any of the nearby granitic bodies, including the ~3150 Ma Cooyerdoo Granite (Fraser et al., 2010), ~1850 Ma Donington Suite, ~1790 Ma Wertigo Granite (Fraser and Neumann, 2010), and most significantly, the ~1585 Ma Hiltaba-affiliated Charleston Granite (Creaser and Fanning, 1993). The potential number of available sources could explain the complexity of different textures and signatures observed along the strike of the MR. In a second scenario, we speculate that ore formation could have been driven by interaction with hydrothermal granite-derived fluids, notably those of Hiltaba affiliation (Fig. 18c). Granites that produce such fluids account for high concentrations of U and other 'granitophile' elements in hydrothermal hematite from the Olympic Dam IOCG deposit, eastern Gawler Craton (Ciobanu et al., 2013, 2015; Verdugo-Ihl et al., 2017b), and are exposed to both the north and south of the MR. The last scenario involves heat generation from regional-scale tectonothermal events. The observed prograde growth of microplaty hematite seen at Iron Knight may, for example, be attributable to a crustal thermal gradient introduced by emplacement of any of the younger granite suites proximal to the MR that postdate BIF deposition, or emplacement of the mafic dike swarms and their metamorphosed equivalents,

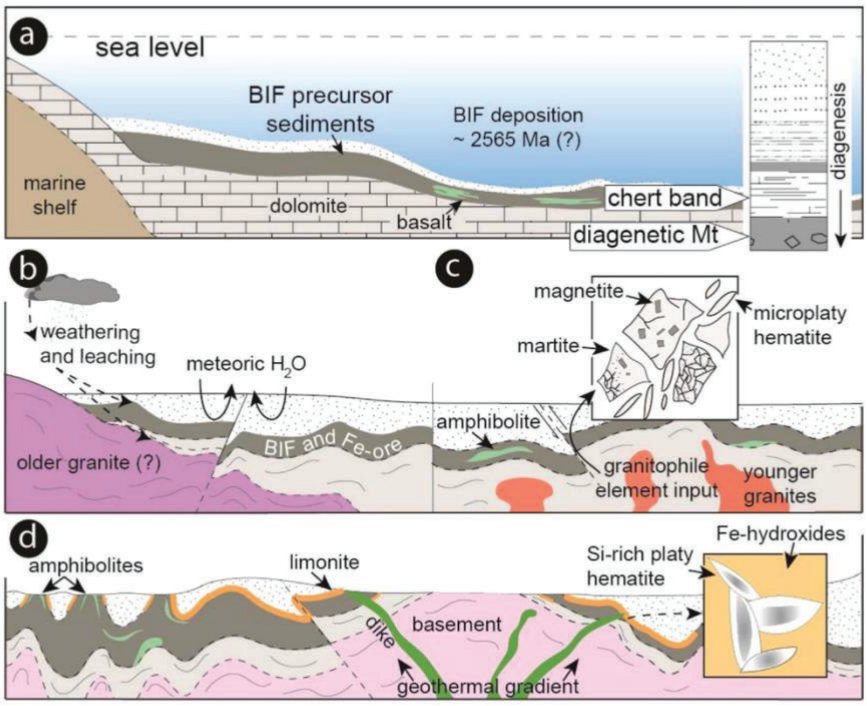

Fig. 18. Schematic showing evolution of iron mineralization in the MR from BIF deposition to ore formation. (a) Mineral precipitation and deposition on the ocean floor at ~2565 Ma followed by diagenesis and formation of hypogene magnetite. (b) Oxidized meteoric waters leach elements from local granites and infiltrate BIF, or (c) granite-derived fluids (Hiltaba-affiliated) interact with BIF. (d) Heating and faulting associated with younger dikes forms prograde, Si-zoned hematite on behalf of Fe-hydroxides (Iron Knight).

amphibolites (concordant or discordant to BIFs stratification) observed in the region. (Fig. 18d). Sulfides, zincite and REE-minerals (monazite, xenotime) are all further evidence for interaction between initial SBIFs and fluids with signatures attributable to lithologies of both mafic and felsic igneous affiliation during iron ore formation.

7.5. Conclusions

The correlation between petrography and trace element signatures in Fe-oxides from the MR shows that ore enrichment processes, although tied to broader evolutionary trends comparable to BIF-related ores elsewhere (e.g., Hensler et al., 2015), are nonetheless subject to overprinting due to superimposed tectono-magmatic events. Our data indicate that the belt can be bracketed into domains with slightly different geochemical signatures. Iron Magnet in the south retains much of the initial BIF environmental signature, whereas the middle and northern domains show more pronounced overprinting, particularly with respect to signatures attributable to Hiltaba Granites in the north. The initial BIF environment and protolith lithologies also likely varied along the strike of the belt with respect to open versus closed sedimentary basins as modeled for deposits off-the main strike at Iron Count.

Several locations along the belt represent outstanding candidates for placing better constraints on overprinting. These include Iron Count, Camel Hills and Iron Monarch, which show the strongest links to Hiltaba Granites and associated IOCG-style mineralization, and Iron Knight, which records a still younger overprint during emplacement of younger dikes.

The recent suggestion of lithologies within the Middleback Formation as Archean (Szpunar et al., 2011) raises questions with respect to understanding the relationship between MBIFs and interbedded mafic rocks metamorphosed at amphibolite facies at Iron Magnet. It is particularly difficult to reconcile the higher metamorphic facies of some mafic lithologies relative to BIF lithologies that contain mineral associations that should record evidence of metamorphism at similar facies if they were contemporaneous with the mafic rocks.

Further studies will include individual deposit studies and an in-depth petrographic-mineralogical study of associated granitoids and mafic rocks combined with U-Pb dating of accessory minerals from these lithologies, as well as U-Pb dating of Fe-oxides (Ciobanu et al., 2013; Courtney-Davies et al., 2016) wherever concentrations of these elements allow.

Acknowledgements

This work is a contribution to the project 'Trace elements in iron-oxides: deportment, distribution and application in ore genesis, geochronology, exploration and mineral processing', supported by BHP Olympic Dam and the South Australian Government Mining and Petroleum Services Centre of Excellence. Logistical support from geologists at Arrium Mining, the former operator, is highly appreciated. Constructive comments from Thomas Angerer and a second, anonymous reviewer, helped us improve the manuscript.

Appendix. Supplementary data

Supplementary data associated with this article (Appendices A–E) can be found, in the online version, at http://dx.doi.org/10.1016/j.oregeorev.2018.01.006.

References

Alibert, C., 2016. Rare earth elements in Hamersley BIF minerals. Geochim. Cosmochim. Acta 184, 311–328.
Alibo, D.S., Nozaki, Y., 1999. Rare earth elements in seawater: particle association, shale-normalization, and Ce oxidation. Geochim. Cosmochim. Acta 63, 363–372.
Angerer, T., Hagemann, S.G., 2010. The BIF-hosted high-grade iron ore deposits in the Archean Koolyanobbing Greenstone Belt, Western Australia: structural control on synorogenic- and weathering-related magnetite-, hematite-, and goethite-rich iron ore. Econ. Geol. 105, 917–945.
Angerer, T., Hagemann, S.G., Danyushevsky, L.V., 2012. Geochemical evolution of the banded iron formation-hosted high-grade iron ore system in the Koolyanobbing Greenstone Belt, Western Australia. Econ. Geol. 107, 599–644.
Aoki, S., Kabashima, C., Kato, Y., Hirata, T., Komiya, T., in press. Influence of contamination on banded iron formations in the Isua supracrustal belt, West Greenland: Reevaluation of the Eoarchean seawater compositions. Geosci. Front.. doi: 10.1016/j.gsf.2016.11.016.
Arrium Mining, 2016. Ore Reserve and Resources Statement, 30th June 2016. Arrium Mining Ltd.
Bau, M., Dulski, P., 1996. Distributions of yttrium and rare-earth elements in the Penge and Kuruman iron-formations, Transvaal Supergroup, South Africa. Precambr. Res. 76, 37–55.
Bau, M., Dulski, P., 1999. Comparing yttrium and rare earths in hydrothermal fluids from the Mid-Atlantic Ridge: implications for Y and REE behavior during near-vent mixing and for the Y/Ho ratio of Proterozoic seawater. Chem. Geol. 155, 77–99.
Bekker, A., Holland, H.D., Wang, P.-L., Rumble III, D., Stein, H.J., Hannah, J.L., Coetzee, L.L., Beukes, N.J., 2004. Dating the rise of atmospheric oxygen. Nature 427, 117–120.
Bekker, A., Slack, J.F., Planavsky, N., Krapež, B., Hofmann, A., Konhauser, K.O., Rouxel, O., 2010. Iron formation: the sedimentary product of a complex interplay among mantle, tectonic, oceanic and biospheric processes. Econ. Geol. 105, 467–508.
Ciobanu, C.L., Wade, B.P., Cook, N.J., Schmidt Mumm, A., Giles, D., 2013. Uranium-bearing hematite from the Olympic Dam Cu-U-Au deposit, South Australia: a geochemical tracer and reconnaissance Pb-Pb geochronometer. Precambr. Res. 238, 129–147.
Ciobanu, C.L., Cook, N.J., Ehrig, K., Wade, B.P., Kamenetsky, V.S., 2015. Trace element signatures in iron oxides from the Olympic IOCG deposit, South Australia. Mineral Resources in a Sustainable World, 13th Biennial SGA Meeting, Nancy, pp. 1071–1074.
Cook, J.N., 1971. Grade control procedures at the Iron Prince quarry Whyalla, South Australia. Australasian Institute of Mining and Metallurgy, Adelaide Regional Conference, Adelaide, South Australia, August 1971, Paper No. 4.
Cook, N.J., Ciobanu, C.L., George, L., Zhu, Z., Wade, W., Ehrig, K., 2016. Trace element analysis of minerals in magmatic-hydrothermal ores by laser ablation inductively-coupled plasma mass spectrometry: approaches and opportunities. Minerals 6, 111; doi:10.3390/min6040111.
Courtney-Davies, L., Zhu, Z., Ciobanu, C.L., Wade, B.P., Cook, N.J., Ehrig, K., Cabral, A.R., Kennedy, A., 2016. Matrix-matched iron-oxide laser ablation ICP-MS U-PB Geochronology using mixed solution standards. Minerals 6, 85; doi:10.3390/min6030085.
Creaser, R.A., Fanning, C.M., 1993. A U-Pb zircon study of the Mesoproterozoic Charleston Granite, Gawler Craton, South Australia. Aust. J. Earth Sci. 40, 519–526.
Davies, M.B., 2000. Iron ore in South Australia. Primary Industries and Resources SA, Commodity Review n. 8, 35 pp.
Debaar, H.J.W., Bacon, M.P., Brewer, P.G., 1983. Rare-earth distributions with a positive anomaly in the Western North-Atlantic Ocean. Nature 301, 324–327.
Dmitrijeva, M., Metcalfe, A.V., Ciobanu, C.L., Cook, N.J., Frenzel, M., Keyser, W.M., Johnson, G., Ehrig, K., in review. Discrimination and variance structure of trace elements in hematite: a case study of BIF-mineralization from the Middleback Ranges, South Australia. Math. Geosci.
Feltus, H., Cook, N.J., Ciobanu C.L., Johnson, G., in prep. Iron oxide copper gold prospects in the Middleback Ranges, South Australia. Ore Geol. Rev.
Fraser, G., McAvaney, S., Neumann, N., Szpunar, M., Reid, A., 2010. Discovery of early Mesoarchean crust in the eastern Gawler Craton, South Australia. Precambr. Res. 179, 1–21.
Fraser, G., Neumann, N., 2010. New SHRIMP U-Pb zircon ages from the Gawler Craton and Curnamona Province, South Australia, 2008–2010. Geoscience Australia, Record, 2010/16.
German, C.R., Elderfield, H., 1989. Rare earth elements in Saanich Inlet, British Columbia, a seasonally anoxic basin. Geochim. Cosmochim. Acta 53, 2561–2571.
German, C.R., Holliday, B.P., Elderfield, H., 1991. Redox cycling of rare earth elements in the suboxic zone of the Black Sea. Geochim. Cosmochim. Acta 55, 3553–3558.
Gourcerol, B., Kontak, D.J., Thurston, P.C., 2016. Do magnetite layers in Algoma-type banded iron formations preserve their primary geochemical signature? A case study of samples from three Archean BIF-hosted gold deposits. Canadian Mineralogist 54, 605–624.
Gourcerol, B., Thurston, P.C., Kontak, D.J., Côté-Mantha, O., Biczok, J., 2016. Depositional setting of Algoma-type banded iron formation. Precambr. Res. 281, 47–79.
Gross, G.A., 1980. A classification of iron formations based on depositional environments. Can. Mineral. 18, 215–222.
Hagemann, S.G., Angerer, T., Duuring, P., Rosière, C.A., Figueiredo e Silva, R.C., Lobato, L., Hensler, A.S., Walde, D.H.G., 2016. BIF-hosted iron mineral system: A review. Ore Geol. Rev. 76, 317–359.
Hagemann, S.G., Rosière, C., Gutzmer, J., Beukes, N.J., Eds., 2008. Banded Iron Formation-related High-Grade Iron Ore. Rev. Econ. Geol. 15, 414.
Hensler, A., Hagemann, S.G., Rosière, C.A., Angerer, T., Gilbert, S., 2015. Hydrothermal and metamorphic fluid-rock interaction associated with hypogene "hard" iron ore mineralisation in the Quadrilátero Ferrífero, Brazil: implications from in-situ laser ablation ICP-MS iron oxide chemistry. Ore Geol. Rev. 69, 325–351.
Huberty, J.M., Konishi, H., Heck, P.R., Fournelle, J.H., Valley, J.W., Xu, H.F., 2012. Silician magnetite from the Dales Gorge Member of the Brockman Iron Formation, Hamersley Group, Western Australia. Am. Mineralogist 97, 26–37.

Ismail, R., Ciobanu, C.L., Cook, N.J., Teale, G.S., Giles, D., Schmidt Mumm, A., Wade, B., 2014. Rare earths and other trace elements in minerals from skarn assemblages, Hillside iron-oxide-copper-gold deposit, Yorke Peninsula, South Australia. Lithos 184–187, 456–477.

Jagodzinski, E.A., Reid, A., Farrell, F., 2011. Geochronology of the Bungalow Prospect. In: Reid, A.J., Jagodzinski, E.A., (Eds.), PACE Geochronology: results of collaborative geochronology projects 2009–10. South Australia Department of Primary Industries and Resources, Report Book 2011/00003, pp. 42–62.

Keyser, W.M., Ciobanu, C.L., Cook, N.J., Courtney-Davies, L., Ehrig, K., Gilbert, S., McPhie, J., 2017. Links between sedimentary protoliths and IOCG-skarn alteration, Island Dam, South Australia, Extended abstract, 14th Biennial SGA Conference, Québec, Canada, vol. 3, pp. 935–938.

Leevers, P., Gaughan, C., Bubner, G., 2005. The Iron Magnet deposit. Australasian Institute of Mining and Metallurgy Publication Series, Iron Ore Conference, Fremantle, WA, 19–21 September 2005.

Lepland, A., Arrhenius, G., Cornell, D., 2002. Apatite in early Archean Isua supracrustal rocks, southern West Greenland: its origin, association with graphite and potential as a biomarker. Precambr. Res. 118, 221–241.

McAvaney, S., 2012. The Cooyerdoo Granite: Paleo- and Mesoarchean basement of the Gawler Craton. MESA J. 65, 31–40.

McDonough, W.F., Sun, S.S., 1995. The composition of the earth. Chem. Geol. 120, 223–253.

Michard, A., Michard, G., Stüben, D., Stoffers, P., Cheminée, J., Binard, N., 1993. Submarine thermal springs associated with young volcanos: The Teahitia vents, Society Islands, Pacific Ocean. Geochim. Cosmochim. Acta 57, 4977–4986.

Morris, R.C., 1993. Genetic modelling for banded iron-formation of the Hamersley Group, Pilbara Craton, Western Australia. Precambr. Res. 60, 243–286.

Morris, R.C., Kneeshaw, M., 2012. Genesis modelling for the Hamersley BIF-hosted iron ores of Western Australia: a critical review. Aust. J. Earth Sci. 58, 417–451.

Otake, T., Wesolowski, D.J., Anovitz, L.M., Allard, L.F., Ohmoto, H., 2010. Mechanisms of iron oxide transformations in hydrothermal systems. Geochim. Cosmochim. Acta 74, 6141–6156.

Parker, A.J., Lemon, N.M., 1982. Reconstruction of the early Proterozoic stratigraphy of the Gawler Craton, South Australia. J. Geol. Soc. Aust. 29, 221–238.

Pirajno, F., Hoatson, D.M., 2012. A review of Australia's Large Igneous Provinces and associated mineral systems: implications for mantle dynamics through geological time. Ore Geol. Rev. 48, 2–54.

Planavsky, N., Bekker, A., Rouxel, O.J., Kamber, B., Hofmann, A., Knudsen, A., Lyons, T.W., 2010. Rare earth element and yttrium compositions of Archean and Paleoproterozoic Fe formations revisited: new perspectives on the significance and mechanisms of deposition. Geochim. Cosmochim. Acta 74, 6387–6405.

Reid, A., Hand, M., 2012. Mesoarchean to Mesoproterozoic evolution of the southern Gawler Craton, South Australia. Episodes 35, 216–225.

Slack, J.F., Grenne, T., Bekker, A., Rouxel, O.J., Lindberg, P.A., 2007. Suboxic deep seawater in the late Paleoproterozoic: Evidence from hematitic chert and iron formation related to seafloor-hydrothermal sulphide deposits, central Arizona, USA. Earth Planet. Sci. Lett. 255, 243–256.

Szpunar, M., Hand, M., Barovich, K., Jagodzinski, E., Belousova, E., 2011. Isotopic and geochemical constraints on the Paleoproterozoic Hutchison Group, southern Australia: Implications for Paleoproterozoic continental reconstructions. Precambr. Res. 187, 99–126.

Xu, J., Ciobanu, C.L., Cook, N.J., Zheng, Y., Sun, X., Wade, B.P., 2016. Skarn formation and trace elements in garnet and associated minerals from Zhibula copper deposit, Gangdese Belt, southern Tibet. Lithos 262, 213–231.

Van Achterbergh, E., Ryan, C., Jackson, S., Griffin, W., 2001. MAC Short Course 29, 239–243.

Vassallo, J.J., Wilson, J.L., 2002. Palaeoproterozoic regional-scale non-coaxial deformation: an example from eastern Eyre Peninsula, South Australia. J. Struct. Geol. 24, 1–24.

Verdugo-Ihl, M.R., Ciobanu, C.L., Cook, N.J., Courtney-Davies, L., Ehrig, K., Gilbert, S., 2017a. Trace element signatures in U-W-Sn-Mo zoned hematite from the IOCG deposit at Olympic Dam, South Australia, Extended abstract, 14th Biennial SGA Conference, Québec, Canada, vol. 3, pp. 967–970.

Verdugo-Ihl, M.R., Ciobanu, C.L., Cook, N.J., Ehrig, K., Courtney-Davies, L., Gilbert, S., 2017. Textures and U-W-Sn-Mo signatures in hematite from the Cu-U-Au-Ag orebody at Olympic Dam, South Australia: defining the archetype for IOCG deposits. Ore Geol. Rev. 91, 173–195.

Ward, L.K., 1949. The genesis of the iron ores of the Middleback Range, South Australia. Proceedings of the Australian Institute of Mining and Metallurgy Monograph 152–153, 229–239.

Woodhead, J.D., Hellstrom, J., Hergt, J.M., Greig, A., Maas, R., 2007. Isotopic and elemental imaging of geological materials by laser ablation inductively coupled plasma-mass spectrometry. Geostand. Geoanal. Res. 31, 331–343.

Yeates, G., 1990. Middleback Range iron ore deposits. In: Hughes F.E., ed. Geology of the Mineral Deposits of Australia and Papua New Guinea. Australian Institute of Mining and Metallurgy Monograph 14, pp. 1045–1048.

Zhang, J., Nozaki, Y., 1996. Rare earth elements and yttrium in seawater: ICP-MS determinations in the East Caroline, Coral Sea, and South Fiji basins of the western South Pacific Ocean. Geochim. Cosmochim. Acta 60, 4631–4644.

CHAPTER 3

IRON-OXIDES CONSTRAIN BIF EVOLUTION IN TERRANES WITH PROTRACTED GEOLOGICAL HISTORIES: THE IRON COUNT PROSPECT, MIDDLEBACK RANGES, SOUTH AUSTRALIA

William Keyser[1], Cristiana L. Ciobanu[1], Nigel J. Cook[1], Marija Dmitrijeva[1], Liam Courtney-Davies[1], Holly Feltus[2], Sarah Gilbert[3], Geoff Johnson[2], Kathy Ehrig[4]

[1]*School of Chemical Engineering, The University of Adelaide, Adelaide, SA 5005, Australia*

[2]*SIMEC Mining, Level 2 169 Fullarton Road, Dulwich, SA 5005, Australia*

[3]*Adelaide Microscopy, The University of Adelaide, Adelaide, SA 5005, Australia*

[3]*BHP Billiton Olympic Dam, Adelaide, SA 5000, Australia*

Article published in Lithos 324-325 (2019), 20-38.

Statement of Authorship

Title of Paper	Iron-oxides constrain BIF evolution in terranes with protracted geological histories: The Iron Count prospect, Middleback Ranges, South Australia
Publication Status	☑ Published ☐ Accepted for Publication ☐ Submitted for Publication ☐ Unpublished and Unsubmitted w ork w ritten in manuscript style
Publication Details	Keyser, W., Ciobanu, C.L., Cook, N.J., Dmitrijeva, M., Courtney-Davies, L., Feltus, H., Gilbert, S., Johnson, G., Ehrig, K., 2019. Iron-oxides constrain BIF evolution in terranes with protracted geological histories: The Iron Count prospect, Middleback Ranges, South Australia. Lithos 324-325, 20-38.

Principal Author

Name of Principal Author (Candidate)	William Keyser		
Contribution to the Paper	Performed analytical work, carried out data processing and interpretation, oversaw development of work and wrote manuscript.		
Overall percentage (%)	68		
Certification:	This paper reports on original research I conducted during the period of my Higher Degree by Research candidature and is not subject to any obligations or contractual agreements with a third party that would constrain its inclusion in this thesis. I am the primary author of this paper.		
Signature		Date	4/6/2019

Co-Author Contributions

By signing the Statement of Authorship, each author certifies that:

i. the candidate's stated contribution to the publication is accurate (as detailed above);

ii. permission is granted for the candidate in include the publication in the thesis; and

iii. the sum of all co-author contributions is equal to 100% less the candidate's stated contribution.

Name of Co-Author	Cristiana L. Ciobanu		
Contribution to the Paper	Helped define direction of research, supervised development of work, assisted with data interpretation and contributed to manuscript preparation.		
Overall percentage (%)	10		
Signature		Date	4th June 2019

Name of Co-Author	Nigel J. Cook		
Contribution to the Paper	Helped define direction of research, supervised development of work, assisted with data interpretation and contributed to manuscript preparation.		
Overall percentage (%)	7		
Signature		Date	4/6/19

Name of Co-Author	Marija Dmitrijeva		
Contribution to the Paper	Assisted with construction of figures and evaluation of manuscript.		
Overall percentage (%)	3		
Signature		Date	30/4/2019

Name of Co-Author	Liam Courtney-Davies		
Contribution to the Paper	Assisted with data processing and interpretation, and evaluation of manuscript.		
Overall percentage (%)	3		
Signature		Date	30/4/2019

Name of Co-Author	Holly Feltus		
Contribution to the Paper	Assisted with sample collection and evaluation of manuscript.		
Overall percentage (%)	3		
Signature		Date	30/4/2019

Name of Co-Author	Sarah Gilbert		
Contribution to the Paper	Assisted with analytical instrumentation and data processing.		
Overall percentage (%)	2		
Signature		Date	3/6/19

Name of Co-Author	Geoff Johnson		
Contribution to the Paper	Assisted with sample collection and evaluation of manuscript.		
Overall percentage (%)	2		
Signature		Date	30/5/2019

Name of Co-Author	Kathy Ehrig		
Contribution to the Paper	Helped define research direction and assisted with evaluation of manuscript.		
Overall percentage (%)	2		
Signature		Date	3/6/2019

Lithos 324–325 (2019) 20–38

Contents lists available at ScienceDirect

Lithos

journal homepage: www.elsevier.com/locate/lithos

Iron-oxides constrain BIF evolution in terranes with protracted geological histories: The Iron Count prospect, Middleback Ranges, South Australia

William Keyser [a,*], Cristiana L. Ciobanu [a], Nigel J. Cook [a], Marija Dmitrijeva [a], Liam Courtney-Davies [a], Holly Feltus [b], Sarah Gilbert [c], Geoff Johnson [b], Kathy Ehrig [d]

[a] School of Chemical Engineering, The University of Adelaide, Adelaide, SA 5005, Australia
[b] SIMEC Mining, Level 2, 169 Fullarton Road, Dulwich, SA 5065, Australia
[c] Adelaide Microscopy, The University of Adelaide, Adelaide, SA 5005, Australia
[d] BHP Olympic Dam, Adelaide, SA 5000, Australia

ARTICLE INFO

Article history:
Received 22 March 2018
Accepted 31 October 2018
Available online 3 November 2018

Keywords:
U—Pb hematite geochronology
Banded iron formation
Middleback Ranges
Iron-oxides
Trace element geochemistry

ABSTRACT

When studied at appropriate scales of observation and using complementary methods, the intrinsic textural and geochemical complexity of iron-oxides can provide unparalleled insights into the evolution of iron ore resources from banded iron formation deposition to ore formation. Iron Count is one of >20 deposits and prospects within the Archean Middleback Ranges iron ore belt, South Australia, in which iron-oxides from BIFs and ores display variable textural and trace element signatures. Integrated petrography, iron-oxide laser-ablation mapping and geochemistry, and in-situ dating of BIF-derived ores was undertaken to assess whether features observed in samples from this representative prospect might be attributed to localized and superimposed overprint processes. The prospect consists of a West and East ridge, each characterized by a sequence of overprints expressed as interconversions between iron-(hydr)oxides and accompanying variation in trace element concentrations. Pseudomorphic replacement of early magnetite by hematite (martite), followed by replacement by iron-hydroxides is recognized in samples from the East Ridge. Further overprints are expressed as veining, brecciation and crystallization of (micro)platy hematite rich in granitophile elements (Sn, Mo, W, U). Martitization of early magnetite in the West Ridge is accompanied by enrichment in Zn, Co and Ni in martite. Subsequent recrystallization of martite/iron-hydroxides by granoblastic hematite is marked by enrichment in Ti, Ta, Nb, REE and granitophile elements, and co-crystallization of REE-minerals. This is followed by crystallization of (micro)platy hematite, similarly rich in these elements. Enrichment in Ti and granitophile elements in granoblastic hematite is interpreted to infer crystallization from highly saline fluids generated by interaction between evaporite-bearing sedimentary rocks and granite-derived fluids. Post-Archean Australian Shale-normalized REY fractionation trends of iron-oxides from the East Ridge are consistent with precipitation of iron-rich minerals from a mixture of anoxic seawater and hydrothermal vent fluids. Analogous trends from the West Ridge lack a seawater signature. Contrasts in REY fractionation trends between the two ridges is interpreted as a combination of the loss of primary seawater signature due to severe overprinting in the West Ridge, and to lateral variation in the marine depositional environment. Results validate the hypothesis that variation in iron-oxide trace element signatures seen throughout the Middleback Ranges iron ore belt results from overprinting due to superimposed tectono-magmatic events that have locally affected each deposit. Despite undergoing different sequences of ore-forming stages, as well as possibly distinct depositional environments, the two ridges share a common overprint, dated here at ~1790 Ma using in-situ U—Pb geochronology of co-existing hematite, monazite and xenotime. This age is considered to represent the timing of interaction between granite-derived fluids with ore-hosting rock. Such interpretation is supported by the geochemical signatures of the dated iron-oxides showing enrichment in granitophile elements and coincident ages for the Wertigo Granite and Myola Volcanics, which occur proximal to the prospect and were emplaced/erupted during intracontinental rifting. The approach undertaken here, combining petrography, iron-oxide geochemistry and in-situ dating of BIF-derived ores is generically applicable to other iron resources within the Middleback Ranges or analogous terranes elsewhere.

* Corresponding author.
E-mail address: william.keyser@adelaide.edu.au (W. Keyser).

https://doi.org/10.1016/j.lithos.2018.10.035
0024-4937/

1. Introduction

Enrichment from banded iron formation (BIF) to high-grade iron ore is characterized by (inter)conversion among iron-oxides and formation of new generations of iron-oxides and -hydroxides resulting from fluid-rock interaction at various scales (Morris, 1980; Hensler et al., 2015). Variation in the concentrations of trace elements incorporated within iron-oxides, and often the textures displayed by those iron-oxides (e.g., Rosière et al., 2001), can reflect changing physiochemical conditions. Recognition of distinct textures and chemical signatures of iron-oxides throughout the enrichment process is central to understanding the overprinting event(s) responsible for generation of economic iron-oxide mineralization (e.g., Angerer et al., 2012).

The Middleback Ranges is a BIF-derived iron ore belt in the Gawler Craton of South Australia, which contains >20 discrete iron ore deposits and prospects located along a 60 km N-S strike (Fig. 1A). Iron-oxides from BIFs and ores throughout the belt exhibit large variation in textural and geochemical signatures; these phenomena that are attributed to multiple and varied enrichment processes (Keyser et al., 2018). These signatures include enrichment in elements characteristic of interaction with mineralizing hydrothermal fluids (chalcophile elements, e.g., As and Sb), such as those observed in samples from deposits in the north of the belt (Keyser et al., 2018). In contrast, the same authors show that deposits from the south of the belt are enriched in elements with a distinct granitic affiliation (Sn, Mo, W, U; hereafter 'granitophile elements') and rare earth elements and yttrium (hereafter REY). Variation in the correlation strength of element pairs further distinguish deposits throughout the belt (Keyser et al., 2018) and highlight the impact of local setting on the upgrading processes associated with individual deposits (e.g., Mn vs. Zn at Iron Magnet deposit, southern Middleback Ranges).

The large variation of iron-oxide signatures observed throughout the Middleback Ranges (Keyser et al., 2018) emphasises the need to investigate local deposit settings and better understand the evolution of

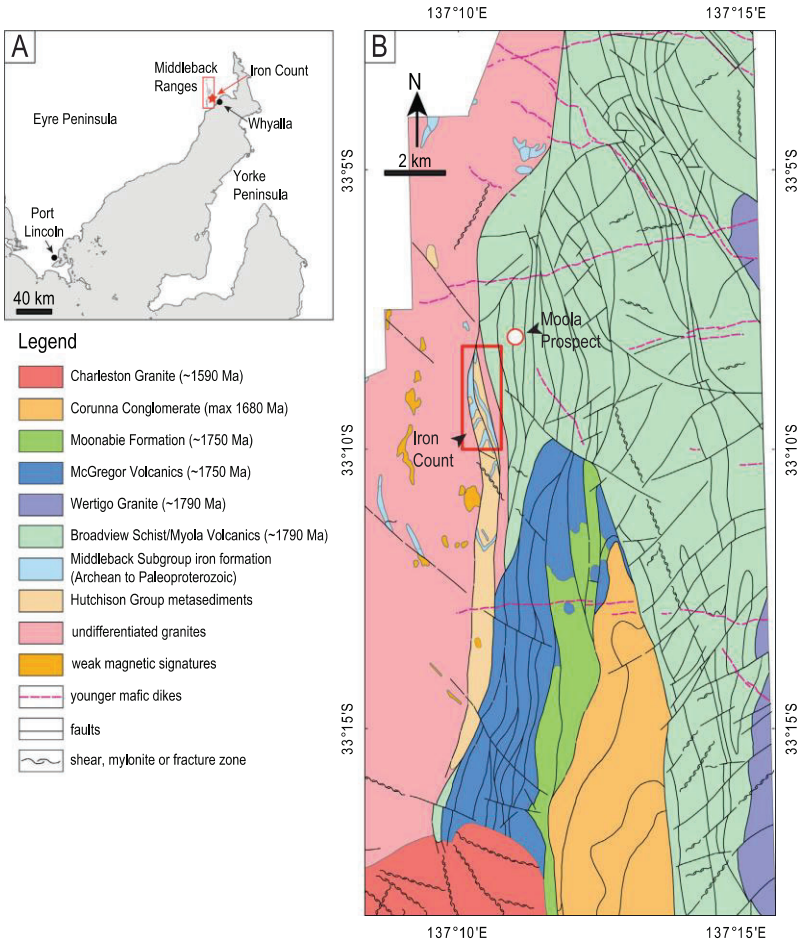

Fig. 1. (A) Location of the Middleback Ranges within the Eyre Peninsula, South Australia. (B) Basement map of middle-eastern segment of MR showing the geological context of the Iron Count prospect (marked by a red rectangle). Data sourced from http://map.sarig.sa.gov.au.

tectonic environments following BIF deposition. For example, the presence of various mafic and granitic rock types spatially associated with the orebodies throughout the ranges, namely granites of the Mesoproterozoic Hiltaba Intrusive Suite (HIS, e.g., Charleston Granite; Creaser and Fanning, 1993) responsible for hydrothermal fluids associated with iron-oxide-copper-gold (IOCG) mineralization elsewhere in the Gawler Craton of South Australia, are reason to consider that overprinting results from interaction between iron-oxides, local lithologies, and fluid-focusing faults. This could explain outlying signatures at locations where iron-oxides are characterized by enrichment in granitophile and chalcophile group elements, such as the Iron Count prospect (Dmitrijeva et al., 2018; Keyser et al., 2018).

Recognition of major rifting associated with emplacement of the ~1790 Ma Wertigo Granite (Fraser and Neumann, 2010; McAvaney et al., 2016), and contemporaneous eruption/deposition of the Myola Volcanics and Broadview Schist, respectively (Fanning et al., 1988), adjacent to the Iron Count prospect raises the question of its impact on hematite mineralization at the prospect. While previous studies have sought to understand mineralization processes during BIF overprinting through iron-oxide trace element geochemistry (e.g., Chung et al., 2015) and/or geochronology of iron-oxides and associated hydrothermal minerals (Farley and McKeon, 2015; Rasmussen et al., 2016; Sheppard et al., 2017), the work reported here is the first integrated petrographic-geochemical-geochronological study of iron-oxides aimed at constraining hematite mineralization in upgraded BIF environments. It is also the first to provide geochronological constraints on ore formation in the Middleback Ranges. The purpose of this contribution is to test the hypothesis that the distinct iron-oxide signatures from the Iron Count prospect in the southern part of the belt can be attributed to interaction between precursor BIF and paragenetically later hydrothermal fluids derived from granites and/or rhyolitic volcanic rocks. Such approach, if tested on comparable BIF sequences in cratonic terranes elsewhere, would emphasize the petrogenetic significance of iron-oxides in constraining protracted geological histories.

2. Geological background

The Middleback Ranges (MR) comprise a ~60 km-long series of discontinuous ridges in the north-eastern Eyre Peninsula (Fig. 1A). The basement rocks of this region of the Gawler Craton are the ~3.15 Ga Cooyerdoo Granite (Fraser et al., 2010), which are overlain by metamorphosed chemical and clastic sediments and bimodal volcanic rocks of the Hutchison Group. Prior studies interpreted the Hutchison Group to unconformably overlie the ~2.0 Ga Miltalie Gneiss (Parker and Lemon, 1982), providing a maximum age of deposition (Hand et al., 2007). Recent re-evaluation of the Hutchison Group (Szpunar et al., 2011) suggests it consists of three isotopically and geochemically distinct subgroups deposited between ~2550 and ~1730 Ma: the Darke Peake; the Cleve; and the Middleback subgroups. The massive iron ore deposits of the MR are hosted within the ~2550 Ma BIF units of the Middleback Subgroup (Szpunar et al., 2011), which lies east of the crustal-scale ~1730 Ma Kalinjala Shear Zone (KSZ; Parker, 1980; Vassallo and Wilson, 2002).

The stratigraphy of the Middleback Subgroup consists of two iron-rich units (the Lower and Upper Middleback Iron Formations) separated by a schist unit (Cook Gap Schist). Major ore mineralization occurs predominantly within the Lower Middleback Iron Formation. It has, however, been suggested that the two iron-rich units are a structural repetition of a single unit via thrusting and folding during regional deformation (Yeates, 1990; Vassallo and Wilson, 2001). The variable deformation recognized in this part of the Gawler Craton is attributed to three orogenic phases. Granulite- to amphibolite-facies metamorphic conditions were reached during the ~2465–2410 Ma Sleafordian and ~1850 Ma Cornian orogenies (Reid et al., 2008). Significant magmatism during the Cornian Orogeny led to emplacement of the Donington Magmatic Suite (Reid et al., 2008). The ~1730–1690 Ma Kimban Orogeny (Hand et al., 2007) led to amphibolite-facies metamorphism and activation of major crustal structures throughout the region, most notably the KSZ.

The period spanning the Cornian and Kimban orogenies has been recognized as an important phase of rifting and basin development (McAvaney et al., 2016). The rhyolitic Myola Volcanics and Broadview Schist were erupted/deposited at ~1790 Ma (Fanning et al., 1988; Fraser and Neumann, 2010; Jagodzinski and McAvaney, 2016), with emplacement of the Wertigo Granite (1792 ± 6 Ma and 1768 ± 4 Ma; Fraser and Neumann, 2010) occurring roughly coevally. Whole-rock trace element data for the Myola Volcanics and the A-type affinity of the Wertigo Granite (McAvaney et al., 2016) suggest rifting likely took place in an intracontinental setting (Fanning et al., 1988; Parker et al., 1993). Further tectonic activity throughout the MR is evidenced by emplacement of the ~1590 Ma Charleston Granite (Creaser and Fanning, 1993) and younger concordant and discordant mafic dikes striking roughly NW-SE throughout the belt (Ward, 1949).

The Iron Count prospect is offset to the east of the main strike of the MR by ~5 km, along the southeastern margin of the belt, <2 km from weak IOCG-style mineralization at the Moola prospect (McIntyre, 2001) (Fig. 1B). In addition to the Myola Volcanics and Broadview Schist, other units adjacent to Iron Count include the ~1755 Ma McGregor Volcanics and volcanoclastic sandstones of the Moonabie Formation (Fraser and Neumann, 2010) (Fig. 1B).

Diamond (CTC001-CTC004) and reverse circulation drilling completed by Arrium Mining at the Iron Count prospect show mixed intervals of metasedimentary rocks including sandstones, quartzites, clays, chlorite schists and BIFs, with gneisses and mafic dikes occurring intermittently, and granites intersected at depth (~78 m). Both dikes and granites are also found locally intruding BIF (Handley et al., 1997). Intervals of massive hematite and goethite ores, ≤6 m in thickness, were intersected throughout the drill holes. These have been described as 'bedded ores,' anomalous from the larger and more massive orebodies seen throughout the Middleback Ranges (Ward, 1949). Their interbedded occurrence with unmineralized sedimentary rocks prompted the hypothesis that mineralization at Iron Count is a product of metasomatic replacement along bedding planes (Ward, 1949). Hematite enrichment has also been observed within hematite and quartz-hematite breccia zones, hosted within BIF and associated with N—S striking faults (Fig. 2A) (Handley et al., 1997).

3. Analytical methodology

Preliminary mineral relationships and textural observations were made on one-inch blocks and 2.5 × 5 cm polished thin-sections prepared from each sample using reflected-light optical microscopy. Further micron-scale characterization was carried out via a FEI Quanta 450 scanning electron microscope (SEM) equipped with an energy dispersive X-ray spectrometer (EDS). Analytical conditions for SEM work in back-scattered electron (BSE) mode were 20 kV acceleration voltage and a beam current of 10 nA. All microanalytical techniques used are housed at Adelaide Microscopy, The University of Adelaide.

Whole-rock geochemical analyses were prepared from eight samples by Intertek Genalysis (Adelaide) and included three BIF samples, four ore samples and one quartz-hematite breccia. The methodology for whole-rock analysis and element minimum detection limits (MDL) are provided in Electronic Appendix A.

Trace element concentrations in iron-oxides were measured with a RESOlution excimer laser ablation system (Australian Scientific Instruments) coupled to an Agilent 7900× Quadrupole ICP-MS using a laser frequency of 5 Hz, fluence of 3.5 J/cm^2 and a spot diameter of 43 μm for martite and granoblastic hematite, and 29 μm for platy hematite and magnetite. LA-ICP-MS element maps were performed using a laser frequency of 10 Hz, fluence of 3 J/cm^2, a spot diameter of 7 μm and a scan speed of 7 μm/s. For quantification of the iron-oxides, ^{57}Fe was used as the internal standard element assuming ideal

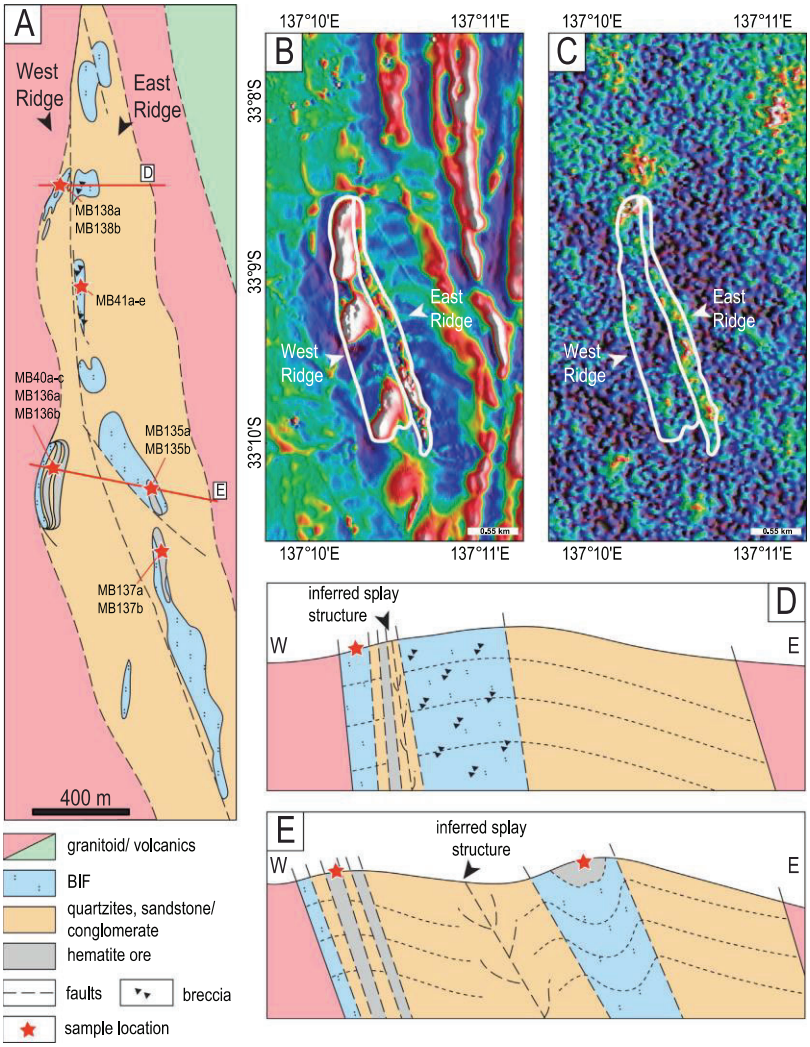

Fig. 2. (A) Simplified geological map showing the West and East ridges at Iron Count, modified after Handley et al. (1997). (B) Total magnetic intensity and (B) uranium radiometric maps of the two ridges. Maps are not to scale. Schematic cross-sections through the northern (D) and middle part (E) of the prospect. Structures are inferred.

stoichiometry. The external reference material used was the synthetic basalt glass standard GSD-1G (USGS; Guillong et al., 2005). Data reduction was performed using the software 'GLITTER' (van Achterbergh et al., 2001). During data reduction, only intervals displaying homogenous, flat signals were selected so as to avoid apparent mineral inclusions or peaks. Furthermore, each analysis was examined in time-resolved depth profiles to ensure negligible influence from included or adjacent minerals during analysis. Examples of such depth profiles are provided in Electronic Appendix A. Average minimum detection limits for the analyzed elements are also provided in the same appendix. LA-ICP-MS element maps were created using 'Iolite' software (Woodhead et al., 2008). See Electronic Appendix A for full details of all analytical methods and detection limits.

Grains of monazite and xenotime for U—Pb geochronology were first identified using BSE imaging. In-situ LA-ICP-MS analysis of the grains was performed using a laser frequency of 5 Hz and a spot diameter of 13 μm at a fluence of 2 J/cm^2. The MAdel monazite standard (TIMS normalization data: $^{207}Pb/^{206}Pb$ = 490.7 Ma, $^{206}Pb/^{238}U$ = 514.8 Ma, and $^{207}Pb/^{235}U$ = 510.4 Ma) was used for mass-bias and drift correction following the method of Payne et al. (2008). The accuracy of corrected ages was confirmed prior to and during analysis of unknowns by regular analyses of an in-house monazite standard (94-222/Bruna-NW), which has a weighted average $^{206}Pb/^{238}U$ age of ca. 450 Ma (Maidment, 2005).

Hematite grains considered suitable for U—Pb geochronology were first screened to ensure they contained sufficient concentrations of U

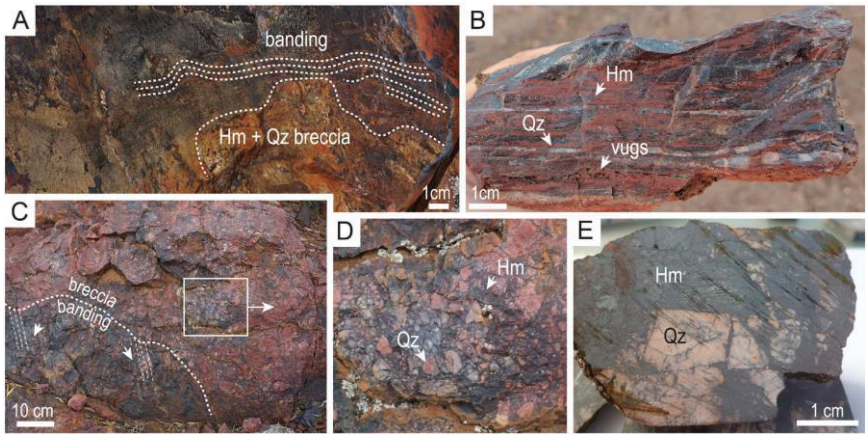

Fig. 3. Field and hand specimen photographs showing representative features of the lithologies from the West and East ridges. (A) Outcrop of BIF from West Ridge. Note banding with slight deformation as well as breccias. (B) Characteristic BIF from West Ridge showing alternating Fe- and Si-rich layers. (C) Outcrop showing brecciation features at East Ridge. (D) Enlarged portion of the boxed area in (C) showing details of quartz breccia cemented by Fe-oxides/hydroxides. (E) Pod of hematite in quartz-hematite breccia from the East Ridge. Hm: hematite; Qz: quartz.

and Pb during trace element acquisition. LA-ICP-MS analysis of the grains was performed with a laser frequency of 5 Hz, a spot diameter of 51 μm and a fluence of 4.5 J/cm^2. Correction of U—Pb fractionation for hematite was completed using the GJ-1 zircon at a fluence of 2.5 J/cm^2 (^{206}Pb/^{238}U age of ca. 600.7 Ma; Jackson et al., 2004) following the approach in Ciobanu et al. (2013).

4. Results

4.1. Prospect description

The present study investigates outcrops on the two N—S striking ridges (West and East Ridge) that constitute the Iron Count prospect (Fig. 2A), and which show strong amplitude on total magnetic intensity images (Fig. 2B). Radiometric images, however, show a stronger U-anomaly in the East Ridge, which is consistent along its strike relative to the spotty U-anomalies of the West Ridge (Fig. 2C). Schematic cross-sections across the northern and middle parts of the prospect show the two ridges as an east-dipping sedimentary package enclosed by granites (Fig. 2D, E). The ridges are separated by a basin that closes towards the north and is marked by brecciation in the East Ridge. The orebody exposed at the West Ridge occurs as a thin lens between BIF and metasedimentary rocks that extends ~1 km along strike, while the orebodies at the East Ridge occur within synclinal structures.

At the outcrop and hand specimen scale, the rocks/ores reflect varying degrees of reworking and/or overprinting of primary depositional fabrics (Fig. 3). The West Ridge is characterized by the presence of BIF banding textures (Fig. 3A, B), which are observed in both BIF and high-grade iron ores. Although banding is also present in outcrops at the East Ridge, it is much less obvious due to intense superimposed brecciation, resulting in brecciated ores and quartz-hematite breccias (Fig. 3C–E). In order to understand the differences between the West and East ridges, and the underlying reasons (e.g., different protoliths or overprints), samples were collected from outcrops at both ridges along a ~2 km strike (Fig. 2A). The samples include BIF, iron ores and quartz-hematite breccias (Table 1).

Table 1
Index of samples studied from Iron Count.

Location	Sample	Texture	Rock type	Iron-oxides					Sulfides	REE-minerals	Accessory minerals
				Mt	Mrt	pHm/Spc	mHm	Feh			
West Ridge	MB40a	banded	Mrt ore	x	X				Znc	Mnz, Xtm, Zrc	
	MB40b	massive	Mrt ore	x	X			x	Cpy	Mnz, Xtm	
	MB40c	banded	BIF	x	X	x		x		Mnz, Xtm, Zrc	
	MB136a	massive	Mrt ore	xx	X	x	x	x	Brt	Mnz	Zrc
	MB136b	massive	Mrt ore	xx	X	xx		x	Brt	Mnz	Zrc, Mg-rich needles included in Mt
	MB138a	massive	Mrt ore	x (Mt_1, Mt_2)	X		x	x		Mnz	Zrc
	MB138b	massive	Mrt ore	x (Mt_1, Mt_2)	X	x		x		Xtm, Mnz	Zrc, Thr
East Ridge	MB41a	brecciated	Hm-Qz breccia	x	X						
	MB41b	banded	BIF	x	X				Brt,		
	MB41c	banded	BIF	x	X	x			Cpy		
	MB41d	brecciated	Hm-Qz breccia	x	X	x					
	MB41e	brecciated	Hm-Qz breccia	x	X						
	MB135a	massive	Mrt-Goe-ore	x	X	xx		x	Brt		secondary Sn-, Cu-bearing phases
	MB135b	massive	Mrt-Goe-ore	x	X	x		X			Cls
	MB137a	massive	Mrt-Goe-ore	x	xx	x		X	Brt		
	MB137b	massive	Mrt-Goe-ore	x	xx	x		X	Brt, Cpy	Mnz	

Mineral abbreviations: Brt: barite; Cls: clausthalite; Cpy: chalcopyrite; Feh: iron-hydroxides; Goe: goethite; Hm: hematite; mHm: microcrystalline hematite; Mnz: monazite; Mrt: martite; Mt.: magnetite; pHm: platy hematite; Qz: quartz; Spc: specular hematite; Thr: thorite; Xtm: xenotime; Zrc: zircon.
X = main Fe-oxide phase; xx = major Fe-oxide component; x = relict or minor Fe-oxide phase.

4.2. Petrography

4.2.1. West ridge

The rhythmic banding preserved in the BIF from the West Ridge consists of alternating mm- to cm-scale Fe- and Si-rich layers. Hematite is the dominant iron-oxide within the Fe-rich layers. It typically occurs as martite (pseudomorphic replacement of magnetite by hematite) based on fine-grained inclusions of relict magnetite, although other hematite morphologies are present. These include (anhedral) microcrystalline, granoblastic, (micro)platy and specular hematite. The Si-rich layers consist of coarse granoblastic quartz, suggesting it recrystallized after chert. Fine-grained aggregates of iron-hydroxides are found throughout Fe-rich layers in minor proportions, typically replacing martite, or intergrown with kaolinite in Si-rich layers.

Rhythms of the Fe- and Si-rich bands within BIFs can fluctuate in terms of thickness, display different orientations, and are often crosscut by iron-oxide- or quartz-rich veins (Fig. 4A). Some bands consist of disseminated fine- to coarse-grained (several hundreds of μm), euhedral martite and interlocking quartz (Fig. 4B). Specular hematite is present in such bands. More massive Fe-rich bands consist of coarse martite, microcrystalline hematite and recrystallized quartz (Fig. 4C). Domains of brecciation consist of martite ± microcrystalline hematite and quartz (Fig. 4D). Rare earth element minerals (such as monazite and xenotime) and also zircon are preferentially concentrated within these brecciated domains (Fig. 4E).

Martite ores, although differing in their bulk $Fe_2O_3^{total}/SiO_2$ ratio, consist of similar minerals as the BIFs and also often display banding. The rhythmic banding however consists of alternating layers of coarser- and finer-grained hematite, each with its own characteristics in terms of size, morphology and inclusions (Fig. 5A, B). Coarser bands consist of euhedral to subhedral martite grains alternating with bands of granoblastic hematite (Fig. 5B). Micron- to nano-scale pores are characteristic of the martite, which are accompanied by iron-hydroxide replacement. Relict magnetite is typically preserved within such grains

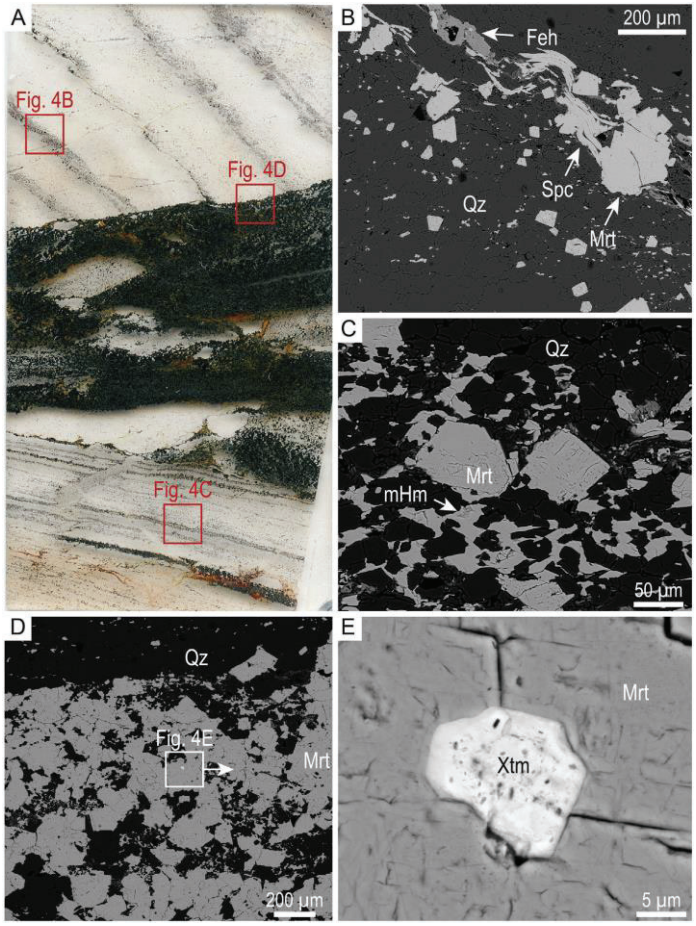

Fig. 4. Scanned image of a polished thin-section (A) from a BIF from the West Ridge and back-scattered electron (BSE) images of representative domains (B–E). Thin-section is 2.5 × 5 cm in size. (A) BIF banding with varying rhythms and orientations relative to a crosscutting iron-oxide-rich vein. (B) Bands and disseminations composed of martite (Mrt) and quartz (Qz) with specular hematite (Spc) and iron-hydroxides (Feh) interspersed. (C) Martite and anhedral microcrystalline hematite (mHm) comprising denser Fe-rich layers. (D) Dense aggregates of coarse martite in the crosscutting vein. (E) Xenotime (Xtm) included in martite within the crosscutting vein.

(Fig. 5C). In rare cases, magnetite contains fine-grained, Mg-rich inclusions (Fig. 5D).

Granoblastic hematite has a clean appearance, lacks inclusions and coexists with fine-grained euhedral magnetite (Fig. 5E). Granoblastic hematite also fills voids within the martite bands and shows replacement of martite oblique to the banding direction. In some cases, where seen recrystallizing martite, granoblastic hematite displays darker intensities on BSE images compared to martite as a result of higher Ti concentrations (see below; Fig. 5F). Significantly, granoblastic hematite displays no replacement by iron-hydroxides. Lastly, the martite ores also include a platy hematite, which range from fine-grained aggregates (microplaty) to coarser grains (up to 100 μm in length). Such large grains also display twinning (Fig. 5G), a feature not observed in other types of hematite textures.

Monazite or xenotime are ubiquitous to the martite ores from the West Ridge. They occur along fractures of porous martite grains, form boundaries between martite and platy hematite (Fig. 5H), and most frequently are intergrown with and occupy the interstices of granoblastic

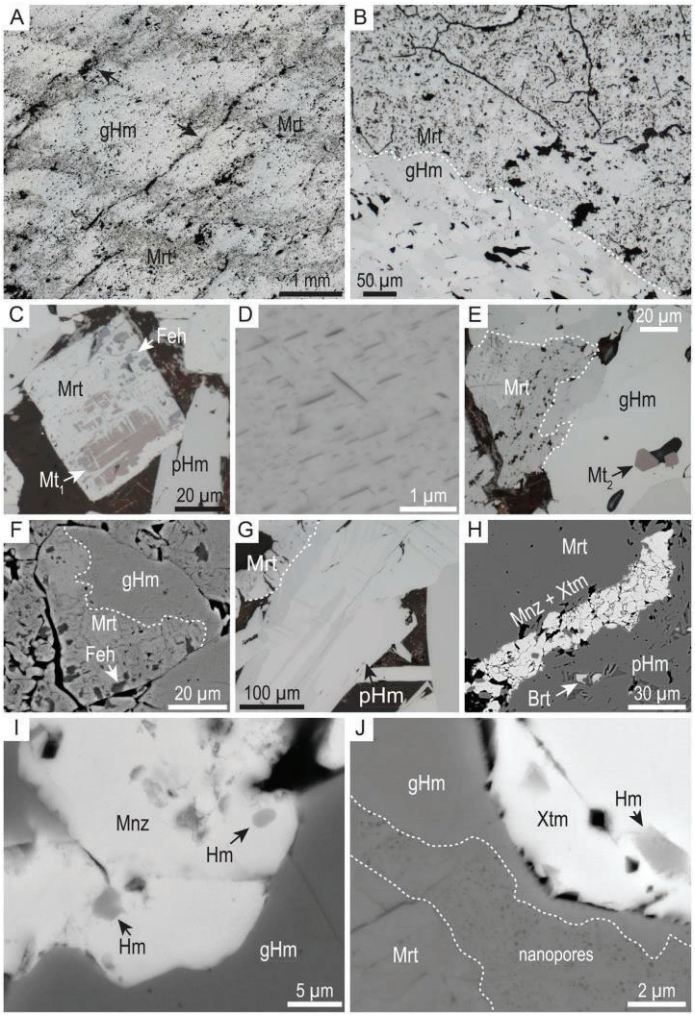

Fig. 5. Reflected-light optical images (A, B, C, E, G) and BSE images (D, F, H, I, J) showing iron-oxide features in martite ores from the West Ridge. (A) Alternating bands consisting of martite (Mrt)- and granoblastic hematite (gHm)-rich layers. (B) Boundary between martite- and granoblastic hematite-rich layers. (C) Euhedral martite with relict magnetite (Mt) inclusions and showing partial replacement by iron-hydroxides (Feh). (D) Needle-like, sub-μm sized inclusions of Mg-rich mineral with preferential crystallographic orientations in relict magnetite enclosed in martite. (*E*-F) Irregular contact between granoblastic hematite and porous martite suggesting boundary replacement of one another has locally taken place. In (E) note the euhedral magnetite (Mt_2) in apparent equilibrium with granoblastic hematite. In (F), martite is replaced by iron-hydroxides (Feh) which in turn are interpreted to be replaced by granoblastic hematite. Note the darker grey of gHm relatively to Mrt on the BSE image due to higher Ti content (thousands ppm). (G) Void-filling platy hematite (pHm) displaying twinning. (H) Fine-grained intergrowths of monazite (Mnz) and xenotime (Xtm) along the boundary between martite and (micro)platy hematite. Barite (Brt) inclusions are also present. (I) Monazite filling the interstices of granoblastic hematite. Note the sub-μm sized inclusions of hematite (Hm) in monazite. (J) Nanopores along the interface between granoblastic hematite and replacing martite. Note the field is adjacent to xenotime with sub-μm to μm-sized inclusions of hematite in xenotime.

hematite (Fig. 5I). Nanopores are a common feature along boundaries where granoblastic hematite replaces porous martite and are also associated with monazite and xenotime (Fig. 5J). When present, monazite or xenotime contain micron-sized inclusions of hematite. Other accessory phases common within the martite ores are zircon, thorite, barite, zincite and chalcopyrite.

4.2.2. East ridge

There is a continuum of variation between samples of BIF and their brecciated equivalents from the East Ridge (Figs. 3C–E and 6). Samples that display banding consist of similar alternating Fe- and Si-rich layers as observed at the West Ridge. Bands of disseminated or amalgamated martite grains characterize the Fe-rich layers, and recrystallized quartz composes the Si-rich layers. Breccias are represented by martite-rich clasts or angular quartz grains within a matrix of martite and iron-hydroxides (quartz-hematite breccias) (Fig. 3D, E).

The ore types found at the East Ridge are mainly martite-goethite ores, although the abundance of iron-hydroxides within them can vary significantly (Fig. 6A, B). In some cases, these minerals form a cement of quartz clasts with subangular to rounded morphology (Fig. 6B), clearly suggesting brecciation and chemical (re)precipitation. Martite-rich specimens consist of coarser martite as clasts within a matrix of fine-grained martite, platy hematite and iron-hydroxides (Fig. 6A). Martite can be variably altered to iron-hydroxides, whereas still preserving relict magnetite. Less altered grains feature only areas with abundant nanopores (Fig. 6C), and advanced iron-hydroxide replacement results in pseudo-skeletal appearance (Fig. 6D). Specular hematite can fill voids between martite grains (Fig. 6E).

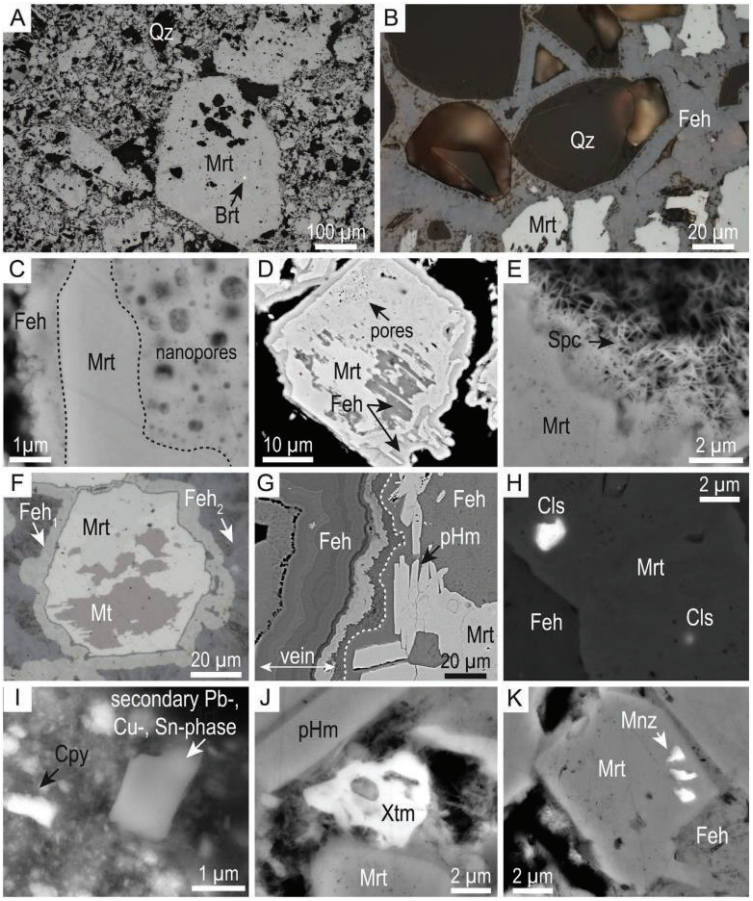

Fig. 6. Reflected-light optical images (A, B, F) and BSE images (C, D, E, G, H, I, J, K) showing iron-oxide features in martite-goethite ores from the East Ridge. (A) Ore breccia consisting of clasts of martite (Mrt) and a matrix composed of fine-grained martite, microplaty hematite, iron-hydroxides and quartz (Qz). Note barite (Brt) inclusions in the clasts. (B) Iron-hydroxides (Feh) cementing clasts of quartz and partially replaced martite. (C) Martite showing abundant nanopores and being replaced by iron-hydroxides. (D) Skeletal martite showing replacement by iron-hydroxides. Note presence of nanopores. (E) Specular hematite (Spc) filling voids between martite grains. (F) Relict magnetite (Mt) in martite. A thin film of pale-grey iron-hydroxides (Feh_1) is marginally replacing martite. The dominant, darker grey iron-hydroxide aggregates (Feh_2) form the ore matrix. (G) Microplaty hematite (pHm) forming along the margins of a vein containing colloform-textured iron-hydroxides. (H) Clausthalite (Cls) inclusions in martite. (I) Sulfides (chalcopyrite; Cpy) and secondary Pb-, Cu-, Sn-phases present as vug-filling in the ores. (J) Fine-grained xenotime (Xtm) at the boundary between (micro)platy hematite and martite typical of martite-goethite ore. (K) Micron-sized inclusions of monazite (Mnz) in martite.

In ores in which iron-hydroxides are more abundant, euhedral- to subhedral-grains of martite are cemented by fine-grained aggregates of iron-hydroxides. Martite contains relict magnetite and is rimmed by iron-hydroxides (Fig. 6F). Brecciated quartz and colloform iron-hydroxides infill veinlets (up to several 100-μm in width) that crosscut such ores, with platy hematite forming along the vein margins (Fig. 6G).

Characteristic of ore samples from the East Ridge is the presence of sulfides, including galena and chalcopyrite, as well as trace selenides such as clausthalite (PbSe) and secondary Pb-, Cu-, Sn-bearing phases (Fig. 6H, I). Barite is also an abundant phase in these samples. Other accessories that occur in minor amounts are xenotime and monazite (Fig. 6J, K). Both are finer-grained and lack the hematite inclusions of their analogues from the West Ridge.

4.3. Paragenetic sequence

The aforementioned observations provide a framework for a paragenetic sequence in which the various textures of iron-oxides from Iron Count are attributed to four distinct ore-forming stages. The proposed paragenetic sequence, with potential application to other locations throughout the MR, is summarized in Fig. 7.

The earliest observed iron-oxide phase in both the West and East ridges is magnetite (Stage 1). It always occurs as relicts within hematite, typically as dusty inclusions, but can also be coarser-grained (Figs. 5C and 6F). Preservation of magnetite relicts and a granular shape suggests hematite is a pseudomorphic replacement of earlier magnetite and is considered martite (Stage 2). In the West Ridge, martitization is accompanied by the formation of microcrystalline hematite and recrystallization of quartz. During Stage 3, iron-oxides become porous and together with quartz are replaced by iron-hydroxides and clays. Stage 4 is expressed differently in the two ridges. In the West Ridge, iron-oxides of this stage include interlocking grains of granoblastic hematite and fine-grained euhedral magnetite (Mt_2), which are interpreted as recrystallization products of earlier martite and iron-hydroxides. Platy hematite also recrystallizes earlier iron-oxides, but also fills voids and fractures. Accessory phases accompanying this stage are zircon and the REE-minerals monazite and xenotime (Fig. 5I, J). In the East Ridge, Stage 4 is expressed by veinlet-hosted colloform-textured iron-hydroxides, platy hematite and quartz breccias associated with veining.

4.4. Major and trace element whole-rock geochemistry

Banded iron formation and quartz-hematite breccia samples from the West and East ridges contain comparable major oxide concentrations and are characterized by high SiO_2 (53–64 wt%) and Fe_2O_3 (34–43 wt%) (Table 2). Minor- to trace-components are Al_2O_3 (0.04–1.04 wt%), MgO (0.02–0.05 wt%), CaO (0.03–0.08 wt%), P_2O_5 (0.07–0.23 wt%), TiO_2 (0.01–0.05 wt%), CO_2 (0.13–0.41 wt%) and LOI (0.11–1.90 wt%). MnO, K_2O and Na_2O are all <0.05 wt%.

Banded iron formations and quartz-hematite breccias contain a range of trace elements at mean concentrations exceeding 10 ppm (Table 2). These include Ba (29 ppm), Sr (10 ppm), Cr (29 ppm), Cu (10 ppm) and V (28 ppm). Elements measured at lesser concentrations are Zr (6 ppm) and W (4 ppm). Mean concentrations of As (19 ppm), Sb (19 ppm) and U (4 ppm) are higher in BIFs and quartz-hematite breccia from the East Ridge than in BIF from the West Ridge (8 ppm As, 2.6 ppm U, <mdl Sb). All other measured trace elements in the BIFs and quartz-hematite breccia are <5 ppm.

Total REY concentrations (ΣREY) in the BIFs and the quartz-hematite breccia range from 17 to 50 ppm (Table 2). Post-Archean Australian Shale (PAAS)-normalized REY fractionation trends for the West Ridge BIF show a signature very different from BIF (seawater), featuring light rare earth element (LREE; La—Gd) enrichment and heavy rare earth element (HREE; Tb—Lu) depletion. This is expressed as $La/Yb_{(SN)} = 1.5$, and slight positive Ce- and Eu-anomalies ($Ce/Ce^* = 1.2$; $Eu/Eu^* = 1.2$) (Fig. 8). The quartz-hematite breccia is similarly LREE-enriched/HREE-depleted ($La/Yb_{(SN)} = 7.0$), with negative Ce- and Y-anomalies and a positive Eu-anomaly ($Ce/Ce^* = 0.78$; $Eu/Eu^* = 1.3$). Contrastingly, the East Ridge BIFs are LREE-depleted/HREE-enriched ($La/Yb_{(SN)} = 0.4$–0.53), and except

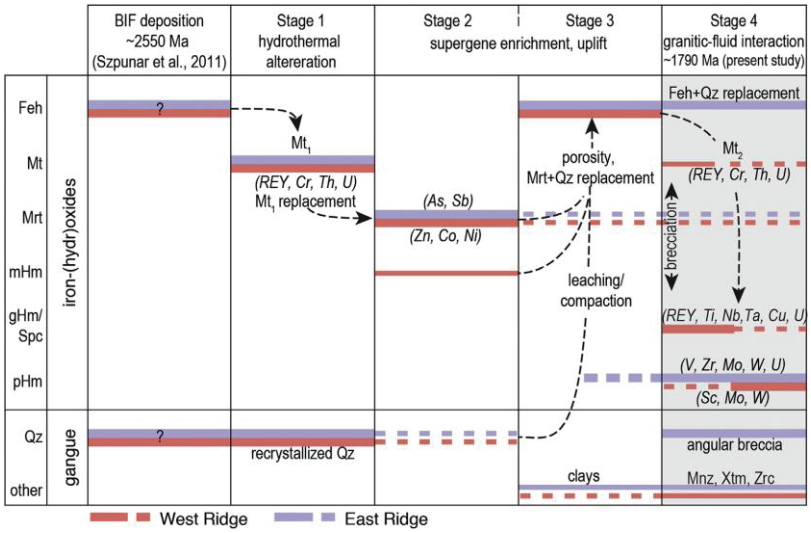

Fig. 7. Paragenetic sequence for iron-oxides and gangue minerals from the Iron Count prospect. Arrows with dashed lines indicate the suggested parent to successor iron-(hydr)oxide phase. Trace elements with increased concentrations in iron-oxide phases are written in italic letters. Shaded region represents the dated ore stage. See text for further details. Feh: iron-hydroxides; gHm: granoblastic hematite; mHm: microcrystalline hematite; Mnz: monazite; Mrt: martite; Mt.: magnetite; pHm: (micro)platy hematite; Qz: quartz; Spc: specular hematite; Xtm: xenotime; Zrc: zircon.

Table 2
Whole-rock geochemical data for studied BIF and ore samples.

Location	West Ridge			East Ridge				
Sample	MB40c	MB136	MB138	MB41A	MB41B	MB41C	MB135	MB137
Description	BIF	Martite ores		Qz–Hm breccia	BIF	BIF	Martite-goethite ores	
(wt%)								
SiO_2	59.58	7.32	2.37	64.48	60.97	53.18	3.98	1.22
TiO_2	0.05	0.06	0.13	0.01	0.01	0.04	0.03	0.14
Al_2O_3	0.57	1.06	1.49	0.04	0.60	1.04	2.42	1.00
Fe_2O_3	38.17	90.73	95.00	34.14	35.06	43.26	89.90	94.77
MnO	0.01	0.03	<mdl	0.01	0.03	0.01	0.05	0.04
MgO	0.05	0.10	0.02	0.02	0.03	0.03	0.07	0.03
CaO	0.03	0.10	0.08	0.03	0.08	0.04	0.07	0.06
Na_2O	0.01	<mdl	<mdl	0.01	0.01	0.01	0.01	<mdl
K_2O	0.02	<mdl	<mdl	0.01	0.01	0.01	0.01	<mdl
P_2O_5	0.07	0.07	0.18	0.09	0.23	0.14	0.21	0.18
CO_2	0.23	0.10	0.22	0.13	0.41	0.24	0.60	0.75
SO_3	0.02	<mdl	0.05	0.02	0.05	0.02	0.10	0.05
LOI	0.55	0.90	1.03	0.11	1.90	0.97	3.70	1.80
Total	99.37	100.46	100.58	99.11	99.40	99.01	101.15	100.04
(ppm)								
Li	0.50	1.1	1.4	0.90	2.7	0.80	0.90	0.70
Ba	24	82	38	56	18	30	43	71
Sr	14	18	11	13	12	5.5	9.7	16
Be	0.6	<mdl	<mdl	0.6	<0.5	0.60	<mdl	<mdl
Rb	2.0	0.20	0.90	<0.1	<0.1	0.90	1.2	0.40
Cs	<0.05	<mdl	<mdl	<0.05	<0.05	0.12	0.13	0.07
Cr	31	<mdl	<mdl	<20	28	<20	25	<mdl
Ni	3.0	9.0	10	1.0	<1	2.0	7.0	5.0
Co	0.40	2.7	2.4	0.70	0.70	2.2	16	3.0
Cu	11	8.0	2.0	7.0	21	7.0	69	68
Zn	<1	<mdl	4.0	2.0	3.0	<1	7.0	12
Cd	<0.05	<mdl	<mdl	<0.05	<0.05	<0.05	<mdl	<mdl
V	20	<mdl	<mdl	26	37	33	68	43
Nb	1.0	1.0	2.1	0.80	0.80	1.0	0.30	1.6
Ta	<0.1	0.20	0.50	<0.1	<0.1	<0.1	<mdl	0.20
Zr	8	16	55	<1	3.0	9.0	11	32
Hf	<0.1	0.5	1.6	<0.1	<0.1	<0.1	0.20	1.0
Sc	<2	4.0	3.0	<2	4.0	<2	22	7.0
Ga	1.9	2.5	2.5	0.20	0.40	2.2	0.90	6.3
Ge	0.20	1.1	2.0	0.30	0.20	0.30	1.6	1.5
In	<0.05	0.02	0.01	<0.05	<0.05	<0.05	0.17	0.08
Ag	0.30	<mdl	<mdl	0.10	0.40	<0.1	0.17	0.06
As	8.0	3.2	3.7	17	22	18	32	21
Sb	<0.5	2.5	4.4	15	17	27	7.3	83
Bi	0.15	0.1	0.11	0.15	0.20	0.47	0.51	3.0
Pb	<5	6.0	<mdl	<5	<5	<5	13	10
Te	1.3	<mdl	<mdl	0.40	0.20	0.30	<mdl	<mdl
Se	<1	<mdl	<mdl	<1	<1	<1	1.2	0.8
Tl	0.20	<mdl	<mdl	0.09	0.06	0.04	0.04	<mdl
Mo	<1	2.0	<mdl	<1	<1	1.0	3.0	3.0
Re	<0.05	<mdl	<mdl	<0.05	<0.05	<0.05	<mdl	<mdl
Sn	<1	<mdl	<mdl	<1	<1	<1	<mdl	<mdl
W	2.0	18	35	5.0	4.0	7.0	17	21
Th	0.60	2.8	19	<0.05	0.55	0.59	0.77	5.3
U	2.6	5.7	4.2	3.9	4.4	3.5	7.3	3.5
La	9.2	18	33	13	5.9	2.1	4.9	57
Ce	23	28	65	19	8.4	4.3	15	50
Pr	2.1	3.5	6.8	2.4	1.4	0.57	1.1	13
Nd	8.2	14	25	7.2	4.1	2	4.7	41
Sm	1.6	3.0	5.2	1.3	0.94	0.59	1.1	6.4
Eu	0.35	0.75	1.1	0.33	0.25	0.14	0.36	1.4
Gd	1.2	3.7	5.0	1.2	1.4	0.74	0.89	3.5
Tb	0.15	0.44	0.77	0.16	0.33	0.14	0.12	0.43
Dy	0.67	2.1	4.0	0.74	2.1	0.85	0.56	2.0
Y	3.1	8.4	17	2.4	10	4.3	2.3	6.7
Ho	0.11	0.35	0.66	0.11	0.46	0.19	0.09	0.28
Er	0.27	0.8	1.7	0.24	1.29	0.45	0.26	0.69
Tm	<0.05	0.09	0.2	<0.05	0.09	<0.05	<mdl	0.09
Yb	0.18	0.61	1.2	0.14	0.82	0.39	0.24	0.63
Lu	<0.02	0.07	0.15	<0.02	0.13	0.04	0.03	0.06
ΣREY	50	83	167	49	38	17	32	182
$(La/Yb)_{SN}$	3.8	2.2	2.0	7.1	0.53	0.40	1.5	6.7
$(Ce/Ce^*)_{SN}$	1.2	0.81	1.0	0.78	0.69	0.90	1.5	0.43
$(Eu/Eu^*)_{SN}$	1.2	1.1	1.0	1.3	1.0	1.0	1.8	1.4

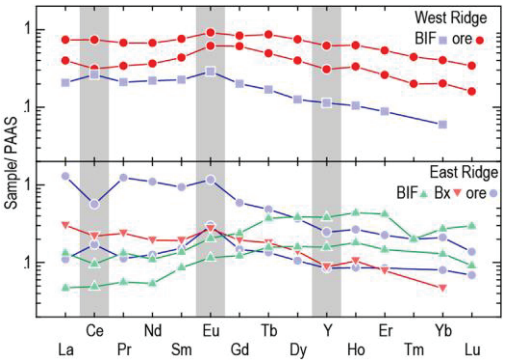

Fig. 8. Whole-rock PAAS-normalized REY fractionation trends of BIF, quartz-hematite breccia (Bx) and ore from the West and East ridges. PAAS values after Pourmand et al. (2012). See text for further explanations.

for a slight negative Ce-anomaly in sample MB41b ($Ce/Ce^* = 0.69$), display no other significant anomalies.

Martite ores from the West Ridge and *martite-goethite ores* from the East Ridge are enriched in Fe_2O_3 (~90–95 wt%) and depleted in SiO_2 (1.22–7.32 wt%) relative to the BIFs and quartz-hematite breccia (Table 2). Other major oxides such as Al_2O_3 (1–2.42 wt%), CaO (0.06–0.10 wt%) and MnO (0.03–0.05 wt%) are also relatively enriched in the two ore types compared to BIFs and quartz-hematite breccia, while P_2O_5 (0.07–0.21 wt%) is similar. Lower concentrations of MgO (0.02–0.10 wt%) and TiO_2 (0.03–0.14 wt%) are noted, while K_2O and Na_2O are both <0.02 wt%. Notable differences between the ore types are higher CO_2 (0.6–0.75 wt%) and LOI (1.8–3.7 wt%) in East Ridge martite-goethite ores compared to the West Ridge martite ores (0.1–0.22 wt% CO_2; 0.9–1.03 wt% LOI).

Martite and martite-goethite ores from both ridges contain similar mean concentrations of Ba (55 ppm), Sr (13 ppm), Zr (24 ppm), Pb (9 ppm), W (22 ppm) and U (5 ppm) (Table 2). There are, however, noticeable differences in the concentrations of some transition elements and metalloids between ores from the two ridges. East Ridge martite-goethite ores contain higher Cu (69 ppm), Zn (9.5 ppm), V (55 ppm), As (26 ppm) and Sb (45 ppm) compared to the West Ridge martite ores (5 ppm Cu, 4 ppm Zn; <mdl V, 3.4 ppm As, 3.5 ppm Sb). Nickel (7.5 ppm), Co (4.2 ppm) and Sc (6.5 ppm) are present at higher mean concentrations in all ore types with all other trace elements typically <5 ppm.

Absolute REY concentrations in ore samples from the two ridges range from 31 to 182 ppm (Table 2). PAAS-normalized REY fractionation trends for the various ore types are enriched in LREE relative to HREE ($La/Yb_{(SN)} = 1.5–6.7$) and feature weak to prominent positive Eu- anomalies and weak negative Y-anomalies (Fig. 8). REY fractionation trends for martite-goethite ores from the East Ridge do, however, show both strong negative ($Ce/Ce^* = 0.43$) and positive ($Ce/Ce^* = 1.5$) Ce-anomalies, whereas the Ce-anomalies from West Ridge ores are negligible or absent ($Ce/Ce^* = 0.81–1$).

4.5. Iron-oxide trace element geochemistry

4.5.1. Magnetite trace element geochemistry

Although magnetite was not studied extensively throughout the sample suite, compositional differences between two apparently different generations of magnetite (relict inclusions of magnetite in martite and euhedral magnetite co-crystallizing with granoblastic hematite from martite ores of the West Ridge) were assessed by LA-ICP-MS analysis. Magnetite of both textural types contains concentrations of a number of elements with overlapping ranges (Electronic Appendix B), including Al (91–1340 ppm), Ga (2–4 ppm), Nb (0.004–1 ppm), Ti (2–490 ppm), V (14–36 ppm), W (0.008–0.65 ppm), Sn (0.22–0.4), As (0.4–5 ppm), Ni (16–28 ppm) and Co (2–9 ppm). However, magnetite relicts within martite (Mt_1) contain markedly higher mean concentrations of Mg, Mn, Zn and Cu relative to magnetite co-existing with granoblastic hematite (Mt_2). In contrast, Mt_2 contains higher Cr, Th and U than Mt_1. Silicon (173–2890 ppm), P (8–220 ppm) and Ca (38–403 ppm) are also present in both types of magnetite.

4.5.2. Hematite trace element geochemistry

Box plots and LA-ICP-MS trace element maps presented in Figs. 9–12 are illustrative of the range of trace element concentrations in the various hematite textures. Trace elements shown in box plots are grouped into high field strength elements (HFSE; Ti, Nb, Sc, Zr and Ta) granitophile elements (Sn, Mo, W, U and Th), transition elements (Mn, V, Cr, Co and Ni) and chalcophile elements (As, Sb, Cu, Zn and Ga). Hematite trace element data is listed in Electronic Appendix C.

All hematite from the West Ridge contains comparable concentrations of several trace elements, including Mg (10–320 ppm), Al (250–1020 ppm), Si (440–1680 ppm), P (28–320 ppm), Ca (40–320 ppm), Mn (1–60 ppm), V (25–60 ppm), Cr (3–15 ppm), Th (0.5–6 ppm), and Zr (1–4 ppm) (Fig. 9). However, Zn, Ni and Co contents are more than twice as much in martite than in granoblastic or platy hematite (Fig. 9C, D). In contrast, granoblastic hematite is characterized by the highest concentrations of Ti (620–1040 ppm), as well as Ta, Cu and importantly U (6–8 ppm) if compared to martite and platy hematite (Fig. 9A-C). Concentrations of Sc, Mo and W are all higher in platy hematite than either martite or granoblastic hematite (Fig. 9A, B). Granoblastic and platy hematite are comparatively enriched in Nb, Sn, As and Sb relative to martite (Fig. 9A–C), whereas martite and platy hematite have higher Ga than granoblastic hematite (Fig. 9C).

The correlation between hematite textures and their most conspicuously enriched trace elements is highlighted in grain-scale LA-ICP-MS element maps (Fig. 10). Fig. 10A shows the relationship between martite and granoblastic hematite, where the latter displays relative enrichment in Ti, V, Nb, Mo, Pb and U in comparison with precursor martite, which is, in turn, enriched in Co and Ni. In Fig. 10B, platy hematite shows an inconsistent distribution of Sc, Ti, V, Nb and W at the grain-scale. A coupling among the HFSE can be recognized in domains enriched in Sc and Nb, whereas Ti shows decoupling from these elements. Titanium enrichment correlates strongly with domains of relative V depletion.

Elements at comparable concentrations in both martite and platy hematite from the East Ridge are Si (435–1490 ppm), P (13–83 ppm), Ca (25–75 ppm), Sc (0.2–0.5 ppm), Ti (4–25 ppm), Cr (0.35–1 ppm), Ni (1.3–10 ppm), Ga (0.3–0.7 ppm) and Sn (0.1–0.5 ppm) (Fig. 11). Martite is however enriched in several elements relative to platy hematite including Mn, Cu, Zn, Co, Nb and Ta. Arsenic (26–51 ppm) and Sb (9–19 ppm) measure particularly high in martite relative to iron-oxides from either ridge (Figs. 9C and 11C). Platy hematite on the other hand contains greater concentrations of V, Zr, Mo, W and U relative to martite (Fig. 11B, D).

4.6. Iron-oxide rare earth elements

Absolute concentrations of REY are higher in Mt_2 (mean 4 ppm) than in Mt_1 (mean 0.91 ppm) (Electronic Appendix B). When normalized to PAAS (Fig. 12A), all samples are LREE-depleted and HREE-enriched, reflecting interaction with post-depositional fluids. Coexisting magnetite textures within a single sample both show positive Ce-anomalies.

All hematite textures from the West Ridge are characterized by PAAS-normalized REY trends with LREE-depletion/HREE-enrichment and $La/Yb_{(SN)}$ values ranging from 0.1–0.64 (Fig. 12A). The hematite textures do, however, vary in terms of ΣREY (Electronic Appendix C). Granoblastic hematite contains the highest ΣREY (7–44 ppm), followed

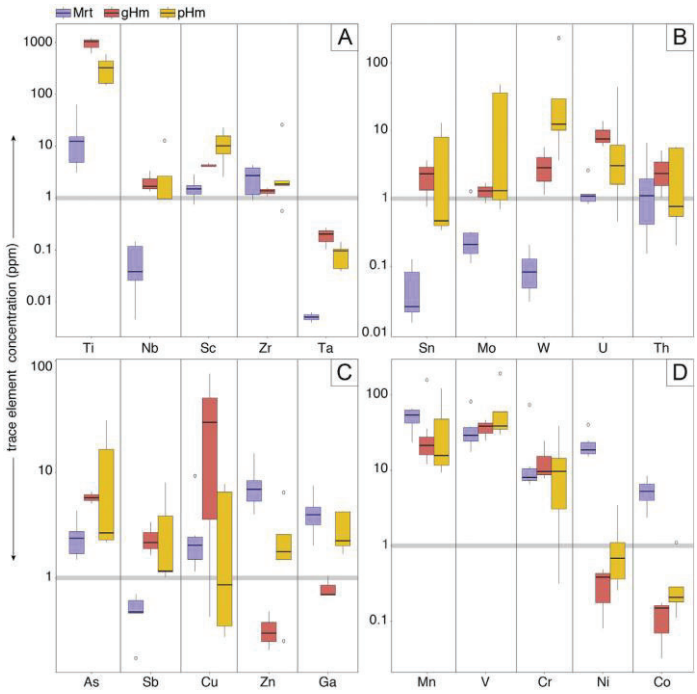

Fig. 9. Box plots showing trace elements concentrations in martite (Mrt), granoblastic hematite (gHm) and (micro)platy hematite (pHm) from the West Ridge. (A) Ti, Nb, Sc, Zr and Ta (high field strength elements). (B) Sn, Mo, W, U and Th (granitophile elements). (C) As, Sb, Cu, Zn and Ga (chalcophile elements). (D) Mn, V, Cr, Ni and Co (transitional elements). The data are plotted in logarithmic scale. The plots display the distribution of data based on minimum, first quartile, median, third quartile and maximum values. The rectangle represents the interquartile range (IQR), a spread between the first and third quartiles within which 50% of the data is placed. Outliers, marked as empty circles, are defined as 1.5 × IQR below or above the first or third quartiles, respectively.

by platy hematite (1–15 ppm) and then martite (1–6.3 ppm). Ce- and Eu-anomalies are generally only slightly positive for all three textures with a few exceptions ($Ce/Ce^* = 0.43$ in martite of sample MB138a); Y-anomalies are generally negative.

Martite from BIFs, quartz-hematite breccias and martite-goethite ores of the East Ridge contain ΣREY abundances ranging from 1.7–6.3 ppm and display similar REY fractionation trends characterized by LREE-depletion and HREE-enrichment ($La/Yb_{(SN)} = 0.24–0.7$) (Fig. 12B). Cerium-anomalies are minor, if present at all, and may be either positive or negative ($Ce/Ce^* = 0.84–1.1$). Eu-anomalies are positive and more pronounced ($Eu/Eu^* = 1–2.4$). Y-anomalies are also slight and are generally positive. Platy hematite in the martite-goethite ore is LREE-depleted/HREE-enriched with positive Eu-anomalies; Ce- and Y-anomalies may be either positive or negative.

5. U—Pb LA-ICP-MS geochronology: hematite and associated accessory minerals

Monazite and xenotime grains, abundant in the martite ores of the West Ridge as mentioned above, display irregular morphologies, inclusions of hematite and rarely show compositional zoning. Their sizes range from very fine-grained (<2 μm) to sufficiently large enough for in-situ U—Pb LA-ICP-MS analysis (>13 μm spot diameter) and in rare cases can exceed >100 μm in length. Monazite from a single BIF sample and monazite and xenotime from martite ore samples were analyzed. Results are summarized in Fig. 13 and presented in Electronic Appendix D.

Uranium-PbLA-ICP-MS dating was performed on large, coherent patches of relatively U-rich (5–17 ppm) granoblastic hematite from three martite ores of the West Ridge, two of which also contained analyzed monazite and xenotime (samples MB40b and MB136a). Martite (U = 2–6 ppm) from a martite goethite ore and microplaty hematite (7–24 ppm U) forming along the margins of a breccia-filled vein in another martite-goethite ore sample from the East Ridge were also suitable for hematite geochronology. The data are presented in Fig. 14 and Electronic Appendix E.

5.1. Monazite, xenotime and hematite

Sample MB40a contained the coarsest grains of monazite (up to >100 μm), from which twenty-seven spot analyses yielded an upper intercept date of 1793 ± 23 Ma ($^{207}Pb/^{206}Pb$ weighted average age; 1803 ± 16, $n = 27$, MSWD = 1.5) (Fig. 13A). Nineteen analyses from sample MB40b yielded an upper intercept date of 1782 ± 34 Ma ($^{207}Pb/^{206}Pb$ weighted average age; 1788 ± 16, $n = 19$, MSWD = 0.54; Fig. 13B). The fine grain size and abundant inclusions within monazite and xenotime aggregates along boundary of hematite grains (Fig. 5H) made analyses within sample MB136a difficult. However, xenotime analyses gave an upper intercept date of 1782 ± 22 Ma ($^{207}Pb/^{206}Pb$ weighted average age; 1786 ± 49, $n = 5$, MSWD = 3.2; Fig. 13C).

All hematite data reported are given as lower intercept dates anddisplayed with Terra-Wasserburg diagrams. The abundant granoblastic hematite from sample MB40b allowed for twenty-nine

points that yielded a date of 1790 ± 73 Ma (MSWD = 1.5) on a Tera-Wasserburg diagram (Fig. 14A). In sample MB136a (Fig. 14B), nineteen points gave a date of 1807 ± 21 Ma (MSWD = 2.1). Twenty points analyzed in sample MB136b were included in the Tera-Wasserburg diagram and produced a date of 1808 ± 29 Ma (MSWD = 2.2) (Fig. 14C).

In samples from the East Ridge, nineteen spot analyses of platy hematite forming along a quartz breccia- and iron-hydroxide-filled vein in a martite-goethite ore (sample MB135b) yielded a date of 1778 ± 230 Ma (MSWD = 28) (Fig. 14D). Twenty-five spot analyses from coarse-grained martite from sample MB137b yielded a date of 1804 ± 42 Ma (MSWD = 1.8) (Fig. 14E).

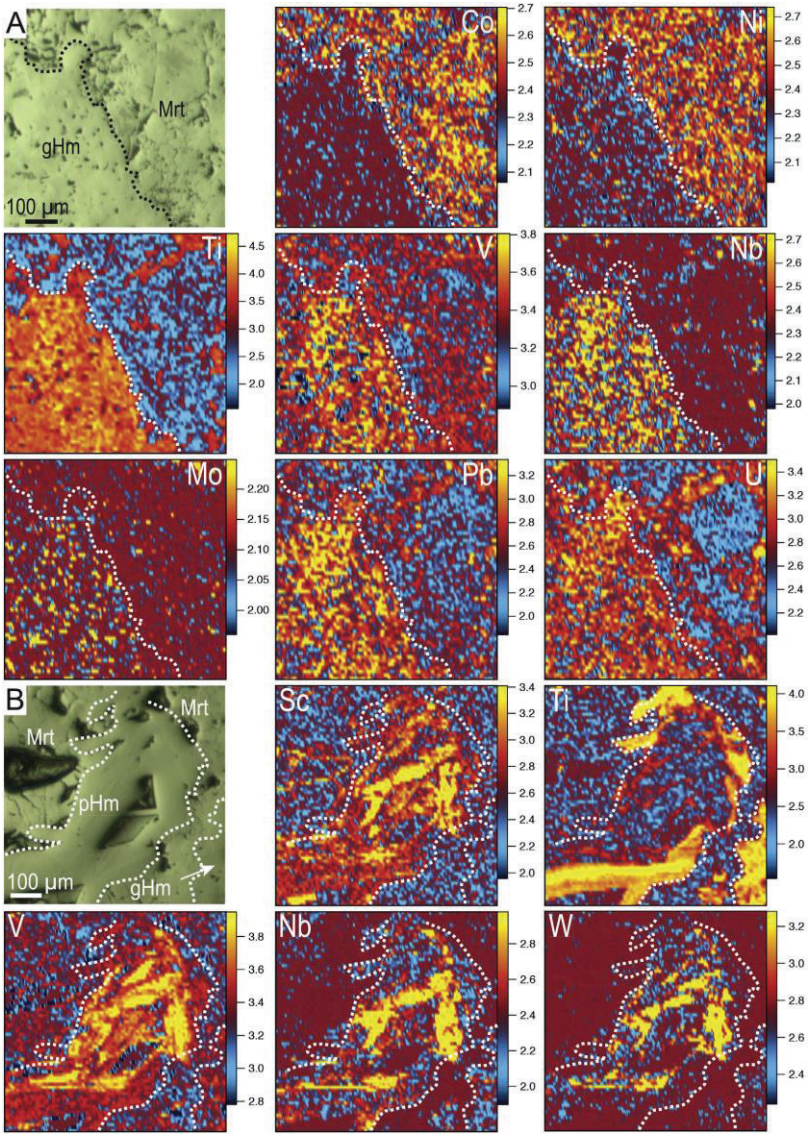

Fig. 10. LA-ICP-MS element maps. (A) Martite (Mrt) and granoblastic hematite (gHm) in martite ore (sample MB136a) from the West Ridge showing Co and Ni enrichment in martite and Ti-, V-, Nb-, Mo-, Pb- and U-enrichment in granoblastic hematite. (B) Microplaty hematite (pHm) filling a void between martite (Mrt) and granoblastic hematite (gHm) in a martite ore (sample MB136a) from the West Ridge showing Sc-, variable Ti-, V-, Nb- and W-enrichment. Mapped area shown on the reflected light photomicrograph at the top left. Scales in counts-per second.

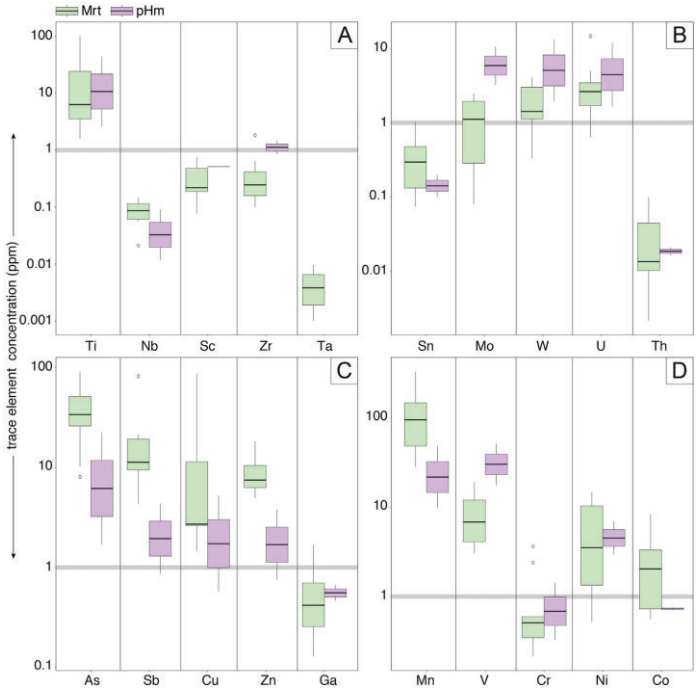

Fig. 11. Box plots showing trace element concentrations in martite (Mrt) and (micro)platy hematite (pHm) from the East Ridge. (A) Ti, Nb, Sc, Zr and Ta (high field strength elements). (B) Sn, Mo, W, U and Th (granitophile elements). (C) As, Sb, Cu, Zn and Ga (chalcophile elements). (D) Mn, V, Cr, Ni and Co (transitional elements). The data are plotted in logarithmic scale.

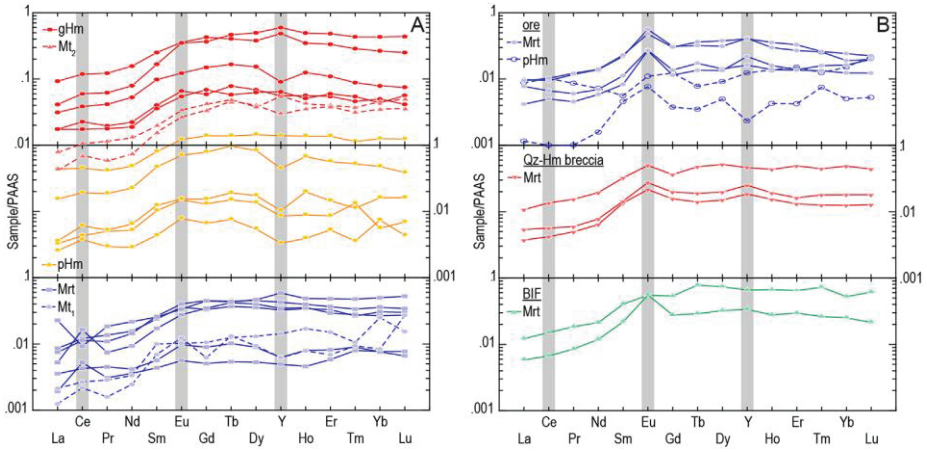

Fig. 12. PAAS-normalized REY fractionation diagrams for (A) magnetite, martite, granoblastic hematite and (micro)platy hematite from the West Ridge and (B) martite and microplaty hematite from BIF, quartz-hematite breccia and martite-goethite ores from the East Ridge. See text for further explanations.

5.2. Assessment of geochronological data

The ages obtained for monazite and xenotime were determined from upper-intercepts on conventional Wetherill concordia diagrams (Fig. 13; Electronic Appendix D), all of which were in good agreement with $^{207}Pb/^{206}Pb$ weighted average ages. This data is interpreted to represent the timing of initial crystallization. All dated hematite contains common-Pb and defines a line of discordia when plotted on Tera-

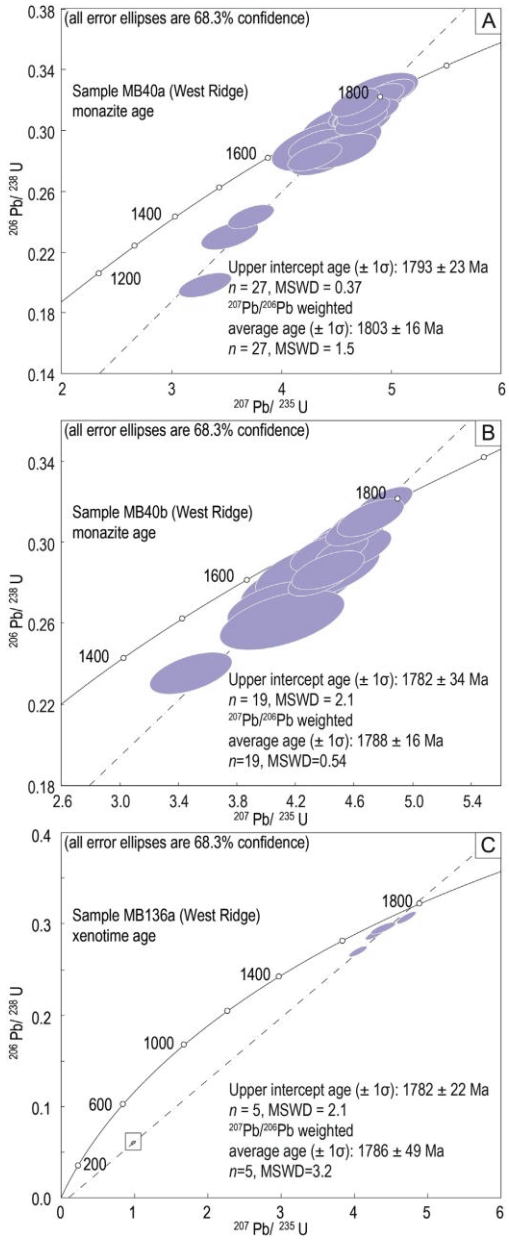

Fig. 13. Concordia diagrams for monazite (samples MB40a and MB40b) and xenotime (samples MB136a) from martite ores of the West Ridge. See text for further explanations.

Wasserburg diagrams (Fig. 14; Electronic Appendix E). However, the common-Pb component within each spot and sample varies, resulting in variable spread through discordia. Samples containing lower concentrations of common-Pb/higher radiogenic-Pb plot closer to the X-axis on Tera-Wasserburg diagrams (West Ridge samples; Fig. 14A–C), and samples containing highest concentrations of common-Pb/lower radiogenic-Pb plot closer to the Y-axis (East Ridge samples; Fig. 14D, E). Nevertheless, the data form a well-fitting regression line with low MSWDs determining lower-intercept dates on Tera-Wasserburg diagrams. The lower intercept of zircon analyses is generally represented by episodic Pb loss, however no evidence of Pb loss is seen in the hematite data. The mixing trend between common- and radiogenic-Pb therefore represents an initial source of common-Pb (~0.7 $^{207}Pb/^{206}Pb$) and the beginning of radiogenic-Pb accumulation at the lower intercept (crystallization age).

6. Discussion

Iron-oxides from BIF have been shown to display REY fractionation trends resembling those of Archean to Paleoproterozoic seawaters as a result of minor elemental fractionation during iron-oxide formation from primary BIF sediments (Bau and Dulski, 1996; Bekker et al., 2010; Keyser et al., 2018). Recognition of events impacting on the primary signatures can, however, be difficult. Primary geochemical signatures in iron-oxides can survive metamorphic overprints (up to amphibolite-facies; Gourcerol et al., 2016a), or can be inherited through iron-oxide conversions (Keyser et al., 2018), such that overprints are most apparent through physical changes (e.g., martitization). Nevertheless, any distortion of a primary signature or formation of successive iron-oxide phases (e.g., granoblastic or platy hematite) is useful in identifying fluid interaction and is generally expressed in iron-oxide trace element variation. Textures and geochemical compositions of iron-oxides from Iron Count record a sequence of overprints in the BIF-to-ore transformation. In the following sections, we discuss the possibility of different depositional settings for primary iron-rich sediments in the West and East Ridges, overprinting recognized from iron-oxide signatures in BIF, ore and breccia samples, and the temporal link between mineralization and local geological setting.

6.1. Assessing BIF depositional environment – West versus East Ridge

PAAS-normalizedREY fractionation trends of both sedimentary rocks and their constituent minerals (e.g., iron-oxides, apatite, carbonates) have been compared to seawater compositions to assess the validity of deposition in a marine environment (e.g., Bolhar and Van Kranendonk, 2007). Dissolved REY in anoxic (pre-Great Oxidation Event–GOE; ~2.45 Ga; Bekker et al., 2004) and modern (post-GOE) seawaters and precipitates thereof (e.g., BIF) display distinct characteristics, such as PAAS-normalized depletion of LREE relative to MREE and HREE and positive La- and Y-anomalies (Bolhar et al., 2004).

Following the above, whole-rock REY fractionation trends for the studied samples were assessed for resemblance to primary seawater signatures. In general, the samples from both ridges display LREE-enriched/HREE-depleted trends that contrast with those of seawater (Fig. 8), with the exception of two LREE-depleted/HREE-enriched BIF samples from the East Ridge. Samples may display one or another of the anomalies present in seawater trends, however are not convincing enough so as to determine a depositional environment.

The REY trends of iron-oxides were also evaluated for their similarity to seawater signatures. As the earliest iron-oxide, magnetite (Mt_1; Fig. 7) is most likely to display a primary signature. Although Mt_1 shows LREE-depletion/HREE-enrichment (Fig. 12A), it lacks positive Eu- and Y-anomalies, the former being characteristic of Archean seawaters as a result of enhanced hydrothermal input from seafloor vents (Michard and Albarède, 1986). Martite, which could potentially have inherited a primary signature, displays a similar REY trend as Mt_1 with stronger positive Ce-anomalies (Fig. 12A), yet again, lacks any significant Eu-anomaly, and in some cases, features a negative Y-anomaly, which may be attributable to preferential incorporation of Y into cogenetic alteration minerals such as apatite or monazite (e.g., Hensler et al., 2017).

Although magnetite from the East Ridge was not measured for trace element geochemistry, the analyzed martite from the various lithologies generally displays REY trends that are more akin to seawater signatures, i.e., LREE-depletion and pronounced positive Eu- and Y-anomalies (Fig. 12B). Furthermore, a lack of significant Ce-anomalies indicates precipitation from anoxic seawaters (German et al., 1991).

In summary, the whole-rock REY fractionation trends for the studied samples lack a strong resemblance to those of seawater; however, their trends may reflect post-depositional overprints resulting from evolving fluid–rock interaction, thus reflecting trace element contamination rather than primary signatures. This is shown by the LREE-enrichment in whole-rock REY fractionation trends, likely influenced by the presence of phosphate phases we have identified (e.g., monazite). Mineral REY fractionation trends of magnetite and martite from the West Ridge are also inconsistent with a seawater signature, further questioning a marine depositional environment. In contrast, despite being affected by numerous overprints, including amphibolite-facies metamorphism, martite from the East Ridge retain REY trends that more strongly resemble seawater signatures, and furthermore, suggest precipitation from anoxic, pre-GOE seawaters. Such a trend would be expected from a BIF deposited in a marine environment during the Archean (Szpunar et al., 2011).

One possible explanation for a difference in signatures between the two ridges could be loss of a seawater signature in the West Ridge during multiple overprints. The West Ridge does show a more complex sequence of mineralization than the East Ridge (Fig. 7). Alternatively, the two ridges may represent lateral variation in a marine depositional environment. This could explain not only the differing REY trends of iron-oxides from the two ridges, but also contrasting trace element signatures (e.g., strong As—Sb signature in the East Ridge vs. Ni—Co signature of the West Ridge, (Electronic Appendices B and C), as well as the presence of Mg-rich inclusions observed in Mt_1 from the West Ridge (Fig. 5D). Deposition in shallower, more oxidized waters and limited mixing with deep hydrothermal vent fluids could result in positive/negative Ce-anomalies and a less pronounced Eu-anomaly as observed in the iron-oxides of the West Ridge. The East Ridge may represent deposition in a deeper, less oxidized setting that was closer to hydrothermal source vents (e.g., Gourcerol et al., 2016b). In all likelihood, the variation in REY trends observed in iron-oxides from the East and West ridges results from some combination of the two scenarios.

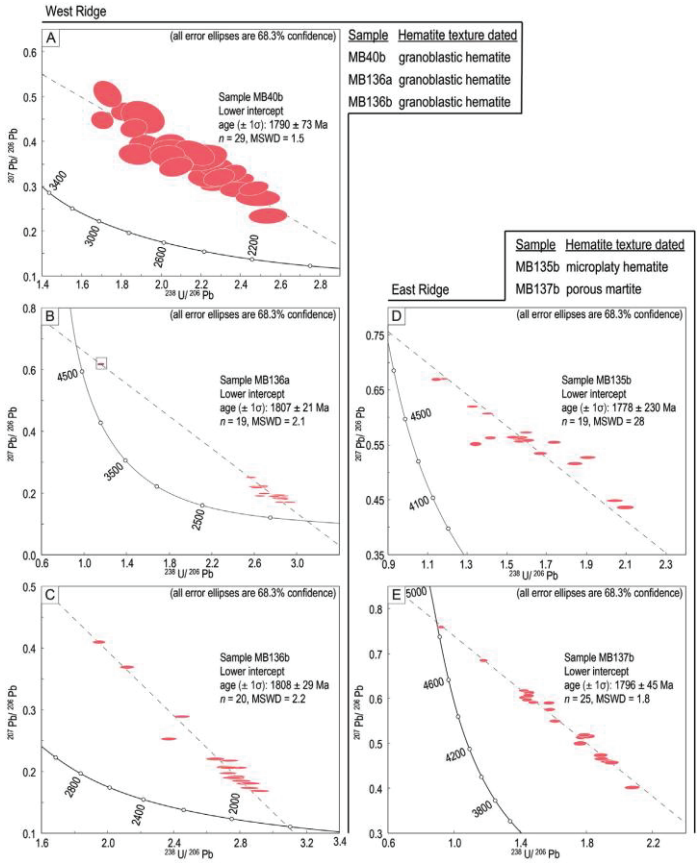

Fig. 14. Tera-Wasserburg diagrams for granoblastic hematite (samples MB40b, MB136a and MB136b) from the West Ridge and microplaty hematite (sample MB135b) and martite (sample MB135b) from martite-goethite ores of the East Ridge. See text for further explanations.

6.2. Overprinting events–iron-oxides record a protracted geological history

The various iron-oxide occurrences, morphologies, textures, mineral associations and trace element chemistry observed at Iron Count are indicative of distinct overprints that can be interpreted as evolution from BIF- to overprinting stages. These stages are, however, expressed differently within the West and East ridges. Understanding iron-oxides within each stage is important for characterizing fluid compositions facilitating mineralization, and thus constraining mechanisms of enrichment. Aside from the typical BIF upgrading history, the iron-oxides and associated accessories (monazite, xenotime) allow for understanding broader geological events such as granite emplacement.

The fact that the earliest iron oxide (Mt_1 from West Ridge; Fig. 7) occurs as relict, dusty inclusions in martite is concordant with earlier interpretations of its diagenetic origin in the MR (Yeates, 1990). The generic scheme for diagenetic processes considers dehydration and reduction of initial BIF sediments containing iron-oxyhydroxides to form hematite, followed by hydrothermal alteration to magnetite (Angerer et al., 2013). Martitization of diagenetic magnetite in the MR was suggested to have occurred during uplift and multiple erosion events (Yeates, 1990). Desilification and compaction are supposed to accompany this process, which generally requires oxidized and acidic fluids (Hagemann et al., 2016, and references therein). Such processes, typical of BIF to ore evolution elsewhere, are recorded in the spectrum of textures exemplifying BIF and ores in the West Ridge (Figs. 4 and 5). Moreover, the fluids involved in the martitization were elevated in Zn, Ni and Co, as inferred by the measured martite compositions (Electronic Appendix C). The presence of iron-hydroxides and their intimate relationships with iron-oxides at the scale of each polished block/section suggests replacement reactions took place subsequent to Stage 2 during an alteration event that likely, by analogy to other work, was supergene in nature and involved interaction with surficial fluids (Stage 3; Fig. 7).

However, in the West Ridge at Iron Count, following Stage 3 is another event recognized from recrystallization of martite and replacement of iron-hydroxides by granoblastic hematite containing newly-formed, fine-grained Mt_2 and with marked increase in Ti (Stage 4; Fig. 7). Comparable trends were reported for Ti-rich granoblastic hematite recrystallizing after martite in itabirite-derived ores from Quadrilátero Ferrífero, Brazil (Hensler et al., 2015). These authors inferred saline, F^--, Cl^--, SO^{2-}_4 and/or CO^-_3-bearing hydrothermal fluids such as basinal brines or magmatic fluids as possible contributors to Ti mobility. The associated granitophile signatures of granoblastic hematite at the West Ridge (Fig. 10A) suggest recrystallization of martite was driven by hydrothermal fluids that show evidence of interaction with a granite-sourced fluid (Dmitrijeva et al., 2018; Keyser et al., 2018). The irregular boundaries between granoblastic hematite and precursor martite (Fig. 5J) suggest that hydrothermal alteration leading to pseudomorphic replacement was facilitated by coupled dissolution (re)precipitation reaction at this stage.

If an anoxic environment is considered for the East Ridge based on iron-oxide REY trends, it is then also plausible that evaporites were also present. Interaction between such sediments and granitic fluids could produce the high-saline (NaCl, F-rich?) fluids necessary for Ti mobilization, as well as further silica removal in Stage 4 to form the rhythmically banded (granoblastic hematite and martite), representing the upgraded ores in the West Ridge. Such a hypothesis, although speculative, would also support lateral variation within a depositional environment as suggested from the REY signatures in iron-oxides (see above). Such a scenario can be related to magmatism resulting in emplacement of the Wertigo Granite and eruption of the Myola Volcanics adjacent to the Iron Count prospect. The presence of co-crystallizing Mt_2 suggests conditions were reducing during replacement of martite by granoblastic hematite. Increased concentrations of REY in both granoblastic hematite and Mt_2 as well as the formation of monazite and xenotime further indicate affiliation with granitic fluids (e.g., Drysdall et al., 1984). Platy hematite shows comparable enrichment of granitophile, HFSE, and chalcophile elements to granoblastic hematite, which may indicate fluid recycling towards the end of Stage 4.

The East Ridge is characterized by a simpler sequence of iron-oxide transformations compared to the West Ridge (Fig. 7). Whereas magnetite is similarly the earliest observed iron-oxide, martitization here is characterized by enrichments in Mn, Cu, Zn, Co, Nb and Ta, and most notably As and Sb (Fig. 11C; Electronic Appendix C). The decoupling in trace element signatures in iron-oxides between the two ridges suggests different fluid sources in Stage 2. Nonetheless, replacement of martite by iron-hydroxides during supergene enrichment is comparable in the two ridges. Moreover, platy hematite forming along the margins of crosscutting veins, filled by colloform-textured iron-hydroxides and quartz breccia, is also enriched in V, Zr as well as granitophile elements Mo, W and U (Fig. 10B), inferring that a granite-affiliated overprint is recognizable at both ridges.

Recognition of varying textural and compositional overprints in iron-oxides from the two ridges suggests localized tectonothermal settings played a role in iron-oxide formation. The two ridges likely represent lateral variation or different stratigraphic levels within a sedimentary succession that are separated by splayed faults (Fig. 2D, E). Such faults are inferred to be formed during deformation associated with earlier orogenies and metamorphism considering the differences in geochemical signatures as early as during Stage 2. In such a setting, small differences in uplift/burial histories and asynchronous interaction with fluids could be driving mechanisms of ore formation with varying mineralogical-geochemical expressions as reported here. This would imply fluids from multiple sources that penetrate along fracture faults, a scenario concordant with previously suggested characteristics of major deposits in the MR (Davies, 2000, and references therein).

6.3. Geochronological interpretation - implications for iron ore formation

The ages obtained for monazite found as coarse grains (1793 ± 23 Ma, sample MB40a) or intergrown with granoblastic hematite (1782 ± 34 Ma, sample MB40b) show a statistical overlap with one another, as well as with the age obtained for the granoblastic hematite in the same sample (1790 ± 73, sample MB40b). This clearly suggests co-crystallization between monazite and granoblastic hematite. A similar assumption can be made for xenotime (sample MB136a), dated at1782 ± 22 Ma, which is intergrown with granoblastic hematite dated at 1807 ± 21 Ma. This age is replicated by dating of granoblastic hematite from sample (MB136b), which yielded a date of 1808 ± 29 Ma.

Although samples from the East Ridge lack sizeable REE-minerals for dating, hematite within martite-goethite ores was found to contain sufficient U and radiogenic-Pb to yield geologically meaningful dates. Platy hematite forming along the margin of veins filled with colloform iron-hydroxides and quartz-breccia (sample MB135b) gave a date of 1778 ± 230 Ma. Although the error of this age is large, it does statistically overlap with the 1796 ± 45 Ma age derived from coarse-grained martite (sample MB137b) from the same East Ridge.

The difficulty in determining the timing of upgrading and modification of the BIF proto-ore in the MR, and undoubtedly in other BIF terranes worldwide, is due in part to an inability to acquire temporal information from the simple and often monomineralic composition of BIF-hosted iron ores. Additionally, the basinal environments that host BIFs typically lack rocks containing minerals amenable for accurate and precise geochronology. However, despite a scarcity of dateable minerals within the rocks, dating of various U-rich hematite types and co-crystallizing REE-minerals yielded ages for mineralization that are meaningful in the geological context of the MR. As shown here for Iron Count, fluids facilitating hematite mineralization in BIFs elsewhere are known to crystallize accessory phases suitable for geochronology, including monazite and xenotime (e.g., Rasmussen et al., 2016; Sheppard et al., 2017).

Importantly, recent advances in hematite dating techniques are validating its use as a reliable geochronometer in environments lacking

suitable grains of more conventional minerals for dating (e.g., zircon). Botryoidal BIF hematite was dated using (U—Th)/^{21}Ne-(U—Th)/He radiometry (Farley and McKeon, 2015). This is however a bulk technique and suitable only for coarse, relatively homogenous iron-oxide samples thus not applicable to samples with intrinsic micron-scale textural heterogeneity as shown here. U—Pb geochronology using microbeam techniques such as LA-ICP-MS was applied to U-bearing, oscillatory-zoned hematite in ore samples with comparable textural complexity from IOCG deposits in South Australia and elsewhere (Ciobanu et al., 2013; Courtney-Davies et al., 2016).

The age constraints provided here from hematite varieties in Stage 4 and associated REE-mineral geochronology indicates that main upgrading took place ~760 Ma years after BIF deposition at ~2550 Ma. Recognition of paragenetically older iron-(hydr)oxide generations (Fig. 7) suggests nonetheless ore formation in the MR was multi-staged. This observation is consistent with studies showing BIF-hosted mineralization as a prolonged process facilitated by extensive fluid-rock interaction likely associated with tectonism (Rasmussen et al., 2007, 2016; Sheppard et al., 2017). It is also in agreement with Parker et al. (1993) who suggested that the ores of the MR formed as a result of multiple cycles of supergene enrichment, likely commencing in the Paleoproterozoic and possibly extending to the Tertiary.

Mineralization throughout the MR is strongly associated with synclinal structures (Davies, 2000, and references therein) attributed to deformational events, recognized as D_1-D_4, formed during the Kimban Orogeny as defined by Parker and Lemon (1982), i.e., 1820–1580 Ma, where the age of D_2 is given as 1795–1745 Ma. Yeates (1990) attributed early recrystallization of diagenetic magnetite in the MR to regional metamorphism during the D_1 and D_2 phases.

Unlike at Iron Count where magnetite is a minor phase within hematite ores, magnetite and hematite form distinct orebodies found along folded and faulted structures that can be structurally tied to the D_2 deformation phase of Kimban Orogeny in the southern part of MR, e.g., the Iron Magnet orebody located down-dip the synclinal structure hosting the hematite orebody at Iron Duke (Leevers et al., 2005; Handley et al., 1997). Based on such structural relationships, Fietz (1989) proposed a lower-age limit for supergene enrichment at Iron Duke of 1795–1745 Ma (Kimban D_2 deformation of Parker and Lemon, 1982). Considering that the timing of the Kimban Orogeny was later re-evaluated such that the deformation phases D_1-D_2 are younger (~1730–1690 Ma; Hand et al. 2007), and if the structural interpretation remains valid, then the granoblastic hematite and associated REE-phases at Iron Count (Stage 4), dated here at ~1790 Ma, not only predates the formation of the supergene ore body at Iron Duke, but also suggests that magnetite recrystallization, supposedly formed during D_1, as well as its successor martite, must be older than ~1790 Ma.

More importantly, the ~1790 Ma date signifies an additional ore-forming event not previously recognized in the MR. The dates from the present study coincide with emplacement of the Wertigo Granite and eruption of the Myola Volcanics resulting from a period of major intracontinental rifting prior to the Kimban Orogeny, but before the ~1850 Ma Cornian Orogeny (Fig. 15). The dated iron-oxides display distinct granitophile signatures relative to earlier generations supporting mineralization driven by interaction between BIF and granite-derived fluids.

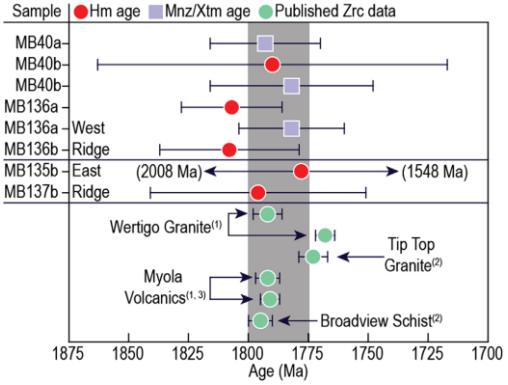

Fig. 15. Summary of U—Pb monazite, xenotime and hematite geochronological data reported here. Published ages for the Wertigo and Tip Top Granties, the Myola Volcanics and the Broadview Schist are from: (1) Fraser and Neumann (2010); (2) Jagodzinski and McAvaney (2016); and (3) Fanning et al. (1988), respectively. Hm: hematite; Mnz: monazite; Zrc: zircon; Xtm: xenotime.

7. Conclusions and implications

The present work serves as a case study to constrain the mechanisms responsible for mineralization within a single prospect of the MR. Prevailing textures and geochemical signatures of iron-oxides at Iron Count indicate conspicuous, discrete stages of mineralization resulting from interaction of pre-existing BIF with fluids of various compositions. Difference in the expression of stages between the two ridges is interpreted to represent lateral variation in depositional environment and superimposed overprints.

Despite experiencing apparently different sequences of ore-forming stages, as well as possibly representing lateral variations within a depositional environment, the West and East ridges share a common overprint, dated here at ~1790 Ma using a combination of hematite, monazite and xenotime U—Pb geochronology. This date is interpreted to represent the timing that fluids, associated with a granitic source, interacted with the ore-hosting rock. Such an interpretation is supported by granitophile signatures of the dated iron-oxides and coincident timing of the Wertigo Granite/Myola Volcanic emplacement proximal to the prospect during intracontinental rifting.

Results shown here validate the suggestion that variation in iron-oxide trace element signatures seen throughout the MR iron ore belt results from overprinting due to superimposed tectono-magmatic events that have locally affected each deposit (Dmitrijeva et al., 2018; Keyser et al., 2018). The approach undertaken here including in-situ dating of BIF-derived ores is generically applicable to other iron resources within the MR or terranes elsewhere. The study highlights the strength of LA-ICP-MS trace element analysis of individual texturally well-characterized minerals to recognize overprint stages in deposit evolution where whole-rock chemistry no longer reflects primary signatures. If studied at appropriate scales of observation and using complementary methods, the intrinsic complexity of the iron-oxides and -hydroxides provides unparalleled insights into the evolution from BIF deposition to ore formation in a given geological context.

Acknowledgements

This work is a contribution to the project 'Trace elements in iron-oxides: deportment, distribution and application in ore genesis, geochronology, exploration and mineral processing', supported by BHP Olympic Dam and the South Australian Government Mining and Petroleum Services Centre of Excellence. Logistical support from geologists at Arrium Mining, the former operator, is highly appreciated. Last but not least, we highly appreciate the insightful comments from two anonymous Lithos reviewers, and Editor Nelson Eby.

Appendix A. Supplementary data

Supplementary data to this article can be found online at https://doi.org/10.1016/j.lithos.2018.10.035.

References

Angerer, T., Hagemann, S.G., Danyushevsky, L.V., 2012. Geochemical evolution of the banded iron formation-hosted high-grade iron ore system in the Koolyanobbing greenstone belt, Western Australia. Econ. Geol. 107, 599–644.

Angerer, T., Hagemann, S.G., Danyushevsky, L., 2013. High-grade iron ore at Windarling, Yilgarn Craton: a product of syn-orogenic deformation, hypogene hydrothermal alteration and supergene modification in an Archean BIF-basalt lithostratigraphy. Miner. Dep. 49, 697–728.

Bau, M., Dulski, P., 1996. Distribution of yttrium and rare-earth elements in the Penge and Kuruman iron-formations, Transvaal Supergroup, South Africa. Precambr. Res. 79, 37–55.

Bekker, A., Holland, H.D., Wang, P.-L., Rumble III, D., Stein, H.J., Hannah, J.L., Coetzee, L.L., Beukes, N.J., 2004. Dating the rise of atmospheric oxygen. Nature 427, 117–120.

Bekker, A., Slack, J.F., Planavsky, N., Krapež, B., Hofmann, A., Konhauser, K.O., Rouxel, O., 2010. Iron Formation: the sedimentary product of a complex interplay among mantle, tectonic, oceanic and biospheric processes. Econ. Geol. 105, 467–508.

Bolhar, R., Van Kranendonk, M.J., 2007. A non-marine depositional setting for the northern Fortescue Group, Pilbara Craton, inferred from trace element s geochemistry of stromatolitic carbonates. Precambrian Res. 155, 229–250.

Bolhar, R., Kamber, B.S., Moorbath, S., Fedo, C.M., Whitehouse, M.J., 2004. Characterisation of early Archean chemical sediments by trace element signatures. Earth Planet. Sci. Lett. 222, 43–60.

Chung, D., Zhou, M.-F., Gao, J.F., Chen, W.T., 2015. In-situLA-ICP-MS trace elemental analyses of magnetite: the late Palaeoproterozoic Sokoman iron formation in the Labrador Trough, Canada. Ore Geol. Rev. 65, 917–928.

Ciobanu, C.L., Wade, B.P., Cook, N.J., Schmidt Mumm, A., Giles, D., 2013. Uranium-bearing hematite from the Olympic Dam Cu-U-Au deposit, South Australia: a geochemical tracer and reconnaissance Pb-Pb geochronometer. Precambrian Res. 238, 129–147.

Courtney-Davies, L., Zhu, Z., Ciobanu, C.L., Wade, B.P., Cook, N.J., Ehrig, K., Cabral, A.R., Kennedy, A., 2016. Matrix-matchediron-oxide laser ablation ICP-MS U-PB Geochronology using mixed solution standards. Fortschr. Mineral. 6, 85. https://doi.org/10.3390/min6030085.

Creaser, R.A., Fanning, C.M., 1993. A U-Pb zircon study of the Mesoproterozoic Charleston Granite, Gawler Craton South Australia. Austr. J. Earth Sci. 40, 519–526.

Davies, M.B., 2000. Iron ore in South Australia. Primary industries and resources SA. Commod. Rev. 8 (35 pp.).

Dmitrijeva, M., Metcalfe, A.V., Ciobanu, C.L., Cook, N.J., Frenzel, M., Keyser, W.M., Johnson, G., Ehrig, K., 2018. Discrimination and variance structure of trace element signatures in hematite: a case study of BIF-mineralization from the Middleback Ranges, South Australia. Math. Geosci. 50, 381–415.

Drysdall, A.R., Jackson, N.J., Ramsay, C.R., Douch, C.J., Hackett, D., 1984. Rare element mineralization related to Precambrian alkali granites in the Arabian Shield. Econ. Geol. 79, 1366–1377.

Fanning, C.M., Flint, R.B., Parker, A.J., Ludwig, K.R., Blissett, A.H., 1988. Refined proterozoic evolution of the Gawler Craton, South Australia, through U-Pb zircon geochronology. Precambr. Res. 40/41, 363–386.

Farley, K.A., McKeon, R., 2015. Radiometric dating and temperature history of banded iron formation–associated hematite, Gogebic iron range, Michigan, USA. Geology 43, 1083–1086.

Fietz, G., 1989. The Geological Structure and Slope Stability of the Iron Duke Iron Ore Deposit. South Australian Institute of Technology.

Fraser, G.L., Neumann, N.L., 2010. New SHRIMP U-Pb zircon ages from the Gawler Craton and Curnomona Province, South Australia, 2008-2010. Geosci. Austr. (2010/16), 256 pp..

Fraser, G., McAvaney, S., Neumann, N., Szpunar, M., Reid, A., 2010. Discovery of early Mesoarchean crust in the eastern Gawler Craton, South Australia. Precambr. Res. 179, 1–21.

German, C.R., Holliday, B.P., Elderfield, H., 1991. Redox cycling of rare earth elements in the suboxic zone of the Black Sea. Geochim. Cosmochim. Acta 55, 3553–3558.

Gourcerol, B., Kontak, D.J., Thurston, P.C., 2016a. Do magnetite layers in Algoma-type banded iron formations preserve their primary geochemical signature? A case study of samples from three Archean BIF-hosted gold deposits. Can. Mineral. 54, 605–624.

Gourcerol, B., Thurston, P.C., Kontak, D.J., Côté-Mantha, O., Biczok, J., 2016b. Depositional setting of Algoma-type banded iron formation. Precambrian Res. 281, 47–79.

Guillong, M., Hametner, K., Reusser, E., Wilson, S.A., Günther, D., 2005. Preliminary characteristics of new glass reference materials (GSA-1G, GSC-1G, GSD-1G and GSE-1G) by laser ablation-inductively coupled plasma-mass spectrometry using 193 nm, 213 nm and 266 nm wavelengths. Geostandards and Geoanalytical Research 29, 315–331.

Hagemann, S.G., Angerer, T., Duuring, P., Rosière, C.A., Figueiredo E Silva, R.C., Lobato, L., Hensler, A.S., Walde, D.H.G., 2016. BIF-hosted iron mineral system: a review. Ore Geol. Rev. 76, 317–359.

Hand, M., Reid, A., Jagodzinski, L., 2007. Tectonic framework and evolution of the Gawler Craton, southern Australia. Econ. Geol. 102, 1377–1395.

Handley, C., Pierini, M., Bubner, G., Harris, D., 1997. Annual Report Exploration License E.L. 2109 Middleback Ranges for the Period 5 October 1995 to December 1996, Version 1, Volume 1, Onesteel Whyalla Report GEO937 (unpublished).

Hensler, A.-S., Hagemann, S.G., Rosière, C.A., Angerer, A., Gilbert, S., 2015. Hydrothermal and metamorphic fluid-rock interaction associated with hypogene "hard" iron ore mineralisation in the Quadilátero Ferrífero Brazil: Implication from in-situ laser ablation ICP-MS iron oxide chemistry. Ore Geol. Rev. 69, 325–351.

Hensler, A.-S., Rosière, C.A., Hagemann, S.G., 2017. Iron oxide mineralization at the contact between phyllite and itabirite of the Pau Branco deposit, Quadilátero Ferrífero, Brazil– implications for fluid-rock interaction during ore formation. Econ. Geol. 112, 941–982.

Jackson, S.E., Pearson, N.J., Griffin, W.L., Belousova, E.A., 2004. The application of laser ablation inductively coupled plasma-mass spectrometry to in-situ U-Pb zircon geochronology. Chem. Geol. 211, 47–69.

Jagodzinski, E.A., McAvaney, S.O., 2016. SHRIMP U-Pb Geochronology Data for the Northern Eyre Peninsula, 2014–2016, Report Book 2016/00001. Department of State Development, South Australia, Adelaide.

Keyser, W.M., Ciobanu, C.L., Cook, N.J., Johnson, G., Feltus, F., Johnson, S., Dmitrijeva, M., Ehrig, K., Nguyen, P., 2018. Petrography and trace element signatures of iron-oxides in deposits from the Middleback Ranges, South Australia: from banded iron formation to ore. Ore Geol. Rev. 93, 337–360.

Leevers, P., Gaughan, C., Bubner, G., 2005. The Iron Magnet Deposit. Australasian Institute of Mining and Metallurgy Publication Series, Iron Ore Conference, Fremantle, WA. pp. 19–21 (September 2005).

Maidment, D., 2005. Palaeozoic High-grade Metamorphism within the Central Superbasin, Harts Range Region, Central Australia. PhD Thesis. Australian National University, Canberra (unpubl.).

McAvaney, S.O., Wade, C.E., Jagodzinski, E.A., 2016. Tip top and Wertigo Granites, c. 1775 Ma magmatism on northeastern Eyre Peninsula. MESA J. 80, 63–76.

McIntyre, J.I., 2001. Middleback ranges project – South Australia. EL2763 Annual Report. Helix Resources N.l. (unpublished).

Michard, A., Albarède, F., 1986. The REE content of some hydrothermal fluids. Chem. Geol. 55, 51–60.

Morris, R.C., 1980. A textural and mineralogical study of the relationship of iron ore to banded iron-formation in the Hamersley Iron Province of Western Australia. Econ. Geol. 75, 184–209.

Parker, A.J., 1980. The Kalinjala Mylonite Zone, eastern Eyre Peninsula. Q. Geol. Notes 76, 6–11 (Geological Survey of South Australia).

Parker, A.J., Lemon, N.M., 1982. Reconstruction of the early Proterozoic stratigraphy of the Gawler Craton, South Australia. J. Geol. Soc. Aust. 29, 221–238.

Parker, A.J., Daly, S.J., Flint, D.J., Flint, R.B., Preiss, W.V., Teale, G.S., 1993. Palaeoproterozoic. *In*: Drexel J.F., Preiss, W.V., Parker, A.J., eds. The Geology of South Australia; Volume 1, The Precambrian, pp. 50–105. Geological Survey of South Australia Bulletin 54.

Payne, J.L., Hand, M., Barovich, K.M., Wade, B.P., 2008. Temporal constraints on the timing of high-grade metamorphism in the Gawler Craton: implications for assembly of the Australian Proterozoic. Aust. J. Earth Sci. 55, 623–640.

Pourmand, A., Dauphas, N., Ireland, T.J., 2012. A novel extraction chromatography and MC-ICP-MS technique for rapid analysis of REE, Sc and Y: revising CI-chondrite and Post-Archean Australian Shal (PAAS) abundances. Chem. Geol. 291, 38–54.

Rasmussen, B., Fletcher, I.R., Muhling, J.R., Thorne, W.S., Broadbent, G.C., 2007. Prolonged history of episodic fluid flow in giant hematite ore bodies: evidence from in situ U–Pb geochronology of hydrothermal xenotime. Earth Planet. Sci. Lett. 258, 249–259.

Rasmussen, B., Zi, J.W., Sheppard, S., Krapež, B., Muhling, J.R., 2016. Multiple episodes of hematite mineralization indicated by U-Pb dating of iron-ore deposits, Marquette Range, Michigan, USA. Geology 44, 547–550.

Reid, A., Hand, M., Jagodzinski, E., Kelsey, D., Pearson, N., 2008. Paleoproterozoic orogenesis in the southeastern Gawler Craton, South Australia. Aust. J. Earth Sci. 55, 449–471.

Rosière, C.A., Siemes, H., Quade, H., Brokmeier, H.G., Jansen, E.M., 2001. Microstructures, textures and deformation mechanisms in hematite. J. Struct. Geol. 23, 1429–1440.

Sheppard, S., Krapež, B., Zi, J.W., Rasmussen, B., Fletcher, I.R., 2017. Young ores in old rocks: proterozoic iron mineralisation in Mesoarchean banded iron formation, northern Pilbara Craton, Australia. Ore Geol. Rev. 89, 40–69.

Szpunar, M., Hand, M., Barovich, K., Jagodzinski, E., Belousova, E., 2011. Isotopic and geochemical constraints on the Paleoproterozoic Hutchison Group, southern Australia: implications for Paleoproterozoic continental reconstructions. Precambrian Res. 187, 99–126.

van Achterbergh, E., Ryan, C.G., Jackson, S.E., Griffin, W.L., 2001. Data reduction software for LA-ICP-MS. In: Sylvester, P.J. (Ed.), Laser-ablation-ICPMS in the Earth Sciences: Principles and Applications. Vol. 29. Mineralogical Association of Canada, Short Course Series Ottawa, Ontario, Canada, pp. 239–243.

Vassallo, J.J., Wilson, C.J.L., 2001. Structural repetition of the Hutchison Group metasediments, Eyre Peninsula, South Australia. Aust. J. Earth Sci. 48, 331–345.

Vassallo, J.J., Wilson, C.J.L., 2002. Palaeoproterozoic regional-scale non-coaxial deformation: an example from eastern Eyre Peninsula, South Australia. J. Struct. Geol. 24, 1–24.

Ward, L.K., 1949. The genesis of the iron ores of the Middleback Range, South Australia. Proceedings of the Australian Institute of Mining and Metallurgy Monograph. 152–153, pp. 229–239.

Woodhead, J.D., Hellstrom, J., Paton, C., Hergt, J.M., Greig, A., Maas, R., 2008. A guide to depth profiling and imaging applications of LA-ICM-PS. In: Sylvester, P.J. (Ed.), Laser Ablation ICPMS in the Earth Sciences: Current Practices and Outstanding Issues. Vol. 40. Mineralogical Association of Canada, Short Course Series Vancouver, British Columbia, Canada, pp. 135–145.

Yeates, G., 1990. Middleback Range iron ore deposits. In: Hughes, F.E. (Ed.), Geology of the Mineral Deposits of Australia and Papua New Guinea. Vol. 14. Australian Institute of Mining and Metallurgy Monograph, pp. 1045–1048.

CHAPTER 4

PETROGRAPHIC AND GEOCHRONOLOGICAL CONSTRAINTS ON THE GRANITIC BASEMENT TO THE MIDDLEBACK RANGES, SOUTH AUSTRALIA

William Keyser[1], Cristiana L. Ciobanu[1], Nigel J. Cook[1], Liam Courtney-Davies[1], Allen Kennedy[2], Benjamin P. Wade[3], Kathy Ehrig[4], Marija Dmitrijeva[1], Alkiviadis Kontonikas-Charos[1], Holly Feltus[5], Geoff Johnson[5]

[1]*School of Chemical Engineering, The University of Adelaide, Adelaide, SA 5005, Australia*

[2]*John de Laeter Centre, Curtin University of Technology, Bentley, WA 6102, Australia*

[3] *Adelaide Microscopy, The University of Adelaide, Adelaide, SA 5005, Australia*

[4] *BHP Billiton Olympic Dam, Adelaide, SA, 5000, Australia*

[5]*SIMEC Mining, Level 2 169 Fullarton Road, Dulwich, SA 5005, Australia*

Article published in Precambrian Research 324 (2019), 170-193.

Statement of Authorship

Title of Paper	Petrographic and geochronological constraints on the granitic basement to the Middleback Ranges, South Australia
Publication Status	☑ Published ☐ Accepted for Publication ☐ Submitted for Publication ☐ Unpublished and Unsubmitted w ork w ritten in manuscript style
Publication Details	Keyser, W., Ciobanu, C.L., Cook, N.J., Courtney-Davies, L., Kennedy, A., Wade, B.P., Ehrig, K., Dmitrijeva, M., Kontonikas-Charos, A., Feltus, H., Johnson, G., 2019. Petrographic and geochronological constraints on the granitic basement to the Middleback Ranges, South Australia. Precambrian Research 324, 170-193.

Principal Author

Name of Principal Author (Candidate)	William Keyser		
Contribution to the Paper	Performed analytical work, carried out data processing and interpretation, oversaw development of work and wrote manuscript.		
Overall percentage (%)	65		
Certification:	This paper reports on original research I conducted during the period of my Higher Degree by Research candidature and is not subject to any obligations or contractual agreements with a third party that would constrain its inclusion in this thesis. I am the primary author of this paper.		
Signature		Date	4/6/2019

Co-Author Contributions

By signing the Statement of Authorship, each author certifies that:

i. the candidate's stated contribution to the publication is accurate (as detailed above);

ii. permission is granted for the candidate in include the publication in the thesis; and

iii. the sum of all co-author contributions is equal to 100% less the candidate's stated contribution.

Name of Co-Author	Cristiana L. Ciobanu		
Contribution to the Paper	Helped define direction of research, supervised development of work, assisted with data interpretation and contributed to manuscript preparation.		
Overall percentage (%)	10		
Signature		Date	4th Jun 2019

Name of Co-Author	Nigel J. Cook		
Contribution to the Paper	Helped define direction of research, supervised development of work, assisted with data interpretation and contributed to manuscript preparation.		
Overall percentage (%)	5		
Signature		Date	4/6/19

Name of Co-Author	Liam Courtney-Davies		
Contribution to the Paper	Assisted with data processing and interpretation, and evaluation of manuscript.		
Overall percentage (%)	5		
Signature		Date	30/4/2019

Name of Co-Author	Allen Kennedy		
Contribution to the Paper	Assisted with analytical instrumentation, data processing and evaluation of manuscript.		
Overall percentage (%)	5		
Signature		Date	

Name of Co-Author	Benjamin P. Wade		
Contribution to the Paper	Assisted with analytical instrumentation, data processing and evaluation of manuscript.		
Overall percentage (%)	2.5		
Signature		Date	

Name of Co-Author	Kathy Ehrig		
Contribution to the Paper	Helped define research direction and assisted with evaluation of manuscript.		
Overall percentage (%)	1.5		
Signature		Date	3/6/2019

Name of Co-Author	Marija Dmitrijeva		
Contribution to the Paper	Assisted with construction of figures and evaluation of manuscript.		
Overall percentage (%)	1.5		
Signature		Date	30/4/2019

Name of Co-Author	Alkiviadis Kontonikas-Charos		
Contribution to the Paper	Assisted with analytical work and manuscript evaluation.		
Overall percentage (%)	1.5		
Signature		Date	29/5/2019

Name of Co-Author	Holly Feltus		
Contribution to the Paper	Helped coordinate sample collection and evaluation of manuscript.		
Overall percentage (%)	1.5		
Signature		Date	30/4/2019

Name of Co-Author	Geoff Johnson		
Contribution to the Paper	Helped coordinate sample collection and evaluation of manuscript.		
Overall percentage (%)	1.5		
Signature		Date	30/5/2019

Precambrian Research 324 (2019) 170–193

Contents lists available at ScienceDirect

Precambrian Research

journal homepage: www.elsevier.com/locate/precamres

Petrographic and geochronological constraints on the granitic basement to the Middleback Ranges, South Australia

William Keyser[a,*], Cristiana L. Ciobanu[a], Nigel J. Cook[a], Liam Courtney-Davies[a], Allen Kennedy[b], Benjamin P. Wade[c], Kathy Ehrig[d], Marija Dmitrijeva[a], Alkiviadis Kontonikas-Charos[a], Holly Feltus[e], Geoff Johnson[e]

[a] School of Chemical Engineering, The University of Adelaide, Adelaide, SA 5005, Australia
[b] John de Laeter Centre, Curtin University of Technology, Bentley, WA 6102, Australia
[c] Adelaide Microscopy, The University of Adelaide, Adelaide, SA 5005, Australia
[d] BHP Olympic Dam, Adelaide, SA 5000, Australia
[e] SIMEC Mining, Level 2, 169 Fullarton Road, Dulwich, SA 5065, Australia

ARTICLE INFO

Keywords:
Middleback Ranges
Archean granites
SHRIMP U-Pb zircon geochronology
Banded iron formation

ABSTRACT

The Middleback Ranges is a 60 km-long BIF-endowed iron ore belt located in the southeastern Gawler Craton and is the largest exploited iron resource in South Australia. The belt is hosted within an Archean- to Paleoproterozoic-aged granitic-gneissic basement terrane. Petrographic and geochronological constraints are given for a suite of granites associated with deposits throughout the Middleback Ranges and compared with other regional granites. Granites from the Middleback Ranges show complex mineralogical and geochemical features indicating multiple overprinting events. Sensitive high-resolution ion microprobe U-Pb zircon ages from all granites across the Middleback Ranges yield Archean ages, suggesting the existence and a more extensive distribution of Mesoarchean crust than previously recognized beneath the entire Middleback Ranges BIF sequence. Grey and pink granites from the central Middleback Ranges (Sultan prospect) produced the oldest $^{207}Pb/^{206}Pb$ weighted mean ages within the sample suite (3241 ± 6 and 3238 ± 9 Ma, respectively). Zircon in the latter granite also features overgrowths dated at ~2.6 Ga and interpreted to be metamorphic. A second group of younger granites from the Iron Monarch deposit and a sample of Cooyerdoo Granite (northern Middleback Ranges) have a minimum crystallization age of 3165 ± 8 Ma and a $^{207}Pb/^{206}Pb$ weighted mean magmatic age of 3134 ± 18 Ma, respectively. The youngest granites analyzed here derive from the Iron Baron deposit in the central part of the belt, which display strong deformation and have a minimum crystallization age of 3089 ± 9 Ma, and from the Iron Magnet deposit in the southern part of the belt ($^{207}Pb/^{206}Pb$ weighted mean age of 3023 ± 33 Ma). Petrographic and geochemical features observed within the sample suite indicate that post-Archean overprinting events led to alteration of the granitic basement and may infer that fluid-rock interaction and granite leaching were important for BIF upgrading processes and iron-oxide formation.

1. Introduction

The Middleback Ranges (MR) is a 60 km-long metallogenetic belt hosting iron ores and located in the Eyre Peninsula, South Australia (Fig. 1). These ores are associated with banded iron formation (BIF) that were initially considered as Paleoproterozoic (~2.0 Ga; Parker et al., 1988) but more recently are recognized as Late Archean (~2.5 Ga; Szpunar et al., 2011). The depositional age of the BIF with lower stratigraphic position relative to the Cook Gap Schist is thus constrained as Neoarchean ("no older than c. 2570 Ma and is likely to have been deposited before 2450 Ma"; Szpunar et al., 2011). Uncertainties nevertheless still exist with respect to the regional correlation of Fe-rich lithologies relative to this horizon along the MR, and to the origin of the basement at the time of BIF deposition.

The MR belt is part of the southeastern Gawler Craton, which comprises magmatic rocks spanning the Archean (Cooyerdoo Granite; ~3.15 Ga, Fraser et al., 2010) to Mesoproterozoic (~1.6 Ga Gawler Range Volcanics and Charleston Granite; Fanning et al., 1988; Creaser and Fanning, 1993) and is crosscut by mafic dikes inferred to be of Gairdner age (~820 Ma; Wingate et al., 1998), but as yet unconfirmed

* Corresponding author.
E-mail address: william.keyser@adelaide.edu.au (W. Keyser).

https://doi.org/10.1016/j.precamres.2019.01.024
Received 26 October 2018; Received in revised form 30 January 2019; Accepted 30 January 2019
Available online 01 February 2019

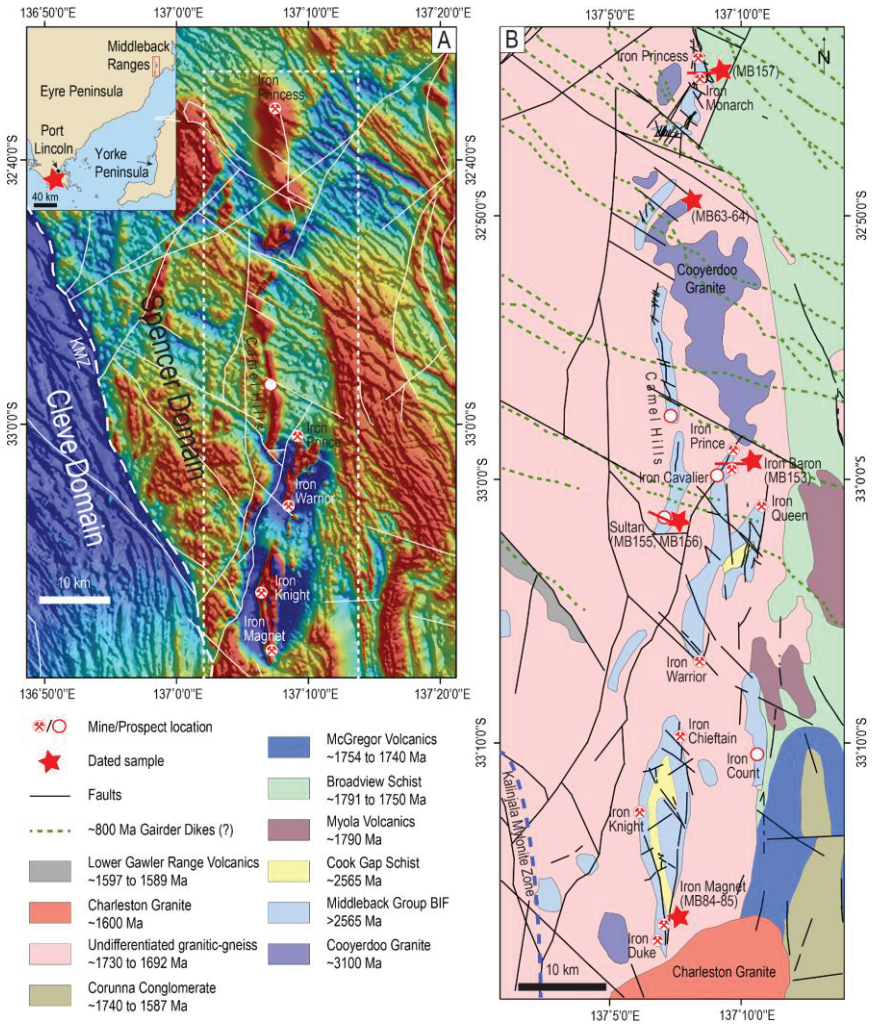

Fig. 1. (A) Total magnetic intensity image of the eastern Eyre Peninsula showing the location of the Middleback Ranges (MR) with respect to the Cleve and Spencer Domains and the Kalinjala Mylonite Zone (KMZ). Inset shows the location of the MR and Port Lincoln within the Eyre Peninsula. The red star represents the location of the Port Lincoln sample (PL8) used for geochronology. Fine dashed line represents area shown in Fig. 1B. (B) Simplified geological map of the MR and locations of iron ore deposits and prospects (sourced from http://map.sarig.sa.gov.au/). Red lines represent cross-sections shown in Fig. 2. Cooyerdoo Granite outcrop after McAvaney (2012). Legend refers to Fig. 1B. (For interpretation of the references to color in this figure legend, the reader is referred to the web version of this article.)

by dating of samples from the MR belt (Fig. 1B). The basement in the area comprises a wide range of igneous and metamorphic lithologies considered as undifferentiated gneissic-granitic rocks with a minimum age of 1.75–1.73 Ga (Fig. 1B).

The ~1.6 Ga granites are known as the Hiltaba Suite with regional expression throughout the Gawler Craton and are represented in the Eyre Peninsula by the Charleston Granite, which outcrops immediately south of the Iron Magnet deposit (Fig. 1B), and by the Samphire Pluton, further east of MR. Granitoids of the Samphire Pluton likely provided a source of uranium for the Blackbush uranium deposit (Domnick et al., 2018). Hydrothermal fluids associated with Hiltaba Suite granite emplacement led to formation of world-class iron-oxide-copper-gold (IOCG)-type deposits (e.g., Olympic Dam; Ehrig et al., 2012) in the Olympic Cu-Au Province (Skirrow et al., 2007) to the north and east of the MR. However, no significant IOCG-style mineralization has been recognized to date in the immediate vicinity of the iron ores.

Current hematite and magnetite reserves in the MR are 32.2 Mt and 56 Mt, respectively (at ~50–55% Fe; Arrium Mining, 2016) and represents the largest exploited iron resource in South Australia. > 20 deposits and prospects are hosted along the ~60 km N-S strike of the belt. The majority of these contain ores interpreted as supergene-enriched (Yeates, 1990; Davies, 2000), however hypogene-enriched ores

are known to exist in the southern part of the belt, e.g., at Iron Magnet, and interpreted to extend southward along strike (the Bungalow prospect; Jagodzinski et al., 2011). The open pits exploiting these deposits and adjacent exploration drilling provide a unique opportunity to sample associated basement rocks that are otherwise very poorly represented in surface outcrop.

Petrographic and trace element geochemical studies of iron-oxides from BIFs and ores throughout the MR have shown that base metal-bearing hydrothermal fluids and granite-affiliated fluids carrying Sn, Mo, W, U and REE + Y were key contributors to upgrading BIF to iron ore (Dmitrijeva et al., 2018; Keyser et al., 2018). One good example of such hydrothermal fluid-rock interaction is recognized at the Iron Count prospect located on the eastern margin of the belt (Keyser et al., 2019). Here, hematite mineralization is characterized by a geochemical signature and U-Pb ages indicating interaction between BIFs and fluids derived from adjacent granitic/volcanic rocks emplaced during a ~1.79 Ga intracontinental rifting event.

Exploration and mining have revealed granitoids of unknown age(s) throughout the belt where they appear spatially associated with the iron orebodies but with contact relationships that are not unequivocally interpretable due to superimposed alteration/overprinting or lack of extended outcrop. The present study therefore aims to provide a petrographic and geochronological foundation for these granitoids. This new information is also relevant for an improved understanding of the environments of BIF deposition. The approach used here in characterization of the granitoids serves two purposes. First, sensitive high-resolution ion microprobe (SHRIMP) U-Pb zircon dating of the granitoids is intended to provide age constraints for the timing of granite emplacement and for overprinting events that may potentially be interpretable from the data. Second, modifications made to the mineralogy and geochemistry of the granitoids record evolving fluid-rock interactions and give insight into overprinting processes that may have influenced upgrading of BIFs throughout the MR. Such information carries direct significance for regional basement correlations in the Gawler Craton. Indirectly, this assists with understanding ore-forming processes and can constrain exploration strategies in complex terranes with protracted geological history in this area and elsewhere.

2. Geological background

The Gawler Craton, which occupies a large part of South Australia, preserves a complex tectono-metamorphic/thermal history spanning the Mesoarchean to Mesoproterozoic (Reid and Hand, 2012). The oldest basement rock discovered in the Gawler Craton is the ~3.15 Ga Cooyerdoo Granite (Parker and Lemon, 1982; Daly et al., 1988; Fraser et al., 2010), which outcrops within an area of high total magnetic intensity known as the Spencer Domain, located in the northeastern Eyre Peninsula (Fig. 1A). Chemical and clastic metasedimentary rocks of the Hutchison Group, including the economically significant BIFs of the MR, comprise the northern Spencer Domain. The southern part of the domain consists predominately of mafic and felsic intrusive rocks affiliated to the Donington Suite, emplaced during a ~1.85 Ga compressional event termed the Cornian Orogeny (Reid et al., 2008a). In addition to the above, Neoarchean gneisses of the Sleaford Complex, deformed during the ~2.47–2.41 Ga Sleafordian Orogeny, form basement units within the Spencer Domain. An anomalous magnetic intensity signature and the presence of Mesoarchean crust beneath the Spencer Domain are the chief distinctions between it and the adjacent Cleve Domain to the west (Reid et al., 2008b).

Subsequent tectonic-magmatic activity has since contributed to the evolution of the Gawler Craton surrounding the MR. The rhyolitic Myola Volcanics and Broadview Schist overlying the main stratigraphic succession in this area are associated with a period of intracontinental rifting at ~1.79 Ga (Fanning et al., 1988; Fraser and Neumann, 2010; Jagodzinski and McAvaney, 2016). Intrusive rocks associated with this event include the ~1.79–1.77 Ga Wertigo and Tip Top Granites east of the MR (Fraser and Neumann, 2010; Jagodzinski and McAvaney, 2016; McAvaney et al., 2016). The subsequent (~1.73–1.69 Ga) Kimban Orogeny (Hand et al., 2007) was a regional transpressional event responsible for amphibolite-facies metamorphic overprinting of basement and development of numerous mylonite zones across the region. The most significant of these is the N-S trending Kalinjala Mylonite Zone (KMZ) that marks the boundary between the Cleve and Spencer Domains (Parker, 1980; Fig. 1). Granitic bodies that surround the MR and are associated with this event include those of the Moody Suite (Schwarz, 1999) and the Burkitt Granite (1742 ± 42 Ma; 1755 ± 19 Ma; Fraser and Neumann, 2010; Fraser et al., 2010). Younger magmatism is recorded in the emplacement of the ~1.6 Ga Hiltaba Suite-equivalent Charleston Granite (Creaser and Fanning, 1993) that occurs immediately south of the MR and forms the bedrock over a 300 km^2 area in the eastern Eyre Peninsula. Abundant, still younger NW-SE trending mafic dikes are observed throughout the belt.

The MR are part of the Middleback Group succession (Fig. 1B), which is isotopically and geochemically distinct from other sedimentary units of the Hutchison Group that lie west of the KMZ in the Cleve Domain (Szpunar et al., 2011). The stratigraphy of the Middleback Group grades upwards from a lower quartzite unit (Warrow Quartzite) into the Katunga Dolomite followed by two iron-bearing units (the Lower and Upper Middleback Iron Formations) separated by the Cook Gap Schist. It has been suggested, however, that the Upper Middleback Iron Formation is a structural repetition of the lower unit via thrusting and folding during regional deformation associated with the Kimban Orogeny (Vassallo and Wilson, 2001). The BIFs of the MR have a minimum deposition age of ~2.56 Ga based on the constraints made on the Cook Gap Schist (Szpunar et al., 2011).

Iron ore deposits of the MR are hosted primarily within the lower iron-bearing unit. Further details of relationships between rock types, structures, and orebodies within individual deposits of the MR are given by Davies (2000), Leevers et al. (2005), and Keyser et al. (2018, 2019).

3. Methodology

Whole rock assays were performed on twenty samples by Intertek Genalysis (Adelaide). These include one sample of Charleston Granite, eight samples from Cape Donington (Donington Suite), two samples of Cooyerdoo Granite, and nine samples taken from outcrops exposed by iron ore mining along the MR belt. Methodology for whole-rock analysis and element minimum detection limits (MDL) is provided in Electronic Appendix A.

Petrographic observations were made on 2.5 × 5 cm polished thin-sections and 2.5 cm polished blocks prepared from twenty-four samples using an optical microscope and a FEI Quanta 450 scanning electron microscope (SEM) with an energy-dispersive X-ray spectrometer (Adelaide Microscopy); analytical conditions were 20 kV acceleration voltage and 10nA beam current.

Quantitative analysis of clinozoisite and pargasite was performed using a Cameca SXFive Electron Microprobe (Adelaide Microscopy) running 'PeakSite' software and equipped with five wavelength-dispersive X-Ray detectors; analytical conditions were 15 kV accelerating voltage and 20nA beam current using a defocused 2 µm beam. Calibration and data reduction were carried out using 'Probe for EPMA' software. Elements analyzed, average MDL, peak/background positions, count times, and standards are listed in Table A2.

Zircon grains used for geochronology were separated and mounted by Geotrack (Melbourne) following conventional separation techniques. Samples were first put through a jaw crusher and disc pulverizer followed by separation methods using a Wilfley table, Franz isodynamic separators and heavy liquid mineral separation. Grains were hand-picked and mounted on 2.5 cm epoxy disks with the zircon standards M257 (561.3 ± 0.3 Ma; Nasdala et al., 2008) and OG1 (3465.4 ± 0.6 Ma; Stern et al., 2009). The mounts were imaged in transmitted light to assess fractures and coloration. A FEI Quanta 600

MLA SEM equipped with a tungsten filament electron source (Adelaide Microscopy, The University of Adelaide) was used for cathodoluminescence (CL) imaging to characterize core-rim relationships and zoning patterns within zircon grains. Zircon grains were dated using the SHRIMP-II at the John de Laeter Centre (Curtin University, Western Australia).

Ion microprobe analytical methods broadly follow those described by Compston et al. (1984) and Williams (1998). Analyses on the SHRIMP II were performed on the 12–23 of October 2017. All isotopic measurements were reduced by off-line computer programs using standard techniques (SQUID2; Ludwig, 2009). Decay constants used are those recommended by IUGS and ^{235}U was calculated using the decay constant of Steiger and Jäger (1977).

During zircon analysis, a 20–30 μm-diameter spot was selected, with a mass-filtered O_2^- primary beam of 2–3nA. Data for each spot are collected in sets of 6 or 7 scans on the $^{196}Zr_2O^+$, $^{204}Pb^+$, background, $^{206}Pb^+$, $^{207}Pb^+$, $^{208}Pb^+$, $^{238}U^+$, $^{248}ThO^+$, and $^{254}UO^+$ mass positions. Concentrations of U, Th and Pb are calculated by referencing the unknowns count rates for the above peaks to the count rates of the standard with known U, Th and Pb abundances (Compston et al., 1984; Claoué-Long et al., 1995; Williams, 1998).

Uncertainties cited for individual analysis include those due to counting statistics, the common Pb correction, and the U-Pb calibration uncertainties based on reproducibility of U-Pb measurements of the standard and are at the 1 sigma level. Error ellipses shown in the figures are 1 sigma uncertainties. Common Pb was corrected for using the ^{204}Pb method rather than ^{208}Pb method due to the relatively high concentrations of Th (Williams, 1998).

4. Results

4.1. Sample Suite

The sample suite comprises granites and muscovite schists collected from drillcore and open pits throughout the northern, central and southern parts of the MR (Table 1). Cross-sections of selected deposits (Fig. 2) illustrate relationships between the sampled granites and schists with the orebodies throughout the belt. These show distinct spatial relationships between granites and orebodies. For example, the granitic body at Iron Monarch (Fig. 2A) occurs ~100 m below surface. Here, BIF and schists overly the granite, and two shallow orebodies flank the granite on its eastern and western margins. At the Sultan prospect (Fig. 2B), a package of BIF and overlying sediments including supergene-enriched ores, schists, clays and bodies of mafic rocks (dolerite and amphibolite), forms a wedge that pinches out towards the eastern margin of the pit and thickens as it dips westward. Along the western margin, the package is faulted, roughly vertically, against the sampled granitic body. The stratigraphy at Iron Baron (Fig. 2C) grades upwards from a basal quartz-sericite schist unit into BIF with the hematite orebody on top. Granites are intersected at depth along the western and eastern margins.

The studied samples vary in color, grain size, and degree of deformation and alteration. None can be considered “fresh”, but some maintain phaneritic textures characteristic of granites, notably those samples from Iron Monarch and the Sultan prospect (Fig. 3A-C). Although the samples from Sultan were taken ~6 m apart, one has a greyish color while the other is pink (Fig. 3B, C). Alteration is evident in other samples that display deformation fabrics, such as the shearing seen in granites from Iron Magnet (Fig. 3D and 4A), or reddish staining (sample MB153; Fig. 3E). The muscovite schists are included due to their association with the orebodies and possible derivation from a granitoid protolith. These include a pale green sample from Iron Baron (Fig. A1) and a muscovite schist from the sheared west wall of the Iron Knight open pit (Fig. 4B).

Three types of granitoids were included in this study:

(1) A grab sample of coarse-grained Charleston Granite from immediately east of the Iron Magnet deposit (Fig. 3F).
(2) Granitoids from beach outcrops at Cape Donington, the southernmost point on the Eyre Peninsula, near Port Lincoln (PL; see also Kontonikas-Charos et al., 2018a), attributed to the *syn*-orogenic Donington Suite, but not previously dated. Samples investigated here include coarse-grained granites displaying deformation (Fig. 3G, H), with leucocratic and melanocratic differentiates (Fig. 4C), foliated leucogranites which are interpreted as representing marginal facies of the magmatic suite (Fig. 4D), rocks displaying migmatitic textures, and a pegmatite (Fig. 4E).
(3) Samples of medium-grained granites representative of the ~3.1 Ga Cooyerdoo Granite collected south of Iron Monarch (Fig. 3I).

4.2. Petrography

The granitoids studied here, those of the MR and the Cooyerdoo Granite, consist primarily of medium-grained (mm-size) alkali feldspars and quartz. Magmatic plagioclase (oligoclase) and biotite are rarely preserved. All samples display various degrees of alteration, not only affecting feldspars and biotite but also magmatic accessories such as zircon, apatite and Fe-Ti-oxides.

Common to all the above granitoids is alteration of primary feldspars, which can be expressed either by reworking of feldspars either by (syn-)metamorphic deformation, or by replacement by later generations of feldspars (Fig. 5). Perthitic textures that are preserved in the reworked grains (Fig. 5A) can be overprinted by patch perthite. Most of the K-feldspar is turbid and porous due to replacement by fine-grained sericite ± albite, and in the Cooyerdoo Granite, new growths of clean albite are also observed. Primary K-feldspar is mantled by a secondary K-feldspar; lobate, recrystallized quartz is also present (sample MB153; Fig. 5B, C). More typically, quartz either forms large anhedral grains and/or recrystallized aggregates. Samples from Iron Magnet and the sheared granite from Iron Baron (sample MB154) show a strong correlation between granite alteration and deformation, evidenced by the presence of micro-shears enveloping K-feldspar associated with quartz and secondary muscovite ± biotite assemblages (Fig. 5D). Similar shear features can be observed within the muscovite schists, with an increase in muscovite component at the expense of K-feldspar, which is not preserved. Accessories common to the granitoids are zircon, apatite and Fe-Ti-oxides with secondary monazite and rutile being abundant in associations derived from alteration of the primary accessories.

In contrast to those described above, PL granitoids and the Charleston Granite are fresher and typically preserve primary igneous assemblages (Fig. 6). These include K-feldspar, plagioclase (An_{10-30}), biotite, and in the case of both leucocratic and melanocratic varieties of the PL granites, also amphibole. All samples are coarse-grained and display porphyritic textures, with K-feldspar phenocrysts ranging from mm- to megacrystic (cm-size) and with angular to well-rounded morphologies. With the exception of the leucogranites, K-feldspar phenocrysts in the PL granites are set in a weakly foliated groundmass composed of K-feldspar, plagioclase, quartz ± mafic silicates, the abundance of which varies and is reflected in whole-rock composition. In the leucogranites, a foliated fabric results from sheared and elongated feldspar grains.

The main minerals within the PL granites and Charleston Granite are K-feldspar and plagioclase. A perthitic texture is typical of the K-feldspar, albeit with varying degree of deuteric alteration expressed as crosscutting veinlets of patch perthite (Fig. 6A). Larger K-feldspar phenocrysts can contain inclusions of plagioclase (Fig. 6B), quartz, biotite and Fe-Ti oxides. Microcline is only observed in the PL migmatites, interstitial to the quartzitic groundmass (Fig. 6C). In the PL granites, plagioclase displays abundant polysynthetic twinning in one or two directions (Fig. 6D, E) and also shows contacts to K-feldspar outlined by myrmekites (plagioclase + quartz; Fig. 6F). In the Charleston Granite, such plagioclase grains are typically replaced by an

Table 1
Samples investigated in the present study.

Location	Sample no.	Rock type	Accessory minerals								Igneous assemblage	Alteration assemblage	Alteration type		
			Igneous/metamorphic				Secondary/hydrothermal								
			Zrc	Ap	Fe-(Ti)-minerals			REE-(U)-		Sulfides/others					
					Ilm	Mt	Rt	Ttn	bearing min				Na	K	Ca
Reference lithologies															
Charleston Granite ~1.58 Ma [1]	MB158	Charleston Granite	x	x	x	x	x	x	Th, Syn	Py, Sp	Kfs (+Mc), Pl ($An_{(0-30)}$ Bt	Ab, Chl	x		
Port Lincoln (Donington Suite)** ~1.85 Ma [2]	PL5	leucogranite	x		x	x					Kfs, Pl($An_{(0-30)}$), Amp, Bt				
	PL9	leucogranite	x		x	x					Kfs, Pl($An_{(0-30)}$), Amp, Bt				
	PL11	leucogranite	x		x	x					Kfs, Pl($An_{(0-30)}$), Amp, Bt				
	PL13	leucogranite	x		x	x					Kfs, Pl($An_{(0-30)}$), Amp, Bt				
	PL3	melanogranite	x		x	x					Kfs, Pl($An_{(0-30)}$), Amp, Bt				
	PL8*	melanogranite	x		x	x					Kfs, Pl($An_{(0-30)}$), Amp, Bt				
	PL6	fine-grained foliated leucogranite	x		x	x					Kfs, Pl($An_{(0-30)}$), Bt	Ab			
	PL12	fine-grained foliated leucogranite	x		x						Kfs, Pl($An_{(0-30)}$)				
	PL1a	mafic migmatite	x		x	x					Kfs (+Mc), Pl($An_{(0-30)}$), Bt				
	PL1b	mafic migmatite	x		x	x					Kfs, Pl($An_{(0-30)}$), Bt				
	PL14	pegmatite	x		x						Kfs, Pl($An_{(0-30)}$), Bt				
Cooyerdoo Granite	MB63*	leucogranite	x	x	x	x	x		Mnz, Syn		Kfs, Pl($An_{(0-30)}$), Bt	Ab		x	
~3.15 Ga [3]	MB64*	leucogranite	x	x	x	x	x		Mnz, Xtm		Kfs, Pl($An_{(0-30)}$), Bt	Ab		x	
Middleback Ranges granitoids															
Iron Monarch	MB157*	leucogranite	x	x	x	x	x	x	Syn, Mnz	Czo, Brt, Py, Cpy, Au, Ag, Znc	Kfs	Chl, Ab, Czo	x	x	x
Sultan	MB155*	pink granite	x	x	x	x	x	x	Xtm, Mnz, Uth		Kfs, Pl($An_{(0-30)}$)	Ab, Chl, Mus	x		
	MB156*	grey granite	x	x	x	x	x	x	Mnz, Uth	Gn, Brt	Kfs	Ab, Chl	x		
Iron Baron	MB153*	altered granite	x	x	x	x	x	x	Mnz	Czo, Th	Kfs	Ab, Chl	x	x	
	MB84*	leucogranite	x	x			x		Mnz, Uth	Py	Kfs	Ab, Mus, Chl	x	x	
	MB85*	leucogranite	x	x	x	x	x		Mnz, Aln, Th		Kfs, Pl($An_{(0-30)}$), Bt	Mus, Ab	x	x	
Middleback Ranges other lithologies															
Iron Baron	MB154	sheared granite	x				x		Uth		Kfs	Mus			
Iron Knight	MB146	muscovite schist	x	x					Mnz	Th		Mus			
Iron Magnet	MB82	muscovite schist	x	x			x		Mnz	Py, Cp, Sp, Gn		Mus			
Iron Magnet	MB83	sheared granite	x	x					Mnz		Kfs	Mus			

Mineral abbreviations: Ab-albite; Aln-allanite; Amp-amphibole; Ap-apatite; Bt-biotite; Chl-chlorite; Cp-chalcopyrite; Czo-clinozoisite; Gn-galena; Ilm-ilmenite; Kfs-potassium feldspar; Mc-microcline; Mnz-monazite; Mt-magnetite; Mus-muscovite; Pl-plagioclase; Py-pyrite; Rt-rutile; Sp-sphalerite; Syn-synchysite; Th-dhorite; Ttn-titanite; Uth-uranothorite; Xtm-xenotime; Zrc-zircon.
[1] Creaser and Fanning, 1993; [2] Reid et al., 2008a; [3] Fraser et al., 2010.
* Dated sample.
** Sample IDs are kept as originally marked to allow comparison with other published papers.

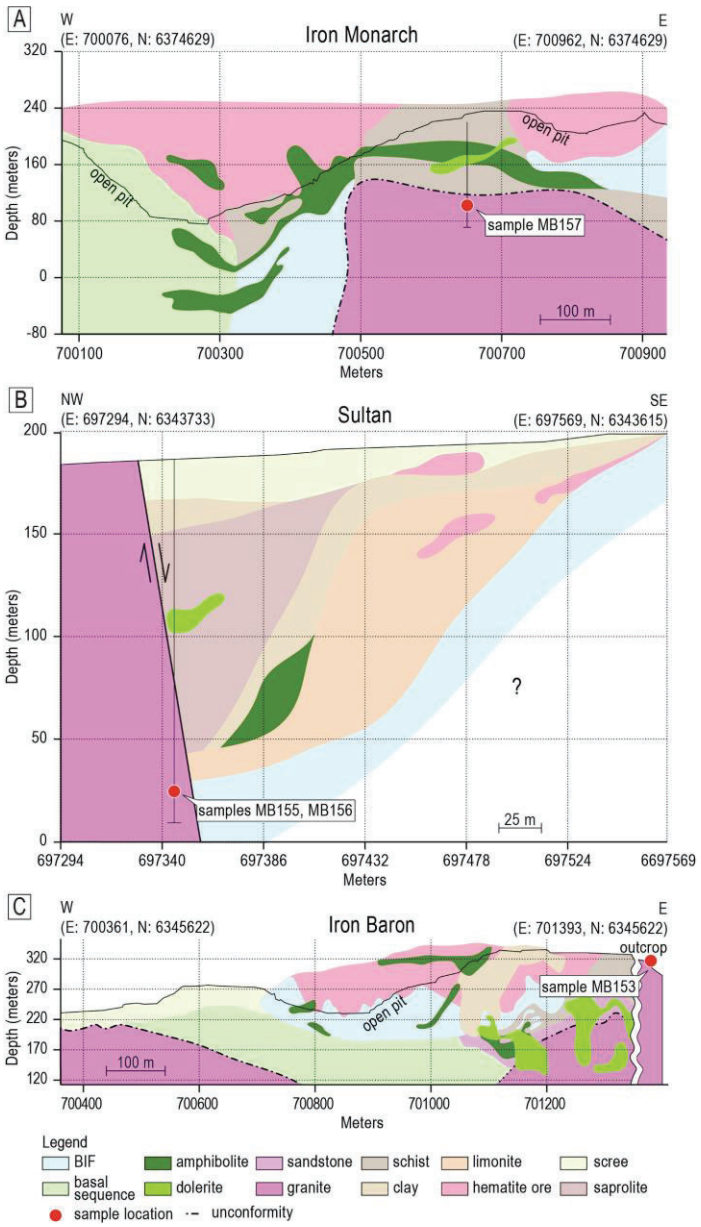

Fig. 2. Cross-sections of (A) the Iron Monarch deposit, (B) the Sultan prospect, and (C) the Iron Baron deposit, showing locations of sampled granites.

assemblage of sericite + albite.

The mafic components of the rocks consist of biotite, and in the PL granites, also pargasite [$NaCa_2(Mg,Fe^{2+})_4Al(Si_6Al_2)O_{22}(OH)_2$] (Table B1; Fig. 6G). Magnetite and ilmenite are abundant magmatic accessories in all granites but these are preserved as such (minor martitization of magnetite) only in the PL granites (Fig. 6H). Titanite, often as coarse, mm-sized grains, is abundant in the Charleston Granite (Fig. 6I). Less common accessory minerals include apatite, monazite, synchysite, pyrite and sphalerite, all of which can be considered as late- or post-magmatic phases.

Fig. 3. Polished blocks (A-C) and hand-specimen (D-I) photographs showing analyzed granites from localities as marked. Abbreviations: Bt-biotite; Kfs-K-feldspar; Prg-pargasite; Qz-quartz. See text for further explanation.

Fig. 4. (A) Augen feldspar in Iron Magnet granite. (B) Field photo of Iron Knight pit showing the location of muscovite schist sample (MB146) from the shear zone parallel to the western wall. (C-E) Field photos showing aspects of Port Lincoln granitoids (Donington Beach outcrop). (C) Leuco- and melanocratic differentiates (LD and MD, respectively), with inset showing a rounded K-feldspar porphyroblast. (D) Foliated leucogranites. (E) Pegmatite vein (sample PL14).

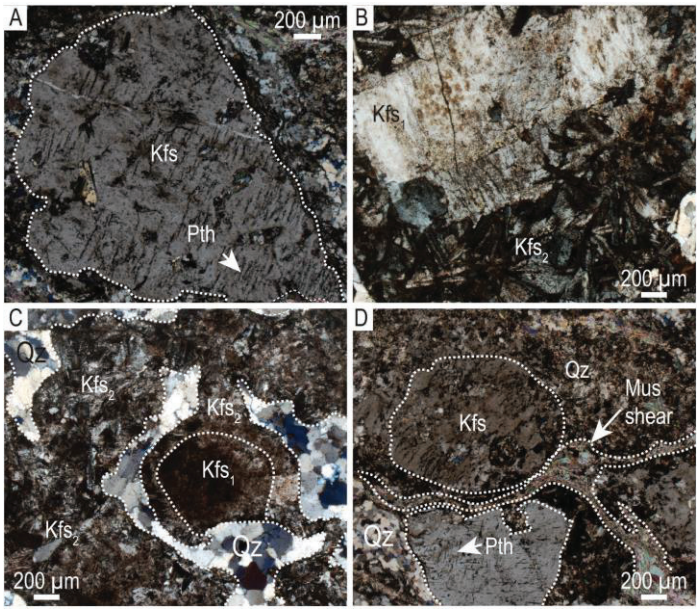

Fig. 5. Photomicrographs in cross-polarized light showing representative features of MR granites and the Cooyerdoo Granite. (A) Rounded K-feldspar phenocryst displaying perthitic textures. (B) K-feldspar phenocryst (Kfs_1) with laths of K-feldspar overgrowths (Kfs_2). (C) Rounded Kfs_1 phenocryst surrounded by Kfs_2. Note polygranular, lobate-shaped quartz. (D) Muscovite as shears around altered Kfs_1. Abbreviations: Kfs-K-feldspar; Mus-muscovite; Pth-perthite; Qz-quartz.

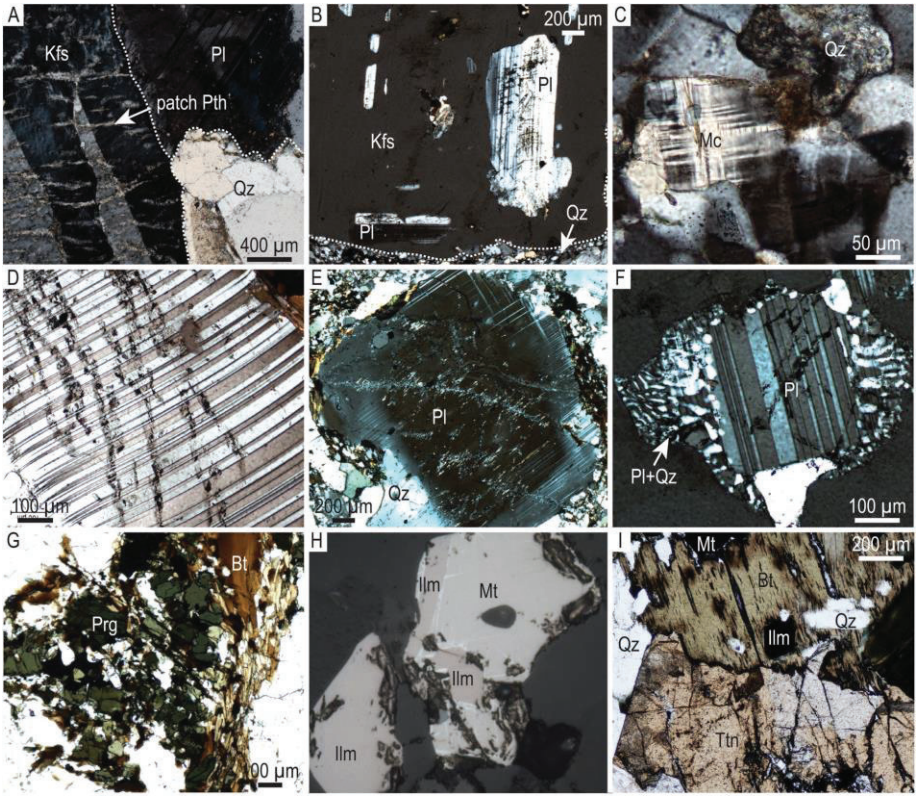

Fig. 6. Photomicrographs in cross-polarized (A-F), plane-polarized (G, I) and reflected light (H) showing representative features of fresh reference granites. (A, B, I) Charleston Granite; (C–H) Port Lincoln rocks. (A) Patch perthite replacing K-feldspar. (B) Fresh plagioclase inclusions in K-feldspar phenocryst. (C) Microcline in the leucogranite. (D) Polysynthetic, curved twins in plagioclase. (E) Compositional zoning in plagioclase. (F) Plagioclase + quartz myrmekites surrounding magmatic plagioclase. (G) Typical assemblages of fresh mafic minerals (pargasite + biotite). (H) Unaltered magmatic magnetite-ilmenite association. (I) Coarse titanite adjacent to unaltered biotite. Abbreviations: Bt-biotite; Ilm-ilmenite; Kfs-K-feldspar; Mc-microcline; Mt-magnetite; Pl-plagioclase; Prg-pargasite; Pth-perthite; Qz-quartz; Tnt-titanite.

4.3. Granite alteration

The alteration types of MR granitoids have been addressed in further detail since it has relevance for understanding superimposed fluid-rock interaction leading to mineralogical changes (Figs. 7 and 8). Potassic alteration is prevalent in the northern part of the MR where at least two generations subsequent to magmatic K-feldspar are distinguishable based upon crosscutting relationships and varying Ba concentrations (Iron Monarch; Fig. 7A, B). Calcic alteration is also present in the same granite, as indicated by the presence of clinozoisite and titanite (Fig. 7C, D). Titanite, pseudomorphically replaced by multi-component (calcite + rutile ± synchysite) symplectites, may however be of magmatic rather than hydrothermal origin, based on association with other magmatic accessories (zircon + apatite). Further overprinting is recognized from crosscutting calcite veins associated with a diverse and eclectic range of fine-grained, minor phases (Fig. 7E), including plagioclase, chlorite, quartz, monazite, rutile, zincite and native gold. The zircon grains, too small to be dated, are clearly not magmatic in origin and their association with metal-bearing minerals indicates that hydrothermal fluids percolating through the granites have assisted metal-(re)distribution (Zn, Au) from/to immediately adjacent orebodies.

Albitization of either K-feldspar or plagioclase is recognized in the central part of the belt (Sultan and Iron Baron; Fig. 8A). This process is always accompanied by development of porosity and minute inclusions of iron-oxides within albite. The Iron Baron granite also displays patch perthite superimposed onto core cryptoperthites in K-feldspar (Kfs_1) phenocrysts (Fig. 8B) and potassic alteration (e.g., Kfs_2 as rims on Kfs_1; Fig. 8C). Secondary mineral assemblages (e.g., chlorite + clinozoisite + iron-oxides) resulting from alteration of mafic components in the granites is often associated with formation of Kfs_2. At the same time, partial melting during deformation can be inferred based on the presence of lobate-shaped, polycrystalline quartz (undulatory anisotropy, e.g., Sawyer, 1999; Fig. 5C and 8D), which makes up ~50–60 vol % of the sample.

Shear-induced deformation of feldspars (Fig. 8E) is best expressed in granitoids from the southern part of the belt (Iron Knight and Iron Magnet). In detail, this is also underlined by growth of albite and micas, myrmekites of plagioclase + quartz, as well as occurrence of Kfs_2 within biotite (Fig. 8F, G). Advanced shearing is accompanied by formation of new REE-minerals, mainly monazite (+thorite) and allanite. The presence of scalloped zircon and apatite indicates that such

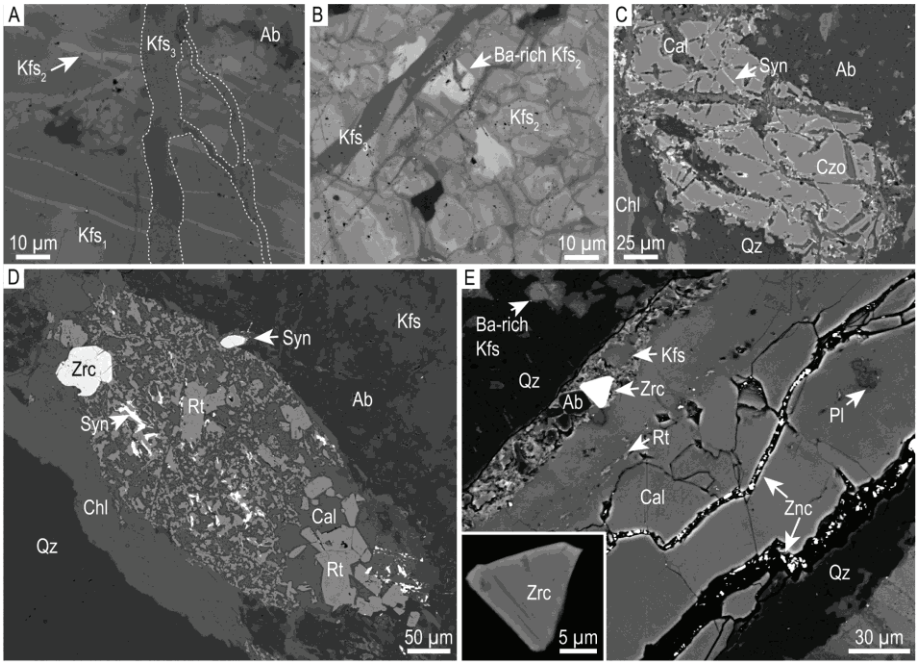

Fig. 7. BSE images showing alteration features observed in granites from the northern part of the MR. (A) Magmatic K-feldspar (Kfs_1) crosscut by Ba-rich K-feldspar (Kfs_2) veins. Note the still later crosscutting veins containing Ba-depleted K-feldspar (Kfs_3). (B) Granoblastic Kfs_2 displaying Ba-zoning and crosscut by veins containing Kfs_3. (C) Clinozoisite replaced by calcite and fine-grained synchysite along fractures. (D) Rutile-calcite ± synchysite symplectite pseudomorphically replacing coarse, lozenge-shaped titanite. (E) Calcite-rich vein containing inclusions of plagioclase and rutile. Note albite, K-feldspar and zircon along vein margin, and zincite hosted in fractures. Inset in (E) shows zircon of possible hydrothermal origin. Abbreviations: Ab-albite; Cal-calcite; Chl-chlorite; Czo-clinozoisite; Kfs-K-feldspar; Pl-plagioclase; Qz-quartz; Rt-rutile; Syn-synchysite; Znc-zincite; Zrc-zircon.

associations result from reworking of magmatic accessories in the granite (Iron Magnet; Fig. 8H). Most intense deformation, close to the contact with the BIF sequences in Iron Magnet, leads to further rounding of Kfs_1, abundant muscovite, and complete obliteration of plagioclase (samples MB82 and MB146).

4.4. Whole-rock geochemistry

Major oxide concentrations in all studied samples are listed in Table 2. Although several samples show indications of overprinting and thus may not fully reflect the composition of the granitoid protolith, discriminative plots are nevertheless useful to compare sample suites and to trace different types of alteration. Alteration is most apparent on the QAP (Streckeisen, 1974) and Ab-An-Or (Barker, 1979) diagrams, which are based on CIPW normative mineralogy. On the QAP diagram (Fig. 9A), a majority of samples cluster tightly within the 'granite' field despite petrographic evidence of alteration, with melanogranites from PL stretching towards the 'granodiorite' field. Samples displaying Ca- (sample MB157) and Na-alteration (sample MB156) extend into the 'granodiorite' and 'tonalite' fields, respectively. The muscovite schists and the sheared granite plot within the 'alkali feldspar granite' field, which reflects the muscovite component within these rocks. The Ab-An-Or diagram (Fig. 9B) shows similar trends as the QAP diagram, with samples mainly plotting within the 'granite' field and the melano-granites plotting towards the 'granodiorite' field. Calcic-alteration in sample MB157 is again reflected by this sample plotting within the 'granodiorite' field, whereas the sample displaying Na-alteration plots within the 'trondhjemite' field.

Significant differences among the sample suites can be observed on both the aluminum saturation index *vs.* $Al_2O_3/Na_2O + K_2O$ (Frost et al., 2001) and the $10^4 \times Ga/Al$ *vs.* Zr (Whalen et al., 1987) diagrams (Fig. 9C, D). All PL granites show a metaluminous composition, with increasing felsic compositions stretching towards the peraluminous field (Fig. 9C) and can be classified as A-type granites. In contrast, the MR samples, the Cooyerdoo Granite and the Charleston Granite plot within the peraluminous field and can thus be classified as I-type and S-type granites.

4.5. Trace element geochemistry

The concentrations of trace elements, including rare earth elements REE + Y within the studied samples are given in Table 3 and illustrated in Fig. 10. On diagrams normalized to continental crust (Fig. 10A, B), the distribution patterns for samples from the various suites are comparable to each other. These similarities include relative enrichment in Rb, Th, K, and Nd, and depletion in Ba, Ta, Nb, Sr, Hf, and Ti. A notable difference in the magnitude of Sr depletion is seen in the MR samples. Anomalous samples among the suites include the granites from Iron Magnet, which lack any significant Sr depletion, and the albitized granite from Sultan (MB156) and the PL marginal facies granite (PL12), which display particularly strong depletion in both Ba and Sr.

Differences in the concentrations of other elements are observed across the dataset and within each sample suite. The Ca-altered granite from Iron Monarch displays higher concentrations of Cr, Ni, Co, Cu, Zn

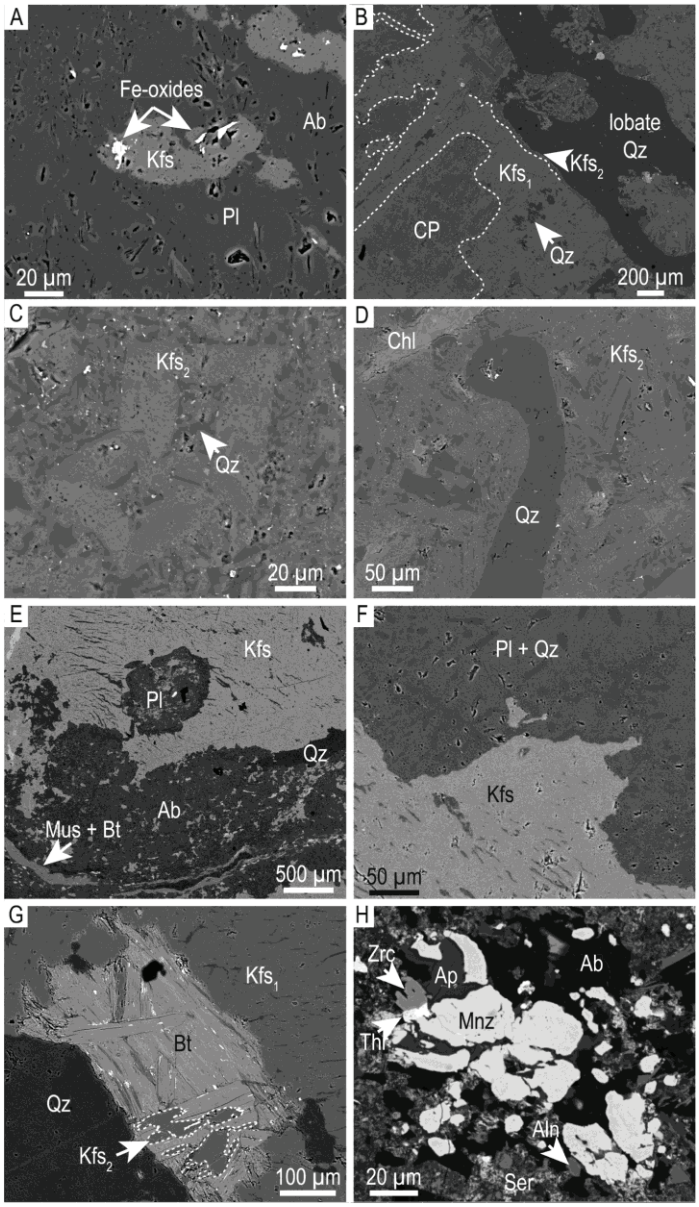

Fig. 8. BSE images showing alteration features observed in granites from the central and southern MR. (A) Albitization of Kfs_1 (present as relicts) and plagioclase. (B) Kfs_1 with cryptoperthite (CP) cores fringed by Kfs_2. Note Kfs_2 as islands in lobate quartz. (C) Square-shaped Kfs_2 with quartz inclusions. (D) Lobate quartz within a Kfs_2 + quartz matrix. (E) Assemblage of albite + muscovite + biotite forming the margin of a sheared Kfs_1 phenocryst. (F) Plagioclase + quartz myrmekites along the margin of perthitic Kfs_1. (G) Biotite with inclusions of Kfs_2 along the margin of Kfs_1 phenocryst. (H) Pocket of secondary REE-bearing minerals (monazite, apatite, thorite, zircon, allanite) and sericite + albite within Kfs_1. Abbreviations: Ab-albite; Aln-allanite; Ap-apatite; Bt-biotite; Chl-chlorite; Kfs-K-feldspar; Mnz-monazite; Mus-muscovite; Pl-plagioclase; Qz-quartz; Ser-sericite; Thr-thorite; Zrc-zircon.

and V relative to all other samples. The melanogranites from PL are enriched in Cu and Zn, and depleted in Pb, relative to the felsic granites. Samples from the MR are also enriched in W and depleted in Sn relative to the PL granites. The Charleston Granite has the highest concentrations of W, Th and U.

Chondrite-normalized REE + Y patterns for the various rock types show similarities in terms of pattern but differ with respect to slope and magnitude of anomalies. All samples display LREE enrichment (Fig. 10C, D). $(La/Yb)_{CN}$ ratios range from 8.3 to 30 (Table 3). Exceptions to this are shown by the Cooyerdoo Granite, which has an average $(La/Yb)_{CN}$ ratio of 73, and a felsic PL granite (PL13) with a $(La/Yb)_{CN}$ = 2.7. Europium anomalies are generally negative ($(Eu/Eu^*)_{CN}$ = 0.44–0.94) with the exception of samples from Iron Magnet, which do not feature significant anomalies, or in the case of the sheared

Table 2
Whole-rock geochemistry; major oxides (wt%).

Location	Sample	Rock type	SiO_2	Al_2O_3	MgO	Fe_2O_3	CaO	K_2O	Na_2O	P_2O_5	TiO_2	MnO	LOI	Total + LOI
Reference lithologies														
Charleston Granite	MB158	Charleston Granite	73.55	12.64	0.40	2.96	1.44	5.20	3.07	0.11	0.34	0.05	0.61	100.38
Port Lincoln	PL5	leucogranite	65.33	14.42	1.21	6.35	3.12	5.49	2.60	0.23	0.80	0.08	0.43	100.06
	PL9	leucogranite	65.70	13.94	1.24	6.29	3.13	5.19	2.47	0.21	0.81	0.08	0.38	99.44
	PL11	leucogranite	64.89	14.79	1.03	5.35	2.74	5.96	2.66	0.09	0.65	0.05	0.49	98.70
	PL13	leucogranite	68.22	14.11	1.03	5.63	2.42	6.05	2.40	0.09	0.66	0.06	0.86	101.54
	PL3	melanogranite	62.64	15.27	1.64	8.41	4.28	4.47	3.06	0.39	1.25	0.10	0.56	102.07
	PL8	melanogranite	60.26	15.27	1.71	8.91	4.09	4.32	2.66	0.39	1.35	0.12	0.56	99.63
	PL12	marginal facies	77.44	11.41	0.10	1.00	0.59	5.47	2.63	0.02	0.10	0.01	0.45	99.22
	PL1b	mafic migmatite	68.22	13.87	0.76	4.75	2.03	5.30	2.63	0.09	0.55	0.05	0.56	98.81
Cooyerdoo Granite	MB63	leucogranite	75.07	13.36	0.08	1.53	0.43	5.30	3.18	0.02	0.13	0.01	0.77	99.89
	MB64	leucogranite	75.43	13.17	0.08	1.39	0.43	5.31	3.14	0.02	0.13	0.01	0.69	99.81
Middleback Ranges granitoids														
Iron Monarch	MB157	leucogranite	61.29	14.59	3.66	6.83	2.71	2.76	3.37	0.23	0.67	0.12	4.14	100.37
Sultan	MB155	pink, altered granite	74.79	13.59	0.58	1.34	0.42	3.76	4.49	0.05	0.11	0.03	1.08	100.23
Sultan	MB156	leucogranite	74.79	13.94	1.04	1.74	0.29	0.43	7.04	0.07	0.12	0.03	0.79	100.29
Iron Baron S.	MB153	altered granite	73.01	12.79	0.71	2.30	0.53	8.24	1.47	0.09	0.24	0.04	1.07	100.50
Iron Magnet	MB84	leucogranite	74.30	13.59	0.51	1.76	0.41	5.04	3.42	0.11	0.16	0.03	0.98	100.30
Iron Magnet	MB85	leucogranite	74.36	13.68	0.61	1.90	0.85	4.42	3.57	< mdl	0.15	0.03	1.04	100.62
Middleback Ranges other lithologies														
Iron Baron S.	MB154	sheared granite	75.73	11.87	1.23	2.30	0.11	7.18	0.18	< mdl	0.19	0.04	1.78	100.60
Iron Knight N.	MB146	muscovite schist	72.63	17.08	0.63	1.56	0.01	5.34	0.20	0.02	0.16	< mdl	2.45	100.09
Iron Magnet	MB83	sheared granite	73.61	13.57	0.88	2.02	0.04	8.14	0.27	0.02	0.10	0.01	1.50	100.16

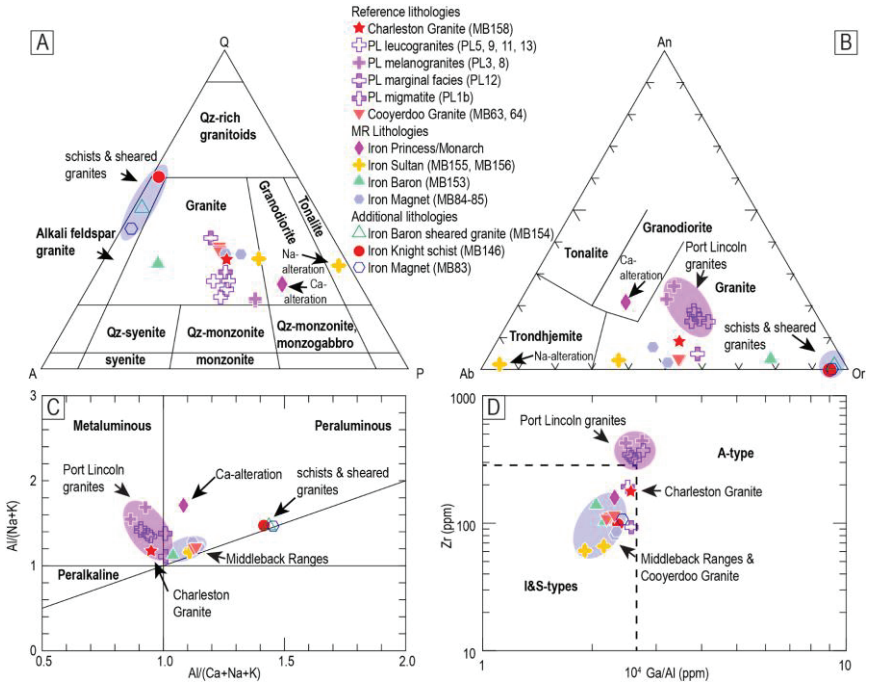

Fig. 9. Ternary and binary plots of whole-rock data for the studied granites and muscovite schists. (A) QAP diagram (Streckeisen, 1974) showing the majority of samples clustered within the 'Granite' field. Samples showing Ca- or Na-alteration plot within the 'Granodiorite' and 'Tonalite' fields, respectively. Samples with sheared fabrics plot within the 'Alkali feldspar granite' field. (B) CIPW normalized data plotted on an Ab-An-Or diagram (Barker, 1979) showing samples plotting within the 'Granite' field and altered granites and schists plotting in the 'Granodiorite' and 'Trondhjemite' fields. Sheared samples plot towards the 'Or' end-member. (C) Alumina saturation index diagram after Shand (1943) showing the PL granites and the Charleston Granite plotting within the 'metaluminous' field, while samples from the MR and the Cooyerdoo Granite plot within the 'peraluminous' field. (D) 10,000 × Ga/Al *vs.* Zr classification diagram (Whalen et al., 1987) showing PL granites plotting as 'A-type' granites and MR samples, Cooyerdoo Granite and the Charleston Granite plotting as 'I and S-type' granites.

Table 3
Trace element geochemistry (ppm).

Location	Sample	Rock type	Li	Ba	Sr	Be	Rb	Cs	Cr	Ni	Co	Cu	Zn	Cd
Reference lithologies														
Charleston Granite	MB158	Charleston Granite	33	494	106	3.3	311	4.0	< mdl	< mdl	3.1	4.0	31	< mdl
Port Lincoln	PL5	leucogranite	14	928	148	2.4	228	2.1	< mdl	11	11	22	73	0.22
	PL9	leucogranite	11	910	144	2.5	217	2.1	< mdl	10	12	23	75	0.26
	PL11	leucogranite	24	1050	155	2.6	243	7.7	< mdl	8.0	9.1	13	68	0.16
	PL13	leucogranite	28	1135	184	2.2	248	6.7	< mdl	7.0	6.5	9.0	55	0.15
	PL3	melanogranite	30	997	190	2.7	201	4.7	< mdl	8.0	13	44	104	0.25
	PL8	melanogranite	17	1175	206	2.4	188	2.3	< mdl	13	17	38	99	0.22
	PL12	marginal facies	2.9	30	18	1.2	332	1.5	< mdl	1.0	0.60	1.0	7.0	0.05
	PL1b	mafic migmatite	17	587	130	2.7	249	10	< mdl	5.0	6.9	15	53	0.13
Cooyerdoo Granite	MB63	leucogranite	2.3	1087	173	1.3	174	2.2	< mdl	2.0	0.80	4.0	15	0.07
	MB64	leucogranite	2.0	1008	161	1.2	161	2.5	< mdl	1.0	0.90	3.0	11	0.07
Middleback Ranges granitoids														
Iron Monarch	MB157	leucogranite	21	1063	183	0.90	99	2.4	58	25	18	33	109	0.03
Sultan	MB155	pink, altered granite	5.0	547	97	0.60	99	0.40	< mdl	< mdl	2.2	< mdl	13	< mdl
Sultan	MB156	leucogranite	5.4	67	33	< mdl	16	0.15	< mdl	4.0	3.0	< mdl	15	< mdl
Iron Baron S.	MB153	altered granite	7.6	1726	190	0.60	219	1.6	< mdl	3.0	3.5	13	22	0.07
Iron Magnet	MB84	leucogranite	4.1	756	141	0.70	130	0.62	< mdl	< mdl	2.1	4.0	25	0.02
Iron Magnet	MB85	leucogranite	4.5	676	166	0.70	115	0.77	< mdl	< mdl	2.3	< mdl	29	0.03
Middleback Ranges other lithologies														
Iron Baron S.	MB154	sheared granite	8.6	2120	55	0.50	249	2.0	< mdl	< mdl	2.4	41	32	< mdl
Iron Knight N.	MB146	muscovite schist	2.5	404	14	< mdl	124	1.6	< mdl	2.0	1.4	< mdl	14	< mdl
Iron Magnet	MB83	sheared granite	6.3	1028	79	0.90	226	1.9	< mdl	10	2.3	5.0	26	0.09

Location	V	Nb	Ta	Zr	Hf	Sc	Ga	Ge	In	Ag	As	Sb	Bi	Pb	Te
Reference lithologies															
Charleston Granite	< mdl	17	1.8	177	5.6	4.0	17	0.7	0.03	0.06	2.2	1.1	0.19	27	< mdl
Port Lincoln	52	16	1.0	314	7.6	14	20	< mdl	0.07	0.1	1.0	< mdl	< mdl	30	< mdl
	63	17	1.1	373	9.3	14	20	< mdl	0.07	< mdl	< mdl	< mdl	< mdl	26	< mdl
	49	15	1.2	330	9.0	14	20	< mdl	0.08	< mdl	2.0	< mdl	0.25	32	< mdl
	32	14	1.1	344	8.2	11	19	< mdl	0.06	< mdl	4.0	< mdl	0.27	30	< mdl
	88	35	2.3	425	10	20	20	0.1	0.12	< mdl	3.0	< mdl	0.11	26	< mdl
	90	25	1.3	443	11	22	22	< mdl	0.10	< mdl	1.0	< mdl	< mdl	20	< mdl
	13	3.3	0.20	93	2.8	2.0	16	< mdl	< mdl	< mdl	3.0	< mdl	< mdl	33	< mdl
	53	11	0.70	193	4.6	7.0	18	< mdl	< mdl	< mdl	5.0	0.90	0.28	42	< mdl
Cooyerdoo Granite	12	5.0	0.20	115	3.2	3.0	16	< mdl	< mdl	< mdl	1.0	< mdl	0.05	44	< mdl
	14	3.1	0.20	108	2.7	2.0	15	< mdl	< mdl	0.10	2.0	< mdl	< mdl	43	< mdl
Middleback Ranges granitoids															
Iron Monarch	125	6.6	0.70	159	4.2	13	18	0.20	0.04	0.11	3.8	1.8	0.34	24	< mdl
Sultan	< mdl	5.7	0.80	66	2.2	< mdl	16	0.30	< mdl	< mdl	1.5	1.2	0.03	16	< mdl
Sultan	< mdl	6.1	0.70	61	1.9	2.0	14	0.10	< mdl	< mdl	1.0	0.80	< mdl	7	< mdl

(continued on next page)

Table 3 (*continued*)

Location	V	Nb	Ta	Zr	Hf	Sc	W	Th	U	La	Ga	Ce	Pr	Nd	Sm	Eu	Gd	Tb	Dy	Y	Ho	Er	Tm	Yb	Lu	ΣREY	$(La/Yb)_{CN}$	$(Eu/Eu^*)_{CN}$
Iron Baron S.	26	7.8	0.70	140	3.8	3.0					14		0.40			0.02		0.15		1.5			0.90		0.02	12			< mdl
Iron Magnet	< mdl	5.1	0.50	81	2.4	< mdl					17		0.20			0.02		0.10		2.6			0.70		0.03	21			< mdl
Iron Magnet	< mdl	4.8	0.50	86	2.6	< mdl					17		0.20			0.01		< mdl		1.3			1.0		0.03	26			< mdl
Middleback Ranges other lithologies																												
Iron Baron S.	23	9.4	1.5	104	3.1	2.0					14		0.30			0.02		< mdl		0.70			0.90		0.20	12			< mdl
Iron Knight N.	< mdl	7.2	0.60	98	3.2	< mdl					21		0.20			0.01		0.14		1.2			1.6		0.02	15			< mdl
Iron Magnet	< mdl	5.0	0.20	107	2.7	3.0					17		< mdl			< mdl		< mdl		2.00			< mdl		< mdl	26			< mdl

Location	Sample	Rock type	Se	Tl	Mo	Re	Sn	W	Sc	Th	U	La	Ga	Ce	Pr	Nd	Sm	Eu	Gd	Tb	Dy	Y	Ho	Er	Tm	Yb	Lu	ΣREY	$(La/Yb)_{CN}$	$(Eu/Eu^*)_{CN}$
Reference lithologies																														
Charleston Granite	MB158	Charleston Granite	1.0	1.5	< mdl	< mdl	4.0	33		72	13	93	163	16	51	8.5	1.3	6.8	1.1	6.5	34	1.3	3.9	0.6	3.9	0.55	391	17		0.52
Port Lincoln	PL5	leucogranite	1.0	1.2	< mdl	< mdl	3.0	1.0	15	2.5	52	107	12	46	8.8	1.5	7.4	1.2	6.4	38	1.3	3.5	0.46	3.4	0.50	290	11		0.55	
	PL9	leucogranite	1.0	1.2	< mdl	< mdl	3.0	1.0	17	2.8	55	113	13	50	9.8	1.5	7.6	1.2	6.9	40	1.4	3.8	0.47	3.6	0.5	308	11		0.51	
	PL11	leucogranite	1.0	1.3	< mdl	< mdl	4.0	2.0	15	3.4	52	109	12	47	9.7	1.5	8.3	1.3	7.6	42	1.5	4.1	0.53	4.0	0.58	302	9.4		0.51	
	PL13	leucogranite	< mdl	1.3	< mdl	< mdl	3.0	2.0	12	2.0	10	26	3.1	15	4.5	1.4	4.3	0.73	4.5	26	0.85	2.6	0.29	2.6	0.29	102	2.7		0.94	
	PL3	melanogranite	2.0	1.1	< mdl	< mdl	3.0	6.0	13	3.5	63	136	17	65	14	1.9	12	1.9	11	61	2.1	6.1	0.81	5.4	0.77	397	8.3		0.44	
	PL8	melanogranite	2.0	1.1	< mdl	< mdl	3.0	1.0	12	1.2	71	139	16	56	11	2.2	9.5	1.4	7.2	42	1.4	3.8	0.47	3.4	0.48	365	15		0.64	
	PL12	marginal facies	< mdl	1.6	< mdl	< mdl	< mdl	1.0	11	1.5	8.8	18	1.6	5.2	1.1	0.18	0.87	0.14	0.87	5.0	0.19	0.57	< mdl	0.58	0.07	43	11		0.55	
	PL1b	mafic migmatite	< mdl	1.2	< mdl	< mdl	2.0	1.0	11	2.4	33	70	8.1	30	5.7	0.94	4.3	0.67	3.7	21	0.71	2.1	0.25	2.0	0.29	183	12		0.56	
Cooyerdoo Granite	MB63	leucogranite	< mdl	1.3	< mdl	< mdl	< mdl	< mdl	40	4.6	36	72	7.5	22	3.3	0.63	1.9	0.27	1.2	5.2	0.20	0.54	< mdl	0.38	0.07	152	68		0.71	
	MB64	leucogranite	< mdl	1.2	< mdl	< mdl	< mdl	< mdl	40	4.6	42	78	8.2	26	3.6	0.73	2.1	0.28	1.4	6.2	0.20	0.54	< mdl	0.38	0.05	170	79		0.75	
Middleback Ranges granitoids																														
Iron Monarch	MB157	leucogranite	0.70	0.90	< mdl	< mdl	2	18	19	2.9	58	106	11	39	6.2	1.4	4.4	0.58	3.2	15	0.60	1.6	0.23	1.5	0.20	248	28		0.79	
Sultan	MB155	pink, altered granite	< mdl	0.80	< mdl	< mdl	< mdl	12	15	1.8	21	38	3.8	12	2.4	0.41	1.9	0.31	1.7	9.4	0.33	1.0	0.17	1.3	0.17	94	12		0.56	
Sultan	MB156	leucogranite	< mdl	0.17	< mdl	< mdl	< mdl	13	20	2.5	25	42	4.4	14	2.7	0.41	2.2	0.34	2.0	11	0.37	1.1	0.17	1.1	0.15	106	16		0.50	
Iron Baron S.	MB153	altered granite	< mdl	1.7	< mdl	< mdl	1.0	15	41	14	47	88	9.0	29	5.2	0.69	3.8	0.54	2.9	15	0.51	1.4	0.19	1.2	0.16	204	28		0.45	
Iron Magnet	MB84	leucogranite	< mdl	0.78	< mdl	< mdl	< mdl	12	31	3.3	15	27	2.8	9.1	1.6	0.43	1.2	0.17	1.0	5.3	0.19	0.52	0.08	0.54	0.07	65	20		0.91	
Iron Magnet	MB85	leucogranite	< mdl	0.67	< mdl	< mdl	< mdl	13	21	4.2	17	30	3.1	9.9	1.9	0.45	1.4	0.20	0.99	4.8	0.17	0.45	0.07	0.51	0.06	70	23		0.81	
Middleback Ranges other lithologies																														
Iron Baron S.	MB154	sheared granite	< mdl	2.0	1.0	< mdl	1.0	14	28	8.2	40	69	6.9	22	3.4	0.55	2.1	0.28	1.5	8.7	0.29	0.86	0.13	0.95	0.14	157	30		0.58	
Iron Knight N.	MB146	muscovite schist	< mdl	0.57	< mdl	< mdl	< mdl	15	25	1.4	27	49	5.3	19	3.2	0.79	2.6	0.36	1.8	9.5	0.33	0.84	0.12	0.76	0.11	120	25		0.80	
Iron Magnet	MB83	sheared granite	< mdl	1.2	< mdl	< mdl	< mdl	< mdl	44	3.1	8.1	15	1.7	5.5	1.2	0.46	1.0	0.16	0.88	5.9	0.18	0.50	< mdl	0.36	0.06	41	16		1.2	

granite (sample MB83), where the Eu-anomaly is positive ($(Eu/Eu^*)_{CN}$ = 1.2) (Fig. 10C). The average ΣREE + Y within the PL granites and Charleston Granite, with the exception of the marginal facies granite (43 ppm), is 292 ppm. The mean ΣREE + Y concentration in the MR and Cooyerdoo Granite samples is 130 ppm (Table 3).

4.6. U-Pb SHRIMP geochronology

4.6.1. Zircon characteristics

Studied zircon grains exhibit a range of sizes, morphologies, colors and textures (Figs. 11 and A2), while also displaying varying types of inclusions, growth textures and degrees of metamictization. Sizes range from 100 to 200 μm with typical aspect ratios of 1:1, 1:2, and rarely 1:3. Many grains are prismatic, with margins that show fracturing; most are sub-rounded to rounded. Zircons are mostly clear to light brown in color but may be cloudy due to either the presence of inclusions or metamictization. Inclusions include apatite and quartz, or replacement by sericite along fractures. Cathodoluminescence (CL) images (Figs. 11 and A2) show that the grains display a range of zoning patterns. Zircons mainly display oscillatory zoning, with sectorial zoning occasionally observed. Although zircon generally displays homogenously dark intensities in CL, grains can also have dark cores with bright rims, bright cores with dark rims, or are bright throughout. Zircon grains throughout the suite contain concentrations of U and Th ranging from 27 to 5,600 ppm and 1 to 1700 ppm, respectively, and Th/U ratios ranging from 0.01 to 2.4 (mean = 0.52).

4.6.2. Port Lincoln – A Donington Suite granite

Zircon grains within sample PL8 are subhedral to euhedral, display oscillatory growth zoning typical of igneous zircon, lack overgrowths and show a low degree, if any, of alteration (Fig. 11A). Fifteen spot analyses were collected from fourteen grains, two analyses having been taken from a single grain displaying a bright core and a dark rim in CL (Fig. A2). However, the core and rim contained comparable concentrations of U and Th (~150 and ~85 ppm, respectively) and have comparable $^{207}Pb/^{206}Pb$ weighted mean ages. Eleven analyses plot within uncertainty of concordia (< 5%), while the remaining four analyses are discordant (7–27%) (Fig. 12A). The individual spot $^{207}Pb/^{206}Pb$ dates range from 1.78 to 1.89 Ga, with uncertainties (± 1σ) between 17 and 101 Ma. The eleven concordant analyses yield a weighted mean $^{207}Pb/^{206}Pb$ age of 1864 ± 17 Ma (MSWD = 1.5). This age is interpreted as the crystallization age of the granite concurrent with the age of the Donington Suite.

4.6.3. Cooyerdoo Granite

Zircon grains from Cooyerdoo Granite (sample MB63-64) are rounded and altered, displaying oscillatory zoning and no apparent overgrowths (Fig. A2). Exceptions are two grains displaying the lowest U and Th concentrations within the population (76 and 28 ppm, respectively), one grain with cleaner margins and sectorial zoning, also the most concordant grain within the zircon population, and a second grain displaying more angular features and brighter CL intensity (Fig. 11B). Twelve analyses were collected from twelve individual zircon grains (Fig. A2). Two points plot reversely discordant, two concordantly, and the remaining discordantly (14–39%) (Fig. 12B). The individual $^{207}Pb/^{206}Pb$ dates and single data point uncertainties (± 1σ) range from 1.87 to 3.14 Ga and 11 to 38 Ma, respectively. The two oldest grains (one concordant and the other reversely discordant) have $^{232}Th/^{238}U$ ratios of 1.3 to 1.9 and a $^{207}Pb/^{206}Pb$ weighted mean age of 3134 ± 18 Ma (MSWD = 0.20), while a single concordant grain ($^{232}Th/^{238}U$ = 0.39) has a $^{207}Pb/^{206}Pb$ age of 2815 ± 23 Ma. Low common Pb ($^{204}Pb/^{206}Pb$ = < 0.003) and similar $^{232}Th/^{238}U$ ratios (0.15–0.85) of the discordant analyses make discriminating data into distinct discordia trends difficult. The $^{207}Pb/^{206}Pb$ weighted mean age obtained from the two oldest grains (3134 ± 18 Ma) is interpreted to represent the igneous crystallization age rather than the single younger concordant point. The sample was taken from a known Cooyerdoo Granite (~3.1 Ga) location.

4.6.4. Iron Monarch

Zircon grains from the Iron Monarch granite (sample MB157) vary in terms of morphology (Fig. A2), many of which have fractured margins. Twenty-three analyses were performed on fifteen zircon grains. Several grains display dark cores and bright rims in CL images and thus were checked for overgrowth ages (Fig. 11C). Although cores always contained higher concentrations of U and Th than rims (Table 4), no significant $^{207}Pb/^{206}Pb$ difference was measured between the two domains within these grains. Three data points are within uncertainty of concordia (≤6%) while the remainder are discordant (15–61%; Fig. 12C). The $^{207}Pb/^{206}Pb$ dates and uncertainties (± 1σ) range from 2.44 to 3.16 Ga and 6 to 50 Ma, respectively. Two points with large uncertainties (86 Ma) were not considered within the above age constraints. A wide range of $^{232}Th/^{238}U$ ratios (0.01–2.43) and $^{204}Pb/^{206}Pb$ ratios < 0.004 make discrimination between analyses for fitting a discordia line impossible. The three most concordant data points have a $^{207}Pb/^{206}Pb$ weighted mean date of 3130 ± 59 Ma with a large MSWD of 12. The oldest individual $^{207}Pb/^{206}Pb$ date from the most concordant data point is therefore used to represent a minimum crystallization age of 3165 ± 8 Ma.

4.6.5. Iron Baron

Zircon from the Iron Baron granite (sample MB153) generally display prismatic morphologies with variable intergranular and marginal corrosion. Several grains show oscillatory zoning or apparent core and rim relationships. However, these grains display a homogenous grey color in CL images (Figs. A2). The exceptions are a scalloped grain that has a bright intensity in CL imaging and the lowest U concertation within the population (108 ppm), and one grain with a bright core containing a dark domain (534 ppm U) and dark rim (862 ppm U) (Fig. 11D). Twenty zircon grains were analyzed. All analyses show discordance ranging from 7 to 95%. Individual $^{207}Pb/^{206}Pb$ dates and uncertainties (± 1σ) range from 917 to 3089 Ma and 8 to 111 Ma, respectively. The analyses plot as a scatter on the Tera-Wasserburg diagram, likely due to non-zero age Pb loss (possibly induced by metamictization) (Fig. 12D), preventing a discordia line to be fit through the analyses. The discordant grains generally contain high U concentrations (> 1,000 ppm). However, a population of six of the oldest grains with U concentrations ranging from ~300–700 ppm was used to derive a $^{207}Pb/^{206}Pb$ weighted average date of 3019 ± 66 Ma (MSWD = 29). This age is likely an underestimation of the true age due to the tendency for non-zero age Pb loss to drag $^{207}Pb/^{206}Pb$ ages towards younger ages. Although the least discordant of the population, these six analyses sit somewhat off discordia (39–51%) and follow a resetting trend along with the remaining zircon to a non-zero lower intercept on concordia. The oldest individual $^{207}Pb/^{206}Pb$ date from this population is used to represent a minimum crystallization age of 3089 ± 9 Ma.

4.6.6. Sultan

Zircon grains from the Sultan granites (samples MB155 and MB156) are generally subhedral and finer-grained. Coarser-grained exceptions within the zircon population display more anhedral morphologies or rim overgrowths (Fig. A2). The grains display weak to strong oscillatory zoning and have mostly homogenously grey colors in CL images, although a few display brighter intensities (Fig. 11E). However, many grains display core and rim relationships, with either bright cores and dark rims or vice versa (Fig. 11F). In sample MB155, twenty-eight analyses were performed on sixteen grains. Eleven analyses plot concordantly (within ≤ 5% uncertainty) on the Tera-Wasserburg diagram; the remaining seventeen analyses are discordant (6–46%) (Fig. 13A). The $^{207}Pb/^{206}Pb$ dates range from 2.38 to 3.26 Ga with uncertainties (± 1σ) ranging from 6 to 20 Ma. Nine of the eleven concordant grains

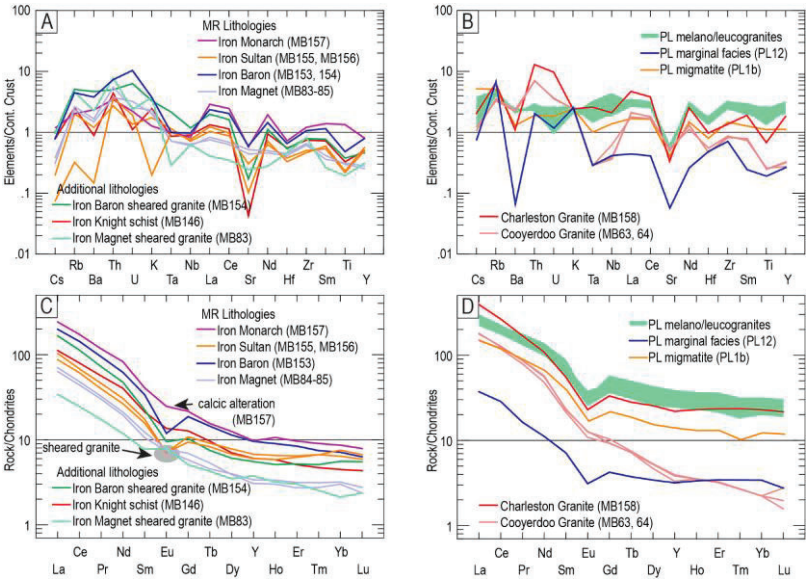

Fig. 10. Continental crust normalized trace element plots (normalization values after Rudnick and Gao, 2004). (A) Distribution of trace elements in MR samples. (B) Distribution of trace elements in the reference lithologies as marked. (C, D) Chondrite-normalized REE + Y patterns for MR samples and reference lithologies.

form a group, while two are younger outliers. The nine grains that comprise the main group give a $^{207}Pb/^{206}Pb$ weighted mean age of 3241 ± 6 Ma (MSWD = 0.97).

A total of twenty-nine analyses were taken from nineteen zircon grains from sample MB156: twenty-one core analyses; and eight rim analyses. Of the analyses, thirteen are concordant, one is reversely discordant, and the remainder are discordant (7–49%). The $^{207}Pb/^{206}Pb$ dates for individual grains are between 1.69 and 3.25 Ga with uncertainties (± 1σ) between 5 and 34 Ma. Eleven of the twenty-one core analyses have discordance < 5% and form a group with a $^{207}Pb/^{206}Pb$ weighted mean age of 3238 ± 9 Ma (MSWD = 3.1; Fig. 13B). Two of the eight rim analyses, although concordant, do not overlap. Therefore, the oldest of these two grains (2606 ± 9 Ma) is used to represent the timing of rim growth. The results for the two samples from the Sultan prospect indicate two stages of zircon growth a ~3.24 Ga and ~2.6 Ga. The former age is interpreted to represent the timing of igneous crystallization while the latter rim age potentially represents the timing of a metamorphic overprint.

4.6.7. Iron Magnet

Zircon grains from Iron Magnet granitoids (samples MB84 and MB85) display well-rounded margins, and although oscillatory zoning is apparent, the grains are homogenous grey throughout with mottled domains in CL images (Fig. 11G). Twenty-six analyses were performed on twenty-six individual zircon grains (Figs. A2). Of these analyses, two are concordant (< 5%), two are reversely discordant, and the remaining analyses have discordance ranging from 14 to 59% (Fig. 13C). The $^{207}Pb/^{206}Pb$ dates range from 2.37 to 3.05 Ga with uncertainties (± 1σ) ranging from 8 to 46 Ma. The large degree of scatter by the analyses does not allow for a discordia line to be formed. However, the

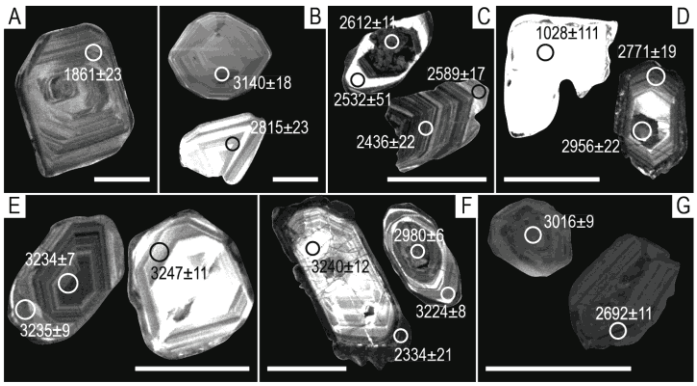

Fig. 11. Cathodoluminescence images of zircon grains and their respective $^{207}Pb/^{206}Pb$ ages (± 1σ) from the dated samples showing representative textures and morphologies within individual samples. (A) Port Lincoln (sample PL8). (B) Cooyerdoo Granite (sample MB63-64). (C) Iron Monarch (sample MB157). (D) Iron Baron (sample MB153). (E, F) Sultan prospect (sample MB155 and MB156, respectively). (G) Iron Magnet (sample MB84-85). Scale bars are 100 μm.

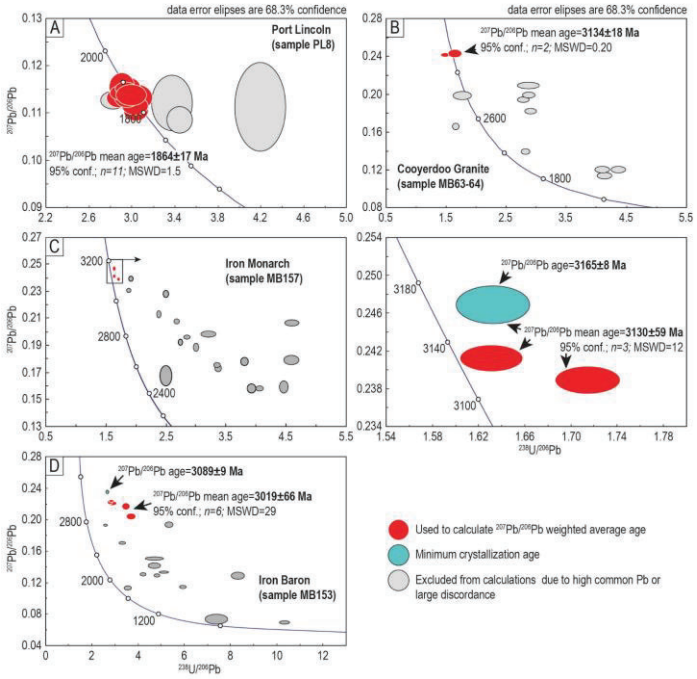

Fig. 12. Tera-Wasserburg diagrams presenting SHRIMP U-Pb data for zircon in granites from (A) Port Lincoln; (B) Cooyerdoo Granite; (C) Iron Monarch; and (D) Iron Baron. Inset in (C) shows enlarged cluster of data used for weighted $^{207}Pb/^{206}Pb$ age.

three most concordant grains (≤7%) give a weighted mean date of 3023 ± 33 Ma (MSWD = 1.5), which is interpreted as the igneous crystallization age of the granite.

5. Discussion

5.1. Significance of granite overprints

The alkali-calcic metasomatism reported here for the first time for the MR granitoids (Figs. 7 and 8) is comparable with alteration reported for Hiltaba Suite granitoids in the Eyre Peninsula (Samphire pluton; Domnick et al., 2018) and in the Olympic Cu-Au province (Ismail et al., 2014; Kontonikas-Charos et al., 2014, 2017, 2018b). Alkali metasomatism occurs early in the formation of IOCG systems (Barton, 2014 and references therein), and is recognized as a regional-scale feature of the Olympic Cu-Au Province on the eastern margin of the Gawler Craton, notably in the Moonta area of the Yorke Peninsula (Conor et al., 2010). However, the aforementioned mineralogical studies have shown that alkali-calcic metasomatism can be difficult to recognize as it can take place via pseudomorphic replacement of minerals and will not necessary lead to changes in the overall chemistry of the rock (Kontonikas-Charos et al., 2017). For example, the Charleston Granite preserves magmatic feldspars and biotite to some extent and appears as 'fresh granite' on discriminant plots (Fig. 9A, B) despite displaying feldspar albitization and chloritization of biotite.

The recognized alteration features within the granites studied here are indicative of fluid-rock interaction with hydrothermal fluids attributable to IOCG-style mineralization. Breakdown of igneous minerals can release some of the enriched elements, e.g., Ca, Na from plagioclase, and Fe, Mg, Ti from mafic minerals, but the presence of Ba-rich K-feldspar and formation of abundant REE + Y (synchysite, Th-rich monazite) is likely introduced from external fluids percolating the granitoids.

Syn-metamorphic ductile deformation leading to augen-gneissic fabrics at Iron Magnet or possibly also partial melting at Iron Baron (lobate-quartz textures; Fig. 8B, E) is distinct from the alkali-calcic alteration described above. Formation of myrmekites (plagioclase + quartz) is observed in all cases and is also a characteristic of the *syn*-orogenic granitoids of Donington Suite (PL granites). At Iron Magnet, granitoid deformation during high-grade metamorphism at amphibolite-facies is a feasible suggestion to account for the observed alteration, considering the presence of amphibolites within the same outcrop face (Keyser et al., 2018). This is also supported by the ~2.6 Ga metamorphic zircon overgrowths within gneissic-granites immediately west of Iron Magnet (Jagodzinski et al., 2011). Metamorphic fluid-rock interaction and possible element remobilization, e.g., REE + Y could lead to local accumulations of secondary REE + Y accessory minerals; Fig. 8H). These show association with shears and are distinct from the highest concentrations of Σ(REE + Y) at Iron Monarch showing a pseudomorphic replacement of clinozoisite or titanite by synchysite (Table 3; Fig. 7C, D) attributable to alkali-calcic metasomatism.

The petrographic evidence for overprinting in granites adjacent to orebodies substantiates the interpretation of trace element signatures in iron-oxides reported from MR deposits (Keyser et al., 2018) as indicative of a granitic affiliation, albeit either released during metamorphism, or alternatively, from younger plutons yet to be discovered. The differences in the alteration styles and intensity within granitoids from north to south along the belt is also concordant with the discriminative and variance structure of trace element signatures in hematite from MR deposits (Dmitrijeva et al., 2018).

Table 4
U, Th and Pb isotope data.

Spot	% ^{206}Pbc	U ppm	Th ppm	^{206}Pb* ppm	^{232}Th/^{238}U	± %	Age ^{206}Pb/^{238}U	± 1σ	Age ^{207}Pb/^{206}Pb	± 1σ	Age ^{208}Pb/^{232}Th	± 1σ	% Disc.	Isotopic Ratio ^{207}Pb*/^{206}Pb*	± %	Isotopic Ratio ^{207}Pb*/^{235}U	± %	Isotopic Ratio ^{206}Pb*/^{238}U	± %	err corr
Sample PL8																				
1	0.15	185	72	52	0.40	2.05	1840	56	1853	30	2319	103	1	0.113	1.7	5.16	3.9	0.330	3.5	0.9
2	0.33	432	173	122	0.41	1.39	1834	40	1808	24	2060	70	−2	0.111	1.3	5.02	2.8	0.329	2.5	0.9
3	0.30	367	172	107	0.48	1.49	1879	44	1854	24	2369	79	−2	0.113	1.3	5.29	3.0	0.339	2.7	0.9
4	0.00	244	94	70	0.40	1.86	1857	51	1861	23	2340	89	0	0.114	1.3	5.24	3.4	0.334	3.2	0.9
5	0.03	495	215	146	0.45	1.32	1902	40	1889	17	2432	68	−1	0.116	0.9	5.47	2.6	0.343	2.4	0.9
6	0.95	633	441	158	0.72	1.11	1643	33	1775	31	903	45	8	0.109	1.7	4.34	2.8	0.290	2.3	0.8
7	−0.07	371	136	109	0.38	1.53	1906	44	1888	31	2422	79	−1	0.116	1.7	5.48	3.2	0.344	2.7	0.8
8	0.07	379	138	115	0.38	1.49	1954	44	1843	20	2459	78	−7	0.113	1.1	5.50	2.9	0.354	2.6	0.9
9	−0.04	563	223	167	0.41	1.21	1914	38	1868	16	2224	60	−3	0.114	0.9	5.45	2.4	0.346	2.3	0.9
10	−0.29	349	155	101	0.46	1.55	1878	45	1885	24	2445	84	0	0.115	1.3	5.38	3.1	0.338	2.8	0.9
11	0.19	421	154	126	0.38	1.47	1924	43	1851	22	2370	78	−5	0.113	1.2	5.43	2.9	0.348	2.6	0.9
12	0.13	391	141	111	0.37	1.47	1840	42	1824	21	2308	75	−1	0.111	1.1	5.08	2.9	0.330	2.7	0.9
13	1.31	156	92	40	0.61	2.32	1675	55	1835	63	2019	117	10	0.112	3.5	4.59	5.1	0.297	3.7	0.7
14	1.42	143	83	29	0.60	2.17	1378	46	1820	101	1577	100	27	0.111	5.6	3.66	6.7	0.238	3.7	0.6
15	−0.02	631	377	184	0.62	1.14	1885	36	1882	15	2372	58	0	0.115	0.8	5.39	2.3	0.340	2.2	0.9
Sample MB62		384																		
1	2.07	620	595	192	0.99	1.16	1981	39	2778	17	1638	101	33	0.194	1.0	9.63	2.5	0.360	2.3	0.9
2	0.30	129	243	67	1.94	2.59	3062	109	3140	18	1735	90	3	0.243	1.1	20.38	4.6	0.608	4.5	1.0
3	3.21	1183	426	233	0.37	0.90	1330	22	1963	35	2120	74	36	0.120	2.0	3.81	2.7	0.229	1.9	0.7
4	4.09	1133	162	238	0.15	0.50	1408	24	1960	34	2682	171	31	0.120	1.9	4.05	2.7	0.244	1.9	0.7
5	1.69	638	230	189	0.37	1.16	1908	36	2673	19	2719	100	33	0.182	1.1	8.65	2.5	0.344	2.2	0.9
6	1.49	590	244	177	0.43	1.22	1927	40	2819	17	2036	94	36	0.199	1.0	9.57	2.6	0.348	2.4	0.9
7	3.32	1065	291	221	0.28	2.00	1395	24	1866	38	1327	101	28	0.114	2.1	3.80	2.9	0.242	1.9	0.7
8	0.09	285	367	165	1.33	1.82	3326	81	3131	11	4090	136	−8	0.242	0.7	22.50	3.2	0.675	3.1	1.0
9	2.87	2039	420	621	0.21	0.70	1957	28	2220	24	4233	150	14	0.139	1.4	6.82	2.2	0.355	1.6	0.8
10	0.00	76	28	37	0.38	3.50	2895	135	2815	23	3415	226	−4	0.199	1.4	15.53	6.0	0.567	5.8	1.0
11	5.00	718	679	373	0.98	1.14	3047	54	2521	23	2392	85	−26	0.166	1.4	13.86	2.6	0.604	2.2	0.8
12	1.74	523	430	157	0.85	2.29	1929	71	2901	17	2072	102	39	0.209	1.0	10.07	4.4	0.349	4.2	1.0
Sample MB157																				
1	0.68	523	435	189	0.86	0.21	2258	20	2928	14	2190	30	27	0.213	0.9	12.32	1.4	0.420	1.0	0.8
2	1.14	614	334	185	0.56	0.76	1941	23	2795	9	1718	37	35	0.196	0.5	9.50	1.5	0.351	1.4	0.9
3	5.98	603	196	173	0.34	1.32	1854	17	2728	16	1790	94	37	0.188	1.0	8.66	1.4	0.333	1.0	0.7
4	0.12	199	339	105	1.76	0.29	3080	32	3165	8	2966	40	3	0.247	0.5	20.85	1.4	0.613	1.3	0.9
5	0.29	407	144	204	0.36	0.28	2962	26	3113	7	2775	47	6	0.239	0.4	19.21	1.2	0.583	1.1	0.9
6	1.95	684	1612	128	2.43	0.73	1271	19	2880	13	332	9	61	0.207	0.8	6.21	1.8	0.218	1.7	0.9
7	1.69	238	329	45	1.43	1.63	1271	20	2647	20	153	15	57	0.179	1.2	5.39	2.1	0.218	1.7	0.8
8	2.71	567	268	182	0.49	1.77	2045	19	2889	11	1068	52	34	0.208	0.7	10.70	1.3	0.373	1.1	0.9
9	3.98	512	510	116	1.03	0.19	1506	14	2637	19	255	25	48	0.178	1.1	6.47	1.6	0.263	1.1	0.7
10	2.59	954	419	202	0.45	1.05	1419	13	2437	14	1196	37	46	0.158	0.8	5.38	1.3	0.246	1.0	0.8
11	0.23	394	72	181	0.19	0.35	2754	25	3059	7	2714	66	12	0.231	0.4	16.98	1.2	0.533	1.1	0.9
12	3.12	870	377	191	0.45	0.53	1465	15	2436	22	1356	54	44	0.158	1.3	5.57	1.7	0.255	1.2	0.7
13	1.71	540	212	138	0.41	2.80	1680	15	2589	17	907	52	40	0.173	1.0	7.11	1.4	0.298	1.0	0.7
14	3.33	670	184	180	0.28	8.89	1754	40	2812	12	1630	188	43	0.198	0.8	8.55	2.7	0.313	2.6	1.0
15	1.78	568	172	195	0.31	0.74	2170	19	3040	12	1733	71	34	0.228	0.8	12.59	1.3	0.400	1.0	0.8
16	6.75	804	137	155	0.18	0.80	1304	12	2446	33	1180	202	51	0.159	1.9	4.92	2.2	0.224	1.0	0.5
17	1.81	470	646	148	1.42	1.16	2006	18	2762	12	166	16	32	0.192	0.7	9.68	1.3	0.365	1.1	0.8
18	2.09	664	458	170	0.71	1.05	1684	15	2612	11	1223	28	40	0.176	0.7	7.23	1.2	0.299	1.0	0.8
19	1.53	27	0.38	9.2	0.01	4.41	2175	51	2532	51	201	5693	17	0.167	3.0	9.26	4.1	0.401	2.7	0.7
20	0.21	279	133	126	0.49	0.74	2715	26	3117	8	2270	40	16	0.239	0.5	17.29	1.3	0.524	1.2	0.9
21	0.05	380	90	200	0.24	0.34	3082	27	3128	6	2922	44	2	0.241	0.4	20.39	1.2	0.613	1.1	0.9

(continued on next page)

Table 4 (*continued*)

Spot	% ^{206}Pbc	U ppm	Th ppm	^{206}Pb* ppm	^{232}Th /^{238}U	± %	Age ^{206}Pb /^{238}U	± 1σ	^{207}Pb /^{206}Pb	± 1σ	^{208}Pb /^{232}Th	± 1σ	% Disc.	Isotopic Ratio ^{207}Pb*/^{206}Pb*	± %	^{207}Pb* /^{235}U	± %	^{206}Pb* /^{238}U	± %	err corr
22	4.49	629	305	243	0.50	6.24	2396	189	2932	85	1878	558	22	0.213	5.2	13.25	10.8	0.450	9.5	0.9
23	4.45	549	293	198	0.55	3.02	2262	164	2929	88	1915	530	27	0.213	5.4	12.35	10.1	0.420	8.6	0.8

Spot	% ^{206}Pbc	U ppm	Th ppm	^{206}Pb* ppm	^{232}Th /^{238}U	± %	Age ^{206}Pb* /^{238}U	± 1σ	^{207}Pb* /^{206}Pb*	± 1σ	^{208}Pb* /^{232}Th	± 1σ	% Disc.	Isotopic Ratio ^{207}Pb*/^{206}Pb*	± %	^{207}Pb* /^{235}U	± %	^{206}Pb* /^{238}U	± %	err corr
Sample MB153																				
1	2.65	509	125	145	0.25	1.17	1784	39	1966	36	3775	161	7	0.121	2.0	5.51	3.0	0.331	2.3	0.7
2	−0.69	108	33	12	0.32	2.49	803	35	1028	111	1146	98	22	0.074	5.5	1.37	7.0	0.135	4.4	0.6
3	0.69	534	321	131	0.62	1.12	1623	53	2956	22	1665	71	51	0.217	1.4	8.57	3.7	0.287	3.4	0.9
4	1.93	862	444	139	0.53	0.96	1131	24	2771	19	734	43	65	0.193	1.2	4.99	2.4	0.187	2.2	0.9
5	2.21	3859	289	321	0.08	0.51	588	8	917	40	1317	84	37	0.070	2.0	0.93	2.4	0.097	1.4	0.6
6	0.22	504	129	152	0.26	1.28	1897	43	3008	10	3259	95	41	0.224	0.6	10.80	2.6	0.350	2.5	1.0
7	0.12	884	196	292	0.23	0.92	2071	35	2769	8	3135	82	28	0.193	0.5	10.24	2.0	0.384	1.9	1.0
8	0.48	1135	558	293	0.51	2.00	1644	49	2561	12	2521	89	38	0.170	0.7	7.06	3.1	0.301	3.0	1.0
9	0.64	1700	110	310	0.07	0.68	1230	62	2351	16	2536	204	52	0.150	1.0	4.40	5.5	0.212	5.4	1.0
10	0.30	1347	253	245	0.19	0.78	1217	43	2247	26	2092	82	49	0.142	1.5	4.14	4.0	0.212	3.7	0.9
11	0.42	1503	235	253	0.16	0.68	1143	29	2143	13	1639	59	50	0.133	0.7	3.60	2.7	0.196	2.6	1.0
12	1.70	1688	378	244	0.23	0.69	988	16	1872	25	1494	73	50	0.115	1.4	2.66	2.1	0.168	1.6	0.8
13	0.46	1435	204	256	0.15	0.69	1213	19	2084	21	1405	59	46	0.129	1.2	3.69	2.0	0.208	1.6	0.8
14	3.77	696	196	162	0.29	0.98	1539	53	2859	21	1708	131	51	0.204	1.3	7.62	3.8	0.271	3.6	0.9
15	0.24	340	79	101	0.24	1.45	1886	85	2986	12	3211	165	41	0.221	0.8	10.56	5.0	0.347	5.0	1.0
16	6.78	5609	1723	77	0.32	0.45	94	3	1817	95	268	17	95	0.111	5.2	0.24	5.9	0.016	2.7	0.5
17	5.73	1995	247	206	0.13	1.16	707	17	2077	41	2174	134	68	0.128	2.3	2.13	3.3	0.120	2.3	0.7
18	0.20	285	74	88	0.27	1.60	1941	49	2997	13	3179	109	39	0.222	0.8	10.99	2.9	0.359	2.7	1.0
19	0.19	606	300	195	0.51	1.17	1967	28	3089	9	3494	75	39	0.235	0.5	12.14	1.6	0.374	1.5	0.9
20	0.77	798	329	162	0.43	1.00	1364	26	2102	20	1498	46	39	0.130	1.1	4.26	2.3	0.237	2.0	0.9
Sample MB155																				
1	0.05	243	124	134	0.53	0.33	3192	31	3230	7	3082	52	1	0.257	0.5	22.73	1.3	0.641	1.2	0.9
2	0.10	179	68	82	0.39	0.90	2767	64	3218	18	3047	100	17	0.255	1.1	18.87	3.1	0.536	2.8	0.9
3	0.15	118	55	65	0.48	1.54	3180	39	3212	11	3059	90	1	0.254	0.7	22.37	1.7	0.638	1.5	0.9
4	0.14	194	106	107	0.56	0.97	3193	33	3246	8	3088	56	2	0.260	0.5	22.97	1.4	0.641	1.3	0.9
5	0.01	239	151	131	0.65	1.37	3178	31	3234	7	3145	58	2	0.258	0.5	22.67	1.3	0.637	1.2	0.9
6	0.07	163	83	92	0.53	0.42	3248	50	3235	9	3079	66	−1	0.258	0.6	23.31	2.1	0.655	2.0	1.0
7	0.08	155	104	85	0.69	1.06	3203	36	3238	9	3104	58	1	0.258	0.6	22.94	1.5	0.644	1.4	0.9
8	0.18	285	120	110	0.43	2.19	2389	24	3100	9	3065	95	27	0.237	0.6	14.67	1.3	0.449	1.2	0.9
9	0.00	236	103	118	0.45	0.74	2969	30	3194	8	3026	66	9	0.251	0.5	20.28	1.3	0.585	1.2	0.9
10	0.21	268	177	117	0.68	0.44	2643	26	3215	8	2615	38	22	0.255	0.5	17.80	1.3	0.507	1.2	0.9
11	0.33	286	32	116	0.12	1.15	2491	26	2881	14	3497	153	16	0.207	0.8	13.45	1.5	0.472	1.2	0.8
12	0.02	203	108	109	0.55	0.35	3135	31	3242	8	3132	46	4	0.259	0.5	22.39	1.4	0.626	1.3	0.9
13	0.68	376	83	101	0.23	2.62	1749	17	2964	17	2193	83	47	0.218	1.1	9.36	1.5	0.312	1.1	0.7
14	0.11	196	154	103	0.81	0.32	3086	31	3214	8	3024	44	5	0.255	0.5	21.56	1.4	0.614	1.3	0.9
15	0.45	236	60	88	0.26	0.43	2312	64	2904	11	1588	87	24	0.210	0.7	12.48	3.4	0.431	3.3	1.0
17	0.05	229	80	120	0.36	0.38	3079	30	3215	8	2947	47	5	0.255	0.5	21.52	1.3	0.612	1.2	0.9
18	0.27	450	277	173	0.64	0.51	2385	21	3108	7	2357	38	28	0.238	0.4	14.71	1.1	0.448	1.1	0.9
19	0.23	210	38	88	0.19	0.49	2557	26	3120	9	2321	75	22	0.240	0.6	16.11	1.4	0.487	1.2	0.9
20	−0.03	66	43	37	0.68	0.59	3218	47	3259	13	3249	71	2	0.262	0.8	23.38	2.0	0.647	1.8	0.9
21	0.13	335	177	172	0.55	0.69	3028	28	3174	7	2996	55	6	0.248	0.4	20.53	1.2	0.599	1.1	0.9
22	0.46	240	39	72	0.17	2.87	1923	21	2966	20	2535	115	40	0.218	1.2	10.45	1.7	0.348	1.2	0.7

(*continued on next page*)

Table 4 (*continued*)

Spot	% $^{206}Pb_c$	U ppm	Th ppm	$^{206}Pb^*$ ppm	$^{232}Th/^{238}U$	± %	Age $^{206}Pb/^{238}U$	± 1σ	$^{207}Pb/^{206}Pb$	± 1σ	$^{208}Pb/^{232}Th$	± 1σ	% Disc.	Isotopic Ratio $^{207}Pb^*/^{206}Pb^*$	± %	$^{207}Pb^*/^{235}U$	± %	$^{206}Pb^*/^{238}U$	± %	err corr
Sample MB156														Spot						
1	−0.01	173	78	95	0.46	0.80	3191	33	3236	8	3045	52	2	0.258	0.5	22.81	1.4	0.641	1.3	0.9
2	0.91	1099	134	201	0.13	0.40	1246	14	2258	12	1878	76	49	0.142	0.7	4.19	1.4	0.213	1.3	0.9
3	0.89	441	65	131	0.15	0.80	1914	17	2683	19	2008	145	33	0.183	1.1	8.73	1.5	0.346	1.0	0.7
4	0.06	204	184	113	0.93	1.21	3209	32	3252	8	3149	55	2	0.261	0.5	23.21	1.4	0.645	1.3	0.9
5	0.15	358	142	156	0.41	0.28	2640	24	3155	7	771	24	20	0.245	0.4	17.13	1.2	0.506	1.1	0.9
6	0.02	327	307	174	0.97	0.55	3112	37	3233	6	3072	48	5	0.258	0.4	22.06	1.5	0.621	1.5	1.0
7	0.00	306	186	159	0.63	0.27	3050	28	3229	6	3080	38	7	0.257	0.4	21.44	1.2	0.605	1.1	0.9
8	−0.03	358	45	197	0.13	0.44	3194	28	3262	6	3187	58	3	0.263	0.4	23.21	1.2	0.641	1.1	0.9
9	1.49	695	46	305	0.07	1.46	2662	22	2606	9	2816	254	−3	0.175	0.5	12.34	1.1	0.511	1.0	0.9
10	0.39	248	309	102	1.29	0.48	2523	25	3223	9	2895	39	26	0.256	0.5	16.92	1.3	0.479	1.2	0.9
11	0.15	533	162	290	0.31	2.58	3161	26	3183	5	3245	97	1	0.250	0.3	21.79	1.1	0.633	1.0	1.0
12	0.20	127	111	70	0.91	0.40	3187	37	3239	10	2805	49	2	0.259	0.7	22.80	1.6	0.639	1.5	0.9
13	0.52	783	198	260	0.26	2.38	2105	22	2662	7	616	43	24	0.181	0.4	9.63	1.3	0.386	1.2	0.9
14	0.09	200	104	108	0.54	1.11	3153	46	3224	8	2982	77	3	0.256	0.5	22.29	1.9	0.631	1.8	1.0
15	1.66	916	56	200	0.06	1.36	1458	16	2291	13	3002	177	41	0.145	0.8	5.09	1.5	0.254	1.3	0.9
16	0.07	242	105	112	0.45	1.99	2792	28	3215	8	2167	86	16	0.255	0.5	19.05	1.3	0.542	1.2	0.9
17	0.01	181	71	99	0.41	0.41	3177	33	3221	8	2933	48	2	0.256	0.5	22.46	1.4	0.637	1.3	0.9
18	0.00	300	254	119	0.88	0.49	2453	24	2531	9	2426	32	4	0.167	0.6	10.68	1.3	0.463	1.2	0.9
19	0.24	200	183	88	0.94	1.10	2656	40	3192	10	1542	38	20	0.251	0.6	17.65	1.9	0.510	1.8	0.9
20	1.82	1560	167	218	0.11	2.97	970	9	1690	34	1116	124	46	0.104	1.9	2.32	2.1	0.162	0.9	0.5
21	0.32	1302	30	326	0.02	0.83	1647	14	2277	7	3427	189	31	0.144	0.4	5.78	1.0	0.291	0.9	0.9
22	0.25	72	38	36	0.55	0.61	2959	43	3247	15	3244	112	11	0.260	1.0	20.89	2.1	0.583	1.8	0.9
23	−0.03	87	56	44	0.66	0.91	2993	40	3240	12	3030	64	10	0.259	0.8	21.10	1.8	0.591	1.7	0.9
24	2.35	953	94	232	0.10	0.91	1610	24	2334	21	3547	201	35	0.149	1.2	5.83	2.1	0.284	1.7	0.8
25	0.03	297	180	163	0.62	0.28	3180	29	3233	6	3073	39	2	0.258	0.4	22.66	1.2	0.638	1.2	0.9
26	0.30	139	65	74	0.49	0.44	3118	35	3243	10	3014	64	5	0.259	0.6	22.25	1.6	0.622	1.4	0.9
27	0.11	243	133	132	0.56	0.32	3156	30	3234	7	3021	44	3	0.258	0.5	22.46	1.3	0.632	1.2	0.9
28	0.24	562	236	232	0.43	2.28	2525	22	2980	6	2708	77	18	0.220	0.4	14.54	1.1	0.479	1.0	0.9
29	0.02	192	17	104	0.09	2.16	3143	32	3224	8	2108	86	3	0.256	0.5	22.21	1.4	0.628	1.3	0.9
Sample MB84																				
1	0.89	1129	205	575	0.19	0.80	2999	44	2636	8	4152	130	−17	0.178	0.5	14.56	1.9	0.592	1.8	1.0
2	1.26	1006	363	278	0.37	0.87	1799	29	2507	17	2408	65	32	0.165	1.0	7.32	2.1	0.322	1.8	0.9
3	0.64	703	79	270	0.12	1.09	2386	42	2753	11	3549	167	16	0.191	0.7	11.81	2.2	0.448	2.1	1.0
4	2.35	704	144	182	0.21	1.06	1698	30	2464	22	3231	136	35	0.161	1.3	6.68	2.4	0.301	2.0	0.8
5	1.59	1234	426	402	0.36	0.81	2072	31	2541	12	2228	66	22	0.168	0.7	8.80	1.9	0.379	1.8	0.9
6	0.86	1748	720	273	0.43	1.12	1076	34	2366	22	1206	59	59	0.152	1.3	3.80	3.7	0.182	3.5	0.9
7	0.59	618	88	239	0.15	1.21	2397	44	2760	12	2922	150	16	0.192	0.7	11.93	2.3	0.450	2.2	0.9

(*continued on next page*)

Table 4 (*continued*)

Spot	% ^{206}Pbc	U ppm	Th ppm	^{206}Pb* ppm	^{232}Th /^{238}U	± %	Age ^{206}Pb* /^{238}U	± 1σ	^{207}Pb* /^{206}Pb*	± 1σ	^{208}Pb* /^{232}Th	± 1σ	% Disc.	Isotopic Ratio ^{207}Pb* /^{206}Pb*	± %	^{207}Pb* /^{235}U	± %	^{206}Pb* /^{238}U	± %	err corr
8	0.73	504	114	174	0.23	1.26	2177	44	2794	14	3004	124	26	0.196	0.9	10.87	2.5	0.402	2.4	0.9
9	0.20	373	145	182	0.40	1.59	2899	62	3020	10	3414	108	5	0.225	0.6	17.65	2.7	0.568	2.7	1.0
10	0.25	414	81	211	0.20	1.42	3003	61	3016	9	4019	134	1	0.225	0.6	18.40	2.6	0.593	2.5	1.0
11	0.34	407	207	152	0.53	1.46	2331	51	2868	17	3381	101	22	0.205	1.1	12.32	2.8	0.436	2.6	0.9
12	0.42	705	180	214	0.26	1.10	1953	35	2692	11	2642	78	32	0.184	0.7	8.99	2.2	0.354	2.1	1.0
13	0.62	1082	380	360	0.36	0.92	2108	34	2605	10	2214	62	22	0.175	0.6	9.33	2.0	0.387	1.9	1.0
14	0.55	734	60	216	0.08	2.25	1896	34	2417	19	2827	291	25	0.156	1.1	7.37	2.4	0.342	2.1	0.9
15	0.30	1843	859	568	0.48	0.67	1977	28	2381	8	2155	47	20	0.153	0.4	7.58	1.7	0.359	1.7	1.0
16	1.49	667	167	192	0.26	1.14	1860	37	2693	16	2729	123	36	0.184	1.0	8.50	2.5	0.334	2.3	0.9
17	0.20	1177	759	321	0.67	0.84	1777	28	2526	8	1119	25	34	0.167	0.5	7.30	1.9	0.317	1.8	1.0
18	0.82	191	60	106	0.32	2.08	3204	54	3046	15	4977	186	−7	0.229	0.9	20.34	2.3	0.644	2.1	0.9
19	0.56	668	70	226	0.11	1.17	2142	40	2624	13	3407	175	22	0.177	0.8	9.61	2.3	0.394	2.2	0.9
20	0.89	971	181	212	0.19	0.45	1458	74	2708	14	2433	169	51	0.186	0.8	6.51	5.8	0.254	5.7	1.0
21	0.75	884	266	271	0.31	10.20	1966	53	2684	12	2061	230	31	0.183	0.7	9.02	3.2	0.357	3.1	1.0
22	0.77	937	233	259	0.26	1.02	1800	31	2381	14	2489	78	28	0.153	0.8	6.80	2.2	0.322	2.0	0.9
23	12.41	400	96	150	0.25	1.50	2340	53	3005	46	9508	401	26	0.223	2.9	13.48	3.9	0.438	2.7	0.7
24	0.63	737	68	289	0.10	1.20	2422	44	2733	11	4053	241	14	0.189	0.7	11.88	2.3	0.456	2.2	1.0
25	0.18	599	204	135	0.35	1.09	1505	28	2597	12	2283	58	47	0.174	0.7	6.31	2.2	0.263	2.1	0.9
26	0.29	768	212	264	0.29	1.09	2174	39	2636	16	2633	72	21	0.178	0.9	9.86	2.3	0.401	2.1	0.9

* Common Pb corrected using measured ^{204}Pb.

5.2. Geochronology and zircon alteration relative to host granite overprinting

SHRIMP U-Pb zircon dating presented here, with the exception of the previously dated Hiltaba Suite-affiliated Charleston Granite (~1.59 Ga, Creaser and Fanning; 1993), shows Archean ages for all MR granites immediately adjacent to orebodies. The varying morphologies/textures of zircon suggest multiple alteration events that caused Pb loss. Granite/zircon alteration within the present dataset is schematically compared to the relative discordance of U-Pb data (on Tera-Wasserburg diagrams; Fig. 14). The distribution of data indicates a likely correlation. For example, sample MB153 (Iron Baron) shows multiple overprints and has $^{207}Pb/^{206}Pb$ ages ranging from 3090 to 920 Ma, whereas less-altered granite from the same area (e.g., sample MB155) contains a zircon population with greater concordance allowing for an accurate $^{207}Pb/^{206}Pb$ weighted average age (3241 ± 6 Ma).

The freshest zircon grains are those from the PL granite (sample PL8), in which the igneous assemblages are largely preserved. Analysis of zircon within this sample showed very little discordance, little $^{207}Pb/^{206}Pb$ age variance, and yields a well-constrained age consistent with published dates for magmatic crystallization of various Donington Suite lithologies from other locations (Parker et al., 1993; Jagodzinski, 2005; Reid et al., 2008a).

The oldest zircon ages within the data set (~3.24 Ga; fresh zircon yielding numerous concordant analyses; Fig. 13A, B) come from granites with sodic alteration at Sultan prospect. Zircon overgrowths give a less well constrained age of ~2.6 Ga (Fig. 14). Comparable zircon rim ages of ~2.5 Ga reported by Jagodzinski et al. (2011) for ~3.2 Ga gneissic-granites west of the southern MR were interpreted as timing of a high-grade metamorphic overprint. Fraser et al. (2010) also reported a metamorphic overprint age of 2510 ± 24 Ma from zircon rims overgrowing ~3.15 Ga magmatic cores in a granite sample (2008371085) collected WNW of Iron Knob.

In contrast to the freshest zircon grains from the PL granite and the generally fresher zircon grains in samples from the Sultan deposit, the samples from Iron Monarch, Iron Baron, Iron Magnet and the Cooyerdoo Granite, contain well-rounded zircon grains displaying corrosion/replacement by secondary minerals, and visible metamictization that give a distinct, second range of ages from ~3.17 Ga to 3.02 Ga. These granites display strong alkali-calcic alteration, and at Iron Baron and Iron Magnet, also evidence of superimposed deformation. Alteration textures shown by zircon suggests leaching and incorporation of common Pb or Pb loss and is reflected in the wide range of $^{207}Pb/^{206}Pb$ ages and greater data-point discordance on Tera-Wasserburg diagrams (Fig. 12B, C).

In summary, the alteration affecting samples from the MR is expressed not only in the formation of secondary assemblages and fabrics but is also seen in the degree of concordance/discordance shown by zircon data when plotted on Tera-Wasserburg diagrams. Irrespective of this, granites from the MR can be grouped into an older magmatic crystallization period: ~3.24 Ga (MB155, MB156); and a younger, less accurately defined period at ~3.17 Ga to 3.02 Ga (MB63-64, MB157, MB153, MB84-85). A high-grade metamorphic event at ~2.6 Ga is recognized from zircon overgrowths in a sample from the Sultan prospect.

Therefore, development of a basinal environment for BIF deposition during the Archean (~2.57–2.45 Ga) took place roughly ~500–600 Ma after granite emplacement (~3.2–3.0 Ga), and prior to the Sleafordian Orogeny at (~2.47–2.41 Ga). Significantly, the new data allow us to infer exposure, erosion and detrital accumulation of zircons from these older, Mesoarchean (~3.2–3.0 Ga) granitoids as local sources during deposition of Middleback Group, including the Cook Gap Schist.

5.3. Correlation of granites across the northeastern Eyre Peninsula

Prior to the present study, basement geology underlying the MR was poorly understood. Earlier studies consider that the Middleback Group

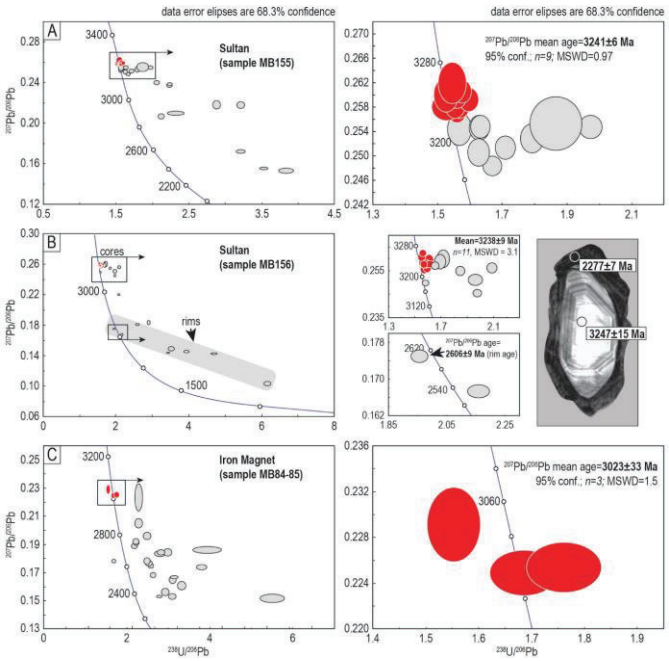

Fig. 13. Tera-Wasserburg diagrams presenting SHRIMP U-Pb data for zircon in granites from (A, B) the Sultan prospect and (C) Iron Magnet. Insets show enlarged clusters of data used for weighted $^{207}Pb/^{206}Pb$ ages. Inset in (B) shows a zircon grain with core and rim features and their respective $^{207}Pb/^{206}Pb$ ages. Data point colors following legend in Fig. 12.

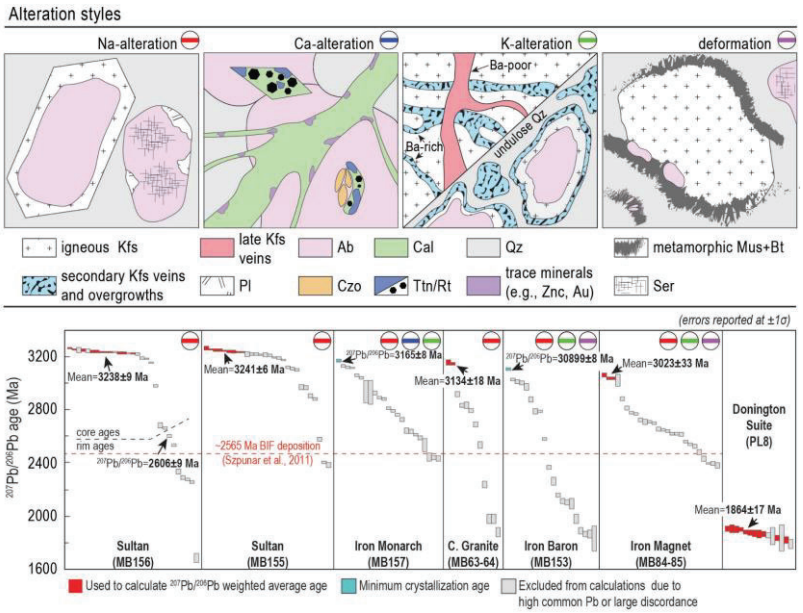

Fig. 14. Schematic diagram showing representative alteration types observed throughout the MR and their impact on the range of individual $^{207}Pb/^{206}Pb$ zircon ages, highlighting the correlation between degree of alteration and discordance throughout the dataset. Abbreviations: Ab-albite; Au-native gold; Bt-biotite; Cal-calcite; Czo-clinozoisite; Kfs-K-feldspar; Mus-muscovite; Pl-plagioclase; Qz-quartz; Rt-rutile; Ser-sericite; Ttn-titanite; Znc-zincite.

overlies gneisses or equivalent rock types belonging to the 2.54–2.45 Ga Sleaford Complex (Parker and Lemon, 1982). The discovery of Mesoarchean crust within the northeastern Eyre Peninsula (Fraser et al., 2010) led to a re-evaluation of the basement within this part of the Gawler Craton. However, the subsurface extent of the Mesoarchean crust remains unknown.

Fraser et al. (2010) defined the KMZ as the western boundary of the Mesoarchean crust. This delineation was based on the absence of Mesoarchean zircons west of the KMZ and surface heat flow differences between domains to the east and west of the KMZ. The northern and eastern extents of Mesoarchean crust are hidden beneath the extensive ~1.6 Ga Gawler Range Volcanics and ~1.75 Ga Wallaroo Group, respectively. The eastern extent was thought to correlate with the western boundary of the Australian Heat Flow Anomaly (SAFHA) in the eastern Gawler Craton (Fraser et al., 2010). The southern reach of the Mesoarchean crust is believed to taper off towards the south amongst splays of the KMZ, and where the regionally expansive ~1.85 Ga Donington Suite appears. Fraser et al. (2010) noted that inherited zircon grains of Mesoarchean age had not been identified in any Donington lithologies and this is also confirmed here. Several studies have observed that younger granites proximal to the MR contain ~3.15 Ga inherited zircon grains (McAvaney, 2012, and references therein). However, the presence of Mesoarchean basement beneath the MR has been largely implied since the discovery of the adjacent Cooyerdoo Granite (Fraser et al., 2010). For example, Szpunar et al. (2011) reported that prominent age peaks within the Cook Gap Schist included a ~3.15 Ga age group, with the Cooyerdoo Granite as the only known source. However, no contact has been found between the stratigraphically lowest unit within the Middleback Group succession, a quartz-sericite schist unit, and the Cooyerdoo Granite (Szpunar et al., 2011). Prior to the present work, interpretation was further impeded by a lack of geochronological work on granites exposed within open pits in the MR, or assessment of the association between granites and iron ores. The recognition of several age groups > 3.0 Ga in the present study suggests a more extensive distribution of the Cooyerdoo Granite suite than previously recognized and supports the presence of Mesoarchean basement beneath the entire MR BIF sequence.

The present study also highlights several age groups that may possibly represent derivatives of one another. McAvaney (2012) suggested that the ~3.25 Ga granites reported to the west of the southern MR by Jagodzinski et al. (2011) may represent a possible source for the younger (~3.15 Ga) Cooyerdoo Granite. The oldest ages observed within the present dataset are those from the Sultan prospect (~3.24 Ga), which likely represent a northward extension of this parent rock along the western margin of the MR. The Iron Monarch granite has a minimum crystallization age of 3165 ± 8 Ma as a result of discordant data, however, the true crystallization age is likely older than this and may also fit within ~3.24 Ga age group. Similarly, the Iron Baron granite has a minimum crystallization age of 3089 ± 9 Ma due to discordant data and may also have a true crystallization age closer to the ~3.24 Ga group, or to the Cooyerdoo Granite. Irrespective of the true age for either granite, it is also possible that the granites of Cooyerdoo age, as seen in the northern parts of the belt, may have been incorporated into magmas responsible for the younger granites (e.g., Iron Magnet ~3.02 Ga).

Protoliths, and thus potential sources, of equivalent age were proposed for the analogous BIF-endowed Hamersley Group (2630–2450 Ma) in the Pilbara Craton, Western Australia (Szpunar et al., 2011). Evidence for two Mesoarchean detrital zircon populations in the Gawler Craton was found lacking in that study, but are shown in the present data.

We see no evidence, based on the present data, for granites associated with either the regionally expansive Donington Suite or the Kimban Orogney (~1.73–1.69 Ga) in the immediate vicinity of the iron ores. The sole ~1.6 Ga Hiltaba-affiliated granite known is the Charleston Granite, to the south of the Middleback Ranges. The presence of other Hiltaba Suite-affiliated granitoids can, however, be inferred based on the extended alkali-calcic alteration of granitoids, which is most intense in the northern part of the belt. Such a finding can assist exploration strategies targeting Cu-Au mineralization of IOCG type in the region.

6. Concluding remarks

SHRIMP U-Pb dating of zircon in this study shows that the granites spatially associated with iron orebodies within the MR are Archean in age. The results support earlier suggestions that the basement beneath the MR sequence is part of a Mesoarchean crust that comprises much of the northern Spencer Domain. This information allows constraints to be placed on the depositional environment of BIFs.

The studied granites and schists from deposits of the MR display complex petrographic features and geochemical signatures that reflect multiple overprinting events due to interaction with fluids of both magmatic and metamorphic origins. In contrast, younger granites in proximity to the MR belt, ~1.85 Ga PL granites of the Donington Suite and ~1.6 Ga Charleston Granite, are fresher in appearance.

These findings expand the current knowledge of granites within this area of the eastern Gawler Craton. Several alteration styles are recognized from mineral associations and textures in rocks along the strike of the MR, highlighting the impact of younger post-emplacement events and implying fluid-rock interaction(s) with metasomatic fluids. Alkali-calcic alteration relating to Hiltaba-magmatism is recognized throughout the Archean MR granites, implying plutons of this affiliation may be present underneath or adjacent to the deposits. Such interactions are consistent with the trace element signatures recorded by iron-oxides from BIFs and ores along the MR (Dmitrijeva et al., 2018; Keyser et al., 2018, 2019), which indicate that ore formation has taken place in evolving environments and in the presence of felsic lithologies.

Acknowledgements

This work is a contribution to the project 'Trace elements in iron-oxides: deportment, distribution and application in ore genesis, geochronology, exploration and mineral processing', supported by BHP Olympic Dam and the South Australian Government Mining and Petroleum Services Centre of Excellence. Logistical support from site geologists at SIMEC Mining is greatly appreciated. Constructive comments from Richard Stern, one anonymous reviewer, and Editor Victoria Pease are highly appreciated and helped to significantly improve this manuscript.

Appendix A. Supplementary data

Supplementary data to this article can be found online at https://doi.org/10.1016/j.precamres.2019.01.024.

References

Arrium Mining, 2016. Ore Reserve and Resources Statement, 30th June 2016. Arrium Mining Ltd.

Barker, F., 1979. Trondhjemite: definition, environment and hypothesis of origin. In: Trondhjemites, Dacites and Related Rocks. Developments in Petrology, vol. 6, Elsevier, Amsterdam, pp. 1–12.

Barton, M., 2014. Iron oxide (–Cu–Au–REE–P–Ag–U–Co) systems. Treatise on Geochemistry. Second Edition, vol. 13. Elsevier, Amsterdam, pp. 515–541.

Claoué-Long, J.C., Compston, W., Roberts, J., Fanning, C.M., 1995. Two carboniferous ages: A comparison of SHRIMP zircon dating with conventional zircon ages and 40Ar/39Ar analysis. In: Berggren, W.A., Kent, D.V., Aubrey, M.P., Hardenbol, J. (Eds.), Geochronology time scales and global stratigraphic correlation. Society of Sedimentary Geology Special Publication 54, Tulsa, Oklahoma, SEPM, pp. 3–21.

Compston, W., Williams, I.S., Meyer, C., 1984. U-Pb geochronology of zircon from lunar breccia 73217 using a sensitive high mass-resolution ion microprobe. J. Geophys. Res. 89, 525–534.

Conor, C., Ramond, O., Baker, T., Teale, G., Say, P., Lowe, G., 2010. Alteration and mineralisation in the Moonta-Wallaroo Cu-Au mining field region, Olympic domain, South Australia. In: Porter, T.M. (ed) Hydrothermal Iron Oxide Copper-Gold &

Related Deposits: A Global Perspective, vol. 3. PGC Publishing, Adelaide, pp. 1–24.
Creaser, R.A., Fanning, C.M., 1993. A U-Pb zircon study of the Mesoproterozoic Charleston Granite, Gawler Craton South Australia. Australia J. Earth Sci. 40, 519–526.
Daly, S.J., Fanning, C.M., Fairclough, M.C., 1988. Tectonic evolution and exploration potential of the Gawler Craton South Australia. In: Hodgson, I., Hince, B. (Eds.), Geology and Mineral Potential of Major Australian Mineral Provinces. AGSO J. Australian Geol. Geophys. 17, 145-168.
Davies, M.B., 2000. Iron ore in South Australia. Primary Industries and Resources SA. Commodity Review No. 8, 35.
Dmitrijeva, M., Metcalfe, A.V., Ciobanu, C.L., Cook, N.J., Frenzel, M., Keyser, W.M., Johnson, G., Ehrig, K., 2018. Discrimination and variance structure of trace element signatures in hematite: a case study of BIF-mineralization from the Middleback Ranges, South Australia. Math. Geosci. 50, 381–415.
Domnick, U., Cook, N.J., Bluck, R., Brown, C., Ciobanu, C.L., 2018. Petrography and geochemistry of granitoids from the Samphire Pluton, South Australia: implications for uranium mineralisation in overlying sediments. Lithos 300–301, 1–19.
Ehrig, K., McPhie, J., Kamenetsky, V., 2012. Geology and mineralogical zonation of the Olympic Dam iron oxide Cu-U-Au-Ag deposit, South Australia. Econ. Geol. 16, 237–267 Special Publication.
Fanning, C.M., Flint, R.B., Parker, A.J., Ludwig, K.R., Blissett, A.H., 1988. Refined Proterozoic evolution of the Gawler Craton, South Australia, through U-Pb zircon geochronology. Precambr. Res. 40 (41), 363–386.
Fraser, G.L, Neumann, N.L, 2010. New SHRIMP U-Pb zircon ages from the Gawler Craton and Curnomona Province, South Australia, 2008-2010. Geoscience Australia 2010/16.
Fraser, G., McAvaney, S., Neumann, N., Szpunar, M., Reid, A., 2010. Discovery of early Mesoarchean crust in the eastern Gawler Craton, South Australia. Precambr. Res. 179, 1–21.
Frost, B.R., Barnes, C.G., Collins, W.C., Arculus, R.J., Ellis, D.J., Frost, C.D., 2001. A geochemical classification for granitic rocks. J. Petrol. 11, 2033–2048.
Hand, M., Reid, A., Jagodzinski, L., 2007. Tectonic framework and evolution of the Gawler Craton, southern Australia. Econ. Geol. 102, 1377–1395.
Ismail, R., Ciobanu, C.L., Cook, N.J., Teale, G.S., Giles, D., Mumm, A.S., Wade, B., 2014. Rare earths and other trace elements in minerals from skarn assemblages, Hillside iron oxide-copper-gold deposit, Yorke Peninsula, South Australia. Lithos 184–187, 456–477.
Jagodzinski, E.A., 2005. Compilation of SHRIMP U-Pb geochronological data, Olympic Domain, Gawler Craton South Australia, 2001-2003. Geoscience Australia Record 2005/20, p. 197.
Jagodzinski, E.A., McAvaney, S.O., 2016. SHRIMP U-Pb geochronology data for the northern Eyre Peninsula, 2014–2016, Report Book 2016/00001. Department of State Development, South Australia, Adelaide.
Jagodzinski, E.A., Reid, A., Farrell, F., 2011. Geochronology of the Bungalow Prospect. In: Reid, A.J., Jagodzinski, E.A., (Eds.), PACE Geochronology: Results of collaborative geochronology projects 2009-10. South Australia Department of Primary Industries and Resources, Report Book 2011/00003, pp. 42–62.
Keyser, W.M., Ciobanu, C.L., Cook, N.J., Johnson, G., Feltus, F., Johnson, S., Dmitrijeva, M., Ehrig, K., Nguyen, P., 2018. Petrography and trace element signatures of iron-oxides in deposits from the Middleback Ranges, South Australia: from banded iron formation to ore. Ore Geol. Rev. 93, 337–360.
Keyser, W.M., Ciobanu, C.L., Cook, N.J., Johnson, G., Dmitrijeva, M., Courtney-Davies, L., Feltus, F., Gilbert, S., Johnson, G., Ehrig, K., 2019. Iron-oxides constrain BIF evolution in terranes with protracted geological histories: the Iron Count prospect, Middleback Ranges, South Australia. Lithos 324–325, 20–38.
Kontonikas-Charos, A., Ciobanu, C.L., Cook, N.J., 2014. Abilitization and redistribution of REE and Y in IOCG systems: Insights from Moonta-Wallaroo, Yorke Peninsula, South Australia. Lithos 208–209, 178–201.
Kontonikas-Charos, A., Ciobanu, C.L., Cook, N.J., Ehrig, K., Krneta, S., Kamenetsky, V.S., 2017. Feldspar evolution in the Roxby Downs Granite, host to Fe-oxide Cu-Au-(U) mineralisation at Olympic Dam, South Australia. Ore Geol. Rev. 80, 838–859.
Kontonikas-Charos, A., Ciobanu, C.L., Cook, N.J., Ehrig, K., Krneta, S., Kamenetsky, V.S., 2018a. Rare earth element geochemistry of feldspars: examples from Fe-oxide Cu-Au systems in the Olympic Cu-Au Province, South Australia. Mineral. Petrol. 112, 145–172.
Kontonikas-Charos, A., Ciobanu, C.L., Cook, N.J., Ehrig, K., Ismail, R., Krneta, S., Basak, A., 2018b. Feldspar mineralogy and rare-earth element (re)mobilization in iron-oxide copper gold systems from South Australia: a nanoscale study. Mineral. Mag. 82 (S1), S173–S197.
Leevers, P., Gaughan, C., Bubner, G., 2005. The Iron Magnet deposit. Australasian Institute of Mining and Metallurgy Publication Series, Iron Ore Conference, Fremantle, WA, 19-21 September 2005.
Ludwig, K.R.A., 2009, SQUID 2.50: A User's manual: Berkeley Geochronology Center, Special Publication No. 5, p. 110, Berkeley, California.
McAvaney, S., 2012. The Cooyerdoo Granite: Paleo- and Mesoarchean basement of the Gawler Craton. MESA J. 65, 31–40.
McAvaney, S.O., Wade, C.E., Jagodzinski, E.A., 2016. Tip Top and Wertigo Granites, c. 1775 Ma magmatism on northeastern Eyre Peninsula. MESA J. 80, 63–76.
Nasdala, L., Hofmeister, W., Norberg, N., Mattinson, J.M., Corfu, F., Dörr, W., Kamo, S.L., Kennedy, A.K., Kronz, A., Reiners, P.W., Frei, D., Kosler, J., Wan, Y., Götze, J., Häger, T., Kröner, A., Valley, J.W., 2008. Zircon M257 - a homogeneous natural reference material for the ion microprobe U-Pb analysis of zircon. Geostand. Geoanal. Res. 32, 247–265.
Parker, A.J., 1980. The Kalinjala Mylonite Zone, eastern Eyre Peninsula. Quarterly Geological Notes 76, 6-11, Geological Survey of South Australia.
Parker, A.J., Daly, S.J., Flint, D.J., Flint, R.B., Preiss, W.V., Teale, G.S., 1993. Palaeoproterozoic. In: Drexel J.F., Preiss W.V. and Parker A.J. eds. The Geology of South Australia; Volume 1, The Precambrian, pp. 50–105. Geological Survey of South Australia Bulletin 54.
Parker, A.J., Fanning, C.M., Flint, R.B., Martin, A.R., Rankin, L.R., 1988. Archean-early Proterozoic granitoids, metasediments and mylonites of southern Eyre Peninsula, South Australia: Specialist Group in Tectonics and Structural Geology, Geological Society of Australia, Field Guide Series, no. 2, p. 90.
Parker, A.J., Lemon, N.M., 1982. Reconstruction of the early Proterozoic stratigraphy of the Gawler Craton, South Australia. J. Geol. Soc. Aust. 29, 221–238.
Reid, A., Hand, M., 2012. Mesoarchean to Mesoproterozoic evolution of the southern Gawler Craton, South Australia. Episodes 35, 216–225.
Reid, A., Hand, M., Jagodzinski, E., Kelsey, D., Pearson, N., 2008a. Paleoproterozoic orogenesis in the southeastern Gawler Craton, South Australia. Aust. J. Earth Sci. 55, 449–471.
Reid, A.J., McAvaney, S.O., Fraser, G.L., 2008b. Nature of the Kimban Orogeny across northern Eyre Peninsula. MESA J. 51, 25–34.
Rudnick, R.L., Gao, S., 2004. Composition of the Continental Crust. In: In: Holland, H.D., Turekian, K.K. (Eds.), Treatise on Geochem. 3. Elsevier, Amsterdam, pp. 1–64.
Sawyer, E.W., 1999. Criteria for the recognition of partial melting. Phys. Chem. Earth Part A 24, 269–279.
Schwarz, M.P., 1999. Definition of the Moody Suite, south Gawler Craton. MESA J. 13, 39–44.
Shand, S.J., 1943. The Eruptive Rocks, 2nd edition. John Wiley, New York.
Skirrow, R.G., Bastrakov, E.N., Barovich, K., Fraser, G.L., Creaser, R.A., Fanning, C.M., Raymond, O.L., Davidson, G.J., 2007. Timing of iron oxide Cu-Au-(U) hydrothermal activity and Nd isotope constraints on metal sources in the Gawler craton, South Australia. Econ. Geol. 102, 1441–1470.
Steiger, R.H., Jäger, E., 1977. Subcommission of geochronology: convention on the use of decay constants in geo- and cosmochronology. Earth Planet. Sci. Lett. 36, 359–362.
Stern, R.A., Bodorkos, S., Kamo, S.L., Hickman, A.H., Corfu, F., 2009. Measurement of SIMS instrumental mass fractionation of Pb isotopes during zircon dating. Geostand. Geoanal. Res. 33, 145–168.
Streckeisen, A., 1974. Classification and nomenclature of plutonic rocks. Geol. Rundsch. 63, 773–786.
Szpunar, M., Hand, M., Barovich, K., Jagodzinski, E., Belousova, E., 2011. Isotopic and geochemical constraints on the Paleoproterozoic Hutchison Group, southern Australia: implications for Paleoproterozoic continental reconstructions. Precambr. Res. 187, 99–126.
Vassallo, J.J., Wilson, C.J.L., 2001. Structural repetition of the Hutchison Group metasediments, Eyre Peninsula, South Australia. Aust. J. Earth Sci. 48, 331–345.
Whalen, J.B., Currie, K.L., Chappell, B.W., 1987. A-type granites: geochemical characteristics, discrimination and petrogenesis. Contrib. Miner. Petrol. 95, 407–419.
Williams, I.S., 1998. U-Th-Pb geochronology by ion microprobe. In: McKibben, M.A., Shanks, W.C. (Eds.), Applications of microanalytical techniques to understanding mineralizing processes: Reviews in Economic Geology; Volume 7, pp. 1–35.
Wingate, M.T.D., Campbell, I.H., Compston, W., Gibson, G.M., 1998. Ion microprobe U-Pb ages of Neoproterozoic basaltic magmatism in south-central Australia and implications for the breakup of Rodinia. Precambr. Res. 87, 135–159.
Yeates, G., 1990. Middleback Range iron ore deposits. In: Hughes F.E., (Eds.) Geology of the Mineral Deposits of Australia and Papua New Guinea. Australian Institute of Mining and Metallurgy Monograph 14, pp. 1045–1048.

CHAPTER 5

EPISODIC MAFIC MAGMATISM IN THE EYRE PENINSULA: DEFINING SYN- AND POST-DEPOSITIONAL BIF ENVIRONMENTS FOR IRON DEPOSITS IN THE MIDDLEBACK RANGES, SOUTH AUSTRALIA

William Keyser[1], Cristiana L. Ciobanu[1], Nigel J. Cook[1], Benjamin P. Wade[2], Allen Kennedy[3], Alkiviadis Kontonikas-Charos[1], Kathy Ehrig[4], Holly Feltus[5], Geoff Johnson[5]

[1]*School of Chemical Engineering, The University of Adelaide, Adelaide, SA 5005, Australia*

[2]*Adelaide Microscopy, The University of Adelaide, Adelaide, SA 5005, Australia*

[3]*John de Laeter Centre, Curtin University of Technology, Bentley, WA 6102, Australia*

[4]*BHP Billiton Olympic Dam, Adelaide, SA, 5000, Australia*

[5]*SIMEC Mining, Level 2 169 Fullarton Road, Dulwich, SA 5005, Australia*

Submitted for publication in Precambrian Research 27 May 2019.

Statement of Authorship

Title of Paper	Episodic mafic magmatism in the Eyre Peninsula: defining syn- and post-depositional BIF environments for iron deposits in the Middleback Ranges, South Australia
Publication Status	☐ Published ☐ Accepted for Publication ☑ Submitted for Publication ☐ Unpublished and Unsubmitted w ork w ritten in manuscript style
Publication Details	Keyser, W., Ciobanu, C.L., Cook, N.J., Wade, B.P., Kennedy, A., Kontonikas-Charos, A., Ehrig, K., Feltus, H., Johnson, G. (in review). Episodic mafic magmatism in the Eyre Peninsula: defining syn- and post-depositional BIF environments for iron deposits in the Middleback Ranges, South Australia. Precambrian Research.

Principal Author

Name of Principal Author (Candidate)	William Keyser		
Contribution to the Paper	Performed analytical work, carried out data processing and interpretation, oversaw development of work and wrote manuscript.		
Overall percentage (%)	65		
Certification:	This paper reports on original research I conducted during the period of my Higher Degree by Research candidature and is not subject to any obligations or contractual agreements with a third party that would constrain its inclusion in this thesis. I am the primary author of this paper.		
Signature		Date	4/6/2019

Co-Author Contributions

By signing the Statement of Authorship, each author certifies that:

i. the candidate's stated contribution to the publication is accurate (as detailed above);

ii. permission is granted for the candidate in include the publication in the thesis; and

iii. the sum of all co-author contributions is equal to 100% less the candidate's stated contribution.

Name of Co-Author	Cristiana L. Ciobanu		
Contribution to the Paper	Helped define direction of research, supervised development of work, assisted with data interpretation and contributed to manuscript preparation.		
Overall percentage (%)	10		
Signature		Date	4 Jun 2019

Name of Co-Author	Nigel J. Cook		
Contribution to the Paper	Helped define direction of research, supervised development of work, assisted with data interpretation and contributed to manuscript preparation.		
Overall percentage (%)	7		
Signature		Date	4/6/19

Name of Co-Author	Benjamin P. Wade		
Contribution to the Paper	Assisted with analytical instrumentation, data processing and evaluation of manuscript.		
Overall percentage (%)	4		
Signature		Date	28/5/2019

Name of Co-Author	Allen Kennedy		
Contribution to the Paper	Assisted with analytical instrumentation, data processing and evaluation of manuscript.		
Overall percentage (%)	4		
Signature		Date	28/5/2019

Name of Co-Author	Alkiviadis Kontonikas-Charos		
Contribution to the Paper	Assisted with analytical instrumentation, data processing and evaluation of manuscript.		
Overall percentage (%)	3		
Signature		Date	29/5/2019

Name of Co-Author	Kathy Ehrig		
Contribution to the Paper	Helped define research direction and assisted with evaluation of manuscript.		
Overall percentage (%)	2		
Signature		Date	3/6/2019

Name of Co-Author	Holly Feltus		
Contribution to the Paper	Helped coordinate sample collection and evaluation of manuscript.		
Overall percentage (%)	3		
Signature		Date	30/4/2019

Name of Co-Author	Geoff Johnson		
Contribution to the Paper	Helped coordinate sample collection and evaluation of manuscript.		
Overall percentage (%)	2		
Signature		Date	30/5/2019

Abstract

Banded iron formation (BIF)-derived iron ore deposits of the Middleback Ranges, Eyre Peninsula, South Australia are hosted within Archean to Paleoproterozoic basement in the southeastern Gawler Craton. Mafic sills and dikes are associated with the orebodies throughout the belt and although described previously, have never been studied in any detail. Two main types of mafic rocks, amphibolites and dolerites, are distinguishable from field occurrence and mineralogy. Amphibolites interbedded with BIFs from the Iron Magnet deposit are characterized by extensive overprinting. These amphibolites contain metamorphic assemblages of coexisting Mg-Fe- and Ca-amphiboles, almandine garnet, corundum, biotite and relict titaniferous magnetite displaying ilmenite exsolution. Crosscutting tourmaline veins indicate post-metamorphic, hydrothermal alteration that may be linked to high-T brines from a granitic source. Amphibolite petrography and geochemistry in the southern part of the belt indicate formation in a complex BIF depositional environment, with possible detrital input of titaniferous magnetite from igneous rocks. In contrast, NW-trending dolerite dikes occur throughout the belt and contain igneous assemblages consisting of magnesiohornblende and plagioclase. SHRIMP U–Pb zircon ages for amphibolites and dolerites yield two age groups. Amphibolite from Iron Magnet yields a $^{207}Pb/^{206}Pb$ weighted mean age of 2542 ± 15 Ma. The most robust $^{206}Pb/^{238}U$ weighted mean age of 782 ± 23 Ma for dolerites comes from the Iron Queen deposit in the central part of the belt. Pyroxene-rich dolerite from the southernmost Eyre Peninsula (Cape Donington) yields a $^{206}Pb/^{238}U$ weighted mean age of 1711 ± 14 Ma. LA-ICP-MS U–Pb geochronology of U-bearing hematite from the Iron Knight South deposit yields ages of ~680 Ma. Altogether, these results suggest mafic magmatism contemporaneous with Archean BIF deposition followed by a high-grade metamorphic event (~2.47-2.41 Ga Sleafordian Orogeny). Dikes from Cape Donington are, instead, associated with the 1.73-1.69

Ga Kimban Orogeny. Dolerite ages provide the first evidence for the presence of the ~800 Ma craton-scale Gairdner large igneous province in the Middleback Ranges. The young U–Pb hematite age from Iron Knight South and post-emplacement alteration of Gairdner dikes from the middle part of the belt provide additional support for multiple events leading to upgrading of iron ores.

5.1 Introduction

Archean to Proterozoic banded iron formation (BIF)-hosted iron deposits are ubiquitously found within complex terranes composed of diverse igneous and metamorphic rock suites, some of which form parts of ancient greenstone belts (e.g., Klein, 2005). Amongst the lithologies making up these terranes are packages of mafic to ultramafic rocks whose petrogenesis can be enigmatic due to ambiguous field relationships and/or extensive reworking and alteration that has obliterated their primary character. The association between BIFs and effusive mafic magmatism (basalts) was discussed in terms of emplacement of large igneous provinces, plume related mafic magmatism, or a complex interplay among mantle, tectonic, oceanic, and biospheric processes impacting on iron formation in sedimentary basins (Barley et al., 1997; Isley and Abbott, 1999; Bekker et al., 2010). Younger intrusive mafic equivalents (e.g., dolerites) are observed within many BIF deposits and are indicative of syn- or post-depositional tectono-magmatic activity. Such rocks, whether dikes or sills, also provide structural controls for ore enrichment in BIF terranes worldwide (Dalstra and Rosière, 2008). Overall, the geochemical and geochronological constraints that can be drawn from co-existing mafic and BIF lithologies can be used for reconstruction of depositional environments and subsequent tectonothermal events leading to iron ore enrichment as well as continent assembly/break-up as shown for deposits of the Hamersley province, Western Australia (e.g., Taylor et al., 2001; Müller et al., 2005).

The Middleback Ranges (MR) is a ~60 km long, N-S-striking metallogenic belt in Eyre Peninsula comprising >20 ore deposits (Fig. 1). This has been and continues to be the most important iron ore resource in South Australia, with hematite and magnetite reserves of 32.2 Mt and 56 Mt, respectively, at ~50-55% Fe (Arrium Mining, 2016). The belt is part of an Archean-Proterozoic terrane in the south-eastern Gawler Craton that has been linked, in Paleoproterozoic continental reconstructions (Szpunar et al., 2011), to the Pilbara Craton, host to the giant Hamersley iron province, Western Australia. Mafic dikes and sills displaying an intimate association with the orebodies throughout the MR belt have been previously reported (Ward, 1949; Yeates, 1990; Davies, 2000; Leevers et al., 2005) but not studied in any detail. Among these are dikes that display regional magnetic signatures akin to those of the ~800 Ma Gairdner large igneous province studied in greater detail in the eastern part of the Gawler Craton (Zhao and McCulloch, 1993; Wingate et al., 1998; Huang et al., 2015).

Petrological and multivariate statistical analysis of trace element signatures of iron-oxides from BIFs and ores have suggested domain heterogeneity throughout MR belt strike interpreted as interaction with fluids derived and/or leaching granite and mafic lithologies during ore upgrading (Dmitrijeva et al., 2018; Keyser et al., 2018). As proof of concept, U–Pb dating of hematite ore with a granite-affiliated signature and the co-existing monazite inclusions at Iron Count prospect, has shown ages concordant with one another and with the emplacement of the Wertigo Granite/volcanic rocks at ~1.79 Ga during an intracontinental rifting episode (Keyser et al., 2019a).

The purpose of the present contribution is to characterize a suite of mafic lithologies that are spatially associated with orebodies throughout the MR, and for purposes of comparison, dolerites from Cape Donington, at the southern end of Eyre Peninsula. Our approach combines detailed petrographic characterization with sensitive high-resolution ion microprobe

(SHRIMP) age constraints in order to distinguish different generations of mafic rocks. In addition, U–Pb dating of hematite from Iron Knight, one of the deposits in the southern part of the belt, is also included. Collectively, the data carry important implications for constraining the BIF depositional environment in the MR and for post-depositional overprinting and ore-forming processes, but also provides additional evidence for an Archean large igneous province connecting BIF-bearing regions in Western Australia and South Australia.

5.2 Geological Background

The deposits of the MR are hosted within the metasedimentary Hutchison Group, whereby the BIF sequences are stratigraphically below the Cook Gap Schist, a marker horizon (comprising garnet-bearing mica schists) that was recently dated at 2565 Ma (Spuznar et al., 2011). The basement rocks of this region of the Gawler Craton comprises the ~3.1 Ga Cooyerdoo Granite (Fraser et al., 2010; Keyser et al., 2019b) and the overlying Hutchison Group. The latter of these is a succession consisting of metamorphosed chemical and clastic sediments subdivided into the Darke Peake, the Cleve and the Middleback Subgroups on the basis of isotopic and geochemical differences (Szpunar et al., 2011). The Middleback Subgroup hosts the massive iron ore deposits derived from BIF (Fig. 1B).

Deformation recognized throughout the MR is attributed to three major orogenic events. Amphibolite- to granulite-facies metamorphism during the ~2.47-2.41 Ga Sleafordian Orogeny led to formation of gneissic basement units in the region, such as the Coolanie Gneiss and the Sleaford Complex. The ~1.85 Ga compressional Cornian Orogeny was of similarly high metamorphic grade and led to expansive emplacement of the Donington Suite granites and charnockites (Reid et al., 2008). Transpressional deformation during the ~1.73-1.69 Ga Kimban Orogeny led to amphibolite- to granulite-facies metamorphism and activation of major crustal structures throughout the region. Most notable of these structures is the Kalinjala

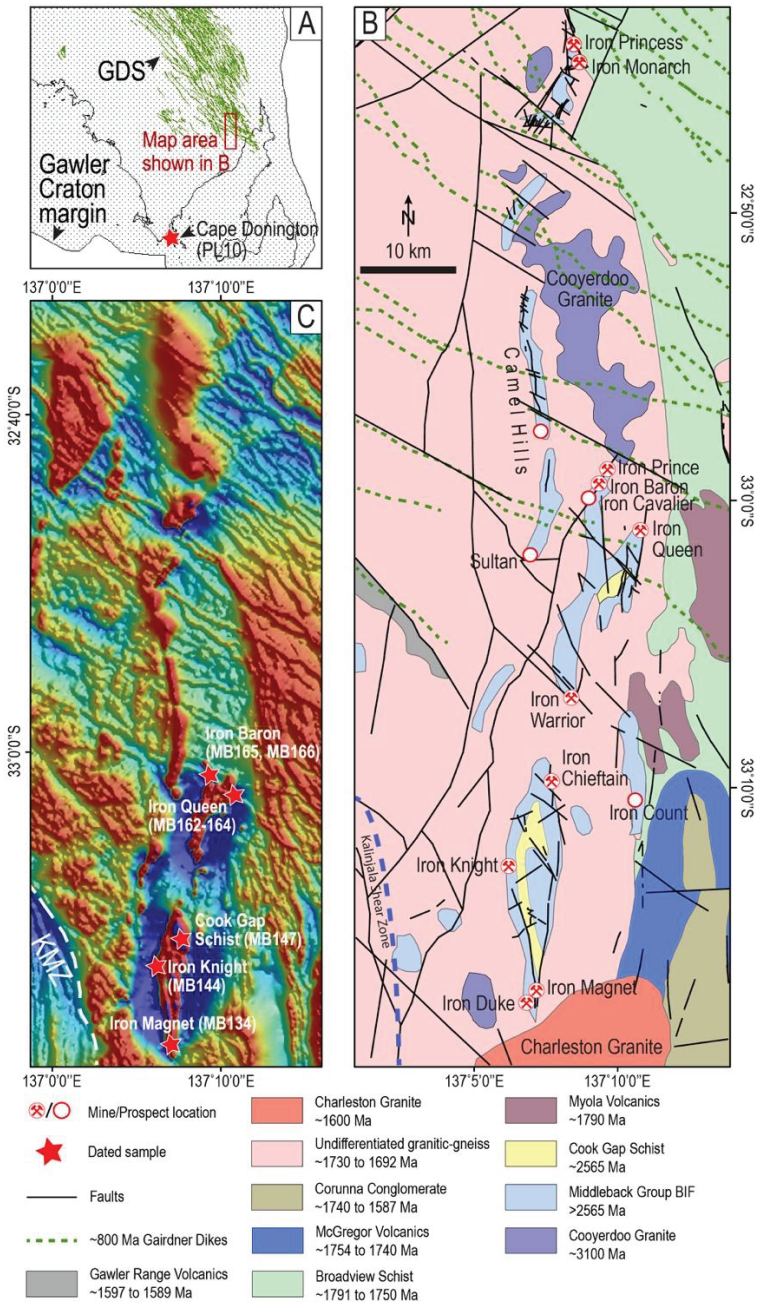

Figure 1: (A) Location of the Middleback Ranges and Cape Donington within the Eyre Peninsula of the Gawler Craton and extent of the Gairdner Dike Swarm (GDS). (B) Simplified geological map showing locations of ore deposits and prospects of the Middleback Ranges (sourced from DMITRE, 2014; http://map.sarig.sa.gov.au/). (C) Total magnetic intensity image of the eastern Eyre Peninsula showing location of the Middleback Ranges and magnetic signatures of NW-SE trending dikes. Legend refers to detail shown on B.

Mylonite Zone (KMZ) that forms a distinct N-S striking boundary between an eastern domain of high magnetic intensity and a western domain of low magnetic intensity within the Eyre Peninsula (Reid et al., 2008). Magmatic suites associated with this orogeny include the 1750-1735 Ma Moola Suite, the 1735-1700 Ma Pinbong Suite and 1709-1701 Ma Moody Suite (Cowley et al., 2017). Post-Kimban magmatism within the region is evidenced by the ~1.6 Ga Hiltaba-affiliated Charleston Granite (Creaser and Fanning, 1993) present immediately south of the MR and younger NW-trending mafic dikes believed to be associated with the ~800 Ma Gairdner Dike Swarm recognizable on the TMI magnetic maps (Fig, 1B, C; Yeates, 1990).

The stratigraphy of the Middleback Subgroup grades upwards from the lower Warrow Quartzite into the Katunga Dolomite, the Lower Middleback Iron Formation, the Cook Gap Schist, and finally the Upper Middleback Iron Formation. Iron ore deposits are hosted predominantly within the Lower Middleback Iron Formation, which has a maximum depositional age of ~2.5 Ga based on U–Pb dating of zircon from the overlying Cook Gap Schist (Szpunar et al., 2011). Detailed descriptions of deposit geology are given by Davies (2000), Leevers et al. (2005), and Keyser et al. (2018, 2019b).

5.3 Methodology

Twenty-five samples were assayed for whole-rock geochemical data by Intertek Genalysis (Adelaide). The samples include twenty-two mafic rocks from the MR, one sample of Cook Gap Schist and two mafic dike samples from Cape Donington. The methodology for whole-rock analysis including element minimum detection limits is provided in Electronic Appendix A.

Polished thin-sections (2.5 x 5 cm) and polished blocks (2.5 cm-diameter) prepared from the samples were examined using plain-polarized and reflected-light optical microscopy. A FEI

Quanta 450 scanning electron micron microscope (SEM) operated at 20 kV and equipped with an energy-dispersive X-ray spectrometer (EDS) was used for further petrographic characterization and back-scattered electron (BSE) imaging.

Selected silicate and oxide minerals were quantitatively analyzed using a Cameca SXFive Electron Microprobe equipped with five wavelength-dispersive X-Ray detectors and running 'PeakSite' software. Analytical conditions were 15 kV acceleration voltage, a 20 nA beam current and a defocused 1 µm beam. Full details of analytical methods for the electron microprobe including standards and minimum detection limits are provided in Electronic Appendix A.

A RESOlution excimer laser ablation system (Applied Spectra Inc., Fremont, SA, USA) coupled to an Agilent 7900x Quadrupole ICP-MS was used for measuring mineral trace element concentrations, LA-ICP-MS element maps and hematite U–Pb geochronology. Data reduction was performed using the software 'GLITTER' (van Achterbergh et al., 2001), with only intervals displaying homogenous and flat signals selected during data reduction as to avoid mineral inclusions or peaks. LA-ICP-MS element maps were created using the software 'Iolite' (Woodhead et al., 2008). Electronic Appendix A gives details of LA-ICP-MS analytical methods and minimum detection limits. The above-mentioned analytical equipment is housed at Adelaide Microscopy, The University of Adelaide.

Zircon grains for geochronology were prepared as mineral separates by Geotrack (Melbourne) following conventional methods including sample crushing, a Wilfley table, Franz isodynamic separators and heavy liquid mineral separation, as well as at the John de Laeter Centre (Curtain University, Western Australia) using the Selfrag electro-pulse disaggregation technique. Grains were handpicked and mounted on epoxy disks (2.5 cm) with the zircon standards OG1 (3465.4 ± 0.6 Ma; Stern et al., 2009), M257 (561.3 ± 0.3 Ma; Nasdala

et al., 2008), Temora-2 (416.8 ± 0.3 Ma; Black et al., 2004) and BR266 (559 ± 0.3 Ma; Stern, 2001).

A FEI Quanta 600 MLA SEM equipped with a tungsten filament electron source (Adelaide Microscopy, The University of Adelaide) was used for cathodoluminescence (CL) imagining of the mounted zircon grains to assess growth zoning. The sensitive high-resolution ion microprobe (SHRIMP-II) at the John de Laeter Centre (Curtin University) was used for U–Pb dating of the mounted zircon grains. Analytical methods for zircon analysis broadly follow those outlined by Compston et al. (1984), Claoué-Long et al. (1995) and Williams (1998). See Electronic Appendix A for full details of methods for SHRIMP U–Pb analysis of zircon. U–Pb hematite dating (Ciobanu et al., 2013; Courtney-Davies et al., 2019) was carried out using the same LA-ICP-MS instrumentation used for trace element analysis.

5.4 Results

5.4.1 Sample suite and occurrence

The present study addressed two main types of mafic lithologies exposed as dikes or sills within iron ore deposits along the MR (Figs. 2-4). These are: (i) amphibolites from the southern part of the belt, represented by the Iron Magnet and Iron Knight North deposits; and (ii) dolerite from locations across the belt.

At Iron Magnet, N-S striking amphibolites are present either as thin, dm- to m-wide sills interbedded with BIF sequences (outcrop #1; Fig. 2A, B), or as a larger sill, tens of meters wide, concordant with the BIF sequence, and exposed along a major shear zone on the eastern side of the orebody (outcrop #2; Fig. 3B, C). Outcrop #1 exposes the contact with the granitic basement (to the west) and aside from amphibolites, displays sub-vertical, rhythmically banded, silica-rich, talc-, carbonate- and magnetite-BIF sequences. Some amphibolite bodies

are strongly boudinaged, crosscut by splays of fractures filled with secondary carbonates (Fig. 2C) and are associated with pyritization, in some cases seen as large, meter-sized pockets of pyrite (Fig. 2D). In contrast, outcrop #2, from the main part of the Iron Magnet orebody exposes both dolerite and adjacent strongly mylonitized amphibolite (Fig. 3A, B). A further example of altered amphibolite was studied from Iron Knight North and is recognizable as a dike that crosscuts BIFs (Fig. 3D).

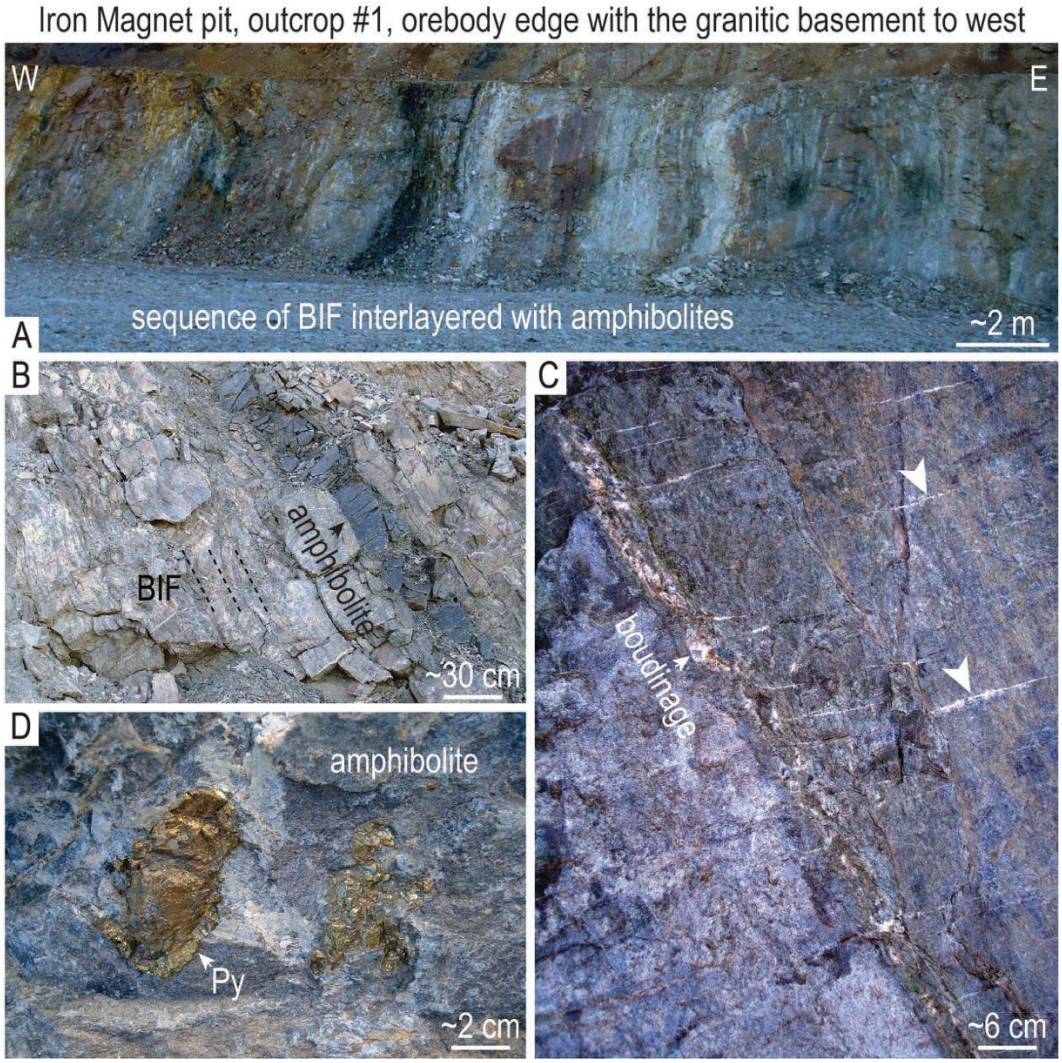

Figure 2: Lithologies exposed in the north wall, Iron Magnet open pit (outcrop #1). (A) Intervals of thin amphibolite layers interbedded with BIF. (B) A vertically-oriented amphibolite sill interbedded with BIF. (C) Boudinage within amphibolite and secondary carbonate splays (large white arrows). (D) Amphibolite with pockets of pyrite (Py).

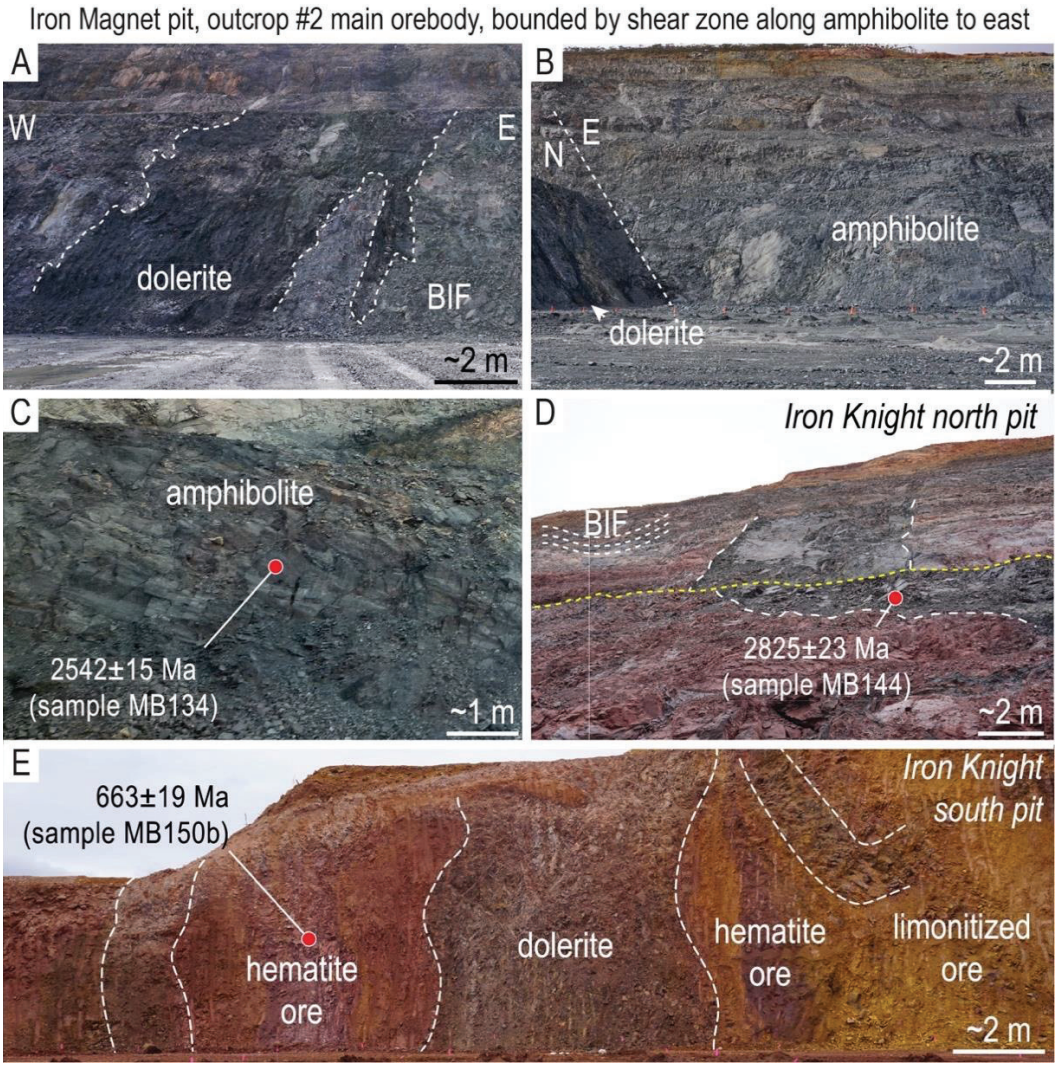

Figure 3: (A-C) Exposures in the Iron Magnet open pit main orebody (outcrop #2) showing lithologies of the north wall and shear zone along the east wall. (A) Dolerite sill concordant with BIF. (B) Massive amphibolite along a major shear zone on the eastern wall of the Iron Magnet orebody. (C) Mylonitized amphibolite along the eastern shear zone of the Iron Magnet orebody. (D) Dike crosscutting BIF at the Iron Knight North open pit. (E) Dolerite dike associated with hematite ore at the Iron Knight South open pit.

Northwest-striking dolerite dikes, reaching up to 15 meters in width and displaying strong amplitude on total magnetic intensity images (Fig. 1C) also show close spatial relationship with the orebodies throughout the belt as seen from outcrops at Iron Magnet (Fig. 3A), and at Iron Knight South (Fig. 3E), Iron Queen (Fig. 4A, B), Iron Baron, Iron Prince and Iron Monarch.

These generally crosscut BIF sequences, as in Iron Queen (Fig. 4A, B), but can also be present as sills concordant with the BIF layering, as for example in outcrop #2 at Iron Magnet (Fig. 3A). In many cases alteration of both BIF and dolerite obliterates mutual relationships (e.g., Iron Knight South; Fig. 3E).

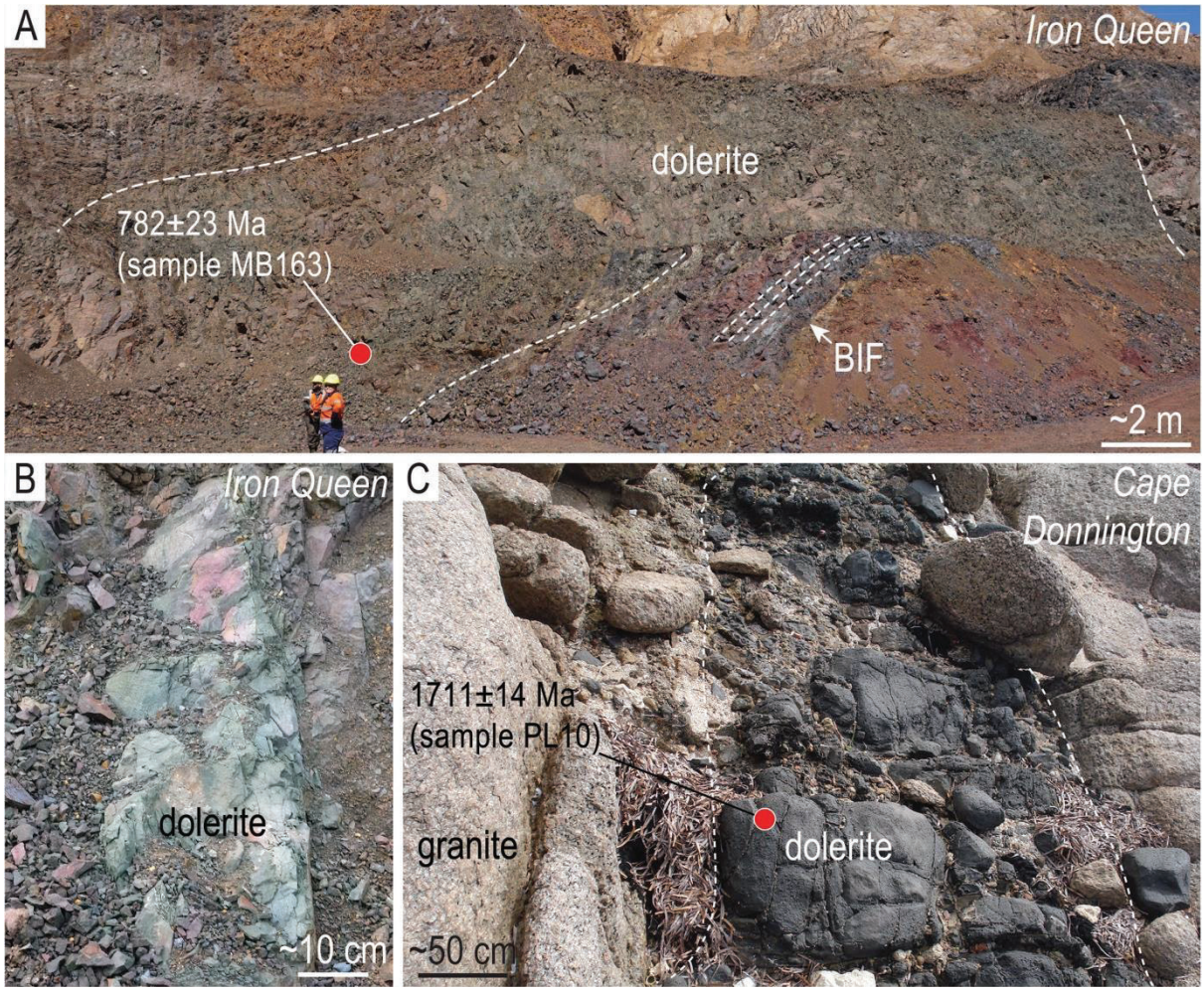

Figure 4: (A, B) The Iron Queen open pit showing the relationship of dolerite dike to BIF and color variation. (C) Dolerite dike crosscutting Donington Granite at Cape Donington.

The sample suite consists of twenty-four specimens of mafic rocks (Table 1). Amphibolites (Electronic Appendix A, Fig. A1) are dark to light green, massive, fine-grained, foliated, and characterized by a marked magnetism as a result of abundant iron-oxides. Porphyroblastic textures are observed with magnetite enveloping coarse apatite. Centimeter-wide, crosscutting

tourmaline-filled veins occur sparsely. The same amphibolite also contains abundant tourmaline porphyroblasts. The dolerite dikes range from coarse- to fine-grained with (sub)ophitic textures preserved in the freshest samples. Coarse grains/aggregates of titanite are very typical of these rocks. Rock colors range from dark-green to reddish to brownish-yellow reflecting different degrees of alteration and/or weathering.

Included in this study for purposes of comparison with the aforementioned mafic lithologies are:

1. Two samples of basaltic rocks occurring as dikes crosscutting granites from the Donington Suite (Electronic Appendix A, Fig. A1; see also Keyser et al., 2019b) from Cape Donington, near Port Lincoln (PL) in the southern Eyre Peninsula (Fig. 4C, Electronic Appendix A, Fig. 1A). These are the freshest mafic rocks studied and the only pyroxene-bearing rocks included.

2. A sample of green-colored, medium-grained quartz-amphibole schist (Electronic Appendix A, Fig. A1), representative of the ~2.5 Ga Cook Gap Schist (Szpunar et al., 2011) collected from an outcrop south of Iron Chieftain (Fig. 1C).

In addition, two samples of hematite-goethite ores from Iron Knight deposit (collected from outcrop and the north wall in the southern pit) were used for U–Pb dating. Altered dolerites are also present in the same location (Fig. 3E). The iron ores are massive, fine-grained, and display a red coloration resulting from oxidation (Keyser et al., 2018).

Table 1A: Fresh samples containing magmatic or metamorphic assemblages

Rock type/ Location	Sample	Mineral assemblage													
		Pyroxene	Amphibole									Feldspar			
			Mg-Fe			Ca									
		Di	(F)Ged	Cum	Gru	(F)Ts	(F/M)Hb	(F)Act/Tr	Hst	Bitotite	Kfsp	Lab(An_{50-70})	And(An_{30-50})	Other
Amphibolite														
Iron Magnet	MB34C				x	x	x			x				
(outcrop #1)	MB80C			x				x		x				
Drillhole-DD03IM001MTT	MB86			x		x				x				Alm
	MB94		x	x			x			x			x	Tur, Crn
	MB95			x				x		x				
	MB127a			x						x				
Dolerite														
Iron Monarch	MB31						x	x		x	x		x	
Iron Baron	MB152						x	x		x	x		x	
	MB166*						x	x		x			x	
Iron Magnet	MB133						x	x		x			x	
(outcrop #2)														
Port Lincoln	PL4	x				x				x	x	x	x	
	PL10*	x							x	x	x	x	x	
Schist														
Cook Gap Schist							x	x					x	

All samples contain common accessories Fe-Ti-oxides and apatite. Minor zircon and baddeleyite in MB152 and MB166.
Mineral abbreviations: Act-actinolite; Alm-almandine; An-anorthosite; And-andesine; Crn-corundum; Cum-cummingtonite; Di-diopside; Ged-gedrite; Gru-grunerite; Hst-hastingsite; Kfs-potassic feldspar; Lab-labradorite Ts-tschermakite; Tur-tourmaline; (F)-ferro-prefix; (M)-magnesio-prefix.
*Dated samples

Table 1B: Altered mafic samples, schists and ores

Rock type/ Location	Sample
Amphibolite	
Iron Magnet	MB134*
(outcrop #2)	
Dolerite	
Iron Prince	MB55A
	MB108
	MB109
	MB111
Iron Baron	MB165*
Iron Queen	MB116
	MB118*
	MB161
	MB162*
	MB163*
	MB164*
Iron Warrior	MB06
	MB07
Iron Knight North	MB144*
	MB145
Iron Knight South	MB149
	MB151
Schist	
Cook Gap Schist	MB147*
Iron ore - hematite	
Iron Knight South	MB98a*
	MB150b*

Samples are intensively altered to chlorite + quartz + carbonate ± talc assemblages.
*Dated samples

5.4.2 Petrography

A detailed petrographic study was conducted on amphibolites from Iron Magnet and dolerite dikes from throughout the belt. Representative aspects of these lithologies are shown in Figures

5-9, with compositional data for relevant constituent mineral phases in Electronic Appendix B and trace element data for selected minerals given in Electronic Appendix C. Despite the often-similar appearance of the amphibolites and dolerites at the macroscopic scale, particularly when samples are intensively altered, plagioclase is absent in amphibolites (with one exception, sample MB94) but is always preserved as a main component in the dolerites.

5.4.2.1 Amphibolites

The amphibolites are primarily composed of multiple species of amphiboles (both Mg-Fe- and Ca-amphiboles, Figure 5; Electronic Appendix B, Tables B1-B6) and also micas, but also include varieties containing garnet, tourmaline, or corundum (Fig. 6). All amphibolites contain variable proportions of secondary chlorite (Mg- and Fe-rich varieties) and talc resulting from pseudomorphic replacement of amphiboles and/or biotite, or as vein/pocket filling.

Amphiboles include species from both Mg-Fe- (cummingtonite, grunerite, gedrite) and Ca [(ferro)tschermakite, (ferro/magnesio)hornblende] groups (Fig. 5A). These occur in various combinations and proportions throughout the sample suite. Relationships between co-existing Mg-Fe- and Ca-amphiboles can be inferred from fine-grained lamellar intergrowths or epitaxial associations (Fig. 5B).

Cummingtonite is the most abundant among the Mg-Fe amphiboles, however, there is a continuous compositional variation across the sample suite between Mg and Fe end-members: grunerite [$\square Fe^{2+}_{1.61\text{-}1.94}(Fe^{2+}_{1.75\text{-}3.39}Mg_{1.46\text{-}3.20})Si_{7.44\text{-}8.01}O_{22}(OH)_{1.92\text{-}2.0}$] and cummingtonite [$\square Fe^{2+}_{1.24\text{-}1.93}$ $(Mg_{3.22\text{-}4.64}Fe^{2+}_{0.09\text{-}1.51})Si_{7.73\text{-}7.98}O_{22}(OH)_{1.95\text{-}2.0}$;] (Fig. 5A). Grunerite [$\square Fe^{2+}_{1.61\text{-}1.94}(Fe^{2+}_{1.75\text{-}3.39}Mg_{1.46\text{-}3.20})Si_{7.44\text{-}8.01}O_{22}(OH)_{1.92\text{-}2.0}$] also occurs together with both ferrotschermakite [$\square Ca_{1.64\text{-}1.88}(Fe^{2+}_{2.10\text{-}2.72}Al_{0.91\text{-}1.45}Fe^{3+}_{0.48\text{-}0.83})(Si_{5.90\text{-}6.37}Al_{1.64\text{-}2.10})O_{22}(OH)_{1.89\text{-}1.94}$] and ferrohornblende in sample MB34c, [$\square Ca_{1.59\text{-}1.84}(Mg_{0.82\text{-}1.30},Fe^{2+}_{2.55\text{-}3.31}Al_{0.25\text{-}0.64})(Si_{6.56\text{-}}$

$_{7.18}Al_{0.82-1.44})O_{22}(OH)_{1.94-1.98}]$. Gedrite $[Na_{0.34}(Na_{0.27}Fe^{2+}_{1.66})(Mg_{2.73}Fe^{2+}_{0.26}Fe^{3+}_{0.91}Al_{1.11})(Si_{5.89}Al_{2.11})O_{22}(OH_{1.95}F_{0.03}Cl_{0.02})]$ is the only primary amphibole observed in more aluminous rocks, which are conspicuous by the presence of co-existing corundum (sample MB94; see below).

Amphiboles containing essential Ca (Ca-amphiboles), including actinolite, show a somewhat continuous spread in terms of C-cation speciation, including Al as a major component, and minor Fe^{3+} and Ti (Fig. 5A). Magnesiohornblende is characterized by wide compositional variation, also observable from zoning at the grain-scale [$\square Ca_{1.71-1.85}[Mg_{2.04-3.68}(Fe^{2+}_{0.59-1.72}Al_{0.21-0.73})](Si_{6.25-7.34}Al_{0.66-1.76})O_{22}(OH)_{1.90-1.98}$; Fig. 5C, D]. Within the amphibolites, replacement of magnesiohornblende by actinolite [$\square Ca_{1.72-1.89}(Mg_{3.22-4.19},Fe^{2+}_{0.67-1.47})Si_{7.57-7.95}O_{22}(OH)_{1.99-2.0}$] is widespread (Fig. 5C) although mutual boundaries suggestive of co-crystallization at equilibrium are also observed (Fig. 5D). A variety of hornblende richer in Fe is present within mm-wide, crosscutting tourmaline veins (Fig. 5E), as is a late generation of acicular cummingtonite that marks shearing within the sample (Fig. 5F).

Accessory Fe-Ti-oxides, represented by titaniferous magnetite and ilmenite (Electronic Appendix B, Tables B7 and B8), are very abundant (~5 vol.% of the rocks) and display variable syn- or post-metamorphism fabrics. Aside from porphyroblastic titaniferous magnetite (Fig. 7A), which is common to all varieties of amphibolite, acicular ilmenite + magnetite occurs along trails that crosscut all amphiboles or tourmaline porphyroblasts (Fig. 6A, B). Such trails stop however at the boundaries of tourmaline veins (Fig. 6C), a texture indicative of formation during post-peak metamorphism. Syn-metamorphic fabrics also include a foliation defined by oriented grains of titaniferous magnetite (Fig. 6D).

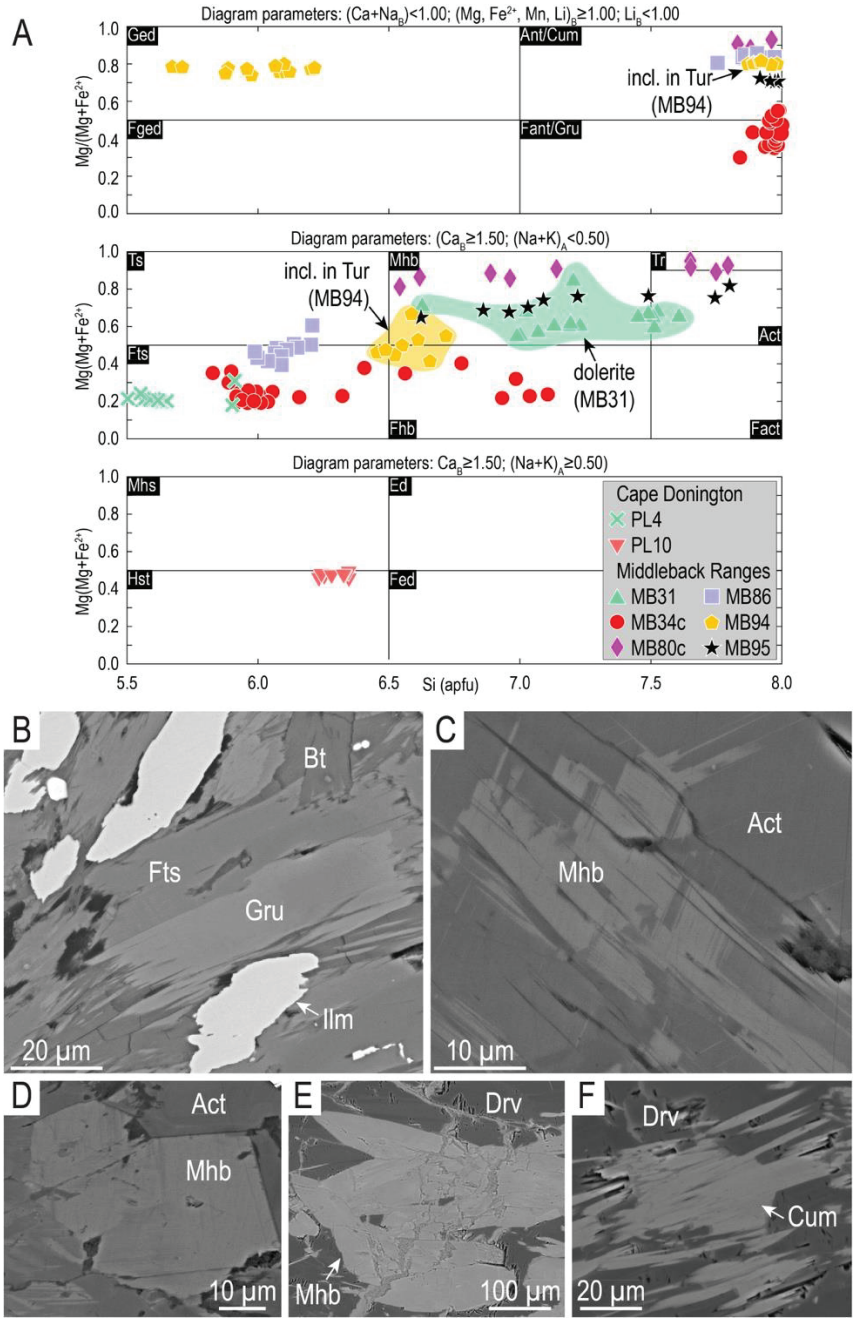

Figure 5: (A) Amphibole classification diagrams (after Leake et al., 1997) and (B-F) BSE images showing textural and compositional variations of Mg-Fe- and Ca-amphiboles from amphibolites. (B) Lamellar intergrowths of ferrotschermakite (Fts) and grunerite (Gru). (C) Compositional zoning and (D) equilibrium grain boundaries between magnesiohornblende (Mhb) and actinolite (Act). (E) Magnesiohornblende and (F) acicular cummingtonite (Cum) within a dravite (Drv)-rich tourmaline vein crosscutting amphibolite. Bt-biotite; Ilm-ilmenite.

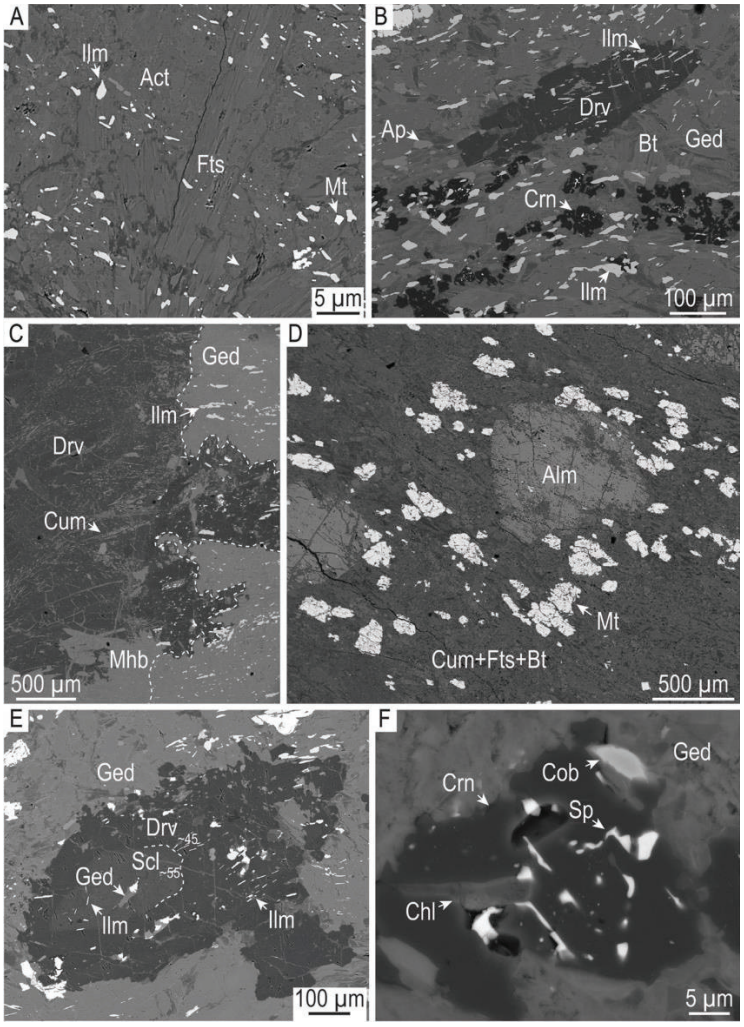

Figure 6: BSE images showing syn-to post-metamorphism fabrics in Al-rich amphibolites. (A) Trails of acicular ilmenite (Ilm) and magnetite (Mt) crosscutting ferrotschermakite (Fts) and actinolite (Act). (B) Ilmenite and apatite (Ap) showing preferred orientation and crosscutting a field consisting of dravite (Drv)-rich tourmaline porphyroblasts and patches of skeletal corundum (Crn). (C) Tourmaline vein, also containing magnesiohornblende (Mhb) and acicular cummingtonite (Cum), crosscutting trails of ilmenite. (D) Field image showing almandine (Alm)-rich garnet porphyroblasts and a foliation fabric defined by oriented grains of titaniferous magnetite. (E) Tourmaline porphyroblast showing compositional zoning from a schorl (Scl)-rich cores to dravite-rich rims. (F) Skeletal corundum showing symplectic growth of sphalerite (Sp). Bt-biotite; Chl-chlorite; Cob-cobaltite; Ged-gedrite.

Porphyroblastic garnet is almandine-rich (Alm_{62-69}) with a slight increase in Mg content (up to Pyp_{16}) towards grain rims (Electronic Appendix B, Table B9). Phyllosilicates are represented by biotite group minerals with wide-ranging Fe/(Fe+Mg) ratios, $[K_{0.48-0.84}(Mg_{0.48-2.04}, Fe^{2+}_{0.85-2.67})Al_{1.34-1.56}Si_{2.52-2.83}O_{10}(OH_{1.82-1.98},F_{0.02-0.12},Cl_{0.01-0.07})]$, and less abundant muscovite with mutual epitaxial intergrowths and also by chlorite which is present down to sub-µm-scale, accounting for the poor fit of EPMA data for micas to ideal stoichiometry (K <1.00 apfu; Electronic Appendix B, Table B10). Biotite is most abundant in garnet-bearing amphibolite (sample MB86). Where present, fine-grained muscovite occurs as aggregates associated with corundum and plagioclase in gedrite-bearing amphibolite (sample MB94). Micas (mainly biotite) are present in relatively high abundance in some samples (Table 1). Tourmaline, whether within veins or as porphyroblasts, is compositionally zoned with respect to $Mg/(Mg+Fe^{2+})$, crossing compositional fields of schorl (brown cores) and dravite (green rims) (Figs. 6E; Electronic Appendix A, Fig. A1; Electronic Appendix B, Table B11). Skeletal corundum, displaying alteration to diaspore, leading to deficient EPMA totals (Electronic Appendix B, Table B12), is abundant within those amphibolites in which plagioclase is preserved (sample MB94; Fig. 4E, F). Such corundum displays unusual symplectites with sphalerite and is always associated with cobaltite (Fig. 6F). Other sulfides present throughout the amphibolites are pyrite and minor chalcopyrite. Trace clausthalite (PbSe) and native gold are also observed particularly along secondary chlorite veins.

Porphyroblastic titaniferous magnetite displays heterogenous internal textures, i.e., fields of silicate inclusions and fractures superimposed onto domains with ilmenite as trellis-like exsolutions (Fig. 7A, B). In contrast to this type of titaniferous magnetite are the smaller aggregates of ilmenite + magnetite, that lack inclusions (at least at the micron-scale of observation; Fig. 7C). Stronger overprint is observed in titaniferous magnetite intergrown with almandine porphyroblasts (Fig. 7D).

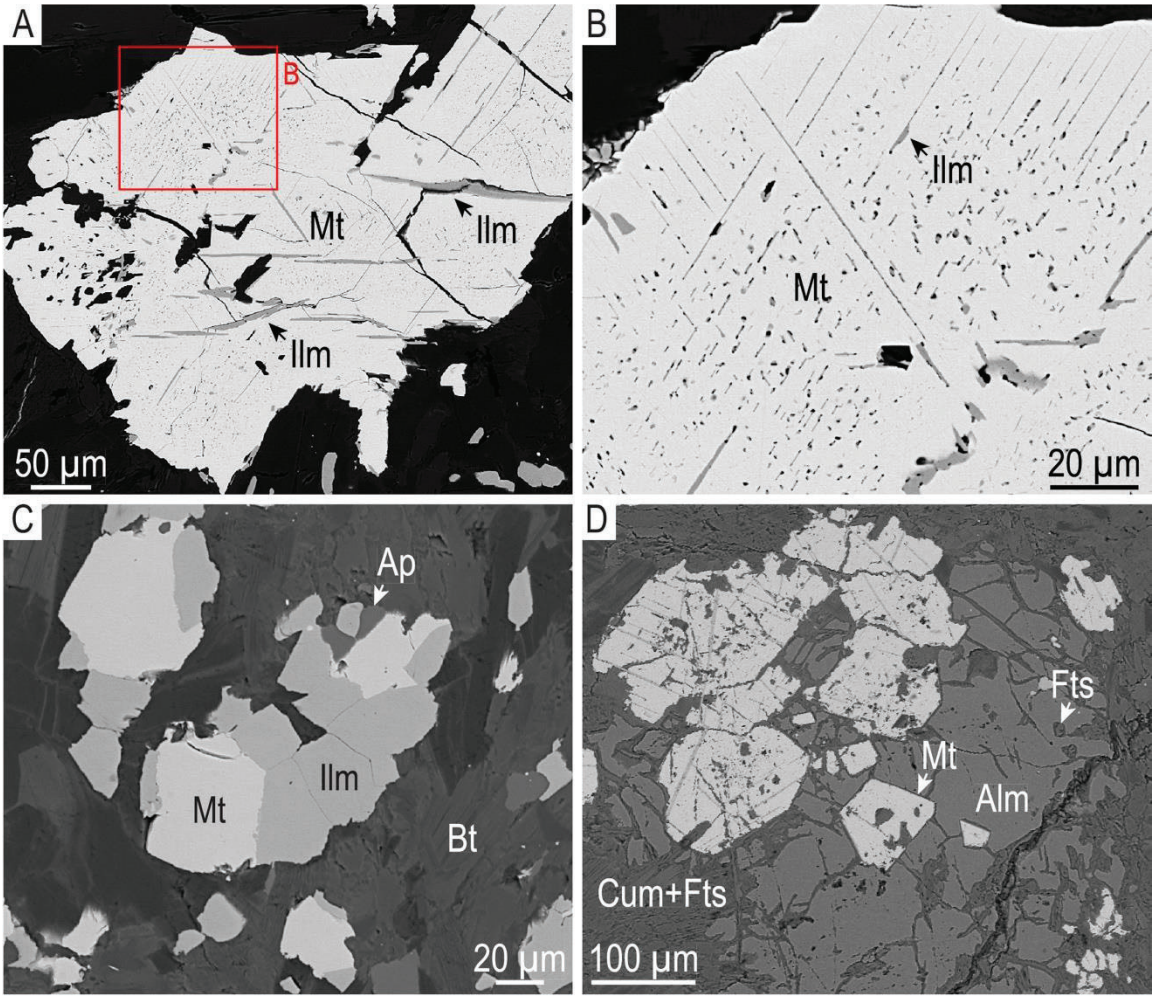

Figure 7: BSE images showing textural features of titaniferous magnetite (Mt) porphyroblasts. (A) Fields of silicate inclusions and fractures within titaniferous magnetite. (B) Ilmenite (Ilm) trellis exsolutions in magnetite from the field outlined in (A). (C) Aggregates of ilmenite + trellis-free magnetite. (D) Intergrowths of titaniferous magnetite and almandine (Alm)-rich garnet. Ap-apatite; Bt-biotite; Cum-cummingtonite; Fts-ferrotschermakite.

5.4.2.2 Dolerites

Igneous, (sub)ophitic textures between Ca-amphiboles (magnesiohornblende and actinolite) and plagioclase (andesine; An_{10-30}, rarely up to $An_{\sim 48}$; Electronic Appendix B, Table B13) are preserved in fresher dolerites from across the MR (Fig. 8A). Some dolerites are also intensively altered (chlorite + calcite alteration) but have been considered as dolerites for this study based

on U–Pb zircon ages (see below). Amphibole in these rocks features a zoning from brown cores to green rims (Fig. 8B, C) broadly corresponding to compositions that range from magnesiohornblende $[\square Ca_{1.61\text{-}1.92}[Mg_{2.15\text{-}3.10}(Fe^{2+}{}_{1.33\text{-}2.03}Al_{0.25\text{-}0.46})](Si_{6.36\text{-}7.36}Al_{0.64\text{-}1.64})O_{22}(OH)_{1.96\text{-}1.99}]$ to actinolite $[\square Ca_{1.86\text{-}2.0}(Mg_{2.56\text{-}2.94},Fe^{2+}{}_{1.70\text{-}2.10})Si_{7.31\text{-}7.64}O_{22}\ (OH)_{1.99\text{-}2.0}]$. Aside from accessory titanite, the dolerites also contain abundant magnetite and ilmenite; the latter is recognizable from breakdown into hematite + rutile ± titanite (Fig. 8D).

The MR dolerites also show superimposed alteration of feldspars and magmatic accessories (Fig. 8E-H). Albitization of plagioclase is accompanied by formation of myrmekites with quartz that are crosscut by stringers of Cl-bearing fluorapatite (Fig. 8E). At Iron Monarch, potassium feldspar with Ba-rich rims is also present in albitized domains (Fig. 8F). In the same sample, titanite that replaces ilmenite (Electronic Appendix B, Table B14) contains inclusions of zircon along grain rims (Fig. 8G). In most dolerites, the occurrence of both relict baddeleyite and zircon is recognized (Fig. 8H).

Dolerite dikes from Cape Donington (Fig. 9) are, by comparison, extremely unaltered. These display (sub)ophitic textures, contain major diopside-augite with lamellar exsolutions of ferrosilite $\{(Ca_{0.80\text{-}0.92}Mg_{0.58\text{-}0.67}Si_{1.93\text{-}1.96}O_6$ and $[(Fe^{2+},Mg)_2Si_2O_6]$, respectively)} and crosscutting Fe-Ti-oxides (Fig. 9E, F) interstitial to plagioclase with composition up to An_{60} (Electronic Appendix B, Table B15). Minor biotite and amphiboles are also present (Fig. 9D), i.e., ferrotschermakite and hastingsite in sample PL4 and PL10, respectively (Electronic Appendix B, Table B16).

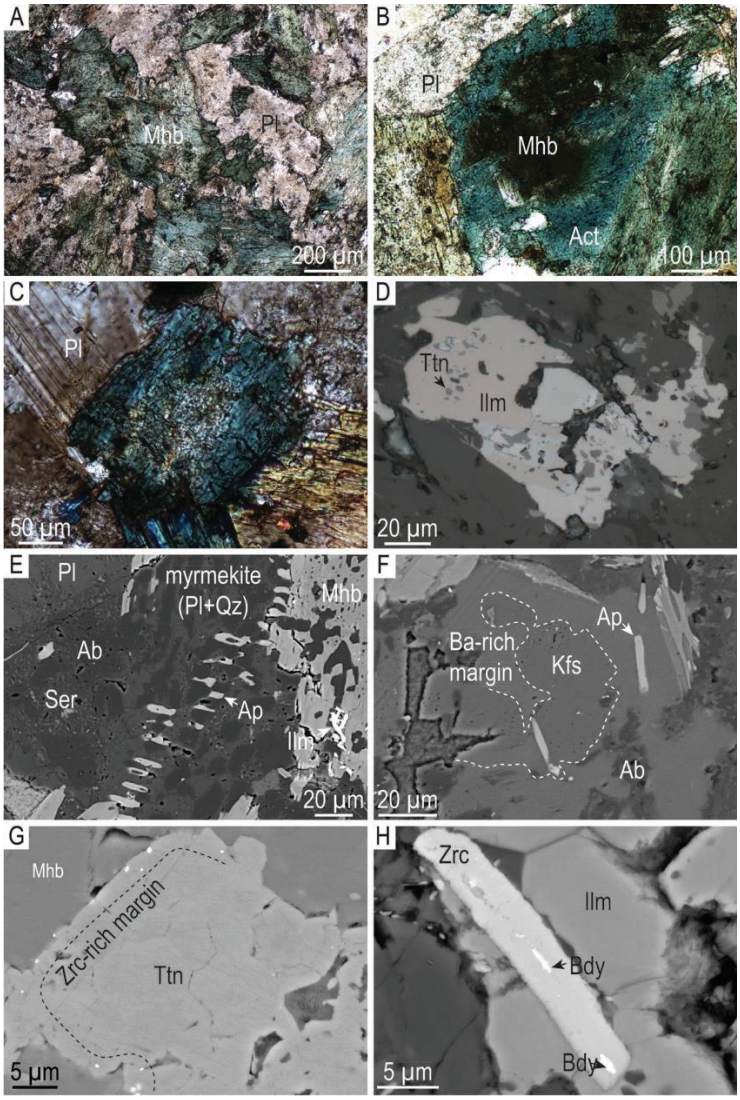

Figure 8: Photomicrographs (in plane-polarized (A, B), cross-polarized (C), and reflected light (D)) and BSE images (E-H) showing representative features of dolerites from the Middleback Ranges. (A) Sub-ophitic textures comprising magnesiohornblende (Mhb) and plagioclase (Pl). (B) Compositional zoning in amphibole from brown magnesiohornblende cores to green actinolite (Act) rims. Replacement of magnesiohornblende cores and twining in plagioclase. (D) Ilmenite (Ilm) showing replacement by titanite (Ttn). (E) Apatite (Ap) stringers crosscutting fields of plagioclase replacement by albite (Ab), sericite (Ser) and myrmekites with quartz (Qz). (F) Potassic feldspar (Kfs) containing Ba-rich rims in albitized domains. (G) Titanite (Ttn) aggregate with fine-grained zircon (Zrc) inclusions along margin. (H) Relict baddeleyite (Bdy) inclusions in zircon.

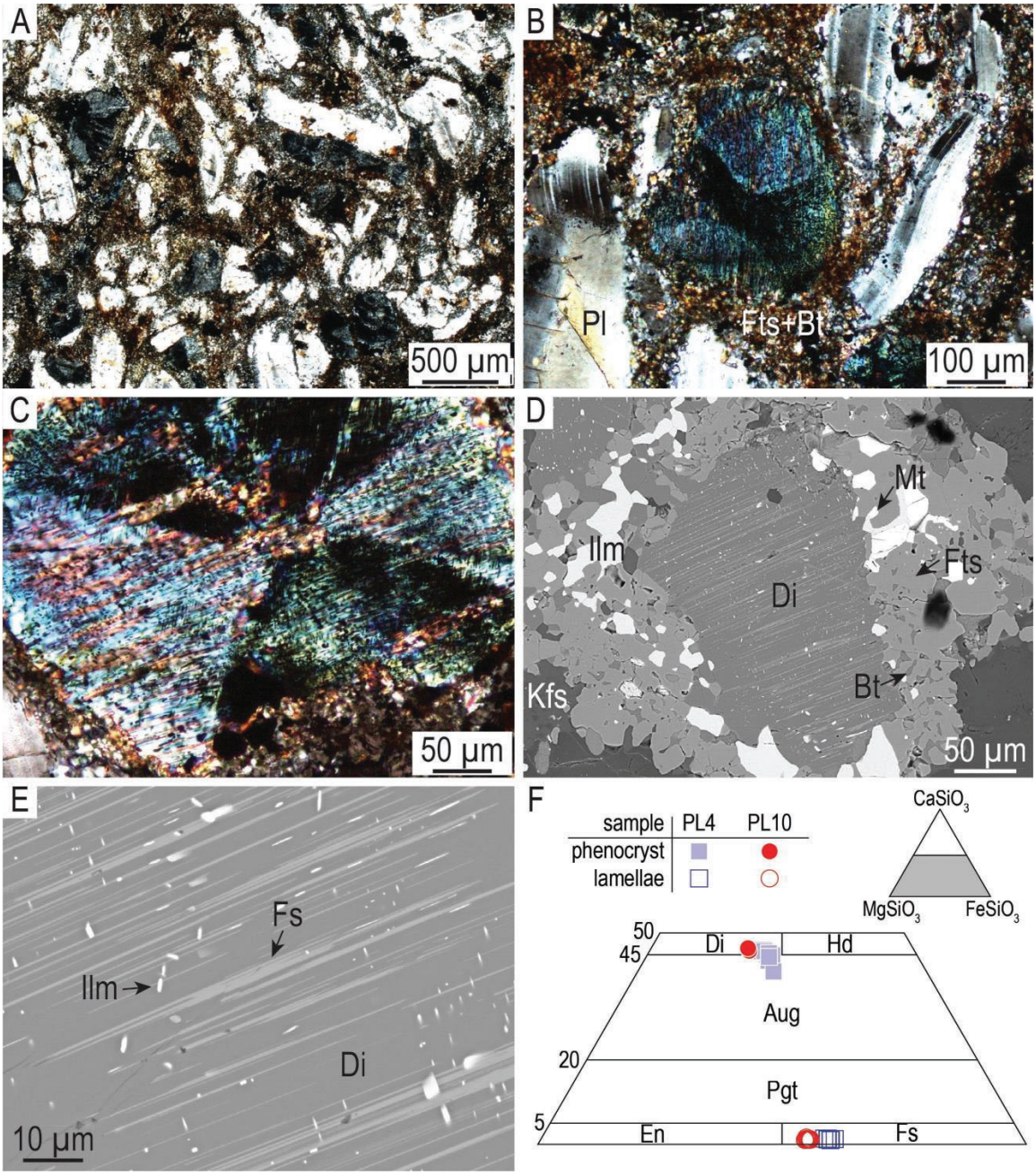

Figure 9: Photomicrographs (in plane-polarized (A) and cross-polarized (B, C) light)) and BSE images (D, E) showing representative features of dolerites from Cape Donington. (A) Sub-ophitic texture composed of diopside (green), amphibole + biotite (brown) and plagioclase laths (white). (B, C) Diopside phenocryst displaying hour-glass-shaped opaque inclusions in a groundmass of fine-grained ferrotschermakite (Fts) + biotite (Bt). (D, E) Ferrosilite (Fs) and ilmenite (Ilm) exsolution features in diopside (Di). (F) Ternary diagram showing compositional variation of pyroxene in terms of $MgSiO_3$-$FeSiO_3$ -$CaSiO_3$.

5.4.2.3 Amphibolite: Fe-Ti-mineral chemistry and geothermometry

The two types of Fe-Ti-oxide associations were analyzed in amphibolites: (1) porphyroblasts of titanomagnetite with 'trellis' ilmenite and (2) small, separate grains of magnetite and ilmenite in the matrix. Magnetite consistently contains minor elements SiO_2, TiO_2, Al_2O_3 and V_2O_3, albeit at concentrations <1.0 wt.%. The SiO_2 content in magnetite ranges from 0.05 to 0.57 wt.% and TiO_2 content from 0.12 and 3.20 wt.%. Magnetite-1 contained higher average Al_2O_3 content (~0.50 wt. %) than magnetite-2 (~0.20 wt.%). Magnesium was also consistently measured in Magnetite-1 from some samples (e.g., sample MB34c; ~0.05 wt.%). Although generally below detection limit, Cr_2O_3, MnO, CaO, WO_3, ZnO and ZrO_2 and SnO_2 were variably measured in both magnetite types. Total element oxide values of ilmenite were closer to stoichiometric in ilmenite-2 than in ilmenite-1, the former of which consistently measured higher TiO_2 (>50 wt.%). Ilmenite of both textures has a range of MnO from 0.83 to 3.67 wt.% and V_2O_3 from 0.24 to 0.33 wt.%.

Both associations of Fe-Ti-oxides from the amphibolites were used for magnetite-ilmenite geothermometry using calculations given by Lepage (2003) and the calibration of Andersen and Lindsley (1985). Results (Electronic Appendix B, Table B17) show temperatures in the range of 527-602 ˚C and log fO_2 between –17.4 and –20.8 for titaniferous magnetite and exsolved ilmenite, and 435-505 ˚C and a log fO_2 range of –23.4 to –27.1 for coexisting magnetite and ilmenite in the matrix.

5.4.3 Whole-rock geochemistry

Whole-rock geochemical data for the studied samples (Tables 2 and 3) are plotted in Figure 10 and as chondrite-normalized rare earth element + yttrium (hereafter, REY) fractionation diagrams in Figure 11A-D.

Table 2: Whole-rock geochemistry; major oxides (wt.%)

Location	Sample	Rock type	SiO_2	Al_2O_3	MgO	Fe_2O_3	CaO	K_2O	Na_2O	P_2O_5	TiO_2	MnO	LOI	**Total+LOI**
Reference lithologies														
Cook Gap Schist	MB147	schist	53.29	14.40	5.79	12.71	8.83	1.26	1.90	0.07	0.76	0.39	1.05	**100.44**
Port Lincoln	PL4		45.01	13.64	4.43	19.64	8.27	2.01	2.48	0.62	3.78	0.25	0.40	**100.53**
	PL10		47.73	13.32	5.95	17.34	9.50	0.90	2.28	0.30	2.53	0.23	0.04	**100.13**
Middleback Ranges lithologies														
Iron Prince	MB55A	chlorite-altered dolerite	45.25	16.95	11.33	15.31	0.17	3.84	0.03	0.05	0.91	0.37	7.43	**101.63**
	MB108	chloritic rock	25.54	16.10	18.79	24.51	0.95	<mdl	0.01	0.66	3.68	0.70	9.57	**100.51**
	MB111	chlorite-altered dolerite	25.59	16.67	12.97	24.18	0.71	0.06	0.27	0.60	3.61	1.83	12.89	**99.37**
Iron Baron	MB152	dolerite	49.25	13.13	5.80	16.58	8.56	1.07	2.26	0.14	1.26	0.25	1.87	**100.18**
	MB165	chlorite-altered dolerite	31.55	14.34	22.40	15.43	0.43	0.12	0.26	0.18	1.06	0.27	13.35	**99.40**
	MB166	dolerite	49.35	13.23	6.07	15.68	9.44	1.07	2.17	0.09	1.25	0.22	1.39	**99.97**
Iron Queen	MB116	chlorite-altered dolerite	33.46	14.66	14.94	21.02	0.64	0.05	0.26	0.46	3.49	0.59	10.62	**100.19**
	MB118	chloritic rock	22.38	15.27	10.79	38.56	0.42	0.04	0.23	0.34	3.28	0.26	8.93	**100.49**
	MB162	chlorite-altered dolerite	35.43	14.11	16.86	17.59	0.21	0.04	0.61	0.16	1.48	0.65	11.68	**98.81**
	MB164	chlorite-altered dolerite	27.53	14.25	16.40	23.02	0.67	0.07	0.43	0.46	3.59	0.61	11.66	**98.69**
Iron Warrior	MB06	chlorite-altered dolerite	30.38	13.91	19.20	21.75	0.34	0.02	0.32	0.23	1.86	0.34	10.61	**98.95**
Iron Knight	MB144	chlorite-altered dolerite	41.44	6.82	22.20	19.09	0.08	<mdl	0.11	0.09	0.35	0.19	9.82	**100.20**
	MB145	chlorite-altered dolerite	43.58	11.98	14.96	19.53	0.45	0.02	0.09	0.25	2.62	0.37	8.54	**102.40**
	MB149	chlorite-altered dolerite	60.46	17.53	3.48	7.88	1.87	2.98	2.66	0.16	0.64	0.14	2.67	**100.47**
	MB151	chlorite-altered dolerite	31.13	16.19	2.80	28.35	0.01	0.37	0.81	0.21	1.76	0.40	17.85	**99.89**
Iron Magnet	MB34C	amphibolite	44.50	1.44	4.53	46.88	0.69	0.05	0.04	0.21	0.34	0.05	0.51	**99.22**
	MB80C	amphibolite	32.50	15.57	10.99	29.55	1.27	1.06	0.84	0.48	2.61	0.22	4.15	**99.24**
	MB94	amphibolite	28.71	11.15	10.78	35.24	0.78	0.70	0.11	0.18	1.87	0.19	8.98	**98.70**
	MB95	amphibolite	40.03	6.44	13.90	26.91	5.14	0.27	0.24	0.21	1.87	0.32	3.69	**99.00**
	MB127	amphibolite	40.99	9.15	12.34	27.22	0.21	1.00	0.15	0.14	0.59	0.12	8.62	**100.51**
	MB133	dolerite	47.66	12.87	7.99	16.73	4.42	1.57	2.24	0.46	2.05	0.27	4.17	**100.43**
	MB134	altered amphibolite	73.76	7.39	4.11	9.89	0.10	0.35	0.03	<mdl	0.26	0.30	3.78	**99.97**

Table 3: Trace element geochemistry (ppm)

Location	Sample	Rock type	Li	Ba	Sr	Be	Rb	Cs	Cr	Ni	Co	Cu	Zn	Cd
Reference lithologies														
Cook Gap Schist	MB147	amphibole schist	7.4	715	232	1.0	35	0.67	154	63	23	13	76	0.35
Port Lincoln	PL4	mafic dike	29	689	279	2.4	72	1.9	44	38	47	87	190	0.23
	PL8	mafic dike	29	243	180	1.2	38	1.5	156	107	53	163	149	0.23
Middleback Ranges lithologies														
Iron Prince	MB55A	chlorite-altered dolerite	69	488	12	1.0	159	2.1	164	104	50	34	144	0.07
	MB108	chloritic rock	59	18	5.1	0.70	0.40	0.11	2979	839	124	20	2003	0.11
	MB111	chlorite-altered dolerite	154	162	24	3.0	3.9	1.4	93	311	183	75	15032	0.56
Iron Baron	MB152	dolerite	10	296	139	<mdl	46	0.68	90	63	53	74	104	0.15
	MB165	chlorite-altered dolerite	168	6.0	17	3.5	6.7	0.34	98	77	48	9.0	147	<mdl
	MB166	dolerite	7.2	261	150	0.50	49	1.1	90	64	60	88	105	0.15
Iron Queen	MB116	chlorite-altered dolerite	50	13	11	1.0	0.70	0.06	21	21	44	<mdl	218	<mdl
	MB118	chloritic rock	21	27	9.7	0.80	5.4	2.0	668	224	50	1501	282	0.08
	MB162	chlorite-altered dolerite	51	19	12	1.1	0.50	<mdl	47	44	49	108	172	<mdl
	MB164	chlorite-altered dolerite	48	18	18	1.2	1.1	0.22	41	28	54	2.0	185	<mdl
Iron Warrior	MB06	chlorite-altered dolerite	97	17	9.1	2.1	1.00	0.31	44	34	33	38	156	0.08
Iron Knight	MB144	chlorite-altered dolerite	36	17	3.8	0.80	0.80	0.48	111	212	44	<mdl	89	<mdl
	MB145	chlorite-altered dolerite	67	11	4.0	0.60	0.90	0.32	43	35	52	202	146	<mdl
	MB149	chlorite-altered dolerite	32	861	183	1.3	83	1.9	145	56	20	13	81	0.04
	MB151	chlorite-altered dolerite	22	10	13	1.3	35	2.8	112	49	24	41	109	0.08
Iron Magnet	MB34C	amphibolite	3.6	13	4.2	2.8	2.8	0.34	<20	6.0	2	6.0	4.0	<mdl
	MB80C	amphibolite	104	275	120	4.6	38	14	<20	15	18	107	102	0.24
	MB94	amphibolite	41	90	6.3	5.7	29	4.1	1691	308	38	74	17	0.11
	MB95	amphibolite	15	35	14	2.1	8.9	1.9	1292	641	59	98	75	0.12
	MB127	amphibolite	29	28	2.3	0.80	46	3.3	215	38	4.2	16	42	<mdl
	MB133	dolerite	24	1197	74	0.50	43	1.4	95	40	46	33	146	0.10
	MB134	altered amphibolite	20	190	3.3	<mdl	13	0.44	61	23	8	4.0	81	<mdl

Table 3 continued: Trace element geochemistry (ppm)

Location	Sample	Rock type	V	Nb	Ta	Zr	Hf	Sc	Ga	Ge	In	Ag	As	Sb
Reference lithologies														
Cook Gap Schist	MB147	amphibole schist	149	9.0	0.80	85	2.4	14	22	1.1	0.08	<mdl	7.6	0.90
Port Lincoln	PL4	mafic dike	309	24	1.5	301	7.0	32	26	<mdl	0.12	<mdl	4.0	<mdl
	PL8	mafic dike	453	11	0.60	162	3.9	36	22	<mdl	0.11	<mdl	1.0	<mdl
Middleback Ranges lithologies														
Iron Prince	MB55A	chlorite-altered dolerite	<mdl	3.1	0.10	47	1.0	44	17	<mdl	<mdl	<mdl	3.0	<mdl
	MB108	chloritic rock	396	27	1.9	230	6.6	48	34	0.20	0.15	0.06	17	1.3
	MB111	chlorite-altered dolerite	456	23	1.6	266	7.6	47	27	0.70	0.13	0.06	10	1.2
Iron Baron	MB152	dolerite	360	4.0	0.30	87	2.6	42	16	0.90	0.08	<mdl	2.6	1.0
	MB165	chlorite-altered dolerite	222	7.9	0.50	134	3.6	32	16	0.70	0.05	<mdl	1.0	<mdl
	MB166	dolerite	339	3.4	0.30	93	2.7	42	17	0.80	0.09	<mdl	2.0	<mdl
Iron Queen	MB116	chlorite-altered dolerite	207	24	1.6	286	7.7	50	19	0.50	0.13	<mdl	2.1	0.60
	MB118	chloritic rock	322	30	2.2	264	7.5	27	31	1.3	0.08	0.17	4.4	0.90
	MB162	chlorite-altered dolerite	354	5.6	0.40	100	2.8	47	16	0.70	0.10	0.20	3.0	<mdl
	MB164	chlorite-altered dolerite	560	23	1.6	292	7.8	47	25	1.0	0.12	<mdl	3.0	<mdl
Iron Warrior	MB06	chlorite-altered dolerite	348	12	0.70	130	3.6	46	19	<mdl	0.15	0.10	6.0	1.3
Iron Knight	MB144	chlorite-altered dolerite	118	4.8	0.50	80	2.2	7.0	8.9	1.3	0.04	<mdl	3.2	1.3
	MB145	chlorite-altered dolerite	445	11	0.90	163	4.9	47	20	0.20	0.11	0.19	2.8	1.2
	MB149	chlorite-altered dolerite	142	9.4	0.80	143	4.3	17	22	0.70	0.05	<mdl	14	1.1
	MB151	chlorite-altered dolerite	420	8.1	0.60	107	3.1	46	20	0.30	0.10	0.17	3.8	1.5
Iron Magnet	MB34C	amphibolite	63	3.8	0.20	14	<0.1	<mdl	2.8	1.2	<mdl	<mdl	2.0	<mdl
	MB80C	amphibolite	275	37	2.2	141	3.4	5.0	23	1.0	<mdl	0.10	13	<mdl
	MB94	amphibolite	276	13	0.80	153	3.9	29	18	0.10	0.13	0.10	11	<mdl
	MB95	amphibolite	220	16	1.1	144	3.6	21	14	0.40	0.12	0.20	16	<mdl
	MB127	amphibolite	124	4.5	0.40	70	2.0	14	13	1.7	0.28	0.57	3.5	0.80
	MB133	dolerite	348	6.9	0.50	127	3.7	34	18	0.60	0.08	<mdl	1.5	0.90
	MB134	altered amphibolite	43	5.8	0.70	91	2.9	4.0	9.3	0.50	0.02	<mdl	1.5	0.70

Table 3 continued: Trace element geochemistry (ppm)

Location	Sample	Rock type	Bi	Pb	Te	Se	Tl	Mo	Re	Sn	W	Th	U
Reference lithologies													
Cook Gap Schist	MB147	amphibole schist	0.16	6.0	<mdl	0.60	0.20	<mdl	<mdl	3.0	13	6.2	1.7
Port Lincoln	PL4	mafic dike	0.06	12	<mdl	2.0	0.36	<mdl	<mdl	2.0	3.0	4.5	1.4
	PL8	mafic dike	0.06	<mdl	<mdl	2.0	0.30	<mdl	<mdl	2.0	<mdl	3.0	0.81
Middleback Ranges lithologies													
Iron Prince	MB55A	chlorite-altered dolerite	0.07	<mdl	<mdl	<mdl	1.1	<mdl	<mdl	<mdl	2.0	0.94	2.1
	MB108	chloritic rock	0.16	55	0.30	0.90	<mdl	<mdl	<mdl	2.0	13	5.4	3.2
	MB111	chlorite-altered dolerite	0.12	151	0.20	1.5	0.04	<mdl	<mdl	2.0	14	3.5	6.0
Iron Baron	MB152	dolerite	0.01	<mdl	<mdl	0.80	0.39	<mdl	0.002	<mdl	14	1.6	0.25
	MB165	chlorite-altered dolerite	<mdl	<mdl	<mdl	<mdl	0.07	<mdl	<mdl	<mdl	<mdl	4.8	0.70
	MB166	dolerite	<mdl	<mdl	<mdl	1.0	0.37	<mdl	<mdl	<mdl	<mdl	1.5	<mdl
Iron Queen	MB116	chlorite-altered dolerite	<mdl	<mdl	<mdl	1.2	<mdl	<mdl	<mdl	3.0	11	3.7	2.6
	MB118	chloritic rock	<mdl	144	<mdl	2.0	<mdl	<mdl	<mdl	<mdl	13	19	12
	MB162	chlorite-altered dolerite	<mdl	<mdl	0.20	2.0	0.06	<mdl	<mdl	<mdl	<mdl	0.72	0.50
	MB164	chlorite-altered dolerite	<mdl	<mdl	0.10	2.0	0.02	1.0	<mdl	3.0	<mdl	3.4	2.6
Iron Warrior	MB06	chlorite-altered dolerite	0.06	<5	0.10	<mdl	0.02	<mdl	<mdl	3.0	2.0	1.8	1.0
Iron Knight	MB144	chlorite-altered dolerite	0.79	<mdl	0.70	<mdl	<mdl	<mdl	<mdl	<mdl	12	4.5	2.6
	MB145	chlorite-altered dolerite	0.08	<mdl	<mdl	1.3	<mdl	<mdl	<mdl	2.0	13	1.2	0.83
	MB149	chlorite-altered dolerite	0.36	10	<mdl	<mdl	0.48	1.0	<mdl	2.0	17	13	3.7
	MB151	chlorite-altered dolerite	0.04	41	<mdl	<mdl	0.06	<mdl	<mdl	2.0	11	1.2	5.3
Iron Magnet	MB34C	amphibolite	<mdl	<mdl	0.10	<mdl	0.08	<mdl	<mdl	<mdl	1.0	0.44	0.18
	MB80C	amphibolite	0.09	<mdl	0.10	<mdl	2.5	1.0	<mdl	2.0	2.0	5.4	1.3
	MB94	amphibolite	0.09	8.0	0.20	<mdl	0.68	1.0	<mdl	3.0	2.0	5.0	1.7
	MB95	amphibolite	0.26	<mdl	0.20	<mdl	0.41	<mdl	<mdl	2.0	1.0	3.1	0.86
	MB127	amphibolite	0.03	<mdl	0.50	<mdl	0.37	<mdl	0.01	7.0	14	4.4	0.65
	MB133	dolerite	0.20	<mdl	<mdl	1.1	0.31	<mdl	<mdl	1.0	13	3.6	0.67
	MB134	altered amphibolite	0.08	<mdl	<mdl	0.70	0.11	<mdl	0.002	<mdl	12	19	5.4

Table 3 continued: Trace element geochemistry (ppm)

Location	Sample	Rock type	La	Ce	Pr	Nd	Sm	Eu	Gd	Tb	Dy	Y	Ho	Er	Tm	Yb	Lu	ΣREY	$(La/Yb)_{CN}$	$(Eu/Eu^*)_{CN}$
Reference lithologies																				
Cook Gap Schist	MB147	amphibole schist	15	38	3.7	13	2.9	1.0	2.9	0.45	2.5	17	0.54	1.6	0.22	1.5	0.21	100	7.4	1.1
Port Lincoln	PL4	mafic dike	38	89	11	44	10	2.7	9.4	1.5	8.7	50	1.7	4.9	0.66	4.6	0.70	277	5.9	0.82
	PL8	mafic dike	19	44	5.7	24	6.2	1.8	6.4	1.1	6.1	35	1.3	3.6	0.44	3.3	0.49	159	4.2	0.87
Middleback Ranges lithologies																				
Iron Prince	MB55A	chlorite-altered dolerite	3.5	8.3	1.1	5.2	1.6	0.67	2.4	0.43	2.9	18	0.65	1.8	0.21	1.9	0.14	49	1.3	1.04
	MB108	chloritic rock	13	30	4.3	21	6.9	2.1	9.4	1.6	9.2	44	1.7	4.4	0.53	3.2	0.43	152	2.9	0.80
	MB111	chlorite-altered dolerite	45	94	11	46	8.5	2.0	7.2	1.1	6.9	47	1.6	4.7	0.78	4.8	0.80	282	6.6	0.76
Iron Baron	MB152	dolerite	8.7	20	2.7	12	3.4	1.1	4.4	0.84	5.2	28	1.1	3.3	0.46	3.0	0.47	95	2.1	0.90
	MB165	chlorite-altered dolerite	6.7	15	1.9	7.3	1.8	0.4	1.7	0.28	1.9	12	0.41	1.3	0.21	1.6	0.27	52	3.1	0.70
	MB166	dolerite	9.0	21	2.6	12	3.3	1.04	4.1	0.72	4.9	29	1.1	3.2	0.47	2.9	0.46	95	2.2	0.86
Iron Queen	MB116	chlorite-altered dolerite	43	96	12	47	9.6	2.1	8.5	1.3	7.8	40	1.7	4.6	0.76	4.9	0.74	280	6.3	0.70
	MB118	chloritic rock	206	326	36	141	23	5.6	13	1.6	8.3	52	1.7	5.0	0.67	4.5	0.68	825	33.1	0.89
	MB162	chlorite-altered dolerite	17	38	6.1	23	5.0	1.29	3.4	0.40	2.5	14	0.52	1.5	0.23	1.6	0.26	114	7.6	0.90
	MB164	chlorite-altered dolerite	14	31	4.2	19	6.0	2.09	9.3	1.8	12	72	2.7	7.3	1.1	6.5	0.95	189	1.6	0.86
Iron Warrior	MB06	chlorite-altered dolerite	7.7	20	2.5	11	2.9	0.80	3.3	0.57	3.4	17	0.70	2.0	0.24	2.1	0.33	74	2.6	0.79
Iron Knight	MB144	chlorite-altered dolerite	14	27	3.0	11	2.2	0.45	2.3	0.37	2.4	16	0.52	1.5	0.19	1.4	0.19	82	7.1	0.61
	MB145	chlorite-altered dolerite	9.9	26	3.8	17	4.8	1.2	5.5	0.97	6.0	31	1.3	3.4	0.54	3.5	0.50	115	2.0	0.70
	MB149	chlorite-altered dolerite	30	62	7.0	25	4.9	1.3	3.8	0.56	3.4	17	0.65	1.9	0.28	1.8	0.27	159	11.5	0.88
	MB151	chlorite-altered dolerite	3.4	5.9	1.0	4.3	1.3	0.46	1.6	0.32	2.2	11	0.48	1.4	0.23	1.7	0.26	35	1.4	0.99
Iron Magnet	MB34C	amphibolite	4.0	6.3	0.7	2.6	0.56	0.32	0.62	0.10	0.60	6.1	0.13	0.39	<0.05	0.39	0.03	23	7.4	1.65
	MB80C	amphibolite	25	45	5.4	21	4.5	1.2	4.0	0.62	3.7	23	0.73	2.0	0.25	2.1	0.27	139	8.5	0.83
	MB94	amphibolite	6.0	14	1.6	6.8	1.8	0.53	1.8	0.32	1.8	10	0.34	1.0	0.1	1.0	0.13	48	4.3	0.90
	MB95	amphibolite	10	25	3.3	14	3.5	0.89	3.1	0.46	2.4	13	0.48	1.3	0.09	1.0	0.14	79	7.3	0.80
	MB127	amphibolite	8.5	18	2.0	7.5	1.6	0.26	1.3	0.15	0.94	4.9	0.17	0.53	0.08	0.57	0.09	47	10.7	0.55
	MB133	dolerite	23	49	6.2	25	6.1	2.0	6.4	1.0	6.4	33	1.3	3.8	0.54	3.5	0.48	168	4.7	0.97
	MB134	altered amphibolite	52	94	9.5	32	5.6	1.0	4.7	0.67	4.2	22	0.85	2.5	0.36	2.5	0.35	233	15.3	0.60

The amphibolites have SiO_2 contents that range from 28-74 wt.%, have high Fe_2O_3 from 10-47 wt.%, variable TiO_2 (0.26-2.60 wt.%), and K_2O, Na_2O, P_2O_5 and MnO concentrations of ≤1 wt.%. Al_2O_3 and MgO concentrations range from 6-16 and 4-14 wt.%, respectively, with the exception of sample MB34c, which has low Al_2O_3 (1.44 wt.%), but the highest Fe_2O_3 (47 wt.%). The CaO content is highest in sample MB95 (5.14 wt.%), but ranges from 0.10-1.27 wt.% in the remaining samples. Loss-on-ignition in all samples is between 0.50 and 8.70 wt.%. Dolerite samples, including those from Cape Donington, have a wide range in major oxide concentrations (Table 2). The freshest samples are those containing igneous mineral assemblages of magnesiohornblende or diopside + plagioclase, as confirmed by petrographic study. Such samples plot within the 'basalt' field on the (Na_2O + K_2O) vs. SiO_2 diagram of LeBas et al. (1986; Fig. 10A). However, on the Zr-Ti/100-Y*3 diagram (Pearce and Cann, 1973; Fig. 10B), dolerites from the MR plot within the 'ocean-floor' field while those from Cape Donington plot within the 'within-plate' field.

A distinction can be made between samples that are considered 'fresh' and those that are affected by varying degrees of alteration. The freshest samples show consistent concentrations of all major oxides and generally contain greater SiO_2 (45-49 wt.%), CaO (4-9 wt.%), K_2O (≤2 wt.%) and Na_2O (~2.5 wt.%) than their altered equivalents, which typically contain SiO_2 ranging from ~22-45 wt.%, and CaO, K_2O and Na_2O <1 wt.%. Altered samples contain higher concentrations of Al_2O_3 (~6-17 wt.%), MgO (~3-22 wt.%), Fe_2O_3 (~15-40 wt.%), MnO (0.14-1.83 wt.%) and LOI (~7-17 wt.%) than their fresher analogues (~13 wt.% Al_2O_3, ~4-8 wt.% MgO, ~0.25 wt.% MnO, 0.04-4 wt.% LOI. TiO_2 concentrations are variable amongst the mafic dikes and range from 0.64 to 3.78 wt.%. Plots of Fe_2O_3 vs. MgO and SiO_2 for all data show distinctive alteration trends and fields (Fig. 10C, D).

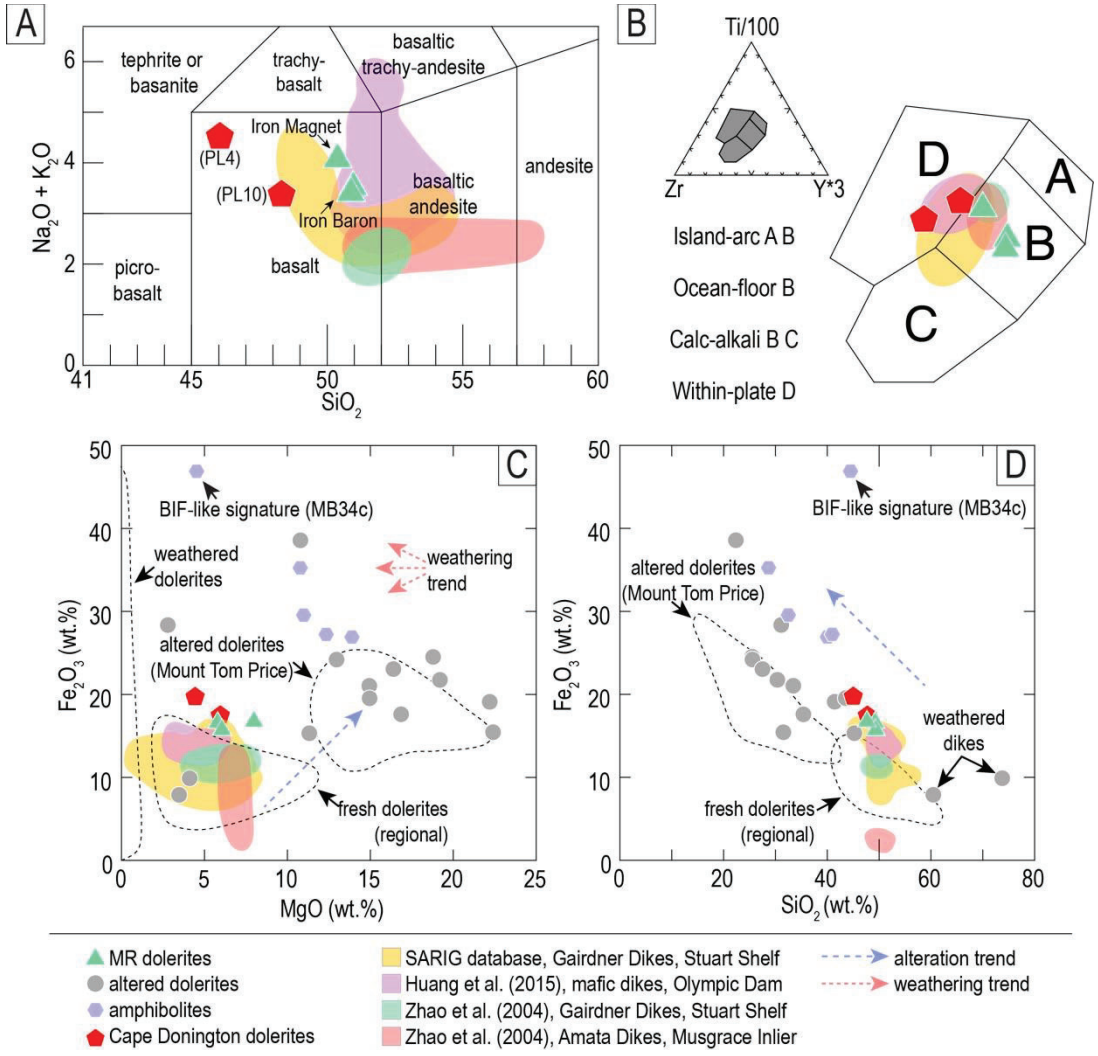

Figure 10: (A) Continental crust-normalized trace element plots and chondrite-normalized REY patterns (B) for amphibolites. (C) ($Na_2O + K_2O$) vs. SiO_2 diagram (after LeBas et al. 1986) showing compositional variation of fresh dolerite dikes from the Middleback Ranges and Cape Donington. (E) Continental crust-normalized trace element plot and chondrite-normalized REY patterns (F) for dolerite dikes. Continental crustal values from Rudnick and Gao (2004), chondrite values from McDonough and Sun (1995).

Trace element patterns of the amphibolites on diagrams normalized to primitive mantle indicate relative depletion in Rb, Ba, K, Sr and Ti, and enrichment in U (Fig. 11A). Sample MB94 stands out amongst the amphibolites with enrichments in K, Pb and Zr. Sample MB134 shows elevated concentrations of Th and U. Other trace elements in the amphibolites show a

range in concentrations, however noticeable differences between the amphibolites are seen in samples MB94 and MB95 compared to the rest of the population (>1200 ppm Cr, >300 ppm Ni, >35 ppm Co). Samples MB80c, MB94 and MB95 also stand out with respect to high V (>200 ppm), Zr (>140 ppm), Sc (>14 ppm) and As (>10 ppm) relative to the other amphibolites.

Chondrite-normalized REY fractionation patterns for the amphibolites resemble those of the dolerites (Fig. 11B), however with a lower mean Σ(REY) content (<250 ppm). The amphibolites are HREE-enriched and LREE-depleted, with $(La/Yb)_{CN}$ ranging from 4.3-15.3 (mean = 7.3). With the exception of sample MB80c, negative Eu anomalies are present in all the amphibolites ($(Eu/Eu^*)_{CN}$ = from 0.55-0.90).

On the diagram normalized to primitive mantle (Fig. 11C), the patterns for dolerites, including Cape Donington, show variability in trace element compositions relative to their degree of alteration. All samples show comparable concentrations of P, Nd, Zr, and REY. However, fresher samples show higher concentrations of Cs, Rb, and Ba, with enrichment in K relative to more altered samples, which generally show relative depletion in Rb, Ba, K and higher concentrations of Nb and Ta, with enrichments in U and Pb also noted. The magnitude of Sr depletion is greater in altered samples than those that are less-altered. All mafic dikes show depletion in Ti relative to Sm and Y. Other trace elements within the suite of dolerites show variability, however Cr, Ni, Co, Cu, Zn, V, Zr, Sc, Ga and W consistently measure in the tens to hundreds of ppm throughout the dolerite suite. Hafnium, As, Sb, Sn and U all measure between 1 and 10 ppm.

Absolute REY concentrations in the dolerites range from 35 to 825 ppm. Chondrite-normalized REY fractionation patterns for all dolerites display similar characteristics with the exception of slope and magnitude of anomalies (Fig. 11D). All samples are heavy rare earth element (HREE)-enriched and light rare earth element (LREE)-depleted, with $(La/Yb)_{CN}$

ranging from 1.3-33. Altered dolerites show greater LREE enrichment. Negative Eu anomalies are visible in all but a single sample, with $(Eu/Eu^*)_{CN}$ ranging from 0.61-1.0.

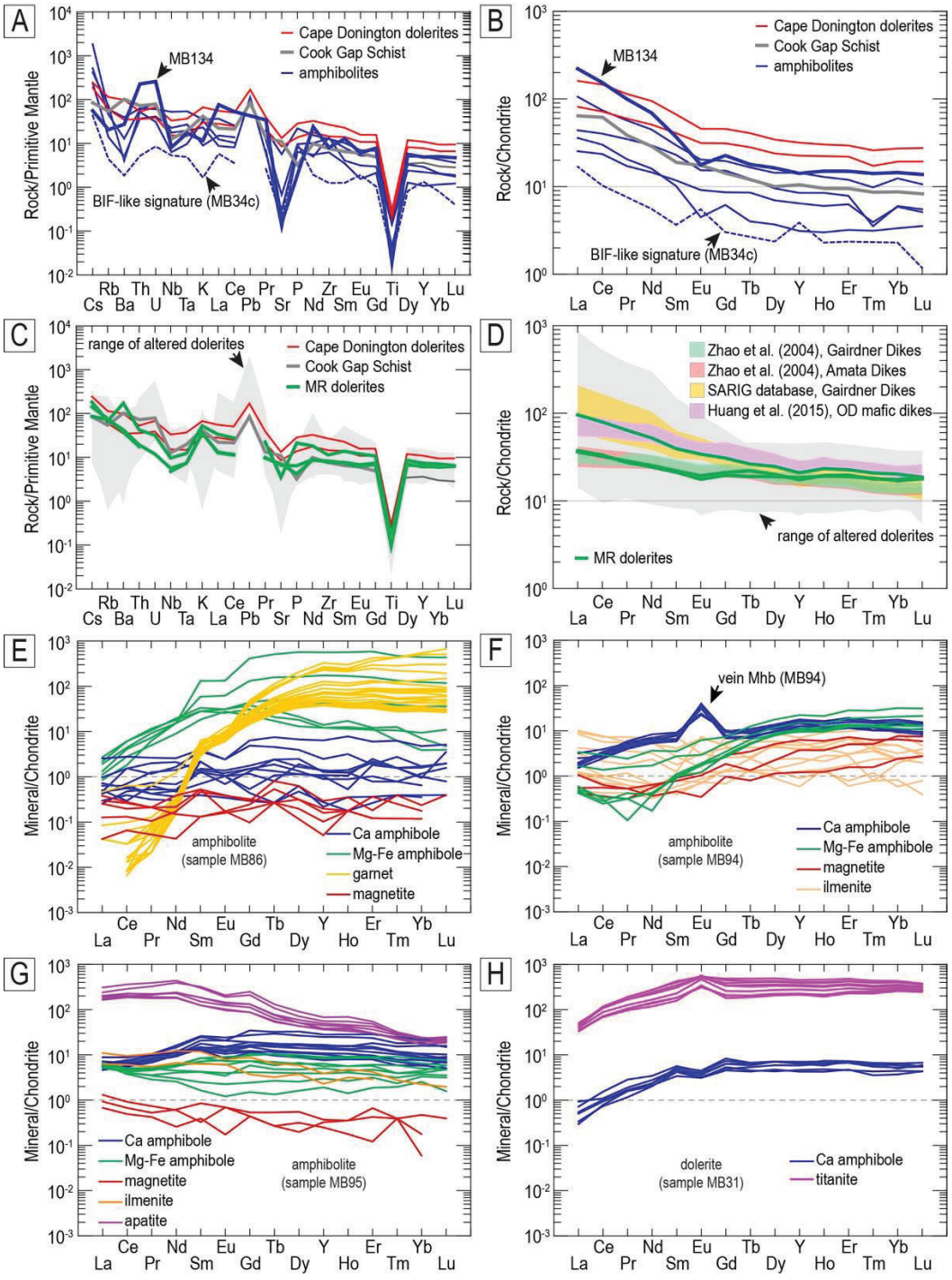

Figure 11: Chondrite-normalized REY fractionation patterns for Mg-Fe and Ca-amphiboles, garnet, apatite, magnetite and ilmenite within amphibolites (A-C), and Ca-amphibole and titanite within dolerite (D).

5.4.4 Mineral trace element geochemistry – LA-ICP-MS data

Considering the assemblages containing REY minerals, a selection of minerals from amphibolites and dolerites was analyzed for trace element concentrations and is described below. These include amphibole (Mg-Fe- and Ca species), garnet, titanite, titaniferous magnetite, ilmenite and apatite. Trace element data (Electronic Appendix C) are plotted (Fig. 11E-H) and shown as element maps (Electronic Appendix C, Figs. C1 and C2).

In the amphibolites, the main REY carrier is garnet (average ΣREY = 180 ppm), which displays a REY fractionation trend showing LREE depletion and HREE enrichment (Fig.11E). Garnet maps show Ho-Y-richer cores relative to rims. Amphiboles, whether Mg-Fe or Ca-types, show mild variation in ΣREY and trend shape. Magnesian-Fe amphibole within samples containing garnet or where it occurs as the only amphibole (sample MB94) are also LREE-depleted and HREE-enriched (Fig. 11F, G). Otherwise, amphiboles display relatively flat REY trends. An exception to this is the ferrohornblende found within the tourmaline veins (sample MB94), which is slightly HREE-enriched and shows a prominent positive Eu-anomaly. Element maps show this is also enriched in Ni, V, Co, Sn and Zn. In general, both magnetite and ilmenite are poor carriers of REY and show relatively flat trends (Fig. 11F, G). However, in some samples, magnetite measured V, Cr, Ni, Zn and Zr in the tens to hundreds ppm. Apatite associated with magnetite shows LREE-enrichment and HREE-depletion with a slight negative Eu-anomaly.

A comparison between major amphibole (magnesiohornblende) and accessory titanite is shown for one of the MR dolerite samples (MB31). Magnesiohornblende contains concentrations of Sc, V, Cr, Co, Ni, Cu and Zn in the tens to hundreds of ppm, and has an average ΣREY of 15 ppm. Titanite on the other hand has a ΣREY of ~1000 ppm, and measures V in the thousands of ppm, Zr and Nb in the hundreds, and Cu, Zn, Sn, Hf and Pb in the tens

of ppm. Both minerals show similar REY fractionation trends that are slightly LREE-depleted and HREE-enriched but with opposite signs for the Eu-anomaly, i.e., positive and negative for amphibole and titanite, respectively (Fig. 11H).

5.4.5 U–Pb SHRIMP zircon geochronology

Zircon grains within the dated samples display a wide range in size and morphology. They vary from fine- (~25 μm)- to coarse-grained (>100 μm) with aspect ratios of 1:1 and 1:2 and mostly subhedral to anhedral shapes, although more prismatic examples are present in amphibolites (samples MB134 and MB144). Cathodoluminescence (CL) images show zircon to have various intensities as well as internal zoning patterns. While most grains display dark to greyish intensities with faint or no oscillatory zoning, some display oscillatory zoning or dark cores with bright rims (e.g., MB134). The U and Th concentrations of zircon range from 13 to 2,320 ppm and 5-1,040 ppm, respectively, with Th/U ratios from 0.03 to 2.2. The individual $^{207}Pb/^{206}Pb$ ages range from 699 Ma to 3275 Ma. Full details of zircon isotopic data can be found in Electronic Appendix D. CL images of individual zircon grains are shown in Electronic Appendix D, Fig. D1. Results for samples MB161, MB162 and MB165 have been placed in Electronic Appendix D, Fig. D2 due to a lack of data, or excessive discordance precluding an interpretation.

5.4.5.1 Amphibolites and dolerites from the Middleback Ranges

A total of twenty-three zircon grains were analyzed from the mylonitized amphibolite in Iron Magnet (sample MB134). These have discordance ranging from 0 % to 31%, U and Th concentrations ranging from 28-283 ppm and 22-273 ppm, respectively, and $^{232}Th/^{238}U$ ratios of 0.3-1.77. The data form two groups on a Tera-Wasserburg diagram (Fig. 12A). The first group (4 grains; Fig. 12B) has individual $^{207}Pb/^{206}Pb$ dates and single data point uncertainties (±1σ) between 3090 Ma and 3155 Ma, and 69 Ma and 76 Ma, respectively. A single grain with

2% discordance has an individual $^{207}Pb/^{206}Pb$ age of 3206 ± 16 Ma. Two other grains have low discordance (2%) and similar individual $^{207}Pb/^{206}Pb$ ages, and were used to obtain a $^{207}Pb/^{206}Pb$ weighted mean age of 3129 ± 24 Ma (MSWD = 1.5; *n* = 2). The remaining two grains have discordance of 6 % and 30 % and plot off the concordia line. The second group of data (18 grains; Fig. 12C) have individual $^{207}Pb/^{206}Pb$ dates and single data point uncertainties (±1σ) between 2528 Ma and 2807 Ma, and 15 Ma and 40 Ma, respectively. A group of four of the youngest and least discordant grains (<4%) were used to obtain a $^{207}Pb/^{206}Pb$ weighted mean age of 2542 ± 15 Ma (MSWD = 0.84; *n* = 4). The older grains representing the first group (3129 ± 24 Ma) are interpreted as inherited and reflect the age of the underlying ~3.1 Ma Cooyerdoo Granite basement complex while the younger age of the second group (2542 ± 15 Ma) is interpreted to reflect the age of dike emplacement.

Nine zircon grains analyzed from the amphibolite dike at Iron Knight North (sample MB144; Fig. 12D), six of which have discordance <7% and contain consistent U (51-81 ppm) and Th (21-71 ppm), with $^{232}Th/^{238}U$ ratios between 0.57-0.91. The remaining three grains have high U (~185 ppm), Th (~125 ppm) and $^{232}Th/^{238}U$ ratios (~0.77), two of which have discordance >10% and the last is 3% discordant. Individual $^{207}Pb/^{206}Pb$ dates and single data point uncertainties (±1σ) between 2700 Ma and 2870 Ma, and 15 Ma and 39 Ma, respectively. The seven grains with discordance <10% were used to obtain a $^{207}Pb/^{206}Pb$ weighted mean age of 2825 ± 23 Ma (MSWD = 0.77; *n* = 6), which is interpreted to reflect the maximum age of dike emplacement.

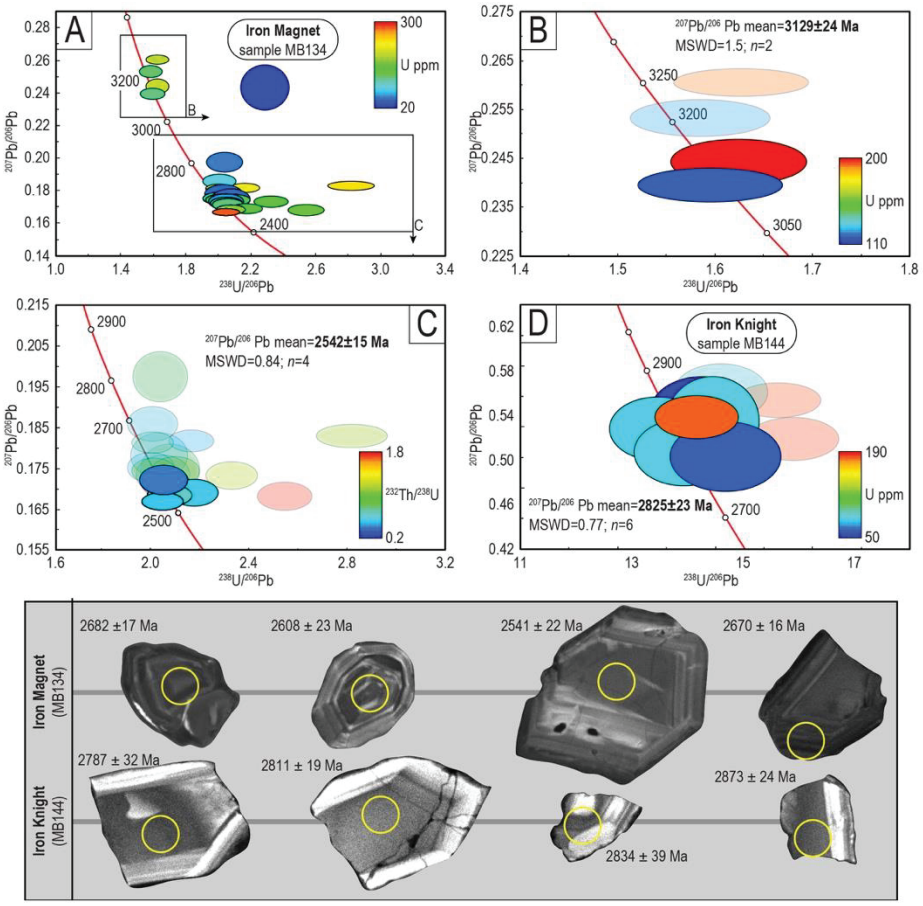

Figure 12: Tera-Wasserburg diagrams presenting SHRIMP U–Pb data for zircon and representative cathodoluminescence images of zircon grains with their respective $^{207}Pb/^{206}Pb$ ages (±1σ) for amphibolites from (A-C) Iron Magnet and (D) Iron Knight North pit. Colored circles on zircon grains represent location of analysis using a 25 µm spot diameter.

A dolerite from Iron Queen (sample MB163) provided the most well-constrained age for this rock group within the MR. Ten analyses were collected from ten grains, all of which plot near the concordia line on the concordia diagram (Fig. 13A). Individual $^{206}Pb/^{238}U$ dates and single data point uncertainties (±1σ) range from 695-1343 Ma and 18-47 Ma, respectively. Three grains have significantly older individual $^{206}Pb/^{238}U$ dates (~1100-1350 Ma) than the remaining analyses (≤810 Ma). Two of these older grains have low U (13 ppm) while the third has a low $^{232}Th/^{238}U$ ratio (0.13) and >1% common ^{206}Pb. The seven remaining spots form a

younger group (Fig. 13B) with $^{206}Pb/^{238}U$ dates from 695-810 Ma, however the youngest of these spots (695 Ma) plots somewhat separate from the group and has the highest U and Th within the dataset (63 ppm and 37 ppm, respectively) and >1% common ^{206}Pb. The remaining six analyses have consistent $^{232}Th/^{238}U$ ratios between 0.31 and 0.42; however only four of the most concordant grains lying on the concordia line were used to obtain a $^{206}Pb/^{238}U$ weighted mean age of 782 ± 23 Ma (MSWD = 0.90; $n = 4$). Older grains within the dataset are interpreted as detrital. The age of 782 ± 23 Ma given by the group of four analyses is interpreted to reflect the timing of the dike emplacement.

Four zircon grains were analyzed from a dolerite in Iron Baron (sample MB166). Three analyses plot concordantly (1-3%) and a single analysis is discordant (16%) (Fig. 13C). Individual $^{206}Pb/^{238}U$ dates and single data point uncertainties (±1σ) range from 840-1923 Ma and 17-34 Ma, respectively. The oldest grain within the dataset (1972 Ma) has U and Th concentrations of 359 ppm and 107 ppm, respectively. The three remaining analyses have U and Th contents between 163 ppm and 891 ppm, and 44 ppm and 154 ppm, respectively. One grain has a $^{206}Pb/^{238}U$ age of 979 ± 26 Ma, and another has 16% discordance and sits above concordia (Fig. 13D). The last grain has only 3% discordance and an individual $^{206}Pb/^{238}U$ age of 872 ± 25 Ma. This age is interpreted as the timing of dike emplacement.

A less well-constrained age came from another dolerite from Iron Queen (sample MB164), from which six zircon grains were analyzed. Two grains are concordant (≤2%) whereas the remainder have discordance ranging from 12-31% (Fig. 13E). A single grain within the data set has U and Th concentrations of 64 ppm and 27 ppm, respectively. Uranium and Th concentrations in all other grains range from 397-1089 ppm and 98-227 ppm, respectively. The individual $^{206}Pb/^{238}U$ dates and single data point uncertainties (±1σ) range from 743-1140 Ma and 23-45 Ma, respectively. The data plot scattered along the concordia line in the concordia

diagram, with the four oldest spots forming a group at ~1000-1100 Ma. A single grain plots concordantly (2%) at 921 Ma and another plots discordantly (20%) at 743 Ma. Although the data are limited, the youngest $^{206}Pb/^{238}U$ age may be interpreted as the maximum age for dike emplacement.

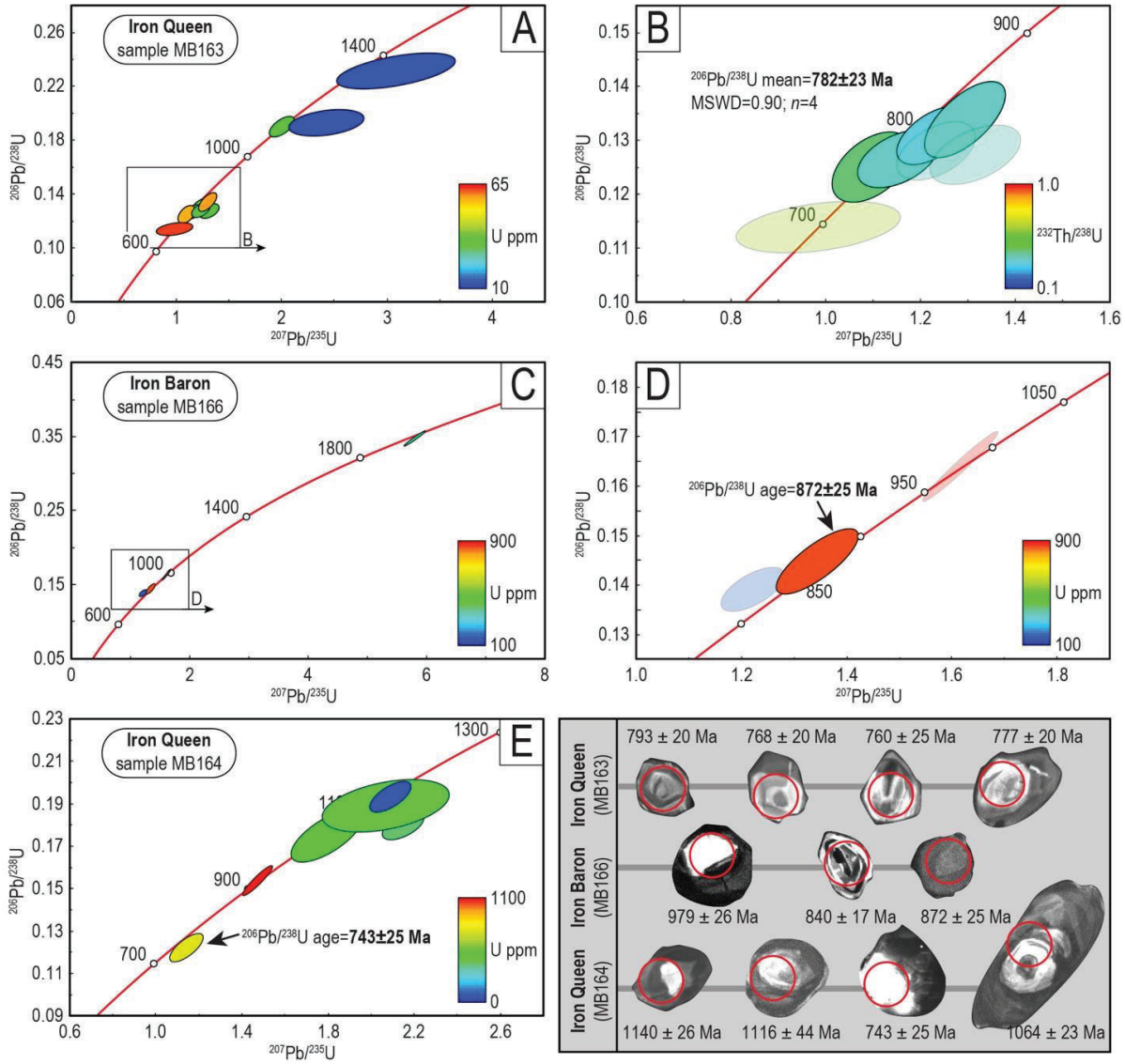

Figure 13: Wetherill diagrams presenting SHRIMP U–Pb data for zircon and representative cathodoluminescence images of zircon grains with their respective $^{206}Pb/^{238}U$ ages (±1σ) for dolerites from (A, B, E) Iron Queen and (C, D) Iron Baron. Colored circles on zircon grains represent location of analysis using a 25 μm spot diameter.

5.4.5.2 Cape Donington dolerite and Cook Gap Schist

Twenty spot analyses were collected from twenty grains from the dolerite dike at Cape Donington (PL10), which have discordance ≤11% and plot as two groups on the concordia diagram (Fig. 14A). A first group (4 grains; Fig. 14B) has high $^{232}Th/^{238}U$ ratios (0.83-1.84) and individual $^{207}Pb/^{206}Pb$ dates and single data point uncertainties (±1σ) between 2992 Ma and 3122 Ma, and 19 Ma and 112 Ma, respectively. This group has a $^{207}Pb/^{206}Pb$ weighted mean age of 3042 ± 28 Ma (MSWD = 0.63; n = 4). The second group (16 grains; Fig. 14C) has low $^{232}Th/^{238}U$ ratios (0.06-0.39) and single data point uncertainties (±1σ) between 1658 Ma and 1809 Ma, and 13 Ma and 42 Ma, respectively. This group has a $^{207}Pb/^{206}Pb$ weighted mean age of 1711 ± 14 Ma (MSWD = 1.19; n = 13). A single grain (10% discordance) with four times the U concentration (~1600 ppm) than the remaining grains (≤600 ppm) was omitted from this calculation, as were two grains with discordance ≥7%. The older grains representing the first group (3042 ± 28 Ma) are interpreted as inherited and reflect the age of the underlying Mesoarchean crust (~3.1 Ma Cooyerdoo Granite basement complex) while the younger age of the second group (1711 ± 14 Ma) is interpreted to reflect the age of dike emplacement.

Twenty-four analyses were taken from twenty-two grains separated from the Cook Gap Schist (sample MB147), including two pairs of analyses deriving from grains displaying dark cores and bright rims. However, these cores and rims show comparable $^{207}Pb/^{206}Pb$ ages. Individual $^{207}Pb/^{206}Pb$ dates and single data point uncertainties (±1σ) range from 2019 Ma and 3276 Ma, and 11 Ma and 39 Ma, respectively. A single grain with a large error (± 210 Ma) was omitted from consideration. The data plot scattered along a concordia line on a Tera-Wasserburg diagram (Fig. 14D), however two main clusters are recognized at ~2.5 Ga and ~3.0 Ga. The concordant (<10%) data form prominent age peaks on a probability density distribution diagram at ~2.5-2.7 Ga and 3.1-3.25 Ga (Fig. 14E). The three largest peaks occur

at 2.59 Ga, 2.68 Ga and 2.71 Ga, with smaller peaks at 2.54 Ga, 3.13 Ga, 3.15 Ga, 3.23 Ga and 3.26 Ga. However, many of the zircon grains comprising the youngest of these age peaks (2.54 Ga) have discordance >5%. Three grains with low discordance (<5%) were used to obtain a $^{207}Pb/^{206}Pb$ weighted mean age of 2585 ± 22 Ma (MSWD = 1.9; n = 3; Fig. 14F), which is interpreted as the maximum depositional age for this schist sample. Grains comprising older age peaks are interpreted as detrital and are inherited from underlying Mesoarchean basement (~3.1 Ga Cooyerdoo Granite).

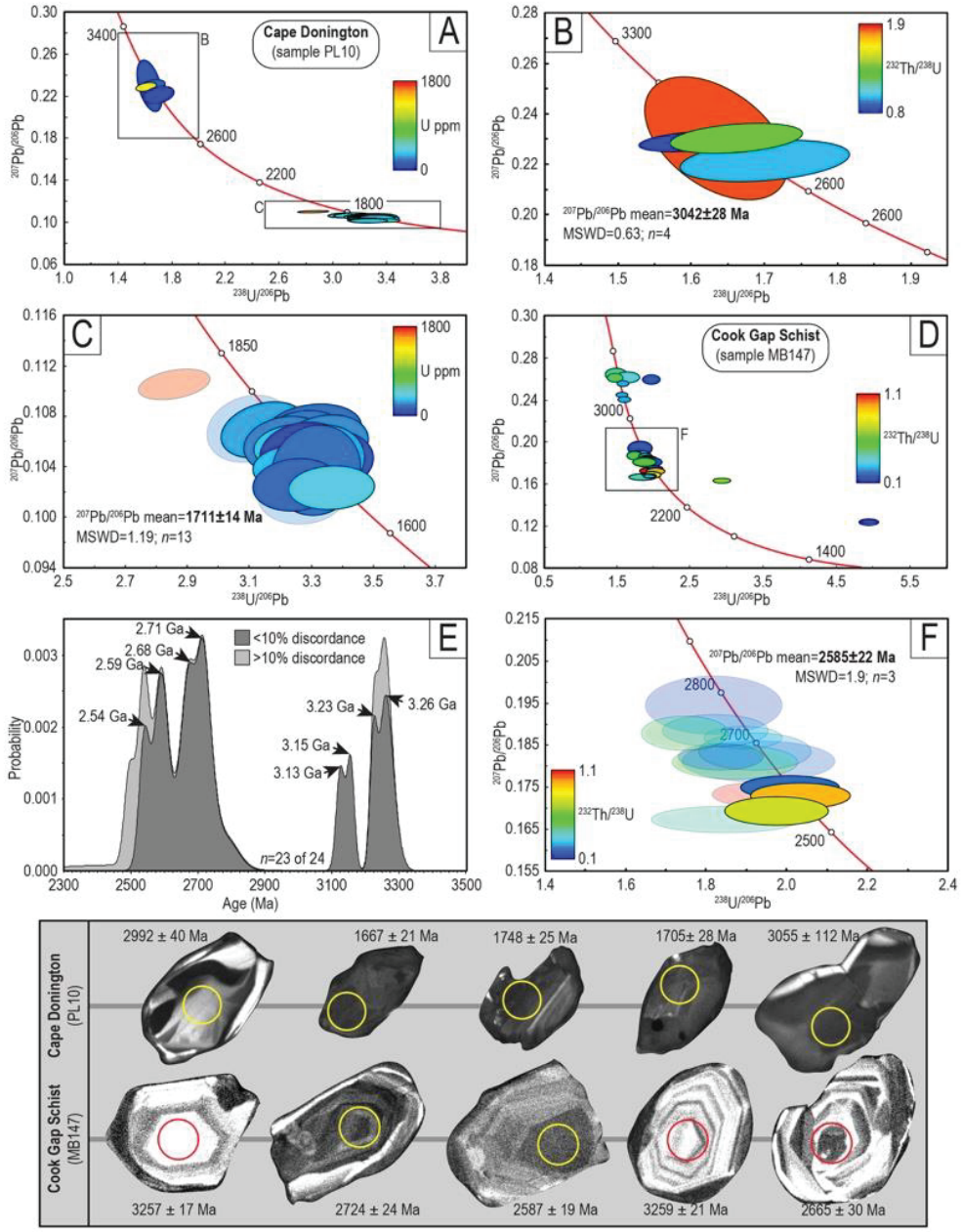

Figure 14: Tera-Wasserburg diagrams presenting SHRIMP U–Pb data for zircon and representative cathodoluminescence images of zircon grains with their respective $^{207}Pb/^{206}Pb$ ages (±1σ) for (A-C) dolerite from Cape Donington and (D-F) the Cook Gap Schist. Colored circles on zircon grains represent location of analysis using a 25 µm spot diameter.

5.4.6 U–Pb LA-ICP-MS hematite geochronology

Hematite within two hematite-goethite ores (Fig. 15) was found to contain sufficient U (average ~25 ppm) and radiogenic-Pb to perform LA-ICP-MS U–Pb hematite geochronology. The hematite data reported are given as lower intercept dates on concordia diagrams and are presented in Figure 15 and Electronic Appendix D, Table D2.

Thirty spot analyses were taken in total, two of which were not included in the calculation due to large errors (Electronic Appendix D, Table D2). The remaining twenty-eight spots fit along a discordia line yielding an intercept age of 687 ± 22 Ma (MSWD = 2.3; n = 28) on a concordia diagram (Fig. 15A). In sample MB150b, coarse-grained (>100 µm) platy hematite aggregates to form layers and are fringed by fine-grained hematite. Twenty spot analyses were taken from the coarse-grained hematite that fit a discordia line (Fig. 15B) yielding an intercept age of 663 ± 19 Ma (MSWD = 5.2). The ages derived from dating of hematite from the two samples are interpreted to reflect the timing of ore formation at ~680 Ma.

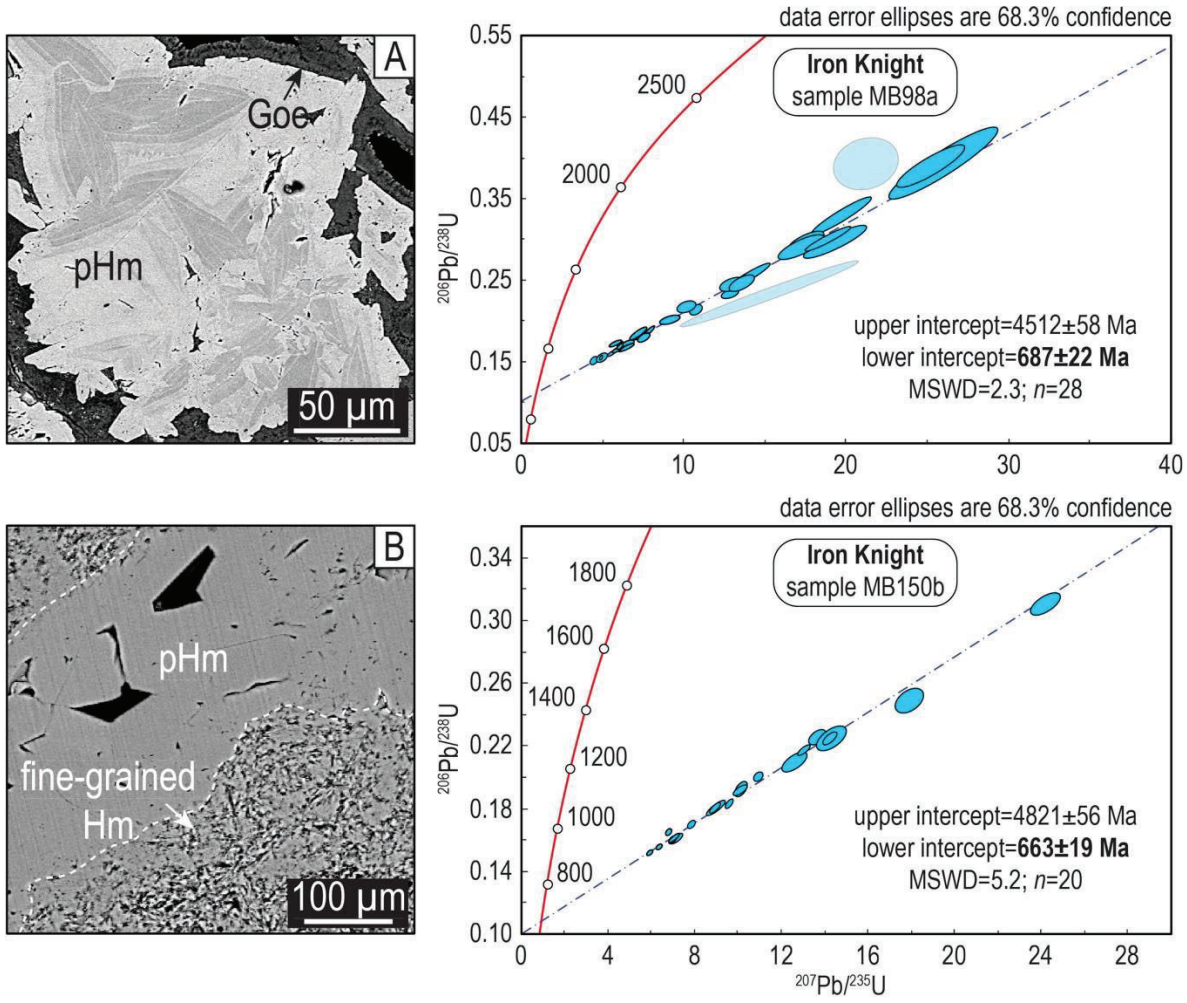

Figure 15: BSE images showing aspects of hematite in ores from Iron Knight (Fig. 3E) used for LA-ICP-MS dating and their respective Wetherill diagrams presenting U–Pb data. Note the oscillatory zoning in hematite with respect to Si in (A).

5.5 Discussion

5.5.1 How many episodes of mafic magmatism in the Eyre Peninsula?

The present data show that both types of MR mafic lithologies are amphibole-bearing. The dolerites, however, contain only Ca-amphiboles and preserve plagioclase (Fig. 8) whereas the amphibolites comprise a diverse range of both Fe-Mg- and Ca-amphiboles (Fig. 5) and rarely preserve plagioclase. In contrast, the Cape Donington dolerites are pyroxene-rich but also

contain Ca-amphibole (Fig. 9). Although the amphibolites from Iron Magnet studied here are concordant with the BIF sequences and the dolerites occur as crosscutting dikes in the central part of the belt, there are cases showing contrasting relationships, e.g., fresh dolerite at Iron Magnet concordant with BIF sequences and altered mafic dike at Iron Knight North (Fig. 3). Considering the lack of geochronological constraints on the Iron Magnet dolerite and the ambiguity on the age obtained for the Iron Knight North dike (see below), the overall understanding of mafic lithologies from the southern part of the belt remain open to debate.

Geochronological results presented here are interpreted in terms of mafic magmatism from the Neoarchean to Neoproterozoic. Zircon populations dated at ~3.0 Ga are found in both dolerite dikes and amphibolites, and reflect the Mesoarchean crust underlying the MR. Zircon from mylonitized amphibolite at Iron Magnet (sample MB134; Fig. 12C) yields a well-constrained $^{207}Pb/^{206}Pb$ weighted mean age of 2542 ± 15 Ma. The ~2.5 Ga age for the Iron Magnet amphibolite, together with the interbedded occurrence of amphibolites and BIFs across exposures in the Iron Magnet mine are evidence that effusive mafic magmatism took place contemporaneously with BIF deposition.

In contrast, zircon grains from within the altered mafic dike at Iron Knight North (sample MB144) yielded a $^{207}Pb/^{206}Pb$ weighted mean age of 2825 ± 23 Ma (Fig. 12D). The crosscutting relationship between this dike and BIF (Fig. 3D) implies it must be younger than the ~2.5 Ga BIF depositional age (Szpunar et al., 2011), suggesting the zircon grains are inherited from an underlying lithology, an observation supported by their fractured character. The lithology closest in age to the inherited grains from the dike is the protolith to the Coolanie Gneiss emplaced at 2823 ± 37 Ma (Fraser et al., 2010), which has a NE-trend and outcrops southwest of the MR. Inherited ages of the Coolanie Gneiss protolith have also been found within the ~1775 Ma Tip Top Granite immediately east of the MR (McAvaney et al., 2016), and also

within a sample of Broadview Schist near Six Mile Hill northeast of the MR (Szpunar and Fraser, 2010). Although it has been suggested that the Middleback Subgroup succession was deposited atop the ~3.1 Ga Cooyerdoo Granite (Keyser et al., 2019b), the NE trend of ~2.8 Ga ages through the MR may imply the presence of an additional ~2.8 Ga basement within the MR area. Alternatively, the initial depositional age for BIF sequences may be ~300 Ma older than the Cook Gap Schist.

The dolerite from Cape Donington (sample PL10) yielded two zircon age populations, the youngest of which has a $^{207}Pb/^{206}Pb$ weighted mean age of 1711 ± 14 Ma. Mafic dikes found crosscutting the Donington Suite in the southern Eyre Peninsula include the syn-orogenic Jussieu mafic dikes and the post-orogenic Tournefort mafic dikes (1812 ± 5 Ma; Schaefer, 1998). The younger age group within sample PL10 postdates both the Tournefort and Jussieu mafic dikes and is thus interpreted to represent mafic magmatism associated with the ~1.73-1.69 Ga Kimban Orogeny. The older age population ($^{207}Pb/^{206}Pb$ weighted mean age of 3048 ± 28 Ma) can be correlated with similar Mesoarchean inherited zircons from other lithologies across the northeastern Eyre Peninsula east of the KMZ (e.g., Fanning et al., 2007; Szpunar et al., 2011) and is interpreted to reflect >3.0 Ga underlying basement complexes (Fraser et al., 2010; Jagodzinski et al., 2011; Keyser et al., 2019b). However, the Mesoarchean basement in the eastern Eyre Peninsula is believed to pinch out towards the south, as no inheritance of Mesoarchean-aged zircon has been reported in Donington Suite lithologies (Fraser et al., 2010). The ~3.0 Ga inherited zircon grains within sample PL10 may suggest further extension of the Mesoarchean basement to the southern Eyre Peninsula. In this study, no pyroxene-rich, ~1.7 Ga age dolerite dikes are recognized along the MR.

Robust ages for the MR dolerites remain somewhat sparse. The best-constrained age within the dataset (782 ± 23 Ma for MB163; Fig. 13B) was obtained from fine-grained, angular zircon

from Iron Queen dolerite. However, zircon grains with similarly young individual $^{207}Pb/^{206}Pb$ ages were also found in other samples (872 ± 25 Ma for MB166; Fig. 13D; 743 ± 25 Ma for MB164; Fig. 13E). Despite the relatively large error, the ages of these dolerite dikes, as well as their aeromagnetic signatures, correlate with those of the 827 ± 26 Ma Gairdner Dike Swarm (Wingate et al., 1998), which can be traced for at least 1,500 km throughout southern Australia (Pirajno and Hoastson, 2012).

The Gairdner event is interpreted as a large igneous province formed during the breakup of the Rodinia supercontinent (Parker et al., 1995). Dikes of the Amata Suite (~760 Ma; Werner et al., 2014, 2018; 790 ± 40 Ma; 797 ± 49 Ma; Zhao et al., 1993, 1994) are widespread throughout the Musgrave Block, are readily correlated to the Gairdner Dike Swarm. These are of similar age to those in this study. This is the first confirmation of the presence of dolerite dikes associated with the Gairdner LIP within the MR, extending its known occurrence within the Gawler Craton. The Gairdner dikes from different domains in South Australia are however distinct in terms of petrography, e.g., pyroxene- and amphibole-bearing in the Olympic Dam area (Huang et al., 2015) and MR, respectively, or plotting within different fields on petrogenetic major and minor element plots (Fig. 10C, D), albeit with overlapping chondrite-normalized REY trends (Fig. 10F). This potentially implies heterogeneity in the magma reservoir(s) and/or differences in geodynamic setting. For example, the higher H_2O content in the magma required to form magnesiohornblende-dolerite is concordant with the ocean floor field indicated by the Zr-Ti-Y (HFSE) plot (Fig. 10D).

5.5.2 Origin, metamorphism and alteration of amphibolites in the southern part of the belt

The Mg-Fe-amphiboles (as well as ferro-tschermakite) within the amphibolites interstratified with BIFs at Iron Magnet are distinct from the conspicuous magnesiohornblende that is

characteristic for the younger and fresher dolerites (Fig. 5). Such amphibole-bearing lithologies are known from BIF sequences elsewhere that have undergone medium-grade metamorphism (Klein, 1973). The amphibole-bearing rocks could result from metamorphic reactions between Fe-rich carbonates and quartz or Mg-Fe-silicates (e.g., greenalite). At Iron Magnet, however, all amphibolites (or amphibole-rich intervals) are typified by the presence of a distinct titaniferous magnetite + ilmenite assemblage, which is not recorded within the interlayered BIF sequences (Keyser et al., 2018). Indeed, reports of such Ti-bearing iron-oxides are rare in the BIF literature. Magnetite displaying exsolutions of ilmenite has, however, been reported from volcanic breccia layers in the Sokoman iron formation, Labrador Trough, Canada (Chung et al., 2015). These layers are attributed to input of detrital material from exhalative volcanism during or shortly after BIF deposition. The comparable ~2.5 Ga age of the Iron Magnet amphibolite would support an analogous origin in which shallow sills (or possibly flows) form interbedded with BIF. The interstratified nature of the amphibolites is, however, particularly fine in some parts, and thus difficult to reconcile with formation via effusive processes.

One possible explanation is to consider detrital input of Fe-Ti-oxides from igneous mafic/ultramafic lithologies. Such input during BIF deposition is feasible close to the margins of the sedimentary basin, where the orebody is bounded by granitic basement at Iron Magnet. An analogous detrital protore has been suggested for Zr-rich hematite ores of the Peculiar Knob deposit in South Australia (Keyser et al., 2019c), or for magnetite-rich gneisses at the Warramboo iron deposit, South Australia (Lane et al., 2015). Whole-rock compositions and mineralogical variation among the amphibolites at Iron Magnet, including the presence of aluminous minerals (e.g., almandine) would support a model of detrital input within BIF, which are otherwise characterized by inherently low Al_2O_3 as shown by studies elsewhere (Klein, 2005). Additionally, some amphibolites still preserve BIF-like REY fractionation signatures (MB34c; Fig. 10B), although they contain magnetite with ilmenite trellis exsolution, which

might support a mixing between detrital input and chemical precipitation. The upper T range obtained from titaniferous magnetite using Fe-Ti-oxide geothermometry (527-602 ˚C) is concordant with a model of redox-controlled ilmenite exsolution from magmatic magnetite-ulvöspinel solid solution (e.g., Buddington and Lindsley, 1964) and matches conditions for amphibolite facies metamorphism.

Irrespective of the above debate, the mixed chemical and detrital sediments have undergone at least amphibolite-facies metamorphism based on the presence of Mg-Fe amphibole + garnet assemblages. Metamorphism and deformation of the BIF-sill package in the southern part of the belt is contemporaneous with formation of amphibolite-bearing rocks in the marker horizon (Cook Gap Schist) during the Sleafordian orogeny at ~2.47-2.41 Ga. The maximum depositional age for this horizon, previously given as 2566 ± 20 Ma (Szpunar et al., 2011), is confirmed here at 2585 ± 22 Ma ($^{207}Pb/^{206}Pb$ weighted mean; Fig. 14F) from the youngest zircon population. As previously reported, the spread of ages from 2.54 Ga to 3.26 Ga indicates supply of detrital zircon from various sources. The older populations (~3.2 Ga and ~3.15 Ga) reflect inheritance from Mesoarchean granites along the western margin of the MR and underlying Cooyerdoo Granite basement (Fraser et al., 2010; Fraser and Neuman, 2010; Jagodzinski et al., 2011; Keyser et al., 2019b) whereas ~2.7 Ga zircon population may represent the age of another basement unit exposed and weathered during sedimentation of the Middleback Subgroup, as also proposed by Szpunar et al. (2011).

Post-peak metamorphic conditions are recorded by Fe-Ti-oxide geothermometry as 435-505 ˚C (separate grains of magnetite and ilmenite). These rocks also record a high-T alteration event related to hydrothermal fluid flow that took place after metamorphism (tourmaline veins crosscutting ilmenite lineation). This alteration event is recognizable by geochemical signatures attributable to a granitic source like the Sn-bearing magnesiohornblende (Electronic

Appendix C, Fig. C2). Extensive pyritization and formation of Cl-rich assemblages (pyrosmalite; Keyser et al., 2018) are attributable to hydrothermal brines focused along contacts between amphibolites and BIFs. These observations emphasize the strong possibility of younger granites being present underneath the Iron Magnet deposit.

5.5.3 How many cycles of ore upgrading?

Alteration of MR dolerite dikes characterized by Mg- and Fe-chlorites increases with proximity to orebodies as shown from deposits in the central part of the belt, an observation previously recognized by Ward (1949). Taylor et al. (2001) report chlorite alteration in dolerite dikes proximal to orebodies in the Hamersley iron province, Western Australia, contrasting with distal dikes that displayed fresh regional signatures. Accordingly, Taylor et al. (2001) suggested that dike alteration at Mount Tom Price takes place prior or during BIF desilification and ore upgrade, i.e., relative enrichment in FeO and MgO and depletions in SiO_2, CaO, K_2O, Na_2O and BaO in altered dikes compared to fresh regional dolerites (Fig. 10C, D). Comparable chemistry and trends are recorded by the MR dolerites (Table 2). The least-altered dolerite dikes plot together near fields of 'fresh dolerites' from the Hamersley province (Taylor et al., 2001) and overlap with other fresh dolerites from across the Gawler Craton. In contrast, the chlorite-rich samples follow alteration trends of increasing Fe and Mg and decreasing Si, indicating Mg-Fe alteration patterns that differ from weathering trends showing depletion in Mg. This implies that ore enrichment in this part of the belt could have been after ~780 Ma.

Younger cycles of ore upgrading are also shown by the U–Pb ages (~680 Ma) obtained from Iron Knight South hematite. The hematite ore is Si-bearing and shows textural evidence of formation via replacement of pre-existing iron-hydroxides (Keyser et al., 2018). Taken together, the textures and ages suggest a second burial cycle in this part of the belt, following

Gairdner dike emplacement. In both cases, these cycles of ore upgrading are ~700 Ma younger than those recorded from the Iron Count prospect (≥1790 Ma; Keyser et al., 2019a).

Overall, alteration trends recognized in dolerite dikes and U-Pb dating of hematite reported here and in Keyser et al. (2019a) provide evidence for a multi-stage formation of high-grade ores. This can be corroborated with previous interpretations of mechanical redeposition following erosion, during cycles of burial and weathering as suggested by Parker et al. (1993). In addition, the data presented here emphasize the compartmentation of the belt in terms of distinct BIF sedimentation-burial-uplift-ore enrichment cycles in different parts of the belt, and with iron-oxide signatures reflecting the influence of both granitic and mafic lithologies (Dmitrijeva et al., 2018; Keyser et al., 2018).

5.6 Conclusions

1. Three episodes of mafic magmatism spanning the Neoarchean to Neoproterozoic are documented from the Eyre Peninsula in this study: ~2550 Ma, ~1710 Ma, and ~780 Ma; only the oldest and youngest are recorded from rocks along the MR. The age of the Cook Gap Schist horizon is confirmed at 2585 ± 22 Ma with zircon derived from multiple basement sources. Magnesiohornblende-bearing dolerite dikes represent the ~780 Ma Gairdner LIP event in MR. These display petrographic and geochemical differences to analogous Neoproterozoic dikes from other domains in South Australia.

2. Amphibolite petrography (Mg-Fe- and Ca-amphiboles) and geochemistry in the southern part of the belt shows a complex BIF depositional environment, with possible detrital input of titaniferous magnetite from igneous mafic lithologies. Post-peak metamorphism at 435-505 ˚C is recorded by ilmenite + magnetite pairs. A post-metamorphic alteration event is recognized

in the amphibolites indicative of high-T, hydrothermal brine circulation along amphibolite/BIF contacts.

3. U–Pb hematite dating from Iron Knight South gives an age of ~680 Ma. Together with post-emplacement alteration of Gairdner dikes in the central part of the belt, this age supports a model of ore upgrading involving a second burial cycle.

5.7 Acknowledgements

This work is a contribution to the project 'Trace elements in iron-oxides: deportment, distribution and application in ore genesis, geochronology, exploration and mineral processing', supported by BHP Olympic Dam and the South Australian Government Mining and Petroleum Services Centre of Excellence. Logistical support from site geologists at SIMEC Mining is greatly appreciated.

5.8 References

Andersen, D.J., Lindsley, D.H., 1985. New (and final!) models for the Ti-magnetite/ilmenite geothermometer and oxygen barometer. Abstract AGU 1985 Spring Meeting. Eos 66 (18), p. 416.

Arrium Mining, 2016. Ore Reserve and Resources Statement, 30th June 2016. Arrium Mining Ltd.

Barley, M.E., Pickard, A.L., Sylvester, P.J., 1997. Emplacement of a large igneous province as a possible cause of banded iron formation 2.45 billion years ago. Nature 385, 55-58.

Bekker, A., Slack, J.F., Planavsky, N., Krapež, B., Hofmann, A., Konhauser, K.O., Rouxel, O.J., 2010. Iron formation: The sedimentary product of a complex interplay among mantle, tectonic, oceanic, and biospheric processes. Economic Geology 105, 467-508.

Black, L.P., Kamoc, S.L., Allen, C.M., Davis, D.W., Aleinikoff, J.J., Valley, J.W., Mundilf, R., Campbell, I.H., Korsch, R.J., Williams, I.S., Foudoulis, C., 2004. Improved $^{206}Pb/^{238}U$ microprobe geochronology by monitoring of a trace-element-related matrix effect; SHRIMP, ID-TIMS, ELA-ICP-MS and oxygen isotope documentation for a series of zircon standards. Chemical Geology 205, 115-140.

Buddington, A.F., Lindsley, D.H., 1964. Iron-titanium oxide minerals and synthetic equivalents. Journal of Petrology 5, 310-357.

Chung, D., Zhou, M.-F., Gao, J.-F., Chen, W.T., 2015. In-situ LA-ICP-MS trace element analyses of magnetite: The late Palaeoproterozoic Sokoman Iron Formation in the Labrador Trough, Canada. Ore Geology Reviews 65, 917-928.

Ciobanu, C.L., Wade, B.P., Cook, N.J., Schmidt Mumm, A., Giles, D., 2013. Uranium-bearing hematite from the Olympic Dam Cu–U–Au deposit, South Australia: a geochemical tracer and reconnaissance Pb–Pb geochronometer. Precambrian Research 238, 129-147.

Claoué-Long, J.C., Compston, W., Roberts, J., Fanning, C.M., 1995. Two carboniferous ages: A comparison of SHRIMP zircon dating with conventional zircon ages and $^{40}Ar/^{39}Ar$ analysis. In: Berggren, W.A., Kent, D.V., Aubrey, M.P., Hardenbol, J. (Eds.), Geochronology time scales and global stratigraphic correlation. Society of Sedimentary Geology Special Publication 54, Tulsa, Oklahoma, SEPM, pp. 3-21.

Compston, W., Williams, I.S., Meyer, C., 1984. U-Pb geochronology of zircon from lunar breccia 73217 using a sensitive high mass-resolution ion microprobe. Journal of Geophysical Research 89, 525-534.

Courtney-Davies, L., Tapster, S.R., Ciobanu, C.L., Cook, N.J., Verdugo-Ihl, M.R., Ehrig, K.J., Kennedy, A.K., Gilbert, S.E., Condon, D.J., Wade, B.P., 2019. A multi-technique evaluation of hydrothermal hematite U-Pb isotope systematics: Implications for ore deposit geochronology. Chemical Geology 513, 54–72.

Cowley, W.M., McAvaney, S.O., Wade, C.E., 2017. Abandonment of Lincoln Complex nomenclature, Gawler Craton, South Australia. MESA Journal 82, 4-14.

Creaser, R.A., Fanning, C.M., 1993. A U-Pb zircon study of the Mesoproterozoic Charleston Granite, Gawler Craton South Australia. Australia Journal of Earth Sciences 40, 519-526.

Dalstra, H.J., Rosière, C.A., 2008. Structural controls on high-grade iron ores hosted by banded iron formation: a global perspective. Reviews in Economic Geology 15, 73-106.

Davies, M.B., 2000. Iron ore in Southern Australia. Primary Industries and Resources SA. Commodity Review No.8, p. 35.

DMITRE Resources and Energy Group (Government of South Australia), 2014. South Australian Resources Information Geoserver. https://sarig.pir.sa.gov.au/Map.

Dmitrijeva, M., Metcalfe, A.V., Ciobanu, C.L., Cook, N.J., Frenzel, M., Keyser, W.M., Johnson, G., Ehrig, K., 2018. Discrimination and variance structure of trace element signatures in hematite: a case study of BIF-mineralization from the Middleback Ranges, South Australia. Mathematical Geosciences 50, 381-415.

Fanning, C.M., Reid, A.J., Teale, G.S., 2007. A geochronological framework for the Gawler Craton, South Australia. Geological Survey of South Australia Bulletin, 55.

Fraser, G.L, Neumann, N.L, 2010. New SHRIMP U-Pb zircon ages from the Gawler Craton and Curnomona Province, South Australia, 2008-2010. Geoscience Australia 2010/16.

Fraser, G., McAvaney, S., Neumann, N., Szpunar, M., Reid, A., 2010. Discovery of early Mesoarchean crust in the eastern Gawler Craton, South Australia. Precambrian Research 179, 1-21.

Huang, Q., Kamenetsky, V.S., McPhie, J., Ehrig, K., Meffre, S., Maas, R., Thompson, J., Kamenetsky, M., Chambefort, I., Apukhtina, O., Hu, Y., 2015. Neoproterozoic (ca. 820-830 Ma) mafic dykes at Olympic Dam, South Australia: Links with the Gairdner Large Igneous Province. Precambrian Research 271, 160-172.

Isley, A.E., Abbott, D.H., 1999. Plume-related mafic volcanism and the deposition of banded iron formation. Journal of Geophysical Research 104, 15,461-15, 477.

Jagodzinski, E.A., Reid, A., Farrell, F., 2011. Geochronology of the Bungalow Prospect. In: Reid, A.J., Jagodzinski, E.A., (Eds.), PACE Geochronology: Results of collaborative geochronology projects 2009-10. South Australia Department of Primary Industries and Resources, Report Book 2011/00003, pp. 42-62.

Keyser, W.M., Ciobanu, C.L., Cook, N.J., Johnson, G., Feltus, F., Johnson, S., Dmitrijeva, M., Ehrig, K., Nguyen, P., 2018. Petrography and trace element signatures of iron-oxides in deposits from the Middleback Ranges, South Australia: from banded iron formation to ore. Ore Geology Reviews 93, 337-360.

Keyser, W.M., Ciobanu, C.L., Cook, N.J., Johnson, G., Dmitrijeva, M., Courtney-Davies, L., Feltus, F., Gilbert, S., Johnson, G., Ehrig, K., 2019a. Iron-oxides constrain BIF evolution in terranes with protracted geological histories: the Iron Count prospect, Middleback Ranges, South Australia. Lithos 324-325, 20-38.

Keyser, W., Ciobanu, C.L., Cook, N.J., Courtney-Davies, L., Kennedy, A., Wade, B.P., Ehrig, K., Dmitrijeva, M., Kontonikas-Charos, A., Feltus, H., Johnson, G., 2019b. Petrographic and geochronological constraints on the granitic basement to the Middleback Ranges, South Australia. Precambrian Research 324, 170-193.

Keyser, W., Ciobanu, C.L., Cook, N.J., Feltus, H., Johnson, G., Slattery, A., Wade, B.P., Ehrig, K., 2019c. Mineralogy of zirconium in iron-oxides: A micron- to nanoscale study of hematite ore from Peculiar Knob. Minerals 9, 244. https://doi.org/10.3390/min9040244.

Klein, C., 1973. Changes in mineral assemblages with metamorphism of some banded Precambrian iron-formations. Economic Geology 68, 1075-1088.

Klein, C., 2005. Some Precambrian banded iron-formations (BIFs) from around the world: Their age, geological setting, mineralogy, metamorphism, geochemistry, and origin. American Mineralogist 90, 1473-1499.

Lane, K., Jagodzinski, E.A., Dutch, R., Reid, A.J., Hand, M., 2015. Age constraints on the timing of iron mineralisation in the southeastern Gawler Craton. Australian Journal of Earth Sciences 62, 55-75.

Leake, B.E., Woolley, A.R., Arps, C.E.S., Birch, W.D., Gilbert, M.C., Grice, J.D., Hawthorne, F.C., Kato, A., Kisch, H.J., Krivovichev, V.G., Linthout, K., Laird, J., Mandarino, J.A., Maresch, W.V., Nickel, E.H., Schumacher, J.C., Smith, D.C., Stephenson, N.C.N., Ungaretti, L., Whittaker, E.J.W., Youzhi, G., 1997. Nomenclature of amphiboles: report of the subcommittee on amphiboles of the international mineralogical association, commission on new minerals and mineral names. The Canadian Mineralogist 35, 219-246.

LeBas, M.J., Le Maitre, R.W., Streckeisen, A., Zanettin, B., 1986. A chemical classification of volcanic rocks based on the total alkali-silica diagram. Journal of Petrology 27, 745-750.

Leevers, P., Gaughan, C., Bubner, G., 2005. The Iron Magnet deposit. Australasian Institute of Mining and Metallurgy Publication Series, Iron Ore Conference, Fremantle, WA, 19-21 September 2005.

Lepage, L.D., 2003. ILMAT: an Excel worksheet for ilmenite-magnetite goethermometry and geobarometry. Computers and Geosciences 29, 673-678.

McAvaney, S.O., Wade, C.E., Jagodzinski, E.A., 2016. Tip Top and Wertigo Granites, c. 1775 Ma magmatism on northeastern Eyre Peninsula. MESA Journal 80, 63-76.

McDonough, W.F., Sun, S.-s., 1995. The composition of the Earth. Chemical Geology 120, 223-253.

Müller, S.G., Krapež, B., Barley, M.E., Fletcher, I.R., 2005. Giant iron-ore deposits of the Hamersley province related to the breakup of Paleoproterozoic Australia: New insights from in situ SHRIMP dating of baddeleyite from mafic intrusions. Geology 33, 577-580.

Nasdala, L., Hofmeister, W., Norberg, N., Mattinson, J.M., Corfu, F., Dörr, W., Kamo, S.L., Kennedy, A.K., Kronz, A., Reiners, P.W., Frei, D., Kosler, J., Wan, Y., Götze, J., Häger, T., Kröner, A., Valley J.W., 2008. Zircon M257 - a homogeneous natural reference material for the ion microprobe U–Pb analysis of zircon. Geostandards and Geoanalytical Research 32, 247–265.

Parker, A.J., Daly, S.J., Flint, D.J., Flint, R.B., Preiss, W.V., Teale, G.S., 1993. Palaeoproterozoic. *In*: Drexel J.F., Preiss, W.V., Parker, A.J. (eds), The Geology of South Australia; Volume 1, The Precambrian, Geological Survey of South Australia Bulletin 54, pp. 50-105.

Parker, J.K., Buchan, K.L., Harlan, S.S., 1995. A proposed giant radiating dyke swarm fragmented by the separation of Laurentia and Australia based on paleomagnetism of c. 780 Ma mafic intrusions in western North America. Earth and Planetary Science Letters 132, 129-139.

Pearce, J.A., Cann, J.R., 1973. Tectonic setting of basic volcanic rocks determined using trace element analyses. Earth and Planetary Science Letters 19, 290-300.

Pirajno, F., Hoaston, D.M., 2012. A review of Australia's Large Igneous Provinces and associated mineral systems: Implications for mantle dynamics through geological time. Ore Geology Reviews 48, 2-54.

Reid, A., Hand, M., Jagodzinski, E., Kelsey, D., Pearson, N., 2008. Paleoproterozoic orogenesis in the southeastern Gawler Craton, South Australia. Australian Journal of Earth Sciences 55, 449-471.

Rudnick, R.L., Gao, S., 2004. Composition of the Continental Crust. In: Holland, H.D. and Turekian, K.K. eds. Treatise on Geochemistry. vol. 3. Elsevier, Amsterdam, pp. 1-64.

Schaefer, B., 1998. Insights into Proterozoic tectonics from the southern Eyre Peninsula, South Australia. Ph.D. Thesis, The University of Adelaide.

Stern, R.A., 2001. A new isotopic and trace-element standard for the ion microprobe: preliminary thermal ionization mass spectrometry (TIMS) U–Pb and electron-microprobe data. Radiogenic Age and Isotope Studies, Report 14, Geological Survey of Canada, Current Research 2001-F, 11 p.

Stern, R.A., Bodorkos, S., Kamo, S.L., Hickman, A.H., Corfu, F., 2009. Measurement of SIMS instrumental mass fractionation of Pb isotopes during zircon dating. Geostandards and Geoanalytical Research 33, 145-168.

Szpunar, M., Fraser, G., 2010. Age of deposition and provenance of Palaeoproterozoic basins on the northeastern Eyre Peninsula. South Australian Department of Primary Industries and Resources, Report Book 2010/08.

Szpunar, M., Hand, M., Barovich, K., Jagodzinski, E., Belousova, E., 2011. Isotopic and geochemical constraints on the Paleoproterozoic Hutchison Group, southern Australia: Implications for Paleoproterozoic continental reconstructions. Precambrian Research 187, 99-126.

Taylor, D., Dalstra, H.J., Harding, A.E., Broadbent, G.C., Barley, M.E., 2001. Genesis of high-grade hematite orebodies of the Hamersley Province, Western Australia. Economic Geology 96, 837-873.

van Achterbergh, E., Ryan, C.G., Jackson, S.E., Griffin, W.L., 2001. Data reduction software for LA-ICP-MS. In: Sylvester, P.J., (Ed.), Laser-ablation-ICPMS in the Earth Sciences: Principles and Applications. Vol. 29. Mineralogical Association of Canada, Short Course Series Ottawa, Ontario, Canada, pp. 239-243.

Ward, L.K., 1949. The genesis of the iron ores of the Middleback ranges, South Australia. Proceedings of the Australian Institute of Mining and Metallurgy Monograph 152-153, 229-239.

Werner, M., Dutch, R., Pawley, M., Krapf, C., 2014. Mafic intrusions in the East Musgraves: new geochemical data set available now. In: Unlocking SA's Technical Wealth-South Australia Resources and Energy Investment Conference, Adelaide.

Werner, M., Dutch, R., Pawley, M., Krapf, C., 2018. Amata Dolerite, Musgrave Province: connections to Neoproterozoic mantle plum magmatism within Rodina. MESA Journal 87, 34-45.

Williams, I.S., 1998. U-Th-Pb geochronology by ion microprobe. In: McKibben, M.A., Shanks, W.C. (Eds.), Applications of microanalytical techniques to understanding mineralizing processes: Reviews in Economic Geology 7, 1-35.

Wingate, M.T.D., Campbell, I.H., Compston, W., Gibson, G.M., 1998. Ion microprobe U–Pb ages for Neoproterozoic basaltic magmatism in south-central Australia and implications for the breakup of Rodinia. Precambrian Research 87, 135-159.

Woodhead, J.D., Hellstrom, J., Paton, C., Hergt, J.M., Greig, A., Maas, R., 2008. A guide to depth profiling and imaging applications of LA-ICP-MS. In: Sylvester, P.J. (Ed.), Laser-ablation-ICPMS in the Earth Sciences: Current Practices and Outstanding Issues. Vol. 40. Mineralogical Association of Canada, Short Course Series Vancouver, British Columbia, Canada, pp. 135-145.

Yeates, G., 1990. Middleback Range iron ore deposits. In: Hughes F.E., (Eds.) Geology of the Mineral Deposits of Australia and Papua New Guinea. Australian Institute of Mining and Metallurgy Monograph 14, pp. 1045-1048.

Zhao, J., McCulloch, M.T., 1993. Sm-Nd mineral isochron ages of Late Proterozoic dyke swarms in Australia: evidence for two distinctive events of mafic magmatism and crustal extension. Chemical Geology 109, 341-354.

Zhao, J., McCulloch, M.T., Korsch, R.J., 1994. Characterisation of a plume-related ~800 Ma magmatic event and its implications for basin formation in central-southern Australia. Earth and Planetary Science Letters 121, 349-367.

CHAPTER 6

LINKS BETWEEN SEDIMENTARY PROTOLITHS AND IOCG-SKARN ALTERATION, ISLAND DAM, SOUTH AUSTRALIA

William Keyser[1], Cristiana L. Ciobanu[1], Nigel J. Cook[1], Liam Courtney-Davies[1],

Kathy Ehrig[2], Sarah Gilbert[3], Jocelyn McPhie[4]

[1]*School of Chemical Engineering, The University of Adelaide, Adelaide, SA 5005, Australia*

[2] *BHP Billiton Olympic Dam, Adelaide, SA, 5000, Australia*

[3] *Adelaide Microscopy, The University of Adelaide, Adelaide, SA 5005, Australia*

[4] *School of Physical Sciences, University of Tasmania, Hobart, TAS 7001, Australia*

Extended conference abstract and poster, Mineral Resources to Discover. Proceedings of the 14th SGA Biennial Meeting, Québec, Canada, August 20-23rd, 2017. ISBN: 978-2-9816898-0-1, Volume 3, 935-938.

Statement of Authorship

Title of Paper	Links between sedimentary protoliths and IOCG-skarn alteration, Island Dam, South Australia
Publication Status	☑ Published ☐ Accepted for Publication ☐ Submitted for Publication ☐ Unpublished and Unsubmitted w ork w ritten in manuscript style
Publication Details	Keyser, W., Ciobanu, C.L., Cook, N.J., Courtney-Davies, L., Ehrig, K., Gilbert, S., McPhie, J., 2017. Links between sedimentary protoliths and IOCG-skarn alteration, Island Dam, South Australia. Proceedings of the 14th SGA Biennial Meeting, Québec, Canada, August 20-23rd, 2017. ISBN: 978-2-9816898-0-1, Volume 3, 935-938.

Principal Author

Name of Principal Author (Candidate)	William Keyser		
Contribution to the Paper	Performed analytical work, carried out data processing and interpretation, oversaw development of work and wrote manuscript.		
Overall percentage (%)	70		
Certification:	This paper reports on original research I conducted during the period of my Higher Degree by Research candidature and is not subject to any obligations or contractual agreements with a third party that would constrain its inclusion in this thesis. I am the primary author of this paper.		
Signature		Date	4/6/2019

Co-Author Contributions

By signing the Statement of Authorship, each author certifies that:

i. the candidate's stated contribution to the publication is accurate (as detailed above);

ii. permission is granted for the candidate in include the publication in the thesis; and

iii. the sum of all co-author contributions is equal to 100% less the candidate's stated contribution.

Name of Co-Author	Cristiana L. Ciobanu		
Contribution to the Paper	Helped define direction of research, supervised development of work, assisted with data interpretation and contributed to manuscript preparation.		
Overall percentage (%)	10		
Signature		Date	4 June 2019

Name of Co-Author	Nigel J. Cook		
Contribution to the Paper	Helped define direction of research, supervised development of work, assisted with data interpretation and contributed to manuscript preparation.		
Overall percentage (%)	8		
Signature		Date	4/6/19

Name of Co-Author	Liam Courtney-Davies		
Contribution to the Paper	Assisted with analytical instrumentation and evaluation of manuscript.		
Overall percentage (%)	5		
Signature		Date	30/4/2019

Name of Co-Author	Kathy Ehrig		
Contribution to the Paper	Assisted with providing samples and evaluation of manuscript.		
Overall percentage (%)	3		
Signature		Date	3/6/2019

Name of Co-Author	Sarah Gilbert		
Contribution to the Paper	Assisted with analytical instrumentation and data processing.		
Overall percentage (%)	3		
Signature		Date	3/6/19

Name of Co-Author	Jocelyn McPhie		
Contribution to the Paper	Assisted with evaluation of manuscript.		
Overall percentage (%)	3		
Signature		Date	4th June 2019

Links between sedimentary protoliths and IOCG-skarn alteration, Island Dam, South Australia

William M. Keyser, Cristiana L. Ciobanu, Nigel J. Cook, Liam Courtney-Davies *University of Adelaide, Australia*

Kathy Ehrig
BHP Billiton Olympic Dam, Australia

Sarah Gilbert
University of Adelaide, Australia

Jocelyn McPhie
School of Physical Sciences, University of Tasmania, Hobart, Australia

Abstract. The Island Dam prospect is located within the Mesoproterozoic Olympic Cu-Au Province, South Australia. Banded iron formation (BIF)-style mineralization is overprinted by amphibole-magnetite alteration we refer to herein as 'skarns'. Iron oxides within BIF and skarn lithologies display textures and geochemical signatures defining the two contrasting mineralization styles. Iron oxide layers in BIF are composed of martite, which features relative enrichment in Ni, Co, Mn, As, Sb, U, Y and REE. Skarn lithologies contain cm-scale laths of hematite that are markedly enriched in W and Sn (thousands of ppm, and compositionally zoned with respect to these elements). Iron oxide-copper-gold (IOCG) mineralization is associated with skarn alteration in some parts of the Olympic Cu-Au Province and is linked to a ~1.6 Ga magmatic-hydrothermal event, which generated the World's largest concentration of iron oxide-copper-gold (IOCG) deposits. Skarn alteration at Island Dam can be attributed to the same event. Iron oxides are ideal tracers of alteration processes in iron oxide-bearing ore systems. At Island Dam, recognition of distinct signatures in iron oxides highlights their capacity to distinguish protolith from alteration products and trace hydrothermal history. Moreover, interpreting the evolution of iron oxide mineralogy may be an important step for understanding the spatial-temporal relationships between BIF and IOCG mineralization.

1 Introduction

The common iron oxides (hematite or magnetite) are the dominant components of both banded iron formations (BIF) and iron oxide-copper-gold (IOCG)-style mineralization. Both types are present in deposits and prospects in the Gawler Craton of South Australia (S.A.). Iron oxides can incorporate a wide variety of different minor/trace elements into their crystal lattices (e.g. Dupuis and Beaudoin 2011). This allows for their use as tracers of ore formation throughout time and space in different types of iron oxide-bearing systems (e.g. Ciobanu et al. 2013, 2015; Dare et al. 2014). Moreover, the presence of U and Pb in hematite (Ciobanu et al. 2013; Courtney-Davies et al. 2016) highlights the applicability of iron oxides as geochronometers to constrain the timing of hydrothermal ore formation. The common spatial association of metasedimentary units hosting BIF-style mineralization with giant IOCG deposits draws attention to possible genetic links between the two styles of mineralization in Precambrian terranes in S.A. and elsewhere, such as Carajas, Brazil. The present study is prompted by such a hypothesis. Iron oxides have been studied from lithologies in the Island Dam prospect, one of several IOCG-type prospects in S.A. hosted within older meta-sedimentary rocks inferred to include BIF horizons. The main question addressed is whether the trace element signatures can distinguish different generations of iron oxides if combined with mineralogical-petrographic studies.

2 Geological background

The Island Dam prospect is located in the eastern Gawler Craton, ~90 km southeast of the World-class Olympic Dam IOCG deposit within the Olympic Cu-Au Province (Fig. 1; see also Ehrig et al. this volume). Mineralization in the Olympic Cu-Au Province is spatially and temporally linked to volcanism and plutonism during generation of a ~1.6 Ga siliceous large igneous province. In contrast to the granite-hosted, hematite-breccia deposit at Olympic Dam, the Cu prospect at Island Dam is hosted within metasedimentary and volcanic rocks of the Wallaroo Group (WG). These were deposited, at 1765-1740 Ma, onto older (~1850 Ma) gneissic granites of the Donington Magmatic Suite (Cowley et al. 2003 and references therein). The WG sequences include impure limestone and dolostone horizons, as well as thin BIF-like layering, which is also observed/inferred, for example, in the northern part of the Olympic Dam district (Fig. 1). These clearly pre-date ~1600-1585 Ma Hiltaba Igneous Suite (HIS) equivalents.

The formation extends from the Mt. Woods Inlier in the northern Gawler Craton to the upper Yorke Peninsula in the south, but paleo-reconstruction and district correlation of WG sequences is hampered not only by younger cover sequences but also by superimposed alteration, including alkali-(calcic) + Fe metasomatism with regional expression in the Moonta area (Conor et al. 2010; Kontonikas-Charos et al. 2014), as well as calcic skarn formation in prospects such as the Groundhog Zn-Cu skarn in the Punt Hill area (Reid et al. 2011), or the Cu-Au skarn at Hillside, Yorke

Peninsula (Conor et al. 2010; Ismail et al. 2014). Thick (~500 m) sequences of interbedded garnet skarn and banded calc-silicate-feldspar rocks are intersected between the Gawler Range Volcanics and Donington Granite in drillholes (e.g. SAR9) west of the Punt Hill area, where meter-scale intervals rich in iron oxides with a BIF-like appearance also occur as horizons within the skarn in SAR9. Mineralization within prospects hosted by the WG are dated at ~1.6 Ma, e.g. Sm-Nd dating of pyroxene-garnet skarn at Groundhog (Reid et al. 2011), or accessory minerals elsewhere (Skirrow et al. 2007).

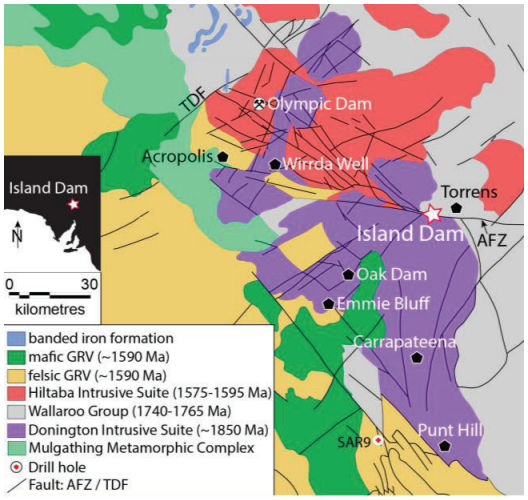

Figure 1. Basement geological map of the middle part of the Olympic Cu-Au Province, S.A., showing the location of the Island Dam Cu prospect, the Olympic Dam deposit and surrounding prospects (diamonds). AFZ-Andamooka Fault Zone; TDF-Todd Dams Fault. Inset location within S.A. (black) Map sourced from https://map.sarig.sa.gov.au/.

3 Approach and methodology

Samples were collected from 10 drillcores within and surrounding magnetically anomalous domains in the Island Dam area. While some cores contain recognizable BIF-like lithologies (e.g. Fig. 2a), others intersect granites underlying the metasedimentary rocks. In most cases the lithologies consist of rock packages that are either strongly altered (chloritized), or display banding with green and pink-reddish colors as for those mentioned above for WG rocks, with skarn alteration (Fig. 2b), and in which magnetite banding can also occur (Fig. 2c). A spectacular specimen displays coarse, cm- to dm-sized lamellar aggregates of specular hematite filling vugs or short veins in association with carbonates (calcite and/or siderite) (Fig. 2d). Development of cavities where mineral growth can reach coarse crystals is always a feature of skarns, either during prograde or retrograde stages. Chalcopyrite and pyrite occur as disseminations and small pockets throughout all lithologies, but are most abundant in the most intensely altered rocks (late carbonates + quartz).

This study focuses on a selection of ~25 samples containing iron oxides from lithologies with BIF and WG-like appearance, as well as several specimens of specular hematite. Polished blocks were analyzed using scanning electron microscopy in back-scatter electron mode (BSE), and laser ablation inductively-coupled plasma mass spectrometry (LA-ICP-MS) for trace elements using BHVO-2G, GSD-1G and NIST610 as reference standards. All instrumentation is housed at Adelaide Microscopy, The University of Adelaide.

4 Results

Distinct generations of iron oxides within the two main lithologies of interest here, BIFs and skarns, are recognized based on textural and compositional variations. Iron oxides within the BIFs are dominantly a martite, readily recognizable from granular shapes, inclusions of magnetite, and often the presence of acicular-shaped mineral relicts that are marked by fine-grained chlorite within the martite mass (Fig. 3a) and could represent original actinolite grains.

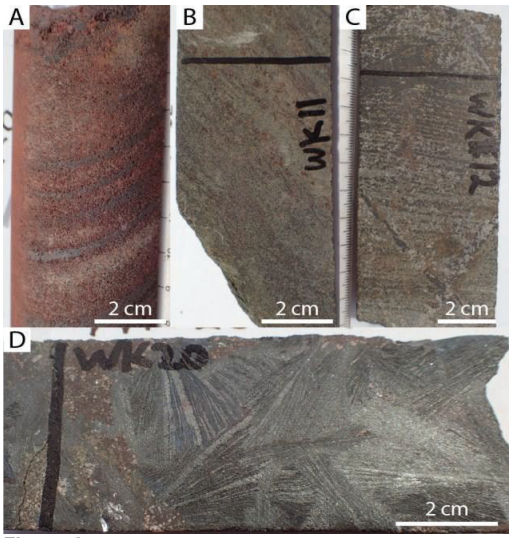

Figure 2. Hand specimen photographs showing characteristic BIF and skarn lithologies discussed in the text. **a** BIF (martite-carbonate-quartz banded rock). **b** Actinolite-magnetite skarn. **c** Rhythmic magnetite banding in altered skarn. **d** Coarse specular hematite in altered skarn.

Quartz, carbonates (mainly siderite) and chlorite are abundant gangue minerals in the BIFs. There is clear evidence for K-Fe alteration as 10-20 µm K-feldspar grains rimmed by film-like hematite within quartz (Fig. 3b).

What we refer here to as skarn is recognized by the presence of actinolite (Fig. 4a), phlogopite, magnetite, apatite, titanite, calcite, fluorite and tourmaline, lending the rocks a green color with patchy alteration domains that may display banding (Fig. 2b, c). Massive or banded actinolite skarn varieties are progressively altered,

particularly by pseudomorphic replacement during the retrograde skarn stage.

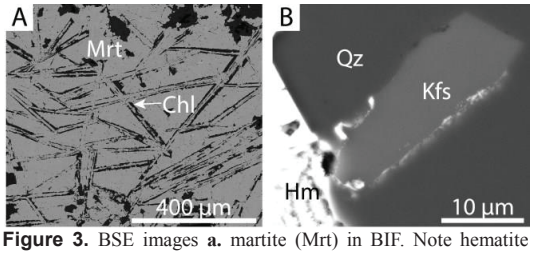

Figure 3. BSE images **a.** martite (Mrt) in BIF. Note hematite replacing a previous lath-shaped mineral with contours marked by chlorite (Chl). **b** K-feldspar (Kfs) with a film of hematite around the margin as inclusions within quartz (Qz).

In contrast to martite from the BIF, euhedral magnetite in the actinolite skarn displays oscillatory zoning with respect to Si and Ca, and may contain inclusions of quartz, calcite and chlorite (Fig. 4b). Thin lamellar aggregates of hematite are also noted. In the actinolite skarn there are numerous pseudomorphs of rutile + calcite after coarse, lozenge-shaped titanite. In detail, the rutile also shows tiny inclusions of scheelite at the boundaries between W-poor cores and W-richer rims.

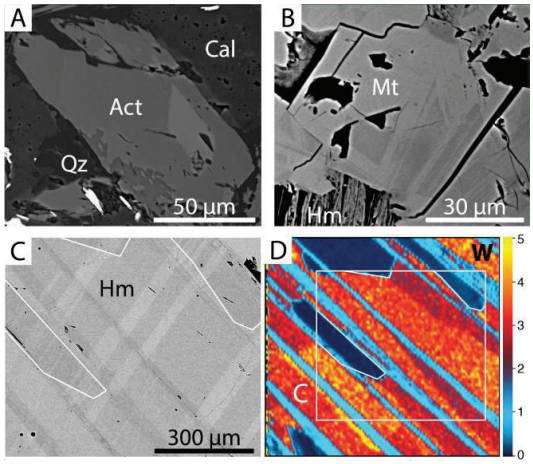

Figure 4. BSE images from amphibole-magnetite (skarn) lithologies showing **a** actinolite (Act) with Fe-rich (bright) domains. **b** Si- and Ca- (dark and bright) zoned magnetite (Mt). **c** and **d** BSE image and LA-ICP-MS element map showing W-zonation in coarse-grained Hm. Scale: parts per million (x10^3).

A close relationship between hematite and sulfides is seen in samples from altered skarn and/or of BIF affiliation. The majority of iron oxides are represented by aggregates comprising martite-magnetite intergrowths with irregular and/or scalloped mutual boundaries.

Sulfides, chalcopyrite, pyrite, and minor bornite occur as patches throughout carbonate + quartz + chlorite assemblages interstitial to the iron oxides, as well as hosted along the aforementioned magnetite margins. A distinct generation of hematite, occurring as small lamellae, occurs within areas of sulphides. This hematite also displays zonation with respect to W. The coarse-grained (as large as 4 cm) specular hematite (Fig. 2d), features polysynthetic twinning as well as strong zonation with respect to W. This is expressed as W-rich and -poor sectors along the lamellae as shown by the LA-ICP-MS map for W (Fig. 4c, d). There are also various overprinting aspects marked by W depletion, either along grain boundaries (as in Fig. 4d) or within brecciation domains in other samples.

The existing trace element dataset for magnetite is small and will not be discussed here; only that for hematite is presented. Martite, representing BIF mineralization, and the coarse lamellar hematite within amphibole-magnetite assemblages show distinct differences (Fig. 5).

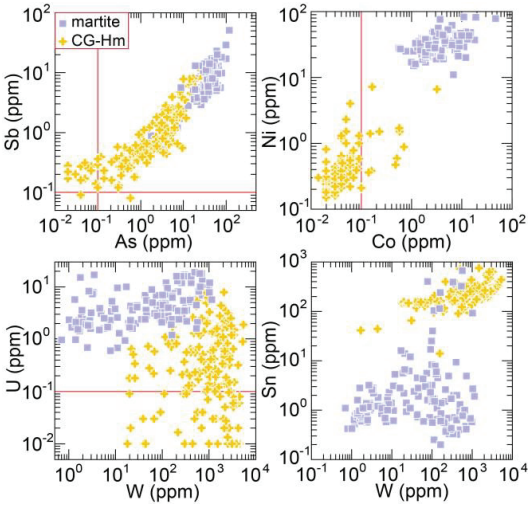

Figure 5. Binary plots of As vs. Sb (top left), Ni vs. Co (top right), U vs. W (lower left) and Sn vs. W (lower right) showing discriminant fields of hematite in Island Dam. CG-Hm - coarse-grained hematite.

Chalcophile elements, As and Sb, (average 39 and 9 ppm, respectively) and transition metals such as Ni, Co and Mn, are higher (tens of ppm) in martite than in coarse-grained hematite. Uranium concentrations in martite average 6 ppm. In contrast, coarse-grained hematite contains higher concentrations of high-field strength elements (HFSE), such as Sc and Nb, than martite. Most interestingly, coarse-grained hematite features a high Sn content (average 240 ppm), and still higher (several thousands of ppm) concentrations of W. In addition to its enrichment in hematite, W is also present in zoned rutile and as inclusions of scheelite, and sometimes in hematite. Martite contains higher ΣREE and Y (ΣREY) than coarse-grained hematite (means 2.6 and 0.38 ppm, respectively). Chondrite-normalized REY fractionation patterns for distinct hematite textures (Fig. 6) also differ. Martite is enriched in LREE relative to HREE whereas coarse-

grained hematite displays a relatively flat trend.

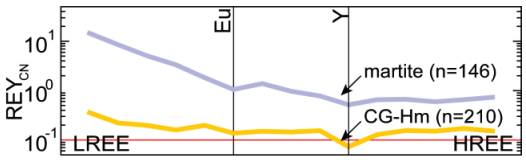

Figure 6. Chondrite-normalized REY fractionation trends of the two textural types of hematite as marked.

5 Discussion and implications

The distinct textural and compositional character of iron oxide populations suggests at least two generations of Fe-mineralization in the Island Dam area. The relative enrichment in transitional metals, chalcophile elements, U and ΣREY in the BIF lithologies, characterized by a martite texture, is most likely attributable to superimposed fluid-rock interaction from sedimentary deposition to supergene enrichment followed by interaction with hydrothermal fluids (IOCG event at ~1.6 Ga), a scenario comparable to that suggested by Ciobanu et al. (2015) for the deposit margins at Olympic Dam. In contrast, the younger skarn lithologies represented by the coarse-grained hematite are rich in HFSE and granitophile group elements and can be directly related to hydrothermal fluids affiliated with Hiltaba magmatism. The W-Sn-rich signatures are attributable to the major 1.6 Ga IOCG event since such signatures are recognized in most deposits and prospects across the region, either in iron oxides (Olympic Dam, Prominent Hill), or in garnet skarns when suitable protoliths are present (Hillside and Punt Hill,).

In contrast with other, potentially analogous terranes, such as the Great Bear Region, where alteration sequences can be directly mapped over large distances (Corriveau et al. 2016), at Island Dam, and in general in the Olympic Cu-Au province, this is not the case. Because of the cover, geological interpretation is almost entirely dependent on available drillcores. Moreover, the present work at Island Dam is carried on drillholes adjacent to the Andamooka fault system, likely with a multiple reactivation history.

Attempts to date the two hematite types from Island Dam via LA-ICP-MS using GJ-1 zircon as primary standard gave an indication of two age groups: (i) older than 1.6 (WG for BIFs); and (ii) ~1.6 Ga or younger (~1.2 Ga) for coarse-grained hematite. These data show, however, large errors either due to the high common Pb, or the low-U concentration. Future work targets alternative dating methods such as (U-Th)/He dating of hematite combined with dating of U-bearing accessory minerals (monazite, apatite, titanite and/or rutile). The pre-existing BIF mineralization is interpreted as a post-WG deposition (1765-1740 Ma), with martitization occurring during later oxidation. Martite signatures presented here are inferred to represent pre-skarn mineralization, as they lack HFSE and W + Sn element signatures of the coarse-grained, skarn-type hematite. This suggests that iron oxides retained primary signatures despite overprinting. The capacity to retain primary signatures shows the potential for iron oxides to not only distinguish protolith from alteration products, but also trace hydrothermal processes. If BIFs are found as protoliths in terranes where IOCGs also occur, then geochemical signatures should still be recognizable when, the textures, of the sedimentary protoliths are retained.

Acknowledgements

This is a contribution to the 'FOX' project, supported by BHP Billiton Olympic Dam and the South Australian Mining and Petroleum Services Centre of Excellence. Sasha Krneta kindly assisted with preparation of Figure 1. Two reviewers are thanked for their helpful suggestions.

References

Ciobanu CL, Wade B, Cook NJ, Schmidt Mumm A, Giles D (2013) Uranium-bearing hematite from the Olympic Dam Cu-U-Au deposit, South Australia; a geochemical tracer and reconnaissance Pb-Pb geochronometer. Precambrian Res 238:129–147

Ciobanu CL, Cook NJ, Ehrig K, Wade BP, Kamenetsky, VS (2015) Trace element signatures in iron oxides from the Olympic IOCG deposit, South Australia. Mineral Resources in a Sustainable World, 13th SGA Biennial Meeting 2015, Nancy, pp 1071–1074

Conor C, Raymond OL, Baker T, Teale G, Say P, Lowe G (2010) Alteration and mineralisation in the Moonta-Wallaroo Copper-Gold Mining Field Region, Olympic Domain, South Australia. In: Porter TM (ed.), Hydrothermal Iron Oxide Copper-Gold & Related Deposits, vol. 3-4. PGC Publishing, Adelaide, pp 1–24

Corriveau L, Montreuil J-F, Potter EG (2016) Alteration facies linkages among iron oxide copper-gold, iron oxide-apatite, and affiliated deposits in the Great Bear magmatic zone, Northwest Territories, Canada. Econ Geol 111, 2045–2072

Courtney-Davies L, Zhu Z, Ciobanu CL, Wade BP, Cook NJ, Ehrig K, Cabral AR, Kennedy A (2016) Matrix-matched iron-oxide laser ablation ICP-MS U-Pb geochronology using mixed solution standards. Minerals 6(3), 85; doi:10.3390/min6030085

Cowley W, Conor C, Zang W (2003) New and revised Proterozoic stratigraphic units on northern Yorke Peninsula. MESA J. 29:46-58

Dare S, Barnes S, Beaudoin G (2014) Trace elements in magnetite as petrogenetic indicators. Ore Geol Rev 49:785–796

Dupuis C, Beaudoin G (2011) Discriminant diagrams for iron oxide trace element fingerprinting of mineral deposit types. Miner Deposita 46:319–335

Ehrig K, Kamenetsky VS, McPhie J,Apukhtina A, Ciobanu CL, Cook NJ, Kontonikas-Charos A, Krneta S (2017) this volume. The IOCG-IOA ore system at Olympic Dam and nearby prospects, South Australia, South Australia. This volume

Ismail R, Ciobanu CL, Cook NJ, Teale GS, Giles D, Mumm AS, Wade B (2014) Rare earths and other trace elements in minerals from skarn assemblages, Hillside iron oxide-copper-gold deposit, Yorke Peninsula, South Australia. Lithos 184-187:456–477

Kontonikas-Charos A, Ciobanu CL, Cook NJ (2014) Albitization and redistribution of REE and Y in IOCG systems: Insights from Moonta-Wallaroo, Yorke Peninsula, South Australia. Lithos 208–209:178–201

Reid AJ, Swain G, Mason D, Maas R (2011) Nature and timing of Cu-Au-Zn-Pb mineralisation at Punt Hill, eastern Gawler Craton. MESA Journal 60:7–17

Skirrow RG, Bastrakov E, Evgeniy N, Barovich K, Fraser GL, Creaser RA, Fanning CM, Raymond OL, Davidson GJ (2007) Timing of iron oxide Cu-Au-(U) hydrothermal activity and Nd isotope constraints on metal sources in the Gawler craton, South Australia. Econ Geol 102:1441–1470

CHAPTER 7

MINERALOGY OF ZIRCONIUM IN IRON-OXIDES: A MICRON- TO NANOSCALE STUDY OF HEMATITE ORE FROM PECULIAR KNOB, SOUTH AUSTRALIA

William Keyser[1], Cristiana L. Ciobanu[1], Nigel J. Cook[1], Holly Feltus[2], Geoff Johnson[2], Ashley Slattery[3], Benjamin P. Wade[3], Kathy Ehrig[4]

[1]*School of Chemical Engineering, The University of Adelaide, Adelaide, SA 5005, Australia*

[2] *SIMEC Mining, Level 2 169 Fullarton Road, Dulwich, SA 5005, Australia*

[3] *Adelaide Microscopy, The University of Adelaide, Adelaide, SA 5005, Australia*

[4] *BHP Billiton Olympic Dam, Adelaide, SA, 5000, Australia*

Article published in Minerals 9 (2019), 1-26.

Statement of Authorship

Title of Paper	Mineralogy of zirconium in iron-oxides: A micron- to nanoscale study of hematite ore from Peculiar Knob, South Australia
Publication Status	☑ Published ☐ Accepted for Publication ☐ Submitted for Publication ☐ Unpublished and Unsubmitted work written in manuscript style
Publication Details	Keyser, W., Ciobanu, C.L., Cook, N.J., Feltus, H., Johnson, G., Slattery, A., Wade, B.P., Ehrig, K., 2019. Mineralogy of zirconium in iron-oxides: A micron- to nanoscale study of hematite ore from Peculiar Knob, South Australia. Minerals 9, 224.

Principal Author

Name of Principal Author (Candidate)	William Keyser		
Contribution to the Paper	Performed analytical work, carried out data processing and interpretation, oversaw development of work and wrote manuscript.		
Overall percentage (%)	60		
Certification:	This paper reports on original research I conducted during the period of my Higher Degree by Research candidature and is not subject to any obligations or contractual agreements with a third party that would constrain its inclusion in this thesis. I am the primary author of this paper.		
Signature		Date	4/6/2019

Co-Author Contributions

By signing the Statement of Authorship, each author certifies that:

i. the candidate's stated contribution to the publication is accurate (as detailed above);

ii. permission is granted for the candidate in include the publication in the thesis; and

iii. the sum of all co-author contributions is equal to 100% less the candidate's stated contribution.

Name of Co-Author	Cristiana L. Ciobanu		
Contribution to the Paper	Helped define direction of research, supervised development of work, assisted with data interpretation and contributed to manuscript preparation.		
Overall percentage (%)	15		
Signature		Date	4 June 2019

Name of Co-Author	Nigel J. Cook		
Contribution to the Paper	Helped define direction of research, supervised development of work, assisted with data interpretation and contributed to manuscript preparation.		
Overall percentage (%)	10		
Signature		Date	4/6/19

Name of Co-Author	Holly Feltus		
Contribution to the Paper	Assisted with sample collection and evaluation of manuscript.		
Overall percentage (%)	3		
Signature		Date	30/4/2019

Name of Co-Author	Geoff Johnson		
Contribution to the Paper	Assisted with sample collection and evaluation of manuscript.		
Overall percentage (%)	3		
Signature		Date	30/5/2019

Name of Co-Author	Ashley Slattery		
Contribution to the Paper	Assisted with analytical instrumentation and data processing.		
Overall percentage (%)	3		
Signature		Date	3/06/2019

Name of Co-Author	Benjamin P. Wade		
Contribution to the Paper	Assisted with analytical instrumentation, data processing, and manuscript evaluation.		
Overall percentage (%)	2		
Signature		Date	28/5/2019

Name of Co-Author	Kathy Ehrig		
Contribution to the Paper	Helped define research direction and assisted with evaluation of manuscript.		
Overall percentage (%)	2		
Signature		Date	3/6/2019

minerals

MDPI

Article

Mineralogy of Zirconium in Iron-Oxides: A Micron- to Nanoscale Study of Hematite Ore from Peculiar Knob, South Australia

William Keyser [1,*], Cristiana L. Ciobanu [1], Nigel J. Cook [1], Holly Feltus [2], Geoff Johnson [2], Ashley Slattery [3], Benjamin P. Wade [3] and Kathy Ehrig [4]

1 School of Chemical Engineering, The University of Adelaide, Adelaide, SA 5005, Australia; cristiana.ciobanu@adelaide.edu.au (C.L.C.); nigel.cook@adelaide.edu.au (N.J.C.)
2 Formerly Arrium Mining, now SIMEC Mining, Level 2, 169 Fullarton Road, Dulwich, SA 5065, Australia; holly.feltus@simecmining.com (H.F.); geoff.johnson@simecmining.com (G.J.)
3 Adelaide Microscopy, The University of Adelaide, Adelaide, SA 5005, Australia; ashley.slattery@adelaide.edu.au (A.S.); benjamin.wade@adelaide.edu.au (B.P.W.)
4 BHP Olympic Dam, Adelaide, SA 5000, Australia; Kathy.J.Ehrig@bhpbilliton.com
* Correspondence: william.keyser@adelaide.edu.au; Tel.: +61-8-8313-3093

Received: 1 April 2019; Accepted: 17 April 2019; Published: 19 April 2019

Abstract: Zirconium is an element of considerable petrogenetic significance but is rarely found in hematite at concentrations higher than a few parts-per-million (ppm). Coarse-grained hematite ore from the metamorphosed Peculiar Knob iron deposit, South Australia, contains anomalous concentrations of Zr and has been investigated using microanalytical techniques that can bridge the micron- to nanoscales to understand the distribution of Zr in the ore. Hematite displays textures attributable to annealing under conditions of high-grade metamorphism, deformation twins (r~85° to hematite elongation), relict magnetite and fields of sub-micron-wide inclusions of baddeleyite as conjugate needles with orientation at ~110°/70°. Skeletal and granoblastic zircon, containing only a few ppm U, are both present interstitial to hematite. Using laser-ablation inductively coupled plasma mass spectrometry (LA-ICP-MS) spot analysis and mapping, the concentration of Zr in hematite is determined to be ~260 ppm on average (up to 680 ppm). The Zr content is, however, directly attributable to nm-scale inclusions of baddeleyite pervasively distributed throughout the hematite rather than Zr in solid solution. Distinction between nm-scale inclusions and lattice-bound trace element substitutions cannot be made from LA-ICP-MS data alone and requires nanoscale characterization. Scandium-rich (up to 0.18 wt. % Sc_2O_3) cores in zircon are documented by microprobe analysis and mapping. Using high-angle annular dark field scanning transmission electron microscopy imaging (HAADF-STEM) and energy-dispersive spectrometry STEM mapping of foils prepared in-situ by focused ion beam methods, we identify $[0\bar{1}1]_{baddeleyite}$ epitaxially intergrown with $[2\bar{2}.1]_{hematite}$. Lattice vectors at 84–86° underpinning the epitaxial intergrowth orientation correspond to directions of r-twins but not to the orientation of the needles, which display a ~15° misfit. This is attributable to directions of trellis exsolutions in a precursor titanomagnetite. U–Pb dating of zircon gives a $^{206}Pb/^{238}U$ weighted mean age of 1741 ± 49 Ma (sensitive high-resolution ion microprobe U–Pb method). Based on the findings presented here, detrital titanomagnetite from erosion of mafic rocks is considered the most likely source for Zr, Ti, Cr and Sc. Whether such detrital horizons accumulated in a basin with chemical precipitation of Fe-minerals (banded iron formation) is debatable, but such Fe-rich sediments clearly included detrital horizons. Martitization during the diagenesis-supergene enrichment cycle was followed by high-grade metamorphism during the ~1.73–1.69 Ga Kimban Orogeny during which martite recrystallized as granoblastic hematite. Later interaction with hydrothermal fluids associated with ~1.6 Ga Hiltaba-granitoids led to W, Sn and Sb enrichment in the hematite. By reconstructing the evolution of the massive orebody at Peculiar

Knob, we show how application of complimentary advanced microanalytical techniques, in-situ and on the same material but at different scales, provides critical constraints on ore-forming processes.

Keywords: hematite; Zr; baddeleyite; zircon; trace elements; HAADF-STEM; Peculiar Knob

1. Introduction

Despite zirconium (Zr) being an element of major petrogenetic interest, there is remarkably little published data on the concentration of Zr in the common iron-oxides, magnetite (Fe_3O_4) and hematite (α-Fe_2O_3). Dawson et al. [1] report a maximum of 0.21 wt. % ZrO_2 in magnetite from African carbonatites, and Reguir et al. [2] present LA-ICP-MS data for magnetite in calciocarbonatite from the Kerimasi volcano, Tanzania, showing that magnetite is a minor host for Zr (490 ppm). Data for Zr incorporation in hematite is particularly scarce. Selmi et al. [3] note up to 25 ppm Zr in hematitite from Quadrilátero Ferrífero iron formations in Brazil, while Cabral and Rosière [4] show values of <10 ppm in specular hematite from Tilkerode, Germany. Comparably low concentrations of Zr are found in iron-oxides from deposits from South Australia. These include, <10 ppm Zr within U-W-Sn-Mo-oscillatory-zoned hematite from the iron-oxide copper gold (IOCG) deposit at Olympic Dam [5] and <10 ppm (but up to ~18 ppm within individual samples) in hematite from banded iron formation (BIF)-derived ores in the Middleback Ranges, Eyre Peninsula [6]. In Fe–Ti deposits hosted by layered intrusions, e.g., Panzhihua, China [7], ilmenite exsolved from titanomagnetite will preferentially concentrate Zr (80–260 ppm) relative to host titanomagnetite (a few ppm at most). Phase diagrams of the systems ZrO_2–FeO and FeO–Fe_2O_3–ZrO_2–SiO_2 show solubility of Zr in iron-oxides at high temperatures [8,9] but have limited relevance to establishing solubility limits under crustal conditions (e.g., 10.3 mol. % ZrO_2 in FeO at 1332 °C).

The Peculiar Knob iron deposit [10] is located ~85 km SE of Coober Pedy within the Mount Woods Inlier of the Gawler Craton, South Australia (Figure 1). The deposit hosts an indicated and inferred resource of 20.9 Mt at an average of 62.95% Fe [11]. The deposit is a metamorphosed iron formation recognized by a prominent aeromagnetic anomaly. The high-grade hematite shows magnetic properties that have been interpreted, based on thermoremanent magnetization (TMR) properties and high Koenigsberger ratios [12], to indicate cooling from temperatures in excess of 680 °C. Peculiar Knob is also of interest as it occurs in a Paleoproterozoic terrane with a complex and much-debated geological history.

In the present contribution, anomalous concentrations of Zr and other trace elements have been measured in a sample containing coarse hematite representing massive iron ores similar to those investigated by Schmidt et al. [12]. We have undertaken a detailed multi-technique microanalytical study at the micron- to nanoscale following an approach analogous to that in Ciobanu et al. [13]. We address the petrography and geochemistry of hematite and the mineralogy of Zr in the ore with the objective of constraining deposit genesis. Understanding the incorporation of Zr in, and release from, iron-oxides in a complex ancient terrane represents a potential tool with broad petrogenetic application.

2. Geological Background

The several iron orebodies comprising the Peculiar Knob deposit are hosted within a poly-metamorphosed and -deformed supracrustal basement complex of Paleoproterozoic age. Basement consists of the Skylark Metasediments, various intrusive rock types, and the overlying Coodnambanna Metaconglomerate. Sequences comprising the Skylark Metasediments include quartz-magnetite-feldspar-clinopyroxene-orthopyroxene-apatite units, assigned to BIF [14,15]. The precise stratigraphy of the complex is, however, poorly constrained due to sparse outcrop at surface. Although the Skylark Metasediments are often correlated with Archean, marine-derived sediments (BIFs) of the Middleback Ranges, ~300 km south in the eastern Eyre Peninsula [16–18],

the current maximum deposition ages for these rocks (~1750 Ma [19]) suggests they are more likely equivalents to the Wallaroo Group metasediments of the Yorke Peninsula. Intrusive rocks recognized within the basement complex include the foliated 1691 ± 25 Ma Engenina Adamellite and the weakly- to non-foliated 1584 ± 18 Ma Balta Granite, affiliated with the ~1.6 Ga Hiltaba Suite [20].

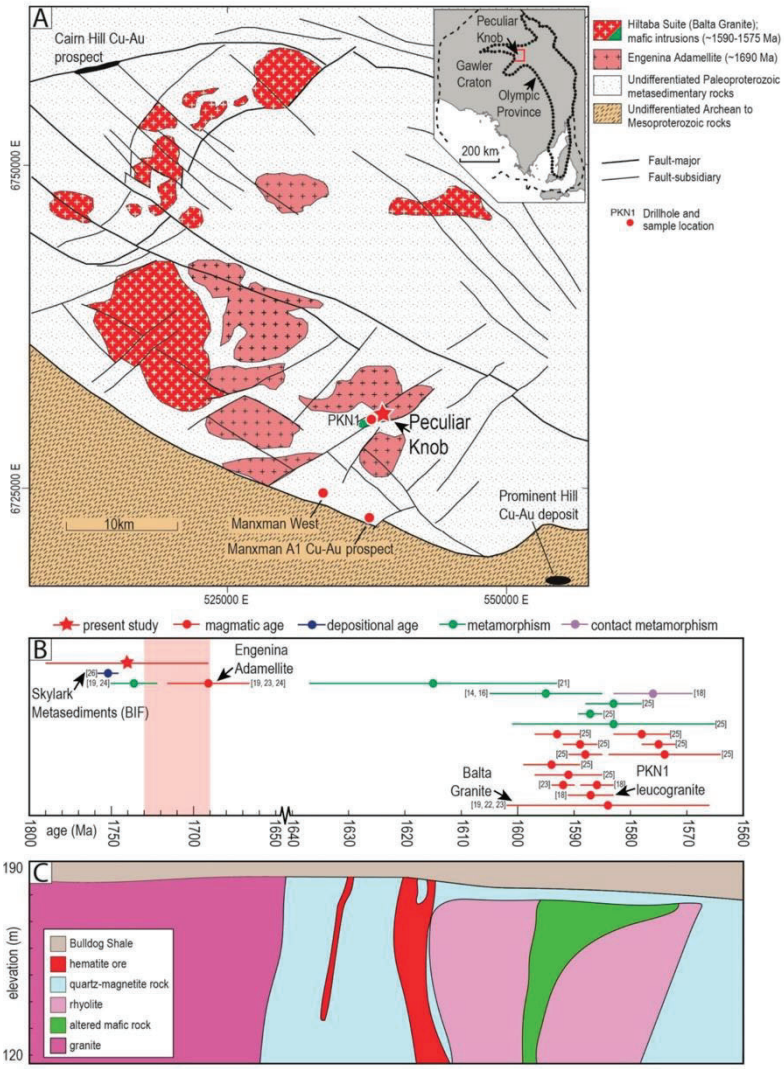

Figure 1. (**A**) Simplified geological map of the Mount Woods Inlier showing location of Peculiar Knob (PK) and other Cu–Au deposits/prospects (modified after [21]). (**B**) Summary of published metamorphic and igneous ages for the Mount Woods Inlier, modified after [22] and data sourced from Ambrose and Flint [23], Fanning et al. [24], Fanning [20], Finlay [25], Holm [26], Jagodzinski [19], Jagodzinski et al. [27], Chalmers [15] and Forbes et al. [22]. (**C**) Schematic cross-section through one of the PK orebodies showing host lithologies (data from Nielson [11]).

The metamorphic history of the Mount Woods Inlier has been extensively debated but is nevertheless important in the context of understanding and constraining sequences of mineralization at Peculiar Knob (Figure 1B). The metamorphic grade within the Mount Woods Inlier is suggested to increase from greenschist facies in the south to granulite facies in the north [28]. Granulite facies metamorphism occurred coincident with early stages of the ~1.73–1.69 Ga Kimban Orogeny ([29] and references therein), based on a 1736 ± 14 Ma SHRIMP (sensitive high-resolution ion microprobe) U–Pb age of interpreted metamorphic zircon [20].

Metamorphic ages of ~1.59 Ga are reported from throughout the Mount Woods Inlier [19,26,27]. Recent monazite CHIME (chemical Th–U-total Pb isochron method) dating, combined with P-T pseudosection modeling of a sample of Skylark Metasediments, provided evidence for a granulite facies metamorphic event that peaked at ~1595 Ma [22]. This sample, however, derived from a location some distance northwest from Peculiar Knob. A potentially still younger overprint is indicated by metamorphic rims dated at 1576.2 ± 7 Ma from a leucogabbro from drillhole PKN1 adjacent to the deposit [27].

The deposit is buried beneath 12–35 m of the flat-lying Cretaceous sediments (Bulldog Shale) and was mined between 2011 and 2015. The deposit consists of a zone of high-grade hematite mineralization, roughly 1 km in length, ~35 m wide and up to ~300 m deep (Figure 1C). The orebodies are steeply NW-dipping and occur as two NE-striking, sub-parallel elongated lensoidal bodies, which are off-set by at least four cross-cutting faults. These are hosted within a sequence of iron-rich units and various high-grade metamorphosed rocks and granitoids. Ultramafic/mafic lithologies within the sequence can be inferred by the presence of altered, chlorite-rich rocks. Similar lithologies are also known associated with BIF sequences from the Middleback Ranges deposits [6]. The ores comprise massive specular hematite and have been considered to represent the metamorphosed hydrothermally-altered equivalents of Fe-rich sediments, including chemical precipitates (BIFs), in several previous studies [10,15,30], and also in the most recent resource report [11]. Early studies also acknowledge the impact on the ores from the adjacent Balta Granite (e.g., [31]). More recently, other authors have speculated on the possible relationships between iron deposits such as Peculiar Knob and IOCG systems of the eastern Gawler Craton (e.g., [32]), although little direct evidence is available to support such a hypothesis.

3. Methodology

The present study was carried out on a sample of massive hematite ore (Figure 2) collected from the Peculiar Knob open pit. The sample was assayed by Intertek Genalysis (Adelaide, Australia). Methodology for the whole-rock analysis and element minimum detection limits (MDL) are provided in Supplementary Material A. All the below mentioned microanalytical instrumentation are housed at Adelaide Microscopy, The University of Adelaide (Adelaide, Australia). Petrographic observations were made on a one-inch polished block using reflected-light optical and scanning electron microscopy (SEM). A FEI Quanta 450 SEM equipped with an energy dispersive X-ray spectrometer (EDS) was used for further µm-scale observations, detection of compositional zonation within hematite and zircon, and for back-scattered electron (BSE) imaging. Analytical conditions for SEM work were 20 kV acceleration voltage and a beam current of 10 nA.

Trace element concentrations in hematite were measured with a RESOlution excimer laser ablation system (Applied Spectra Inc., Fremont, SA, USA) coupled to an Agilent 7900x Quadrupole ICP-MS using a frequency of 10 Hz, fluence of 3.5 J/cm^2 and a spot diameter of 60 µm. Laser ablation element maps were performed using a laser frequency of 10 Hz, fluence of ~3 J/cm^2, and a spot diameter and scan speed of 7 µm and 7 µm/s, respectively. ^{57}Fe was used as an internal standard element for quantification of hematite assuming ideal stoichiometry. External reference materials used were the synthetic basalt glass standard GSD-1G glass (USGS; [33]) and the NIST-610 glass [34]. "GLITTER" software [35] was used for data reduction. To avoid element contamination from trace minerals included in hematite, only those intervals within individual spot analyses showing flat signals were selected during the data reduction process. Time-resolved depth profiles were used to further

assess trace element data quality and to ensure negligible influence from included minerals during analysis. Average minimum detection limits (MDL) for the analyzed elements are also provided in the same appendix. Laser ablation element maps were constructed using "Iolite" software [36]. See Supplementary Material A for full details of analytical methods.

Zircon compositions were quantitatively determined using a Cameca SX-Five Electron Microprobe (Adelaide Microscopy) running "PeakSite" software and equipped with five wavelength-dispersive X-Ray detectors. Calibration and data reduction were carried out using "Probe for EPMA" software. Analytical conditions, elements measured, average MDL, peak/background positions, count times, and standards are listed in Supplementary Material A.

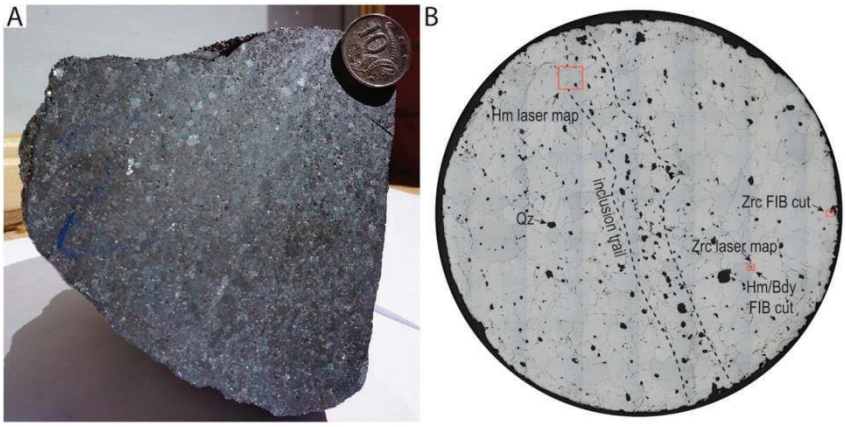

Figure 2. (**A**) Hand-specimen photograph of the studied hematite ore (cut face). (**B**) Reflected light photograph of one-inch polished block showing coarseness of granoblastic hematite. Note gangue as (i) interstitial grains (mostly quartz (Qz), black), and (ii) an array of dense grains throughout hematite (arrowed). Areas with analyzed zircon and the focused ion beam cuts in hematite (Hm)/baddeleyite (Bdy) and zircon (Zrc) are also marked.

A FEI-Helios nanoLab Dual Focused Ion Beam (FIB) SEM was used for preparing foils for transmission electron microscopy (TEM) study. Procedures for extracting and thinning (to <100 nm) of foils by beam (Ga^+) milling and attachment to Cu grids followed those outlined previously [37]. High-angle annular dark field-scanning transmission electron microscopy (HAADF-STEM) imaging and energy-dispersive X-ray spectrometry (EDS)-STEM mapping were performed on a high-resolution, probe-corrected, FEI Titan Themis S/TEM equipped with the X-FEG Schottky source and Super-X EDS geometry, operated at 200 kV.

Cathodoluminescence (CL) imaging to characterize core-rim relationships and zonation patterns within granular zircon interstitial to hematite was performed on a FEI Quanta 600 MLA SEM (Adelaide Microscopy) equipped with a tungsten filament electron source. In-situ U–Pb dating of zircon was performed with the high-resolution ion microprobe (SHRIMP-II) at the John de Laeter Centre, Bentley, Curtin University, Western Australia. Analytical methods used broadly follow those described by Compston et al. [38] and Williams [39]. Further details are given in Supplementary Material A.

4. Results

4.1. Petrography

The massive ore consists of mm-sized, polyhedral grains of hematite with granoblastic texture (Figure 2). Gangue minerals (mostly quartz and minor siderite) are located at hematite grain boundaries

or concentrated along trails within the hematite (Figure 2B). Mutual grain boundaries, often with triple junctions at 120°, exhibit both straight and serrated margins (Figure 3A,B). Polysynthetic twinning, following one or two crystallographic directions, is a common feature of hematite (Figure 3A–C). Small grains, from <1 µm to a few µm in size, of magnetite are ubiquitous throughout the hematite (Figure 3D–I). The morphology of these grains varies from thin lamellae to (sub)-euhedral grains of hexagonal to octagonal shape in cross-section. Magnetite is closely associated with the twin planes in hematite, either at their margins, along, or slightly offset/across them (Figure 3E–G). Pressure gashes filled with gangue minerals (quartz and siderite) and tiny blebs of magnetite are observed along microfractures crosscutting the twin planes (Figure 3I).

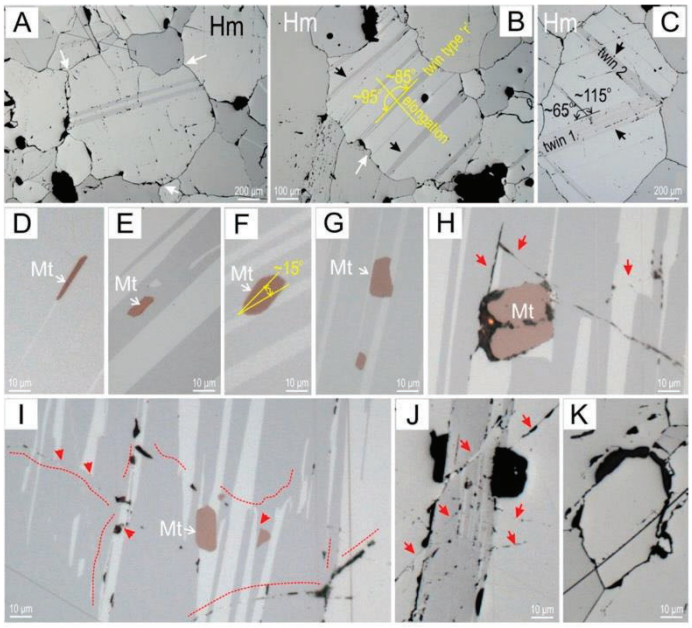

Figure 3. Reflected light microphotographs showing petrographic aspects of hematite (Hm). (**A**) Granoblastic texture with triple junctions at 120° (white arrows) and straight boundaries. (**B**) Serrated boundaries (white arrows) around a grain with dense twins (black arrows). Note orientation of twin plane relative to Hm elongation as marked, attributable to rhombohedral (r) twins. (**C**) Two sets of twins with angles as marked in coarse Hm with different orientation to the grain in (**B**). (**D**–**I**) Magnetite (Mt) grains associated with twin planes. Note varying morphologies from acicular, in (**D**), to (sub)euhedral, and changing relationships with the twin planes, i.e., along the twin planes in (**D**) and (**E**), slightly offset as marked in (**F**) and (**G**), and across them in (**H**). Rounding and marginal replacement of Mt in (**H**) is associated with microfractures (red arrows). (**I**) Microfractures (red lines) marked by pressure gashes filled with gangue minerals and tiny blebs of Mt (arrowed). Note that twins are displaced by the microfractures. (**J**) Microfractures oblique to twin boundaries (arrowed) producing intra-lamellar brecciation. Note the presence of gangue minerals (black) and pores along the fractures inferring fluid percolation. (**K**) Deformation of a small hematite grain associated with rounding and mantling by gangue.

Rounding and replacement of coarser magnetite by gangue is also observed at junctions of microfractures (Figure 3H). More advanced reworking of hematite is observed along the trail of gangue minerals that runs through the middle part of the polished block. This includes brecciation within

twin planes associated with small displacements of finer sets of twins (Figure 3J) and deformation of smaller hematite grains (Figure 3K).

One of the unusual characteristics of the hematite is the presence of fields comprised of micron to sub-micron inclusions with bright appearance on BSE images (Figure 4A–C). These are identified from the nanoscale study (see below) as baddeleyite (monoclinic ZrO_2). Such fields are, however, absent in some grains (Figure 4A), or are effectively invisible, at least at this scale of observation. The baddeleyite inclusions display bleb, or more often needle-like morphologies, are generally <3 µm in length and <1 µm in width and are preferentially oriented in two or three directions. The obtuse/acute angles between two arrays of inclusions are ~110°/70°.

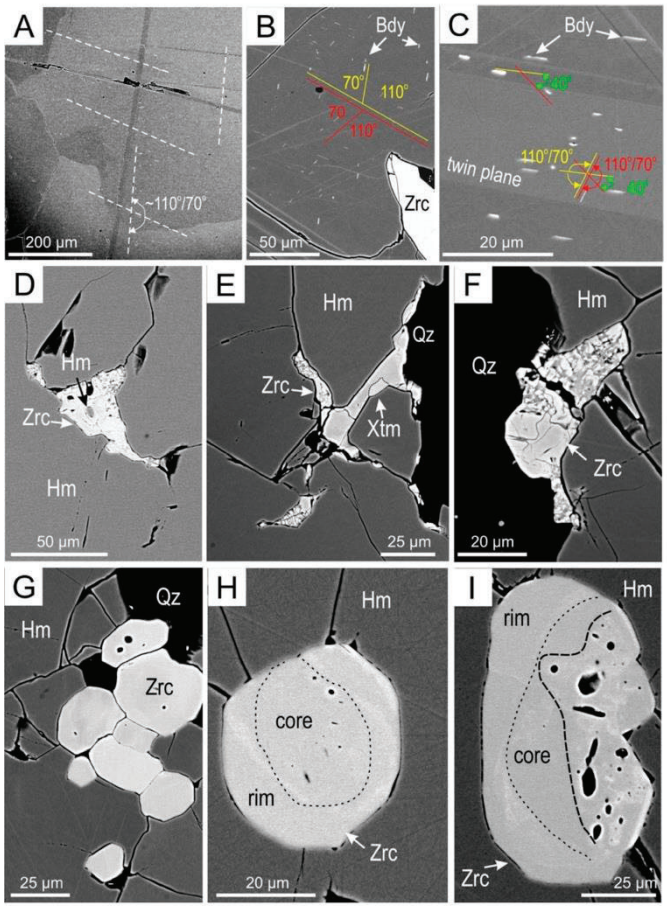

Figure 4. BSE images showing Zr-minerals in hematite (Hm) as baddeleyite (Bdy) inclusions (in **A**–**C**), and as zircon (Zrc) with skeletal and granular morphology (in **D**–**F** and **G**–**I**), respectively. Note the preferential arrangement of the Bdy needles (orientation angles as marked) across grain boundaries marked as dashed lines in (**A**), or along twin planes in Hm in (**C**). Note the lack of any direct contact between Bdy and Zrc when present in the same area in (**B**). Inclusions of Hm, xenotime-(Y) (Xtm) and fluorapatite (Ap) in zircon are associated with presence of pores and alteration. The boundary between core and rim in granular Zrc is marked by dashed lines in (**H**) and (**I**).

The baddeleyite arrays can cross over grain boundaries (Figure 4A), form locally denser domains within the same grain (Figure 4B), or be present within/along twin planes, remarkably with the same preferential orientation as elsewhere (Figure 4C). Some of the twins in hematite are also visible on BSE images (Figure 4C). Zircon is also present in the sample and displays morphology varying from skeletal (Figure 4D–F) to granular (Figure 4G–I). The skeletal zircon, restricted to grain boundaries in hematite or between hematite and quartz, features marginal alteration and tiny inclusions of hematite and xenotime-(Y) (Figure 4D,E). A transition from skeletal to granular morphology is observed towards the boundaries with quartz (Figure 4F). The granular zircon form aggregates towards larger quartz pockets (Figure 4G). Larger, single grains of zircon occur within hematite and these are surrounded by radial cracks (Figure 4H,I). Such grains display asymmetric cores and rims with brighter bands marking the two domains on BSE images. Fluorapatite, xenotime-(Y) and pores are noted particularly within the cores or towards corroded margins in zircon (Figure 4I).

Both hematite and quartz display textures indicative of fluid percolation (Figure 5A,B). Pores and inclusions of siderite and magnetite mark zones of microbrecciation within sets of twin lamellae (Figure 5A). Coarser quartz grains with partially resorbed/hooked boundaries display rotational textures comprising sub-µm size grains of hematite and acicular Ti-oxides (probably rutile) (Figure 5B–D). Hematite aggregates nucleate within pores in such quartz (Figure 5C). Siderite is present between hematite lamellae and also forms interstitial pockets with quartz (Figure 4E,F). Rotational textures between the two minerals are observed in the latter case (Figure 5F). Sub-rounded grains of fluorapatite are also noted within hematite (Figure 5G).

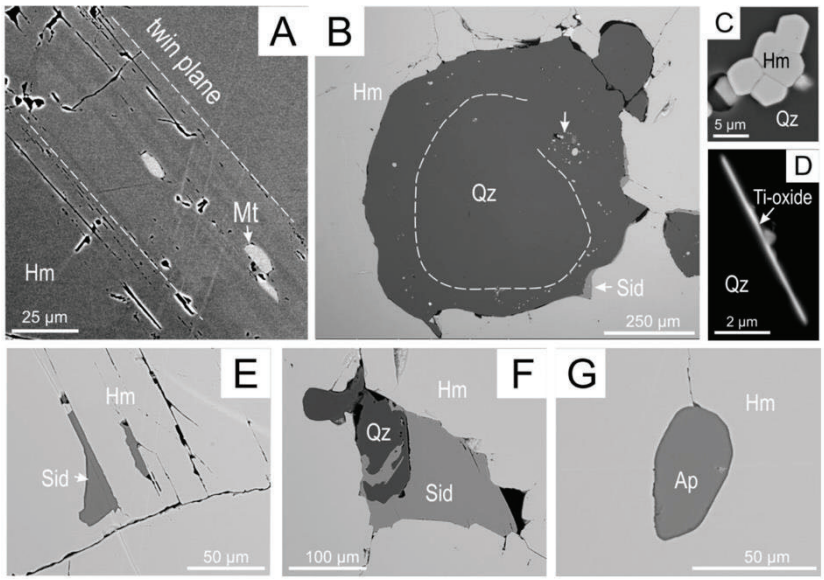

Figure 5. BSE images showing hematite overprint (**A**) and gangue minerals (**B**–**G**). (**A**) Brecciation of hematite (Hm) marked by pores and inclusions of magnetite (Mt). (**B**) Rotational texture in quartz (Qz) marked by trails of inclusions (dashed line). (**C**) Aggregate of hematite formed within a pore in Qz. (**E**) Typical needle of Ti-oxide in Qz. (**F**–**H**) Inclusions of siderite (Sid), Qz and fluorapatite (Ap) within Hm.

4.2. Geochemistry

4.2.1. Whole-Rock Data

Whole-rock geochemical data for the studied ore sample shows it is composed predominantly of Fe_2O_3 (Table 1). A minor amount of SiO_2 is present, which is represented mainly by quartz. Other components are TiO_2, P_2O_5 and CO_2, the latter two likely resulting from fluorapatite and carbonates, respectively. The oxides Al_2O_3, MgO, CaO, K_2O and MnO are present in concentrations <0.05 wt. %.

A suite of trace elements was measured at notable concentrations (Table 1). The chalcophile element Sb measured 7.5 ppm whereas typically associated As measured only 1 ppm. The transitional elements Cr and V are both present at concentrations ≥25 ppm. Besides relatively high TiO_2 (0.26 wt. %), other high-field strength elements (HFSE) that were measured, albeit at lower concentrations (<6 ppm), include Nb and Hf. Zirconium concentration in whole-rock is 94 ppm. Typical granite-related elements Sn (4 ppm) and W (4 ppm) are also present.

Table 1. Whole-rock major and trace element geochemistry.

Element (wt. %)		Element (ppm)									
SiO_2	0.96	Li	1.4	V	25	Sb	7.5	La	2.3	Tm	<0.05
Al_2O_3	0.06	Ba	1	Nb	5.8	Bi	<0.05	Ce	5.2	Yb	0.16
MgO	0.02	Sr	1.2	Ta	0.3	Pb	<5	Pr	0.55	Lu	0.03
Fe_2O_3	97.81	Be	<0.5	Zr	94	Te	0.1	Nd	2	ΣREE	12.8
CaO	0.01	Rb	<0.1	Hf	2.2	Se	<1	Sm	0.27		
K_2O	0.01	Cs	<0.05	Sc	<2	Tl	<0.02	Eu	0.08		
Na_2O	0.01	Cr	27	Ga	1.7	Mo	<1	Gd	0.21		
P_2O_5	0.16	Ni	<1	Ge	0.1	Re	<0.05	Tb	0.03		
TiO_2	0.26	Co	0.2	In	<0.05	Sn	4	Dy	0.22		
MnO	0.01	Cu	<1	Au	<0.01	W	4	Y	1.5		
LOI	0.03	Zn	<1	Ag	<0.1	Th	0.14	Ho	0.05		
Total + LOI	99.47	Cd	<0.05	As	1	U_3O_8	0.16	Er	0.18		

LOI: loss on ignition.

With the exception of La, Ce, Y and Nd, rare-earth elements occur at concentrations <1 ppm (ΣREE = 12.8 ppm). The chondrite-normalized REE fractionation trend shows LREE enrichment (La_{CN}/Yb_{CN} = 10.31) and no Ce- or Y-anomaly (Figure 6).

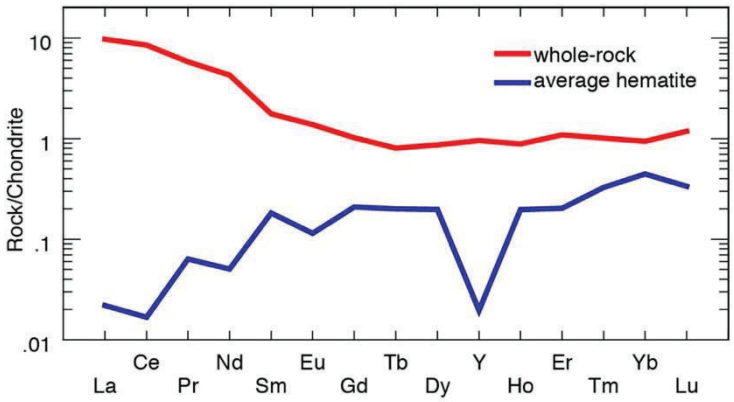

Figure 6. Chondrite-normalized REE fractionation trends for whole-rock and hematite. Chondrite values from [40]. Note the marked differences for LREE (high in whole-rock, low in hematite) and the negative Y-anomaly for hematite. These features are attributable to presence of Zr-minerals and fluorapatite.

4.2.2. Trace Element Concentrations and Grain-Scale Distribution in Hematite

LA-ICP-MS trace element compositional data for hematite show the presence of several elements that likely account for a large portion of the whole-rock budget (Table 2). Aluminum, Si, Cr, V and P measured in the tens to hundreds ppm. Antimony is present at a concentration more than an order of magnitude higher than As. Tin and W both measured ~5 ppm. Among the HFSE, Ti and Zr were measured at high concentrations, i.e., average ~1490 ppm and ~250 ppm, respectively; Nb and Hf measured at ~5 ppm. Zirconium concentration varies, as expected, depending upon the presence or absence of visible baddeleyite inclusions on the surface of the polished block, i.e., between 68 ppm up to 600 ppm. However, given the nm-size of baddeleyite inclusions, these are not observable as fluctuating signals for Zr on the time-resolved depth profiles for individual LA-ICP-MS spot analyses (Figure 7).

The concentrations of all other trace elements were <1 ppm. The chondrite-normalized REE fractionation trend for a mean analysis of hematite shows relative LREE depletion and HREE enrichment (La_{CN}/Yb_{CN} = 0.049), noticeable negative Ce-, Eu-anomalies and a strong negative Y-anomaly (Figure 6). The differences between the whole-rock and hematite data are attributable to the role of Zr-minerals (particularly Y) and fluorapatite (LREE).

Trace element LA-ICP-MS maps of hematite reveal grain-scale compositional zoning (Figure 8). This is expressed by relative enrichment in elements such as Zr, Hf, Ti and Cr in hematite cores and respective depletion of these elements on grain margins. The latter are, however, enriched in Nb, Sb, W and Sn. Although the fields with baddeleyite are visualized on the LA-ICP-MS element maps (Zr in Figure 8A), Zr is relatively homogenously distributed throughout hematite grain cores, as also shown by time-resolved depth profiles, with measurable, still high concentrations of Zr in hematite grains that are apparently free of baddeleyite (Figure 7). The maps also show that Zr and Hf are depleted along the margins of hematite wherever granular zircon is present (Figure 8B). Zircon grains on the maps illustrated in Figure 8B show rims that are enriched in U relative to cores.

Table 2. LA-ICP-MS trace element (ppm) data for hematite from Peculiar Knob.

Element	Geomean	Max.	Min.	s.t.d.	Element	Geomean	Max.	Min.	s.t.d.
Mg	6.3	48	1.3	11	Hf	6.7	24	1.3	6.6
Al	421	444	382	14	Ta	0.50	0.59	0.42	0.04
Si	206	325	174	32	W	5.0	9.4	1.1	2.4
P	14	22	9.6	3.1	^{206}Pb	0.24	1.3	0.05	0.30
Ca	63	99	40	30	^{208}Pb	0.17	0.66	0.04	0.16
Sc	1.1	1.5	1.0	0.15	Th	0.03	1.2	0.002	0.48
Ti	1492	1881	1218	124	U	0.06	1.0	0.002	0.29
V	36	39	34	1.2	La	0.005	0.03	0.002	0.007
Cr	22	40	16	4.7	Ce	0.01	0.13	0.002	0.04
Mn	3.1	3.9	2.4	0.41	Pr	0.006	0.02	0.001	0.007
Co	0.69	1.1	0.31	0.25	Nd	0.02	0.09	0.008	0.03
Ni	0.72	1.2	0.32	0.25	Sm	0.03	0.10	0.01	0.03
Cu	0.55	0.68	0.41	0.11	Eu	0.007	0.02	0.002	0.008
Zn	0.28	0.55	0.16	0.12	Gd	0.04	0.34	0.01	0.11
Ga	1.8	2.1	1.5	0.16	Tb	0.007	0.08	0.002	0.03
As	1.3	3.4	0.44	0.78	Dy	0.05	0.58	0.006	0.20
Sr	0.03	0.55	0.01	0.16	Y	0.03	5.6	0.003	1.5
Zr	260	609	68	145	Ho	0.01	0.09	0.002	0.03
Nb	5.3	5.9	4.2	0.40	Er	0.03	0.56	0.005	0.19
Mo	0.76	1.0	0.59	0.09	Tm	0.008	0.09	0.002	0.03
Sn	6.4	11	4.8	1.6	Yb	0.08	0.77	0.01	0.25
Sb	20	25	12	3.2	Lu	0.009	0.14	0.002	0.04
Ba	0.16	0.53	0.08	0.16					
(n = 20 hematite analyses)									

Geomean: geometric mean; s.t.d.: standard deviation; Max.: maximum; Min.: minimum.

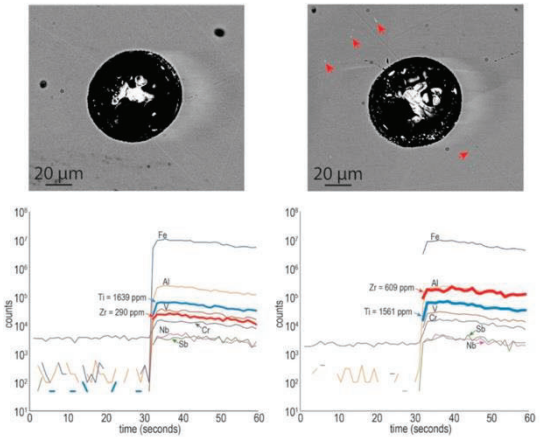

Figure 7. BSE images and representative time-resolved depth profiles of (**left**) "clean" hematite and (**right**) hematite with baddeleyite inclusions (marked by red arrows). Note the smooth signal for Zr in both cases but a difference in the intensity of the signal, which is an order of magnitude higher in the second case. Titanium shows comparable smooth signals and similar count intensity in both cases.

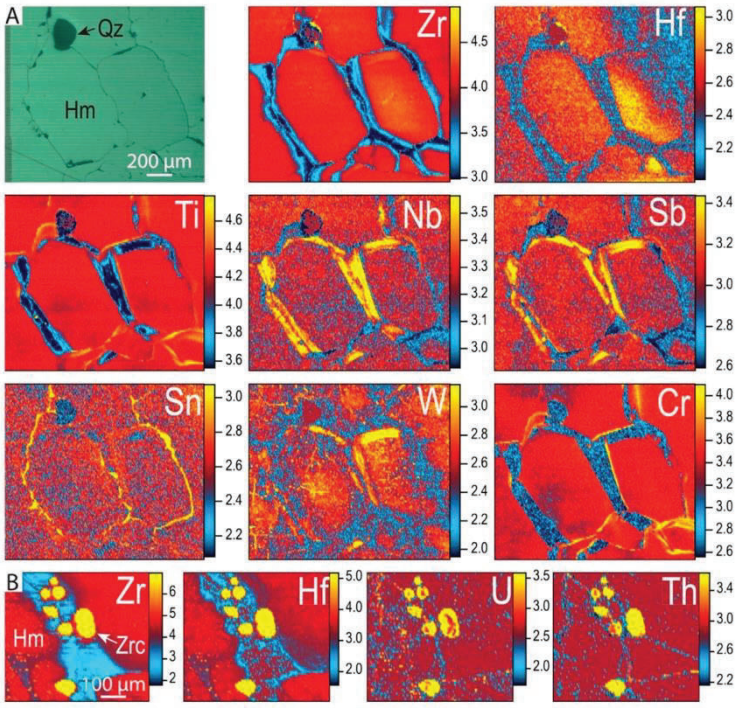

Figure 8. (**A**) Reflected light image (top left) and LA-ICP-MS element maps of granoblastic hematite (Hm) showing hematite cores enriched in Zr, Hf, Ti and Cr, with margins depleted in these elements but enriched in Nb, Sb, Sn and W. (**B**) LA-ICP-MS element maps showing aggregates of granular zircon (Zrc) along hematite margins that are depleted in Zr and Hf. Scales in counts-per second.

4.2.3. Zircon Electron Microprobe Data

Electron microprobe spot analysis (Table 3) and mapping of the various zircon textures show distinct compositional differences between the cores and rims of granular and skeletal zircon (Figures 9 and 10). Besides ZrO_2 and SiO_2, all textural variants of zircon contain measurable concentrations of MgO (~0.02 wt. %) and HfO_2 (~1.5 wt. %). The cores of granular zircon, however, contain higher concentrations of Al_2O_3 (~0.2 wt. %), P_2O_5 (~0.5 wt. %) and Y_2O_3 (0.05 wt. %) relative to the rims of the same grains and also the skeletal zircon. Additionally, Sc_2O_3 (~0.1 wt. %) was measured in zircon cores whereas rims and skeletal zircon measured below detection limit.

The core and rim textures in granular zircon are well-marked on the maps, particularly by the presence of Sc (Figure 9). The boundary between the core and rim is marked by depletion in P, but enrichment in U corresponding to the bright and dark zones on BSE and CL images, respectively (Figure 9). The highest concentrations of P, Al and Y occur along the grain boundaries and cracks suggesting secondary element remobilization from zircon. Occurrence of xenotime-(Y) along the margin of zircon is common (e.g., the BSE image in Figure 10). The area mapped for the skeletal zircon (Figure 10) can be considered as transitional toward the granular texture. This shows comparable trace element enrichment as in the granular type but with a patchy appearance, also due to the much smaller size of the map. Notable is the marginal enrichment in P, Al and Y on one side of the zircon.

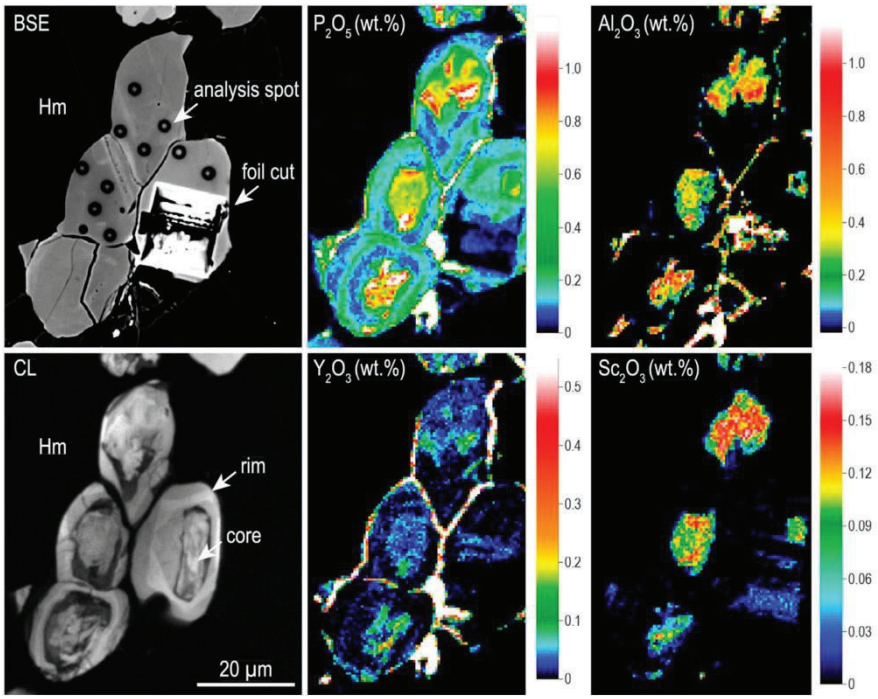

Figure 9. EPMA element map of granular zircon from the studied hematite (Hm) ore. Top left image is a BSE image showing analysis spots and location of foil cut via FIB and described in Section 4.3. The CL image of the same aggregate is shown in the bottom left panel. Note the core and rim textures with a dark ring on CL image and slightly brighter appearance on BSE image corresponding to U-richer zones in zircon. The maps reveal the clear geochemical differences between cores and rims in the granular zircon. Scales in wt. %.

Table 3. Electron microprobe data for zircon.

Texture	Granular										Skeletal		
	Core					Rim							
#	1	2	3	4	5 **	1	2	3	4	5	1	2	3
SiO_2	32.91	33.76	33.16	33.15	29.47	33.64	33.18	33.32	33.08	33.73	33.52	33.09	33.37
Al_2O_3	0.25	0.27	0.28	0.26	0.09	0.19	0.19	0.18	0.24	0.21	<mdl	<mdl	0.19
Fe_2O_3 *	1.33	1.25	0.81	0.88	2.18	0.67	1.96	1.26	1.11	1.06	1.55	1.03	0.80
MgO	0.05	0.03	0.05	0.05	0.02	0.02	0.02	0.01	0.02	0.03	0.01	0.01	0.02
CaO	<mdl	<mdl	0.01	<mdl	0.09	0.02	<mdl	<mdl	0.01	<mdl	<mdl	0.03	<mdl
Na_2O	<mdl	0.03	<mdl	0.02	0.05	<mdl	<mdl	<mdl	0.02	<mdl	0.04	0.05	<mdl
P_2O_5	0.72	0.51	0.69	0.70	0.23	0.08	0.18	0.10	0.18	0.13	0.17	0.09	0.10
Sc_2O_3	0.18	0.13	0.11	0.13	0.03	<mdl	<mdl	<mdl	<mdl	<mdl	<mdl	<mdl	<mdl
ZrO_2	65.85	65.35	65.92	65.86	65.73	65.94	65.67	66.42	65.35	66.53	67.35	67.03	66.39
HfO_2	1.36	1.40	1.46	1.55	0.98	1.39	1.64	1.65	1.73	1.77	0.99	1.03	1.55
PbO	<mdl	0.02	<mdl	0.03	<mdl	0.02	0.02	<mdl	0.02	<mdl	<mdl	<mdl	<mdl
Y_2O_3	0.04	0.03	0.05	0.06	0.10	0.02	0.02	0.01	0.16	0.01	0.06	0.03	0.02
Eu_2O_3	<mdl	<mdl	<mdl	<mdl	<mdl	<mdl	<mdl	<mdl	<mdl	<mdl	<mdl	0.04	<mdl
Gd_2O_3	<mdl	<mdl	<mdl	<mdl	0.05	0.05	<mdl	<mdl	<mdl	<mdl	0.07	<mdl	<mdl
Tb_2O_3	0.03	<mdl	<mdl	<mdl	0.07	<mdl	0.04	<mdl	<mdl	<mdl	<mdl	<mdl	0.03
Dy_2O_3	0.05	<mdl	<mdl	<mdl	<mdl	0.03	0.04	<mdl	<mdl	0.03	<mdl	<mdl	<mdl
Er_2O_3	0.05	<mdl	0.03	0.03	<mdl	<mdl	0.05	<mdl	0.05	0.03	0.03	<mdl	<mdl
Yb_2O_3	0.09	0.09	0.09	0.11	<mdl	0.06	0.06	<mdl	0.09	0.04	<mdl	<mdl	0.05
Cl	<mdl	<mdl	<mdl	<mdl	<mdl	0.01	<mdl	<mdl	<mdl	<mdl	<mdl	0.01	<mdl
Total	101.58	101.62	101.84	101.96	96.91	101.47	101.11	101.69	100.95	102.51	102.23	101.42	101.73
Zircon formula: (ABZ_4); calculated based on 4 oxygen per formula unit													
Al	0.009	0.010	0.010	0.009	0.003	0.007	0.007	0.006	0.008	0.007	-	-	0.007
Mg	0.002	0.001	0.002	0.002	0.001	0.001	0.001	-	0.001	0.001	0.001	-	0.001
Ca	-	-	-	-	0.003	0.001	-	-	-	-	-	0.001	-
Na	-	0.001	-	0.001	0.003	-	-	-	0.001	-	0.002	0.003	-
Sc	0.005	0.003	0.003	0.003	0.001	-	-	-	-	-	-	-	-
Zr	0.964	0.952	0.962	0.960	1.029	0.967	0.969	0.975	0.966	0.968	0.982	0.987	0.974
Hf	0.012	0.012	0.012	0.013	0.009	0.012	0.014	0.014	0.015	0.015	0.008	0.009	0.013
Pb	-	-	-	-	-	-	-	-	-	-	-	-	-
Y	0.001	0.001	0.001	0.001	0.002	-	-	-	0.003	-	0.001	0.001	-
Eu	-	-	-	-	-	-	-	-	-	-	-	-	-
Gd	-	-	-	-	0.001	-	-	-	-	-	0.001	-	-
Tb	-	-	-	-	-	-	-	-	-	-	-	-	-
Dy	-	-	-	-	-	-	-	-	-	-	-	-	-
Er	0.001	-	-	-	-	-	0.001	-	-	-	-	-	-
Yb	0.001	0.001	0.001	0.001	-	0.001	0.001	-	0.001	-	-	-	-
Tot. (A site)	0.994	0.981	0.991	0.992	1.052	0.989	0.993	0.996	0.996	0.993	0.995	1.001	0.996
ΣREY	0.003	0.001	0.002	0.002	0.002	0.002	0.002	0.000	0.004	0.001	0.002	0.001	0.001
Si	0.988	1.008	0.992	0.991	0.946	1.011	1.004	1.003	1.003	1.006	1.002	0.999	1.004
P	0.018	0.013	0.017	0.018	0.006	0.002	0.005	0.003	0.005	0.003	0.004	0.002	0.003
Tot. (B site)	1.006	1.021	1.009	1.009	0.953	1.013	1.009	1.005	1.007	1.009	1.006	1.001	1.006
O	4.000	4.000	4.000	4.000	4.000	4.000	4.000	4.000	4.000	4.000	4.000	4.000	4.000
Cl	-	-	-	-	-	-	-	-	-	-	-	-	-
Tot. (Z site)	4.000	4.000	4.000	4.000	4.000	4.000	4.000	4.000	4.000	4.000	4.000	4.000	4.000

mdl: minimum detection limit. F, La_2O_3, Ce_2O_3, Pr_2O_3, Nd_2O_3, Ho_2O_3, Tm_2O_3 and Lu_2O_3 measured below detection limit. TiO_2 was found to be <mdl in all analyses. * Measured Fe_2O_3 attributed to effects of adjacent hematite and not included in formula calculation or totals. ** Measured MnO (0.05 wt. %), UO_2 (0.04 wt. %), Sm_2O_5 (0.08 wt. %).

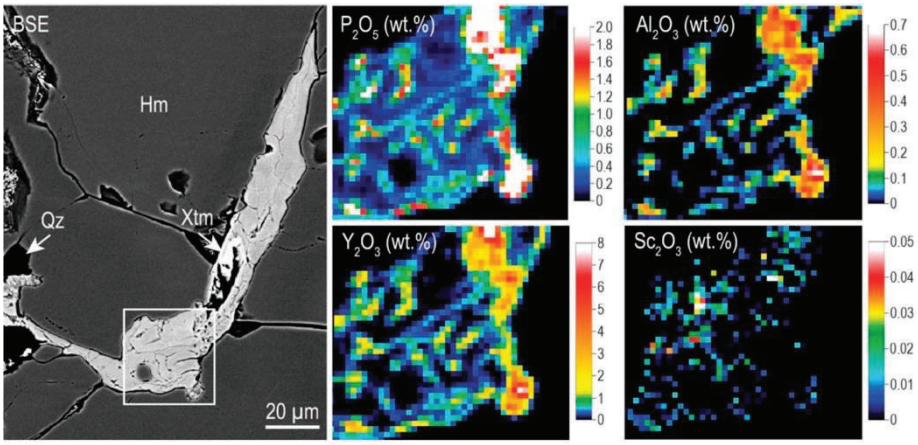

Figure 10. EPMA element map of skeletal zircon from the studied hematite (Hm) ore. The mapped area is shown in the rectangle on the BSE image to the left. Note the presence of the same elements as in the granular zircon (Figure 9). In this case, P, Al and Y show strongest enrichment on one side of the zircon. Despite the low resolution of these images, Sc is nonetheless notable as spots of higher concentration corresponding to patchy areas of enrichment in the other mapped elements. Scales in wt. %.

4.3. Nanoscale Mineral Study

The nanoscale study was carried out for identification of: (i) Zr-rich needles as baddeleyite; and (ii) the core and rim texture in granular zircon mapped in Figure 9.

4.3.1. Baddeleyite

One of the typical fields with inclusions of baddeleyite was selected for the nanoscale study (Figure 11A). Two areas containing needle-like inclusions were assessed by FIB cross-sectioning (Figure 11B–D). Needles present beneath the surface were observed and the presence of two sets of lamellae with orientation at ~110°/70° measured on the surface of the polished block could also be confirmed at depth (Figure 11D).

HAAD-STEM imaging and EDS mapping/spectra of the foil obtained from cut #1 (Figures 11 and 12) show one of the widest (~60 nm) and longest (~3 µm) needles that were identified as baddeleyite, the monoclinic polymorph of ZrO_2. High-resolution imaging was performed with the sample tilted on the $[2\bar{2}.1]$ zone axis in hematite. Baddeleyite and host hematite are crystallographically oriented along lattice directions with ~3.7 Å repeats in each case, i.e., $(011)_{baddeleyite}$ parallel to $(10.\bar{2})_{hematite}$ (Figure 12B–D). In closer detail, stepwise defects are observed to occur that adjust the ~2° misfit between the lattice vectors (012)^(10.-2)~86° and (100)^(011)~84° on $[2\bar{2}.1]_{hematite}$ and $[0\bar{1}1]_{baddeleyite}$ zone axes, respectively (Figure 12D). The bright dots on the atomic-scale images correspond to Fe and Zr atoms in hematite and baddeleyite, respectively, with stacking corresponding to crystal structure models on each respective zone axis (Figure 12E,F).

STEM-EDS element maps of baddeleyite show the major elements Zr and O, with minor Hf and trace concentrations of Si, U and Ti, confirming that the chemistry of the nm-scale Zr-bearing phase in hematite as ZrO_2 (Figure 13A). Relative variation in major and trace elements between the needle and host hematite is shown on the EDS profiles (Figure 13B). We note the relatively high concentration of Ti in baddeleyite (monoclinic) relative to hematite (rhombohedral) (Figure 13C), inferring preferential partitioning during needle crystallization. Titanium affinity for monoclinic ZrO_2 (so-called baddeleyite-TiO_2) has been documented from synthetic studies at the nanoscale [41].

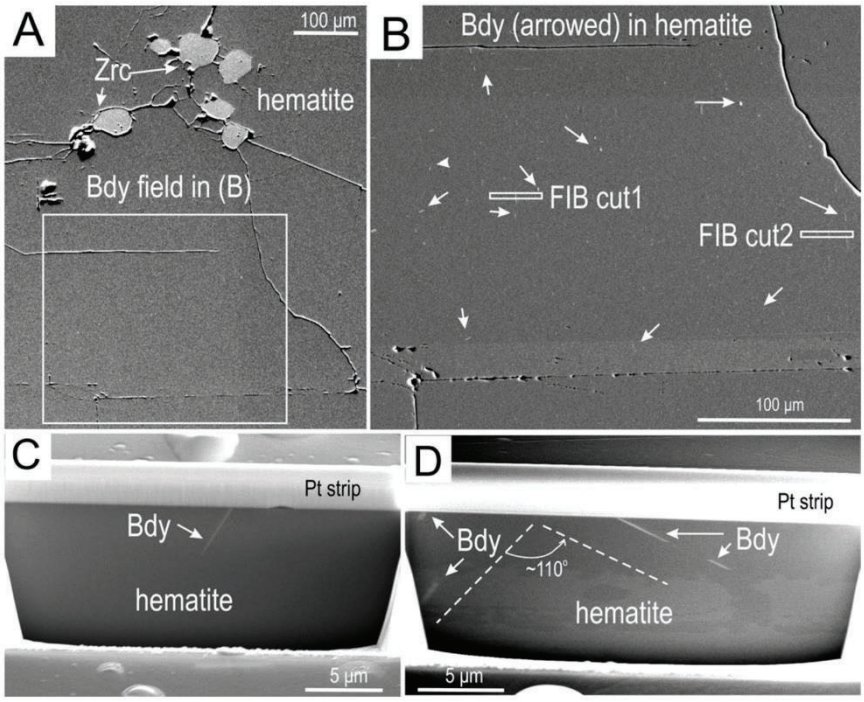

Figure 11. Secondary electron (SE) images showing the field of baddeleyite (Bdy) inclusions in hematite that was sampled for nanoscale analysis after cross-section imaging by FIB-SEM prior to foil preparation for TEM. (**A**) Location of inclusion field adjacent to a cluster of granular zircon (Zrc). (**B**) Location of the two FIB cuts across Bdy inclusions. Note that FIB cut #2 is closer to a fracture. (**C**,**D**) Cross section images of the two FIB cuts in (**B**) showing the Bdy needles and their relative orientations at depth. Note that more needles are aligned along two directions in cut #2, closer to the fracture, and also that the orientation of these needles is different at depth and in FIB cut #2.

4.3.2. Zircon

A second foil, obtained from one of the granular zircon grains was prepared from a slice cut across the core to rim boundary (Figure 14A,B). Imaging of the foil in both BF and HAADF-STEM modes does not show this boundary, even though a number of spotty trails and streaks are present, more abundant within the core than the rim (Figure 14C). No lattice defects or other structural changes could be identified by imaging and no chemical difference could be detected by STEM-EDS spot analysis or mapping. It is most likely that the intensity variation observed on both the BF and HAADF-STEM images is due to cumulative effects of trace element contents, even if the concentrations of individual elements are below the detection limit of the detectors. High-resolution imaging was performed with the specimen tilted on the [001] zone axis in zircon (Figure 14D,E). The core and rim domains are parts of the same grain (single crystal with the same orientation throughout the foil) and the zircon lattice is generally free of defects. Bright spots on the HAADF-STEM images correspond to positions of overlapping Zr and Si atoms on the [001] zone axis in zircon (Figure 14D).

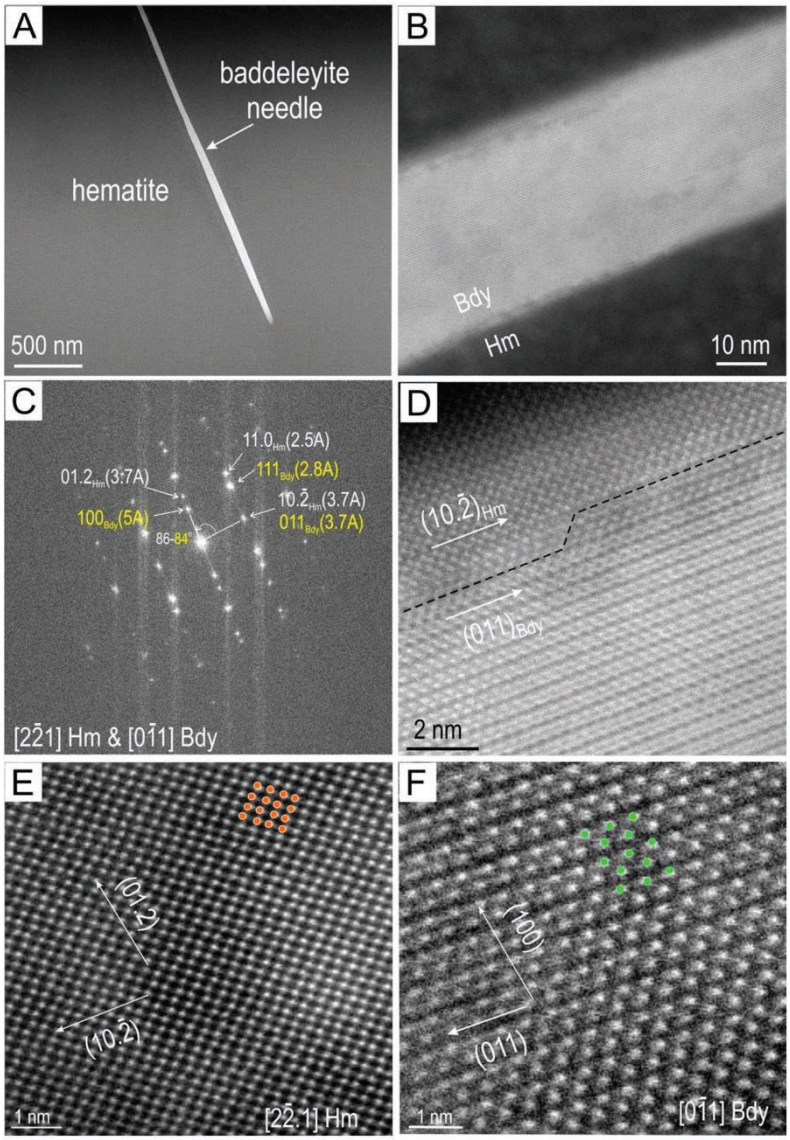

Figure 12. HAADF-STEM images showing baddeleyite (Bdy) in hematite (Hm). (**A**,**B**) Low- and higher-magnification images of Bdy needle (~60 nm-wide; ~3 μm long) within Hm. (**C**) Indexed Fast Fourier Transform (FFT) obtained from image in (**B**) showing the orientation between the two phases on zone axes as marked. (**D**) Coherent orientation between the Bdy on [01$\bar{1}$] zone axis and host Hm on [22$\bar{.}$1] zone axis. The two lattice vectors with parallel orientation are marked. Note, however, the stepwise defect (dashed line) at the immediate contact between the two minerals. (**E**,**F**) High-resolution images showing distribution of Fe (red) and Zr (green) in Hm and Bdy, respectively, on zone axes as marked. Arrangement of atoms (bright spots) correspond to crystal structure models for the zone axis in each mineral as marked.

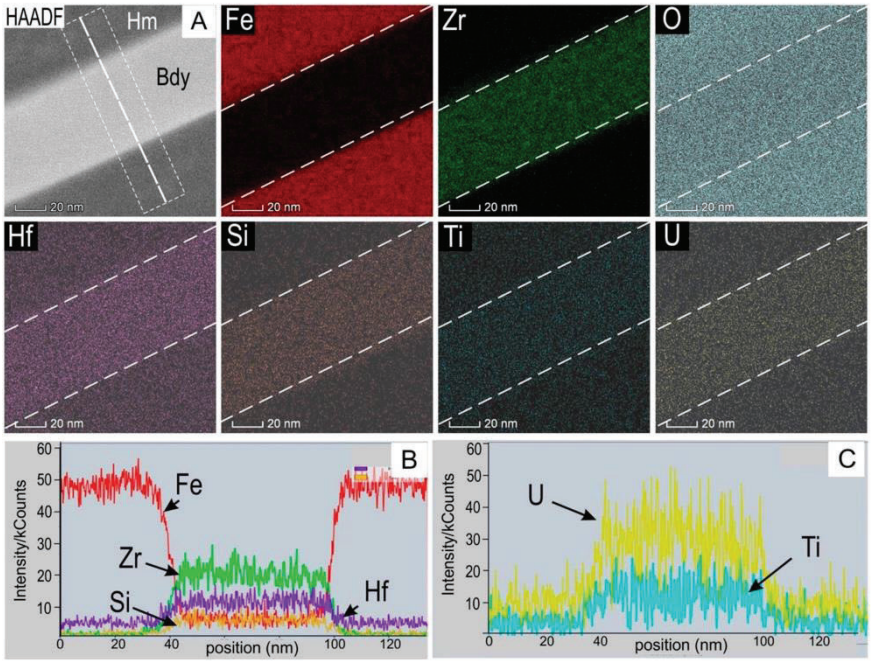

Figure 13. (**A**) HAADF-STEM image and EDS element maps of baddeleyite in host hematite. Elements shown as atom.%. Note that Si is present only in trace amounts. (**B**) Element variation along the profile (dashed line) shown in (**A**). (**C**) Uranium and Ti variation along the same profile in (**B**).

STEM-EDS element mapping shows a relative enrichment in Sc within the grain core (Figure 15A) but no direct correlation between chemistry and the bright streaks/spots on the HAADF image. A profile across the mapped area also shows notable Y, and interestingly, the contact between the rim and core domains is marked by an increase in Y and less pronounced increase in Sc concentration over a distance of 1 µm (Figure 15B). This information complements other data about the distinct chemistry of the core and rim zones, the rims appearing depleted in P on EPMA maps, and are seen to be enriched in U on BSE and CL images (Figure 9). Such chemical variation suggests that the core and rim domains in granular zircon result from an overprint event traceable down to the nanoscale rather than primary growth.

4.4. U–Pb SHRIMP Zircon Geochronology

Cathodoluminescence imaging of zircon aggregates interstitial to hematite and displaying rounded textures shows that the grains lack oscillatory growth zonation typical of magmatic zircon. The grains instead feature core-rim relationships more representative of hydrothermal growth (Figure 16 and Supplementary Figure S1).

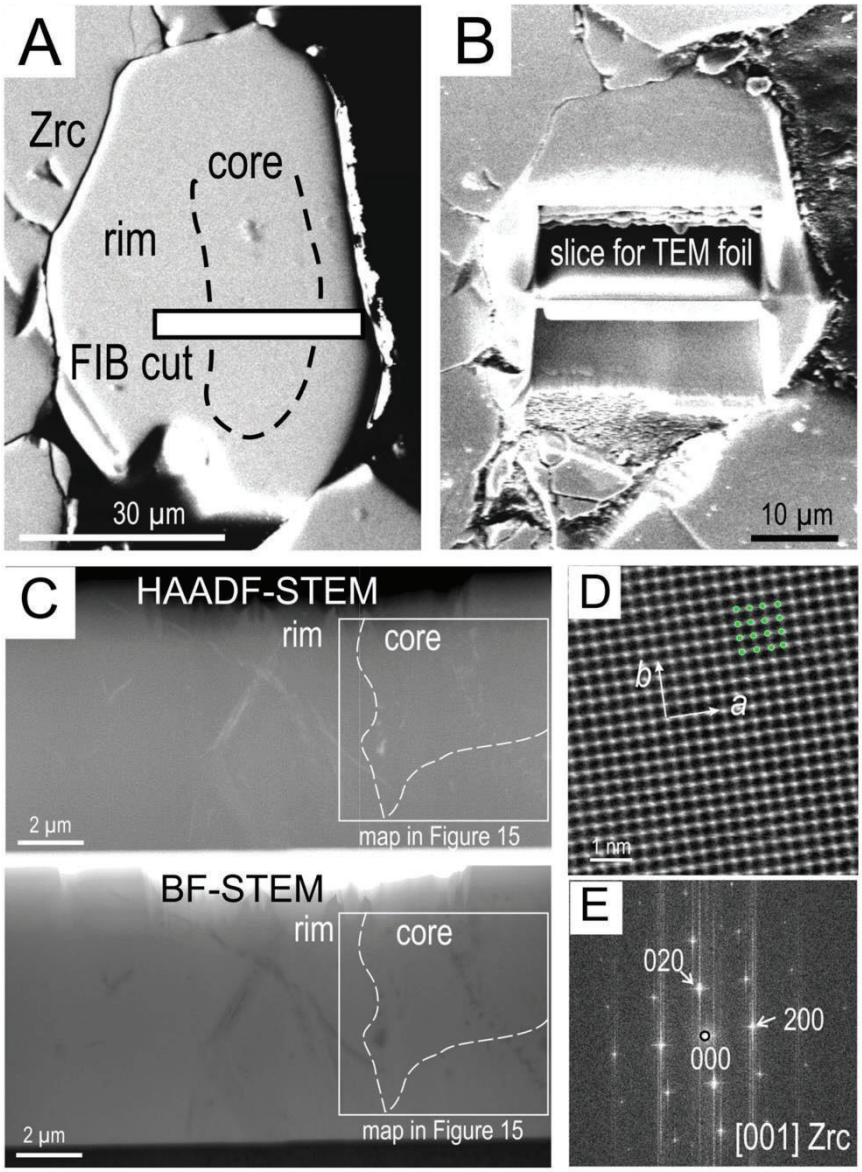

Figure 14. (**A**,**B**) SE images showing location of FIB cut and slice obtained across core and rim of granular zircon (Zrc). (**C**) Bright Field (BF)- and HAADF-STEM images of zircon foil. (**D**) High resolution image of Zrc on [001] zone axis and corresponding indexed FFT in (**E**). The bright spots represent Zr + Si atoms (green circles) with arrangement corresponding to crystal structure model on [001] zone axis in Zrc.

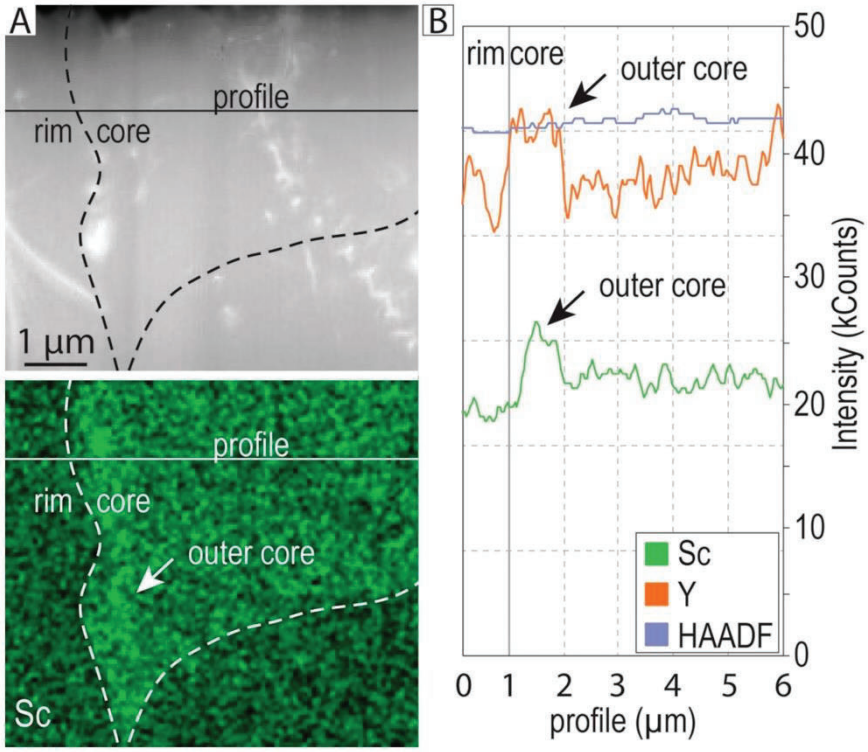

Figure 15. (**A**) HAADF-STEM image and EDS map for Sc (wt. %) in zircon, showing an area across core to rim domains. Note the lack of correlation between bright features in the top image and Sc distribution in the lower image. (**B**) Profile across the boundary between core and rim as marked in (**A**) showing variation in Sc and Y. Note that the contact between the two domains is depicted by a ~1 µm-wide zone enriched in Y and to a lesser extent, also Sc.

Eight spot analyses were collected from the zircon grains. A single grain contained high U (25 ppm), low Th (4.3 ppm), and large discordance (300%) and was not considered for further calculation. Another two grains had $^{206}Pb/^{238}U$ ratios <0.3 and were also not considered further. The remaining five analyses contained low concentrations of U and Th (from ~2–3.5 ppm and ~7–27 ppm, respectively; Table 4). One analysis is reversely discordant (−13) while the remaining four had discordance ranging from 6 to 32%. When anchored to a common-Pb upper intercept at 4500 ± 50 Ma, the data form a discordia line with a lower intercept age of 1731 ± 50 Ma (MSWD = 0.024). A $^{206}Pb/^{238}U$ weighted mean age was used due to the presence of common-Pb affecting the $^{207}Pb/^{206}Pb$ weighted mean and yielding an artificially old age. The three most concordant grains were used to obtain a $^{206}Pb/^{238}U$ weighted mean age of 1741 ± 49 Ma (MSWD = 0.86), which is interpreted to reflect the timing of zircon formation.

Table 4. U, Th and Pb isotope data.

							Age							Isotopic Ratio						
	%	U	Th	^{206}Pb *	^{232}Th		^{206}Pb		^{207}Pb		^{208}Pb		%	^{207}Pb *		^{207}Pb *		^{206}Pb *		Err
#	^{206}Pbc	ppm	ppm	ppm	/^{238}U	±%	/^{238}U	±1σ	/^{206}Pb	±1σ	/^{232}Th	±1σ	Disc.	/^{206}Pb *	±%	/^{235}U	±%	/^{238}U	±%	Corr
1	−1.54	3.2	7	0.84	2.3	1.99	1717	105	1805	253	1883	175	6	0.110	14	4.64	16	0.305	6.9	0.4
2	1.92	6.8	18	1.8	2.7	2.92	1720	74	1538	292	1512	109	−13	0.096	16	4.03	16	0.306	4.9	0.3
3	−2.03	2.4	11	0.68	4.6	2.25	1809	128	2186	250	1850	233	20	0.137	14	6.11	17	0.324	8.1	0.5
4	2.37	7.3	23	1.6	3.2	1.30	1449	63	1183	335	1376	90	−25	0.079	17	2.76	18	0.252	4.9	0.3
5	−2.58	12	34	2.7	3.0	2.62	1537	87	1843	265	1624	140	19	0.113	15	4.18	16	0.269	6.3	0.4
6	−2.23	7.5	21	2.1	3.0	1.63	1790	89	2103	201	1938	173	17	0.130	11	5.75	13	0.320	5.7	0.4
7	−3.44	1.8	27	0.52	15	5.43	1842	171	2545	543	1514	186	32	0.169	32	7.69	34	0.331	11	0.3

* Common Pb corrected using measured ^{204}Pb.

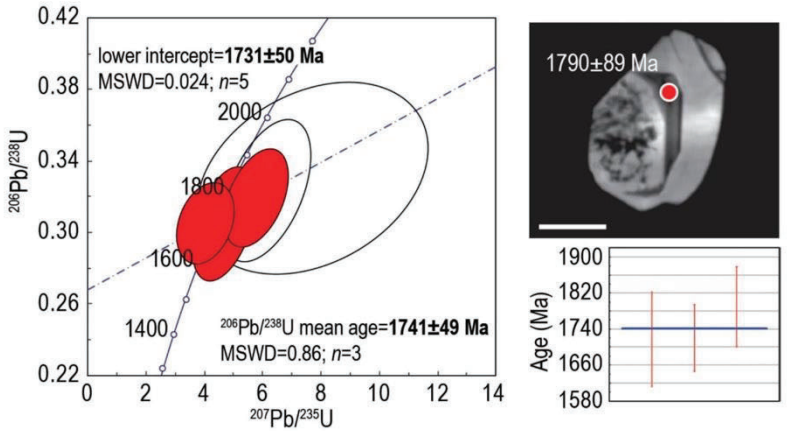

Figure 16. Concordia diagram presenting SHRIMP U–Pb data for zircon along with a CL image of a representative zircon grain and its respective ^{206}Pb/^{238}U age. Zircon grains used for a ^{206}Pb/^{238}U weighted mean age are colored red.

5. Discussion

5.1. Recognition of Metamorphic Textures

Hematite displays textures attributable to annealing under conditions of high-grade metamorphism, e.g., 120° triple junction "foam" textures comparable with those observed in many metamorphosed massive pyrite ores [42]. This is concordant with an interpretation in which the Peculiar Knob ore underwent metamorphism at $T > 680$ °C based on the thermoremanent magnetization history of comparable coarse hematite [12]. Although no fine-scale lamellar microstructure is observed in samples studied here, the presence of twins and tiny inclusions of magnetite are common features of the coarse hematite at Peculiar Knob and are analogous to those reported by Schmidt et al. [12]. In addition, we show that, although no metamorphic silicates are present, the gangue minerals also exhibit fabrics indicative of metamorphism, e.g., rotational patterns within quartz, or imbricate intergrowths between siderite and quartz. Nonetheless, superimposed textures in hematite, including decussate boundaries, microfractures, pressure gashes, porosity are evidence for deformation associated with fluid percolation during retrograde metamorphism or to a later tectono-magmatic event.

This is the first report of high Zr (hundreds of ppm) and Ti (1,500 ppm) concentrations in hematite from Peculiar Knob. We show that only Ti can be inferred as lattice-bound, whereas sub-μm inclusions of baddeleyite can account for the Zr content as measured by LA-ICP-MS. Formation of such Zr- and Ti-bearing hematite cannot be reconciled with chemical precipitation alone in a BIF environment, as had been previously considered (e.g., [10]).

5.2. Bridging Micron- to Nanoscale Observations in Hematite: Reconstruction of Ore Evolution

Nanoscale twinning has been shown in hematite grown from acicular goethite [43], a mechanism we consider feasible during diagenesis. Nonetheless, the studied hematite is markedly coarse-grained and the twinning is most likely related to syn-metamorphic deformation, in which case accommodation of strain takes place along glide planes ([44], and references therein). The ~85° angle between twins and crystal elongation in some hematite grains (Figure 3b) is comparable to the 84–86° angle between the reciprocal lattice vectors in epitaxial intergrowths of baddeleyite and hematite, i.e., $(011)^*_{\text{baddeleyite}}$ II $(10.\bar{2})^*_{\text{hematite}}$ and $(100)^*_{\text{baddeleyite}}$ II $(01.2)^*_{\text{hematite}}$ (Figure 12). Rhombohedral ("*r*") type twins in metamorphosed hematite were measured relative to the parent crystal by a rotation of 85° about the $r = (02\bar{2}1)$ direction [44], equivalent to the $(01\bar{1}2)^*$ direction in reciprocal space (indicated as $(01.2)^*$ on Figure 12C). This implies that twinning in hematite can be correlated with the fine adjustment of epitaxial intergrowths with baddeleyite during the same syn-deformational metamorphic event.

On the other hand, the angle between baddeleyite needles is distinct, by ~15°, from the "r" twin angle discussed above, with conjugate set of needles at ~110°/70° (Figure 4A–C and Figure 11D). These values correspond to the obtuse/acute angles between $(111)\hat{}(\bar{1}\bar{1}\bar{1})$ and $(\bar{1}\bar{1}\bar{1})\hat{}(\bar{1}1\bar{1})$ pairs of lattice vectors, respectively, in magnetite, and such crystallographic directions are often marked by trellis exsolutions formed during cooling of titanomagnetite (Ti–Mt) (e.g., [45], and references therein). The 15° offset is observed between the crystal orientations of some relict magnetite grains relative to the twin planes in hematite in which they are located (Figure 3F). Whereas relict magnetite can be preserved within hematite, the two minerals share equilibrium boundaries on $fO_2 - fS_2$ phase diagrams over temperature ranges of many geological environments, ilmenite is not stable with hematite. However, knowing that ilmenite is a good host for Zr relative to magnetite [46], decomposition of ilmenite could have led to: (i) exsolutions of baddeleyite within magnetite undergoing transformation into hematite; and (ii) subsequent relative enrichment of Ti in that hematite.

5.3. Zirconium Mineralogy: Geological Evolution at Peculiar Knob

Metamorphic differentiation can lead to migmatite formation, thus accounting for segregation of mafic and felsic minerals in a pre-existing lithology via sub-solidus remobilization and/or partial melting. For example, based on zircon geochronology indicating the presence of detrital zircon, the Warramboo

magnetite gneisses in the southeastern Gawler Craton, which was previously considered an Archean BIF, has been reinterpreted as a package of Fe-rich sediments that underwent deformation and granulite facies metamorphism during the Kimban Orogeny [47]. An increase in Fe content and the large-scale structural architecture of the Warramboo deposit was ascribed to melt loss and deformation during metamorphism. Such a process of iron-oxide concentration is, however, unlikely, by itself, to explain formation of hematite-rich orebodies at Peculiar Knob considering their high-grade, deposit size and the absence of metamorphic silicates (pyroxene, amphibole, garnet, etc.) at least not in the studied ore, among other arguments.

A potential source for the hematite protore could therefore be detrital titanomagnetite sourced from mafic/ultramafic rocks and deposited within a sedimentary basin. Such heavy mineral horizons could have been of sufficient volume to have formed an Fe-rich sediment with or without chemical precipitates. This hypothesis would also explain the Cr concentrations in hematite. A diagenesis-uplift cycle typical of Fe-rich sediment packages of this type could have led to transformation of magnetite into martite (pseudomorphic replacement of magnetite by hematite) with subsequent granoblastic coarsening and annealing during a high-grade metamorphic event such as the Kimban Orogeny. Ilmenite has been recognized as an important source of Zr during granulite facies metamorphism and baddeleyite associated with magmatic ilmenite in mafic granulites was interpreted as an exsolution product [48]. This infers that, ilmenite, although no longer present, may have been the source of Zr in the studied hematite. The age yielded by U–Pb SHRIMP analysis of zircon reported here, although not well constrained (1741 ± 49 Ma), is nevertheless similar to the age reported for the Kimban Orogeny with peak metamorphism at granulite facies (1736 ± 14 Ma; [24]).

The zircon cannot be readily linked to formation of baddeleyite in the same sample given the lack of similarity in the geochemical signature between the two Zr-minerals (e.g., Ti in baddeleyite, Sc in zircon), difference in both size and grain morphology, as well as lack of any observable relationships between the two minerals. A detrital origin was considered for Sc-bearing zircon found in association with pretulite ($ScPO_4$) and xenotime-(Y) in an Ordovician apatite-rich, oolitic ironstone from the Armorican Massif, France [49]. Low-temperature, P-bearing hydrothermal fluids were considered responsible for mineral reactions leading to Zr remobilization to form the Sc-phosphate during diagenesis and low-grade metamorphism. Scandium-rich zircon was also reported from xenotime-rich veins attributed to percolation of acidic, volatile-rich fluids, possibly granite-derived, through porous arkose units in the Browns Ranges REE deposit, Western Australia [50].

Although detrital zircon from a granitic source is an option, both the metamorphic age obtained, and the very low U concentrations represent arguments against a granitic source. Nonetheless, the association between Sc and P, as well as the inclusions of fluorapatite within the zircon cores (Figure 9) could be indicative of comparable low-T, P- and Si-bearing, acidic fluids that could have locally interacted with inclusions of ilmenite/baddeleyite within the titanomagnetite at the time of martitization, producing the observed Sc-bearing cores in the granular zircon. Scandium could have been remobilized by such fluids from the same Fe-Ti-oxides, since magmatic ilmenite can carry tens of ppm Sc (e.g., [7]). Baddeleyite can also be converted to zircon as a result of increased silica activity [51]. Recent assessment of the P-T conditions controlling zircon behavior during metamorphism indicates that growth occurs during late-stage exhumation/cooling, whereas prograde metamorphism is responsible for zircon dissolution ([52], and references therein). Therefore, growth of the granular zircon with Sc-P-Al-bearing cores during uplift could have been followed by zircon partial dissolution resulting in the skeletal zircon, locally preserving granular morphology with Sc-bearing domains preserved (Figure 10).

The distinct Sc-free rims in zircon with a narrow Sc- and Y-rich boundary depicted at the nanoscale (Figure 11B), are attributable to later fluid percolation, possibly associated with granite-derived hydrothermal fluids associated with the ~1.6 Ga Hiltaba Suite intrusions intersected in drillholes at depth beneath the deposit (Figure 1A). The modest recrystallization along the margins of hematite

grains, featuring a conspicuous Sn–W–Nb–Sb trace element signature is consistent with hydrothermal overprinting associated with Hiltaba magmatism [5,53].

6. Conclusions and Implications

The measured Zr concentration in hematite of average ~260 ppm is directly attributable to nm-scale inclusions of baddeleyite. These are likely pervasively distributed throughout the sample based on the inclusions observed beneath the surface and with smaller size. A distinction between such nm-scale inclusions and lattice-bound trace element substitutions cannot be made from LA-ICP-MS data alone and can only confirmed by nanoscale sample characterization [54].

The evidence presented here suggests that multiple events contributed to formation of the massive orebody at Peculiar Knob. Detrital titanomagnetite is considered to have been a source for Zr, Ti, Cr and Sc in a sedimentary environment via erosion of mafic rocks. The Fe-rich sedimentary package underwent diagenesis, followed by uplift and supergene ore enrichment leading to desilicification, compaction and martitization. This was followed by subsequent burial, deformation and high-grade metamorphism during the Kimban Orogeny. Later interaction with Hiltaba granitoids and distal hydrothermal fluids associated with those granites, led to W, Sn and Sb enrichment in hematite.

Zirconium mineralogy and geochemistry, the presence and distribution of Zr in iron-oxides and of Sc in zircon could represent potential indicators of ore formation. Similar characteristics might be anticipated in other Fe-rich prospects in South Australia and elsewhere. This study further demonstrates that observations bridging the micron- to nanoscales, using complimentary advanced microanalytical techniques, can provide critical constraints on ore-forming processes [12].

Supplementary Materials: The following are available online at http://www.mdpi.com/2075-163X/9/4/244/s1, Supplementary Material A: Details of analytical Methods; Figure S1, Cathodoluminescence images of zircon grains. References [55–64] are cited in the supplementary materials.

Author Contributions: W.K. and C.L.C. conceived this contribution and conducted all analytical work, assisted by A.S. with operating the Titan Themis instrument and B.P.W. with EPMA set-up. H.F. and G.J. provided the sample and unpublished background information on Peculiar Knob. The manuscript was written by W.K., C.L.C. and N.J.C., with contributions from K.E., B.P.W., H.F., G.J., and A.S.

Funding: This research is a contribution to the project "Trace elements in iron-oxides: deportment, distribution and application in ore genesis, geochronology, exploration and mineral processing", supported by BHP Olympic Dam and the South Australian Government Mining and Petroleum Services Centre of Excellence. N.J.C. acknowledges additional support from the ARC Research Hub for Australian Copper-Uranium (Gran IH130200033).

Acknowledgments: The authors acknowledge the facilities, and the scientific and technical assistance, of the Microscopy Australia node, Adelaide Microscopy at The University of Adelaide. Logistical support from site geologists at Southern Iron is greatly appreciated. Allen Kennedy is thanked for assistance with SHRIMP operation. Wenyuan Liu and Animesh Basak assisted with FIB operation. Sarah Gilbert assisted with LA-ICP-MS analysis. We gratefully acknowledge the helpful comments of two *Minerals* reviewers.

Conflicts of Interest: The authors declare no conflicts of interest.

References

1. Dawson, J.B.; Steele, I.M.; Smith, J.V.; Rivers, M.L. Minor and trace element chemistry of carbonates, apatites and magnetites in some African carbonatites. *Mineral. Mag.* **1996**, *60*, 415–425. [CrossRef]
2. Reguir, E.P.; Chakhmouradian, A.R.; Halden, N.M.; Yang, P.; Zaitsev, A.N. Early magmatic and reaction-induced trends in magnetite from the carbonatites of Kerimasi, Tanzania. *Can. Mineral.* **2008**, *46*, 879–900. [CrossRef]
3. Selmi, M.; Lagoeiro, L.E.; Endo, I. Geochemistry of hematite and itabirite, Quadrilátero Ferrífero, Brazil. *Revista Escola de Minas* **2009**, *62*, 35–43. [CrossRef]
4. Cabral, A.R.; Rosière, C.A. The chemical composition of specular hematite from Tilkerode, Marz, Germany: Implications for the genesis of hydrothermal hematite and comparison with the Quadrilátero Ferrífero of Minas Gerais, Brazil. *Mineral. Depos.* **2013**, *48*, 907–924. [CrossRef]

5. Verdugo-Ihl, M.R.; Ciobanu, C.L.; Cook, N.J.; Ehrig, K.; Courtney-Davies, L.; Gilbert, S. Textures and U-W-Sn-Mo signatures in hematite from the Cu-U-Au-Ag orebody at Olympic Dam, South Australia: Defining the archetype for IOCG deposits. *Ore Geol. Rev.* **2017**, *91*, 173–195. [CrossRef]
6. Keyser, W.M.; Ciobanu, C.L.; Cook, N.J.; Johnson, G.; Feltus, F.; Johnson, S.; Dmitrijeva, M.; Ehrig, K.; Nguyen, P. Petrography and trace element signatures of iron-oxides in deposits from the Middleback Ranges, South Australia: From banded iron formation to ore. *Ore Geol. Rev.* **2018**, *93*, 337–360. [CrossRef]
7. Gao, W.; Ciobanu, C.L.; Cook, N.J.; Huang, F.; Mang, L.; Gao, S. Petrography and trace element signatures in silicates and Fe-Ti-oxides from the Lanjiahuoshan deposit, Panzhihua layered intrusion, Southwest China. *Lithos* **2017**, *294–295*, 164–183. [CrossRef]
8. Jones, T.S.; Kimura, S.I.; Muan, A. Phase relations in the system FeO–Fe_2O_3–ZrO_2–SiO_2. *J. Am. Ceram. Soc.* **1967**, *50*, 137–142. [CrossRef]
9. Bechta, S.V.; Krushinov, E.V.; Al'myashev, V.I.; Vitol, S.A.; Mezentseva, L.P.; Petrov, Y.B.; Lopukh, D.B.; Khabenskii, V.B.; Barrachin, M.; Hellmann, S.; et al. Phase relations in the ZrO_2–FeO system. *Russian J. Inorg. Chem.* **2006**, *51*, 325–331.
10. Morris, B.J.; Hough, J.K. *South Australia Steel and Energy Project, Peculiar Knob Prospect, South Australia*; Department of Mines and Energy Resources Report Book 97/9; Department of Primary Industries & Resources: Adelaide, Australia, 1997.
11. Nielson, S. *Peculiar Knob Resource Model Development*; Arrium Mining: Adelaide, Australia, 2014; 55p.
12. Schmidt, P.W.; McEnroe, S.A.; Clark, D.A.; Robinson, P. Magnetic properties and potential field modeling of the Peculiar Knob metamorphosed iron formation, South Australia: An analog for the source of the intense Martian magnetic anomalies? *J. Geophys. Res.* **2007**, *112*, B03102. [CrossRef]
13. Ciobanu, C.L.; Cook, N.J.; Maunders, C.; Wade, B.P.; Ehrig, K. Focused Ion Beam and Advanced Electron Microscopy for Minerals: Insights and Outlook from Bismuth Sulphosalts. *Minerals* **2016**, *6*, 112. [CrossRef]
14. Flint, R.B.; Benbow, M.C. *Geology of the Mount Woods Inlier*; Department of Mines, South Australia Report Book 77/134; Department for Energy and Mining: Adelaide, Australia, 1977; 50p.
15. Chalmers, N. *The Mount Woods Domain: A Geological Review and Discussion on Mineralisation Potential*; Department of Primary Industries and Resources Report Book 2007/7; Department of Primary Industries & Resources: Adelaide, Australia, 2007; 62p.
16. Parker, A.J.; Lemon, N.M. Reconstruction of the early Proterozoic stratigraphy of the Gawler Craton, South Australia. *J. Geol. Soc. Aust.* **1982**, *29*, 221–238. [CrossRef]
17. Vassallo, J.J.; Wilson, C.J.L. Structural repetition of the Hutchison Group metasediments, Eyre Peninsula, South Australia. *Aust. J. Earth Sci.* **2001**, *48*, 331–345. [CrossRef]
18. Szpunar, M.; Hand, M.; Barovich, K.; Jagodzinski, E.; Belousova, E. Isotopic and geochemical constraints on the Paleoproterozoic Hutchison Group, southern Australia: Implications for Paleoproterozoic continental reconstructions. *Precambr. Res.* **2011**, *187*, 99–126. [CrossRef]
19. Jagodzinski, E.A. Compilation of SHRIMP U-Pb geochronological data, Olympic Domain, Gawler Craton, South Australia, 2001–2003. *Geosci. Aust. Rec.* **2005**, *20*, 2005.
20. Fanning, C.M. *Ion-Microprobe U–Pb Zircon Dating of the Mount Woods Inlier, Preliminary Results*; Research School of Earth Sciences, Australian National University: Canberra, Australia, 1993; 8p.
21. Skirrow, R.G.; Bastrakov, E.N.; Barovich, K.; Fraser, G.L.; Creaser, R.A.; Fanning, C.M.; Raymond, O.L.; Davidson, G.J. Timing of iron oxide Cu-Au-(U) hydrothermal activity and Nd isotope constraints on metal sources in the Gawler Craton, South Australia. *Econ. Geol.* **2007**, *102*, 1441–1470. [CrossRef]
22. Forbes, C.J.; Giles, D.; Hand, M.; Betts, P.G.; Suzuki, K.; Chalmers, N.; Dutch, R. Using P-T paths to interpret the tectonothermal setting of prograde metamorphism: An example form the northeastern Gawler Craton, South Australia. *Precambr. Res.* **2011**, *185*, 65–85. [CrossRef]
23. Ambrose, G.J.; Flint, R.B. BILLA KALINA, South Australia. Explanatory Notes 250000 geological series Sheet SH/53-7. *Geol. Surv. South Austr.* **1981**, *1*, 36.
24. Fanning, C.M.; Flint, R.B.; Parker, A.J.; Ludwig, K.R.; Blisset, A.H. Refined Preoterozoic evolution of the Gawler Craton, South Australia, through U–Pb zircon geochronology. *Precambr. Res.* **1988**, *40/41*, 363–386. [CrossRef]
25. Finlay, J. Structural Interpretation of the Mount Woods Inlier. Ph.D. Thesis, Monash University, Melbourne, Australia, 1993.
26. Holm, O. New geochronology of the Mount Woods Inlier and the central Gawler gold province. In *Gawler Craton: State of Play 2004*; Report Book; Department of Primary Industries & Resources: Adelaide, Australia, 2004.

27. Jagodzinski, E.A.; Reid, A.J.; Chalmers, N.; Swain, G.; Frew, R.A.; Foudoulis, C. *Compilation of SHRIMP U-Pb Geochronological Data for the Gawler Craton, South Australia*; Department of Primary Industries & Resources Report Book 2007/21; Department of Primary Industries & Resources: Adelaide, Australia, 2007.
28. Belperio, A.; Flint, R.; Freeman, H. Prominent Hill: A hematite-dominated, iron oxide copper-gold system. *Econ. Geol.* **2007**, *102*, 1499–1510. [CrossRef]
29. Betts, P.G.; Valenta, R.K.; Finlay, J. Evolution of the Mount Woods Inlier, northern Gawler Craton, Southern Australia: An integrated structural and aeromagnetic analysis. *Tectonophysics* **2003**, *366*, 83–111. [CrossRef]
30. Davies, M.B. *Iron ore in South Australia*; Commodity Review No. 8; Primary Industries and Resources: Adelaide, Australia, 2000; 35p.
31. Daly, S.J.; Fanning, C.M.; Fairclough, M.C. Tectonic evolution and exploration potential of the Gawler Craton South Australia. *AGSO J. Aust. Geol. Geophys.* **1988**, *17*, 145–168.
32. Reid, A.J.; Fabris, A. Influence of preexisting low metamorphic grade sedimentary successions on the distribution of iron oxide copper-gold mineralization in the Olympic Cu-Au Province, Gawler Craton. *Econ. Geol.* **2015**, *110*, 2147–2157. [CrossRef]
33. Guillong, M.; Hametner, K.; Reusser, E.; Wilson, S.A.; Günther, D. Preliminary characteristics of new glass reference materials (GSA-1G, GSC-1G, GSD-1G and GSE-1G) by laser ablation-inductively coupled plasma-mass spectrometry using 193 nm, 213 nm and 266 nm wavelengths. *Geostand. Geoanal. Res.* **2005**, *29*, 315–331. [CrossRef]
34. Jochum, K.P.; Weis, U.; Stoll, B.; Kuzmin, D.; Yang, Q.; Raczek, I.; Jacob, D.E.; Stracke, A.; Gunther, D.; Enzweiler, J. Determination of reference values for NIST SRM 610-617 glasses following ISO guidelines. *Geostand. Geoanal. Res.* **2011**, *35*, 397–429. [CrossRef]
35. Van Achterbergh, E.; Ryan, C.G.; Jackson, S.E.; Griffin, W.L. Data reduction software for LA-ICP-MS. In *Laser-ablation-ICPMS in the Earth Sciences: Principles and Applications*; Sylvester, P.J., Ed.; Mineralogical Association of Canada: Quebec City, QC, Canada, 2001; pp. 239–243.
36. Woodhead, J.D.; Hellstrom, J.; Paton, C.; Hergt, J.M.; Greig, A.; Maas, R. A guide to depth profiling and imaging applications of LA-ICM-PS. In *Laser Ablation ICP-MS in the Earth Sciences: Current Practices and Outstanding Issues*; Mineralogical Association of Canada, Short Course Series 40; Sylvester, P.J., Ed.; Mineralogical Association of Canada: Quebec City, QC, Canada, 2008; pp. 135–145.
37. Ciobanu, C.L.; Cook, N.J.; Utsunomiya, S.; Pring, A.; Green, L. Focussed ion beam transmission electron microscopy applications in ore mineralogy: Bridging micro and nanoscale observations. *Ore Geol. Rev.* **2011**, *42*, 6–31. [CrossRef]
38. Compston, W.; Williams, I.S.; Meyer, C. U-Pb geochronology of zircon from lunar breccia 73217 using a sensitive high mass-resolution ion microprobe. *J. Geophys. Res.* **1984**, *89*, 525–534. [CrossRef]
39. Williams, I.S. U–Th–Pb geochronology by ion microprobe. In *Applications of Microanalytical Techniques to Understanding Mineralizing Processes*; McKibben, M.A., Shanks, W.C., Eds.; Society of Economic Geologists: Littleton, CO, USA, 1998; Volume 7, pp. 1–35.
40. McDonough, W.F.; Sun, S.S. Composition of the Earth. *Chem. Geol.* **1995**, *120*, 223–253. [CrossRef]
41. Swamy, V.; Dubrovinsky, L.S.; Dubrovinskaia, N.A.; Langenhorst, F.; Simionovici, A.S.; Drakopoulos, M.; Dmitriev, V.; Weber, H.-P. Size effects on the structure and phase transition behavior of baddeleyite TiO_2. *Solid State Commun.* **2005**, *134*, 541–546. [CrossRef]
42. Craig, J.R.; Vaughan, D.J. *Ore Microscopy and Ore Petrography*, 2nd ed.; John Wiley & Sons: Hoboken, NJ, USA, 1994.
43. Löffler, L.; Mader, W. Anisotropic X-ray peak broadening and twin formation in hematite derived from natural and synthetic goethite. *J. Eur. Ceram. Soc.* **2006**, *26*, 131–139. [CrossRef]
44. Avila, C.F.; Lagoeiro, L.; Barbosa, P.F.; Graca, L. EBSD analysis of rhombohedral twinning in hematite crystals of naturally deformed iron formations. *J. Appl. Crystallogr.* **2015**, *48*, 212–219. [CrossRef]
45. Gao, W.; Ciobanu, C.L.; Cook, N.J.; Slattery, A.; Huang, F.; Wang, D. Nanoscale study of lamellar exsolutions in clinopyroxene from olivine gabbro: Recording crystallization sequences in iron-rich layered intrusions. *Am. Mineral.* **2018**, *104*, 244–261.
46. Morisset, C.; Scoates, J.S.; Weis, D.A. Partitioning of trace elements during exsolution in ilmenite-hematite series minerals by LA-ICP-MS. In Proceedings of the AGU Fall Meeting Abstracts, San Francisco, CA, USA, 12–16 December 2010.

47. Lane, K.; Jagodzinski, E.A.; Dutch, R.; Reid, A.J.; Hand, M. Age constraints on the timing of iron ore mineralisation in the southeastern Gawler Craton. *Aust. J. Earth Sci.* **2015**, *62*, 55–75. [CrossRef]
48. Bingen, B.; Austrheim, H.; Whitehouse, M. Ilmenite as a source for zirconium during high-grade metamorphism? Textural evidence from the Caledonides of western Norway and implications for zircon geochronology. *J. Petrol.* **2001**, *42*, 355–375. [CrossRef]
49. Moëlo, Y.; Lulzac, Y.; Rouer, O.; Palvadeau, P.; Gloaguen, É.; Léone, P. Scandium mineralogy: Pretulite with scandian zircon and xenotime-(Y) within an apatite-rich oolitic ironstone from Saint-Aubin-des-Châteaux, Armorican Massif, France. *Can. Mineral.* **2002**, *40*, 1657–1673. [CrossRef]
50. Cook, N.J.; Ciobanu, C.L.; O'Reilly, D.; Wilson, R.; Das, K.; Wade, B. Mineral chemistry of rare earth element (REE) mineralization, Browns Range, Western Australia. *Lithos* **2013**, *172*, 192–213. [CrossRef]
51. Harley, S.L.; Kelly, N.M.; Möller, A. Zircon behavior and the thermal histories of mountain chains. *Elements* **2007**, *3*, 25–30. [CrossRef]
52. Kohn, M.J.; Corrie, S.L.; Markley, C. The fall and rise of metamorphic zircon. *Am. Mineral.* **2015**, *100*, 897–908. [CrossRef]
53. Keyser, W.M.; Ciobanu, C.L.; Cook, N.J.; Courtney-Davies, L.; Ehrig, K.; Gilbert, S.; McPhie, J. Links between sedimentary protoliths and IOCG Links between sedimentary protoliths and IOCG-skarn skarn alteration, Island Dam, South Australia. In Proceedings of the 14th SGA Biennial Meeting, Quebec City, QC, Canada, 20–23 August 2017; pp. 935–938.
54. Cook, N.J.; Ciobanu, C.L.; George, L.; Zhu, Z.-Y.; Wade, B.; Ehrig, K. Trace Element Analysis of Minerals in Magmatic-Hydrothermal Ores by Laser Ablation Inductively-Coupled Plasma Mass Spectrometry: Approaches and Opportunities. *Minerals* **2016**, *6*, 111. [CrossRef]
55. Ludwig, K.R.A. *SQUID*, version 2.50; Special Publication No. 5; A User's Manual; Berkeley Geochronology Center: Berkeley, CA, USA, 2009; p. 110.
56. Steiger, R.H.; Jäger, E. Subcommission of geochronology: Convention on the use of decay constants in geo- and cosmochronology. *Earth Plan. Sci. Lett.* **1977**, *36*, 359–362. [CrossRef]
57. Armstrong, J.T. Quantitative analysis of silicate and oxide minerals: Comparison of Monte Carlo, ZAF, and φ(ρz) procedures. In *Microbeam Analysis*; Newbury, D.E., Ed.; San Francisco Press: San Francisco, CA, USA, 1988; pp. 239–246.
58. Claoué-Long, J.C.; Compston, W.; Roberts, J.; Fanning, C.M. Two carboniferous ages: A comparison of SHRIMP zircon dating with conventional zircon ages and $^{40}Ar/^{39}Ar$ analysis. In *Berggren, Geochronology Time Scales and Global Stratigraphic Correlation*; Berggren, W.A., Kent, D.V., Aubrey, M.P., Hardenbol, J., Eds.; Society of Sedimentary Geology Special Publication: Tulsa, OK, USA, 1995; pp. 3–21.
59. Goemann, K.; Donovan, J.J. Electron probe microanalysis of complex natural sulphides using shared background measurements. In Proceedings of the 14th Biennial Australian Microbeam Analysis Symposium (AMAS 2017), Brisbane, Australia, 6–10 February 2017; pp. 61–62, ISBN 978-0-9580408-6-0.
60. Goemann, K.; Donovan, J.J.; Feig, S.T.; Thompson, J. "Sharing" Background Measurements in Wavelength Dispersive Electron Probe Microanalysis. In Proceedings of the Microanalysis Society—Topical Conference on Electron-Probe Microanalysis, Program Guide with Abstracts, Madison, WI, USA, 16–19 May 2016; pp. 28–29, ISBN 978-1-5323-0217-6.
61. Goemann, K.; Donovan, J.J.; Feig, S.T.; Thompson, J. Shared backgrounds in wavelength-dispersive electron probe microanalysis. In Proceedings of the 15th European Workshop on Modern Developments and Applications in Microbeam Analysis, 7th Meeting of the International Union of Microbeam Analysis Societies, Konstanz, Germany, 7–11 May 2017; pp. 378–379, ISBN 978-90-8827-693-0.
62. Donovan, J.J.; Rowe, M. Techniques for Improving Quantitative Analysis of Mineral Glasses. *Geochim. Cosmochim. Acta* **2005**. Goldschmidt abstracts.
63. Donovan, J.J.; Tingle, T.N. An Improved Mean Atomic Number Background Correction for Quantitative Microanalysis. *Microsc. Microanal.* **1996**, *1*, 1–7. [CrossRef]
64. Donovan, J.J.; Singer, J.W.; Armstrong, J.T. A new EPMA method for fast trace element analysis in simple matrices. *Am. Mineral.* **2016**, *101*, 1839–1853. [CrossRef]

CHAPTER 8

SUMMARY, RECOMMENDATIONS AND CONCLUDING REMARKS

CHAPTER 8: SUMMARY, RECOMMENDATIONS AND CONCLUDING REMARKS

8.1 Summary

Iron-oxides are ubiquitous components of many deposit types (e.g., iron-oxide-copper-gold, iron-oxide-apatite), but in iron deposits hosted by, or derived from BIFs, they constitute the main ore. Within such environments, iron-oxides undergo extensive alteration resulting from different types of fluid-rock interaction that yield complex paragenetic sequences in which iron-oxides can, and do, occur as successive generations. The findings presented in this research show that iron-oxides from BIFs and ores in the Middleback Ranges display textural and geochemical changes that, if characterized at appropriate scales of observation, provide an understanding of those processes and can track transition from BIF deposition to ore formation. Many of the iron-oxide characteristics described here are recognizable in analogous terranes elsewhere. However, other characteristics are unique to specific geological settings, and as shown in this thesis, thorough investigations of both the iron ores, host and associated lithologies, can define signatures that are attributable to specific regional-scale events.

8.1.1 Iron-oxide geochemistry: fingerprinting a protracted geological history

All iron-oxides studied throughout the Middleback Ranges belt show evidence for extensive overprinting in the transformation from BIF to ore. Although the occurrence of iron-oxides varies depending on ore type (e.g., magnetite BIF vs. goethite ore), the overprinting process can be generically defined by the sequence: magnetite → martite → microplaty hematite ± goethite (with exceptions, e.g., microplaty hematite from Iron Knight), with the transformation from one iron-oxide into another reflected in changing ΣREY concentrations and fractionation

trends. For example, the pseudomorphic replacement of magnetite by hematite is characterized by increasing ΣREY and LREE-enrichment. However, the presence of specific element groups measured within iron-oxides from various parts of the belt, e.g., 'granitophile elements' (U, W, Sn, Mo), or transition metals (Cr, Mn, Co, Ni, Ti, V, Nb), suggests interaction with evolving fluids in the presence of hydrothermal fluids associated with felsic and mafic igneous rocks, respectively. Moreover, the marked As and Sb enrichment in iron-oxides from the northern segment of the belt, and of Sn, Mo, W and U enrichment in the south, highlight the impact of local settings on ore formation.

The most exemplary display of petrographic-textural changes in iron-oxide attributable to a specific geological setting along the Middleback Ranges belt are those from the case study on the Iron Count prospect (Keyser et al., 2019a, Chapter 3). Here, the first integrated petrographic, geochemical and geochronological characterization of iron-oxides in the prospect identified the cause of ore formation as resulting from interaction between BIF and fluids associated with the ~1.79 Ga Wertigo Granite, emplaced during an intracontinental rifting event. This interpretation was derived from hematite trace element geochemistry and U–Pb hematite ages, as well as from observed mineral associations (e.g., monazite). An important implication of this study was direct evidence of magmatically-derived fluid involvement.

Central to many genetic models for BIF-derived ore deposits is the role of interactions between BIF and magmatic fluids in hypogene alteration processes, based on fluid inclusion studies (e.g., Rosière and Rios, 2004; Figueiredo e Silva et al., 2013). However, direct evidence of magmatic fluid interaction is often hampered by a lack of complementary geochronological data for the intrusive bodies interpreted to have supplied hydrothermal fluids (Hagemann et al., 2016). Findings from the Iron Count prospect provide additional support for genetic models centered on the hypothesis that magmatic hydrothermal fluids interact with BIF in upgrading

processes. Additionally, iron mineralization at the Island Dam prospect and Peculiar Knob deposit are also attributable to comparable interactions between BIF-like protoliths with granitic fluids based on W-Nb-Sb-Sn-rich signatures within iron-oxides, a key characteristic of regional IOCG-metasomatism in the eastern Gawler Craton generated through emplacement of the ~1.6 Ga Hiltaba Suite intrusives.

8.1.2 Defining pre-, syn- and post-depositional BIF environments

Recognition of a large variation in iron-oxide signatures within BIFs and ores, observed throughout the Middleback Ranges but certainly also present in BIFs elsewhere, calls for a better understanding for local deposit settings and their tectonothermal history. As a consequence of the studies performed on iron-oxides in Chapters 2 and 3, new findings regarding regional geology were also established in connection to iron-oxide formation (Chapters 4 and 5). These chapters, although focusing on regional geological context rather than directly on the iron-oxides themselves, are within the scope of the study and assess the impact of local geology on iron-oxide formation, the results of which have implications for analogous BIF terranes with protracted geological histories.

A key finding of the research performed in Chapter 4 was recognition of Mesoarchean crust as the depositional site for BIF in the Middleback Ranges. This interpretation was based upon U–Pb SHRIMP ages of 3.0-3.2 Ga for granites associated with the orebodies throughout the belt. In addition to these ages, granite petrography indicated post-emplacement overprints, possibly inferring fluid-rock interactions and granite leaching as important attributes of the BIF upgrading process and iron-oxide formation, further supporting signatures presented in Chapters 2 and 3. Significant among these overprints were features indicative of fluid-rock interactions with hydrothermal fluids attributable to a regional ~1.6 Ga IOCG-style mineralization in the Gawler Craton.

Further constraints made on local lithologies associated with the orebodies throughout the Middleback Ranges belt led to recognition of a craton-scale event impacting on ore formation. Mafic sills and dikes associated with the orebodies were found to be distinguishable based on field occurrence, mineralogy and U–Pb SHRIMP zircon ages. The results showed that older amphibolites (~2.5 Ga) were emplaced contemporaneous with BIF deposition, after which they were affected by multiple overprints leading to complex metamorphic assemblages consisting of coexisting Mg-Fe- and Ca-amphiboles. A detrital origin is proposed as a possible explanation for relict titaniferous magnetite displaying ilmenite exsolution identified within these amphibolites, an interpretation that bears significance for understanding factors contributing to BIF depositional environments. Contrastingly, NW-trending dolerite dikes crosscutting BIF contain igneous assemblages of magnesiohornblende + plagioclase. U–Pb SHRIMP zircon data showed the dikes to be associated with the ~800 Ma Gairdner large igneous province, while their alteration features and young hematite ages from associated ores suggested multiple events leading to upgrading or iron ores.

8.2 Recommendations

Bridging micron- to nanoscale observations of ore minerals using complementary techniques and particularly advanced transmission electron microscopy on the same sample material (e.g., van Tendeloo et al., 2014; Ciobanu et al., 2011; 2016; Cook et al., 2017) has become increasingly recognized as an important tool for bolstering interpretations of ore deposit genesis and refining those models. Not only can such an approach address the presence of specific trace elements in ore minerals (e.g., Si-Fe nanoprecipitates in magnetite; Xu et al., 2014; Ciobanu et al., 2019 and references therein), but can also assist in unravelling the evolution of ore deposits (e.g., Keyser et al., 2019a; Chapter 7). Within the research presented

in this thesis, there are several topics that demand further attention, some of which are described in the following sections.

8.2.1 Nanoscale studies to understand formation of hematite ores

A range of different iron-oxide (inter)conversions are required to achieve transformation from BIF to various ore types (e.g., martite ores, martite-goethite ores), as described in this thesis. Martitization is essential to the enrichment process and is the most widespread expression of iron-oxide transformation observed in ores from the Middleback Ranges. This process is followed by supergene weathering leading to martite replacement by goethite. However, dehydration processes have also been proposed leading to formation of microplaty hematite within ores (martite-microplaty hematite ores), an important ore-type within the Hamersley Province. Morris (2012) compared two models for formation of microplaty hematite ores of the Hamersley Province. The first model discusses burial of martite-goethite ores at low-temperature (~80-100 ˚C) regional metamorphic conditions. This leads to dehydration of goethite to form microplaty hematite (mplH), with residual fluids generated by the process crystallizing additional microplaty hematite through iron transfer within voids. This model was favored over a second model, in which oxidation of introduced siderite resulted in mplH + ankerite by reaction of heated meteoric fluids with hydrothermally metasomatized BIF 'protore'.

Hematite ores from Iron Knight show textural evidence for replacement of goethite by microplaty hematite. Here, Si-bearing hematite (up to 1.8 wt% SiO_2; Keyser et al., 2018) displays oscillatory crystal zonation at the micron-scale (Fig. 8.1A). High-angle annular dark field scanning transmission electron microscopy imaging (HAADF-STEM) and energy-dispersive spectrometry STEM mapping at the nanoscale confirm the presence of Si-bearing bands (Fig. 8.1B). The bands show a mottled texture with Si-Fe-nanoparticle (<100 nm) inclusions (NPs; Fig. 8.1C, D) rather than being continuous as apparently displayed at the

micron-scale (BSE image in Figure 8.1A). High-resolution HAADF STEM imaging show the NPs are coherent with host hematite (Fig. 8.1D). The Si-bearing patterns at the micron-scale can be attributed to formation of Si-Fe-nanoprecipitates during transformation of iron-hydroxides into hematite. Further work is nonetheless required to assess the crystal structure of the Si-Fe-NPs. STEM EDS mapping at different scales (Fig. 8.1E,F) shows that the mottling texture is depictable only at higher magnification.

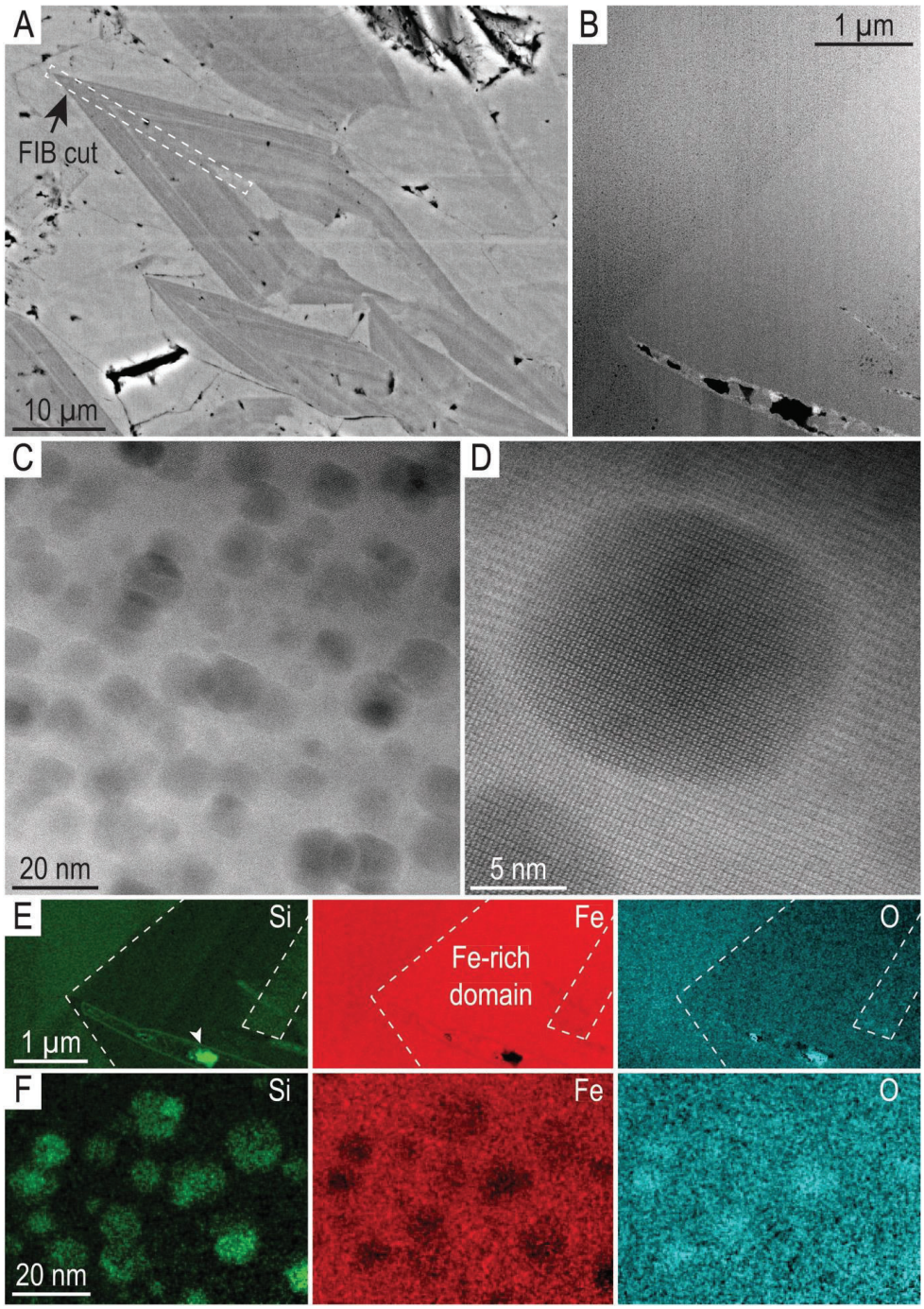

Figure 8.1: (A) BSE imagine showing hematite displaying oscillatory zoning with respect to Si. Location of focused ion beam (FIB) cut indicated by dashed rectangle. HAADF-STEM images showing (B) banding within hematite, (C) mottled texture with agglomeration of Si-Fe-bearing NPs and (D) one of the NPs with epitaxial relationship relative to host hematite. (C, D) STEM-EDS element maps showing (E) alternating of Si-rich and -poor bands in hematite and (F) a field of Si-Fe NPs. White arrow in (E) indicates a SiO_2 inclusion along a later fracture.

The hydroxides would contain Si and other impurities which, upon burial and dehydration, tend to reorganize within the crystal structure of hematite. Work in progress suggests that the Si-Fe-NPs show evidence for changes into a superstructure that can be interpreted as maghemite (γ-Fe_2O_3) with ordered vacancies. Although further work will be needed in order to confirm this interpretation, preliminary findings support burial dehydration to form ores at the Iron Knight deposit in the Middleback Ranges.

8.2.2 Inclusions in magnetite from BIF and associated lithologies

Recognition of titaniferous magnetite displaying ilmenite exsolution from amphibolites at Iron Magnet (Chapter 5), interpreted as detrital input from a mafic source into a marginal sedimentary basin, holds important implications for understanding processes occurring during BIF deposition. Such magnetite is absent in the adjacent interbedded BIF, which also lack the metamorphic assemblages (Mg-Fe- and Ca-amphiboles, almandine) present in the amphibolites, despite containing assemblages suitable for formation of Mg-Fe-amphiboles (e.g., talc, minnesotaite). Magnetite within these BIFs does, however, contain magnetite with fine-grained inclusions (Keyser et al., 2018; Fig. 6F), which may, in fact, be relict igneous, metamorphic phases or BIF-depositional related inclusions, e.g., Si-Fe-nanoprecipitates in metamorphosed BIF magnetite from the Dales Gorge Member of the Brockman Iron

Formation, Hamersley Group, Western Australia (Huberty et al., 2012; Xu et al, 2014). Fine-grained, oriented, Mg-rich inclusions were also observed in magnetite from Iron Count (Keyser et al., 2019b; Fig. 5D). A nanoscale comparison of various magnetite types that display inclusions is needed in order to identify possible relict phases, which would shed further light on early processes that occur during, or immediately following BIF deposition.

8.2.3 Understanding the link between BIF and IOCG deposits

Banded iron formation- and IOCG-deposits are common ore systems that span the Archean to the Proterozoic (with a limited number of younger analogues) and are found spatially and temporally associated with one another in several regions of the Earth (e.g., Brazil, South Africa, South Australia). This raises the question of their relationships to one another and the crustal processes underpinning that relationship. For example, Hagemann et al. (2016) noted the need to investigate the relationship between contemporaneous BIF upgrading in the Serra Sul iron ore district in Carajás Mineral Province, Brazil, and formation of IOCG deposits within distances of no more than a few kilometers. The Olympic Cu-Au Province in South Australia is characterized by a regional-scale IOCG mineralization attributed to a regional alteration event resulting from emplacement of the ~1.6 Ga Hiltaba Suite granites. Within this province, BIF lithologies are represented in various metasedimentary packages (e.g., the Wallaroo Group metasedimentary rocks). Keyser et al. (2019a, b; Chapters 6 and 7) describe cases in which hematite from BIF-like lithologies show enrichment in elements such as W, Nb, Sb and Sn, elements that are characteristic of IOCG alteration/mineralization in the region. From this perspective, future studies of the two deposit types, where associated, need to address how the two may be genetically linked, including the long-standing but still unproven suggestion that pre-existing BIFs may have been an important source of iron within IOCG systems.

8.3 Concluding remarks

The ore deposits of the Middleback Ranges have been known and explored since the late 19th century and under continuous mining for more than 100 years. Despite this, detailed mineralogical studies have not been conducted on the BIF and ores that comprise the deposits until now, much less the geology or mineralogy of the host basement sequence and associated lithologies. The research presented within this thesis provides much-needed mineralogical and geochronological information for understanding iron ore genesis within the Middleback Ranges, and complements existing, but limited, structural, geophysical, and geochemical studies on the belt (e.g., Bubner et al., 2003; Leevers et al., 2005; Szpunar et al., 2011). Moreover, it contributes to the growing field of studies on BIF, their constituent minerals, BIF-hosted ore deposits and the processes leading to their formation, as well as the regional geology of the Eyre Peninsula, South Australia.

Key conclusions from the research conducted in this thesis are:

1. Iron-oxides from BIF and ores across the Middleback Ranges iron ore belt, the Island Dam prospect and the Peculiar Knob iron deposit, show a range of compositional and textural variations indicative of multiple overprints defining the ore forming processes.
2. A Mesoarchean granitic basement extends beneath the entire Middleback Ranges BIF sequence and records overprinting events that contributed to iron-oxide formation.
3. Episodic mafic magmatism, distinguishable from field occurrence, mineral assemblages and U–Pb SHRIMP zircon ages, occurred contemporaneous with BIF deposition at ~2.5 Ga and in association with emplacement of the ~800 Ma Gairdner large igneous province, both of which impacted on iron-oxide chemistry.
4. U–Pb hematite geochronology can be successfully applied to BIF ores. Ore formation in the Middleback Ranges, as shown from U–Pb hematite age at the Iron Count prospect and

from Iron Knight South, was multistage and occurred over a prolonged geological history, with local deposit geology playing an important role in the process.

5. Detailed petrographic and geochemical studies combined with U–Pb hematite geochronology can be used to give insights into trace element incorporation into, and later release from, iron-oxides.

References

Bubner, G., Dentith, M., Dhu, T., Hillis, R., 2003. Geophysical exploration for iron ore in the Middleback Ranges, South Australia. Australian Society of Exploration Geophysicists Special Publications 3, 29-46.

Ciobanu, C.L., Cook, N.J., Maunders, C., Wade, B.P., Ehrig, K., 2016. Focused ion beam and advanced electron microscopy for minerals: Insights and outlook from bismuth sulphosalts. Minerals 6, 112. https://doi.org/10.3390/min6040112.

Ciobanu, C.L., Cook, N.J., Utsunomiya, S., Pring, A., Green, L., 2011. Focussed ion beam-transmission electron microscopy applications in ore mineralogy: Bridging micro- and nanoscale observations. Ore Geology Reviews 42, 6-31.

Ciobanu, C.L., Verdugo-Ihl, M.R., Slatter, A., Cook, N.J., Ehrig, K., Courtney-Davies, L., Wade, B.P., 2019. Silician magnetite: Si-Fe-nanoprecipitates and other mineral inclusions in magnetite from the Olympic Dam deposit, South Australia. Minerals 9, 311. https://doi.org/10.3390/min9050311.

Cook, N.J., Ciobanu, C.L., Ehrig, K., Slattery, A., Verdugo-Ihl, M.R., Courtney-Davies, L., Gao, W., 2017. Advances and opportunities in ore mineralogy. Minerals 7, 223. https://doi.org/10.3390/min7120233.

Figueiredo e Silva, R.C., Hagemann, S.G., Lobato, L.M., Rosière, C.A., Banks, D.A., Davidson, G.J., Vennemann, T.W., Hergt, J.M., 2013. Hydrothermal fluid processes and evolution of the giant Serra Norta jaspilite-hosted iron ore deposits, Carajás Mineral Province, Brazil. Economic Geology 108, 739-779.

Hagemann, S.G., Angerer, T., Duuring, P., Rosière, C.A., Figueiredo e Silva, R.C., Lobato, L., Hensler, A.S., Walde, D.H.G., 2016. BIF-hosted iron mineral system: A review. Ore Geology Reviews 76, 317-359.

Huberty, J.M., Konishi, H., Heck, P.R., Fournelle, J.H., Valley, J.W., Xu, H., 2012. Silician magnetite from the Dales Gorge Member of the Brockman Iron Formation, Hamersley Group, Western Australia. American Mineralogist 97, 26-37.

Keyser, W., Ciobanu, C.L., Cook, N.J., Feltus, H., Johnson, G., Slattery, A., Wade, B.P., Ehrig, K., 2019b. Mineralogy of zirconium in iron-oxides: A micron- to nanoscale study of hematite ore from Peculiar Knob. Minerals 9, 244. https://doi.org/10.3390/min9040244.

Keyser, W., Ciobanu, C.L., Cook, N.J., Johnson, G., Dmitrijeva, M., Courtney-Davies, L., Feltus, H., Gilbert, S., Johnson, G., Ehrig, K., 2019a. Iron-oxides constrain BIF evolution in terranes with protracted geological histories: the Iron Count prospect, Middleback Ranges, South Australia. Lithos 324-325, 20-38.

Keyser, W.M., Ciobanu, C.L., Cook, N.J., Johnson, G., Feltus, F., Johnson, S., Dmitrijeva, M., Ehrig, K., Nguyen, P., 2018. Petrography and trace element signatures of iron-oxides in deposits from the Middleback Ranges, South Australia: from banded iron formation to ore. Ore Geology Reviews 93, 337-360.

Leevers, P., Gaughan, C., Bubner, G., 2005. The Iron Magnet deposit. Australasian Institute of Mining and Metallurgy Publication Series, Iron Ore Conference, Fremantle, WA, 19-21 September 2005.

Morris, R.C., 2012. Microplaty hematite–its varied nature and genesis. Australian Journal of Earth Sciences 59, 411-434.

Rosière, C.A., Rios, F.J., 2004. The origin of hematite in high-grade iron ores based on infrared microscopy and fluid inclusion studies: the example of the Conceição mine, Quadrilátero Ferrífero, Brazil. Economic Geology 99, 611-624.

Szpunar, M., Hand, M., Barovich, K., Schwarz, M., Jagodzinski, E., Belousova, E., 2011. Isotopic and geochemical constraints on the Paleoproterozoic Hutchison Group, southern

Australia: Implications for Paleoproterozoic continental reconstructions. Precambrian Research 187, 99-126.

Van Tendeloo, G., Bals, S., van Aert, S., Verbeeck, J., van Dyck, D., 2012. Advanced electron microscopy for advanced materials. Advanced Materials 24, 5655-5675.

Xu, H., Shen, Z., Konishi, H., 2014. Si-magnetite nano-precipitates in silician magnetite from banded iron formation: Z-contrast imaging and ab initio study. American Mineralogist 99, 2196-2202.